UNIVERSITY OF SILESIA
IN KATOWICE

FACULTY OF SCIENCE AND TECHNOLOGY,

INSTITUTE OF CHEMISTRY

ALICJA MENŻYK

Ph.D. thesis

TOWARD A SPECTROSCOPY-BASED APPROACH FOR ESTIMATING TIME ELAPSED SINCE BLOODSTAINS DEPOSITION

DEVELOPMENT OF A NOVEL FRAMEWORK FOR BLOOD EVIDENCE EVALUATION

PRINCIPAL SUPERVISOR: PROF. GRZEGORZ ZADORA, DSc

UNIVERSITY OF SILESIA IN KATOWICE, POLAND
INSTITUTE OF FORENSIC RESEARCH, KRAKOW, POLAND

ASSISTANT SUPERVISOR: AGNIESZKA MARTYNA, PhD

UNIVERSITY OF SILESIA IN KATOWICE, POLAND

KATOWICE, 2021

ACKNOWLEDGMENTS

Throughout the research and writing process of this dissertation, I have received a great deal of support and assistance, without which I would not have made any headway in the project. Therefore even though a doctoral thesis is often described as a solitary endeavor, the following list proves the exact opposite.

First and foremost, I am deeply grateful for the continuous guidance, insight, and – most importantly – **PATIENCE** of my principal supervisor, **Prof. Grzegorz ZADORA**. Without his constant trust (often on the verge of deadlines and breakdowns) enhanced with gentle prodding, this thesis would not have been completed. The received possibility of making independent decisions has shaped me as a researcher. My gratitude extends to **Dr. Agnieszka MARTYNA** – my assistant supervisor – whose experience and knowledge of the subject matter steered me through the research. Mainly its computational part. Her hard work, immense knowledge, and plentiful experience keep encouraging me in all the time of my academic research.

I am indebted to **Prof. Marco VINCENTI** from the Università degli Studi di Torino for all his generous support. His heartfelt welcoming me into the Italian academic community and providing the crucial research equipment has removed one of the main infrastructure concerns from this journey. Above all, however, his scientific mentorship was really influential in shaping my experiment methods and taming my inner compulsive writer.

My appreciation also goes out to **Prof. Gianmario MARTRA**† from the Università degli Studi di Torino for guiding me to the world of Raman spectroscopy. The meetings and conversations were vital in maintaining the desired blood sugar level and inspiring me to think outside the box, investigate the problem at hand from multiple perspectives to form a comprehensive and objective critique.

I am particularly grateful to **Dr. Alessandro DAMIN** – my "Master and Commander" from the Università degli Studi di Torino – who had no choice but to put up with my stresses and moans for the "disgusting" time spent together in the Raman lab. Without his expert knowledge and cold blood (its aging kinetics has to be still verified), I would not have started this research, let alone complete it.

I also would like to thank all other representatives of Italian academia who cannot be officially listed here. Their never-ending generosity, intelligence, attitude to research and life have never failed to amaze me. Thanks to you (or perhaps because of you), a part of me will stay in Italy forever.

I also appreciate all the support I received from the group of **Prof. Michał DASZYKOWSKI,** who kindly provided me with working space and good-quality coffee at the beginning of my Ph.D. journey.

To conclude, I cannot forget to thank my family and friends for all the unconditional support in this very intense period. Your patience and encouragement enabled this research to be possible. I also wish to thank all my Italian housemates who always made me feel at home and taught me the authentic Carbonara recipe.

Finally, it should be clearly stated that any omission in these brief acknowledgments does not mean a lack of gratitude, just a lack of sleep!

“ART IS NEVER FINISHED, ONLY ABANDONED.”

– LEONARDO DA VINCI

*Dedicated to the memory of PROFESSOR **GIANMARIO MARTRA***

ABSTRACT

A batch of evidence that has gained prominence in courtrooms are bloodstains, often the main driving force behind an investigation process. Unfortunately, in the era of DNA testing, it is frequently overlooked that verifying who was the "source" of the trace is not always the critical issue. And this is because it is fairly common among suspects not to question the identification of his/her blood but rather the time at which it was deposited at the crime scene. Therefore, to increase the evidential value of the trace in question, it is often necessary to demonstrate a unity of time and place, proving that the person of interest was on the crime scene within a given time interval. This can be done by providing the final piece of the forensic puzzle – information about bloodstains' age.

The attempt to estimate the time elapsed since trace deposition is possible due to aging processes, which lead to alterations in physicochemical properties of the examined bloodstain. Surprisingly, despite the nearly century-old research efforts, a reliable method for estimating bloodstains' age is still missing. Having looked into previous examples of dating studies, it can be concluded that it is the wrong approach for data analysis, which should be blamed for the delayed exploitation of already developed methods in forensic practice. It seems that there is a significant discussion, but any proposed way forward leads to the same intractable crossroads. According to the universally adopted strategy, the majority of proposed dating techniques have been guided by a simple principle – they have sought the dependency between some dynamic properties of degrading blood and time, usually through the employment of regression analysis. The aging process, however, is not only a matter of time. No two crime scenes are ever precisely the same. Neither are the degradation pathways of blood deposits; hence, using dating models trained on the very limited datasets might lead to misestimations of bloodstains' age, depriving these conventional methods of entire practical value.

The present dissertation takes a few steps back to investigate the dating problem from an entirely different perspective and, eventually, proposes the novel framework for estimating time elapsed since bloodstains deposition. It is hypothesized that impediments resulting from variability of aging kinetics can be addressed by substituting a case-suited comparison problem for the conventional dating approach. The critical aspect of this concept is the likelihood ratio-based assessment of the (dis)similarity between the stage of evidence decomposition and sets of reference materials obtained through supervised aging. This means that every dating procedure would be constructed on a case-by-case basis, each time tailored to fit the examined traces. In such a way, the influence of external factors (donor characteristics, environmental conditions, nature of the substrate) on the analysis's validity should be considerably reduced.

Establishing such a procedure was considered a dual problem that required addressing two distinct issues. In the first part of the research, an analytical method for characterizing the state of bloodstains degradation was developed. Given the characteristics of the examined trace, the choice of

Raman spectroscopy seemed a logical decision. And, indeed, the obtained results proved the effectiveness of Raman spectroscopy as a method capable of delivering information inherent to chemical changes accompanying the degradation process of heme-containing proteins. After establishing a Raman-based strategy for non-invasive and representative probing of the chemical alterations of aging bloodstains, the research entered the next phase. The second part of the study focused on designing the hybrid likelihood ratio (LR) models for solving the so-called comparison problem between the Raman signatures characterizing questioned bloodstain and reference material(s) created in a supervised manner. Results of models' validation provided preliminary confirmation of the effectiveness of the proposed dating approach. Best performing LR models were deemed satisfactory (with false positive and false negative rates oscillating around 20% and 10%, respectively) but provided that samples used for training and validating models were characterized by similar aging kinetics. This conclusion, however, should not come as a surprise since providing reference materials as similar as possible to the evidence deposited during the offense is, in fact, a fundamental requirement of the proposed novel dating methodology.

STRESZCZENIE

Grupą materiałów dowodowych, która na dobre zagościła na salach sądowych, są ślady krwawe stanowiące często główną siłę napędową procesu dochodzeniowego. Wdrożenie do praktyki sądowej genetycznych badań identyfikacyjnych bezsprzecznie stanowiło kamień milowy w rozwoju kryminalistyki, rozpoczynając swoistą „dominację" badań DNA. Okazuje się jednak, że wyniki analiz genetycznych nie zawsze pozwalają udzielić wyczerpującej odpowiedzi na stawiane pytania, a czasowy aspekt utworzenia śladów krwawych niejednokrotnie bywa równie istotny, co przebieg zdarzeń prowadzących do ich powstania. Informacja o czasie uformowania plam krwawych może bowiem wspomóc proces dochodzeniowy w wieloraki sposób. W przypadku ujawnienia śladów krwawych pochodzących od podejrzanego, tak naprawdę dopiero informacja o czasie powstania śladu stanowi dla zleceniodawcy silną przesłankę przemawiającą za udziałem podejrzanego w zdarzeniu. Rezultaty datowania śladów pozwalają więc potwierdzić jego obecność na miejscu zdarzenia w konkretnym czasie, stanowiąc cenniejszy dowód w sprawie aniżeli same wyniki badań genetycznych.

Podjęcie próby odpowiedzi na pytanie o czas powstania śladów krwawych jest możliwe dzięki procesom starzeniowym, które prowadzą do zmian właściwości fizykochemicznych badanego materiału. Niestety, wieloletnie próby stworzenia metodyki bezwzględnego datowania krwi nie dały jak dotąd pozytywnego rezultatu, przez co informacja o czasowym aspekcie powstania śladów krwawych wciąż pozostaje poza zasięgiem biegłych. Analiza dotychczasowych badań prowadzi jednak do pewnych wniosków – przyczyna owych niepowodzeń najprawdopodobniej ma swoje źródło w nieodpowiednim podejściu do problemu datowania. Okazuje się bowiem, że zgodnie z powszechnie przyjętą strategią, większość zaproponowanych rozwiązań sprowadzała się do zdefiniowania pewnego mierzalnego parametru, odzwierciedlającego stopień degradacji krwi, a następnie powiązania jego zmian z upływającym czasem (najczęściej za pomocą technik kalibracyjnych). Problem jednak w tym, że proces starzeniowy to nie tylko kwestia czasu. Materiał dowodowy może degradować w różnym tempie w zależności od wielu czynników zewnętrznych – przede wszystkim warunków środowiskowych panujących na miejscu zdarzenia. Tym samym, owe konwencjonalne modele datowania, opracowywane dla próbek degradujących w warunkach laboratoryjnych, okazywały się zawodne podczas prób przeniesienia ich na grunt praktycznych analiz.

Rozwiązanie, zaproponowane w ramach nieniejszej rozprawy, stanowi ujęcie zagadnienia datowania jako problemu porównawczego, rozpatrywanego w ramach podejścia korzystającego z ilorazu wiarygodności (LR, ang. likelihood ratio), który uwzględniać będzie wpływ czynników zewnętrznych na proces degradacji krwi. Podstawą owej nowej metodyki szacowania "wieku" śladów krwawych jest ocena podobieństwa pomiędzy stopniem degradacji materiału dowodowego a rozkładem materiałów porównawczych, uzyskanych podczas procesu kontrolowanego starzenia krwi, oddającego – tak dokładnie, jak to tylko możliwe – degradację materiału dowodowego na miejscu zdarzenia. Każda

procedura datowania jest więc niejako “szyta na miarę”, dostosowana każdorazowo do zabezpieczonego materiału dowodowego, prowadząc do zminimalizowania wpływu czynników zewnętrznych (jak chociażby warunków środowiskowych) na poprawność procesu datowania.

Opracowanie nowej metodyki datowania wymagało rozwiązania dwóch odrębnych zagadnień. W pierwszej części badań, podjęto próbę utworzenia metody analitycznej pozwalającej na charakterystykę stopnia degradacji plam krwawych. Biorąc pod uwagę właściwości fizykochemiczne badanego śladu, wybór spektroskopii ramanowskiej wydawał się dobrze uzasadnioną decyzją, co też zostało potwierdzone przez uzyskane wyniki. Spektroskopia Ramana pozwoliła bowiem na monitorowanie zmian fizykochemicznych, towarzyszących procesom degradacji głównego składnika śladów krwawych – hemoglobiny – w nieinwazyjny i reprezentatywny sposób.

Druga część badań polegała na opracowaniu hybrydowych modeli LR służących rozwiązywaniu tzw. problemu porównawczego widm ramanowskich, które charakteryzowały ślady krwawe o nieznanym czasie powstania (potencjalne materiały dowodowe) oraz ślady utworzone w procesie kontrolowanego starzenia (tzw. materiały referencyjne). Wyniki procedury walidacyjnej pozwoliły na wstępne potwierdzenie skuteczności nowo zaproponowanej metodyki datowania śladów krwawych. Najlepsze spośród opracowanych modeli LR dostarczały akceptowalne poziomy odpowiedzi fałszywie pozytywnych i fałszywie negatywnych, które oscylowały odpowiednio wokół 20% oraz 10%. Warunkiem skuteczności procedury było jednak utworzenie materiałów referencyjnych w warunkach środowiskowych jak najbardziej zbliżonych do tych, które panowały podczas degradacji dowodowych śladów krwawych. Wniosek ten nie powinien jednak dziwić – zapewnienie porównywalnej kinetyki procesów starzeniowych materiałów referencyjnych i dowodowych jest w istocie podstawowym wymogiem metodologii opracowanej w ramach nieniejszej rozprawy doktorskiej.

CONTENTS

AFM	**A**tomic **F**orce **M**icroscopy
ATR	**A**ttenuated **T**otal **R**eflectance
BPA	**B**loodstain **P**attern **A**nalysis
CCD	**C**harge-**C**oupled **D**evice
CMYK	**C**yan, **M**agenta, **Y**ellow, Blac**k**
CV	**C**ross-**v**alidation
CWT	**C**ontinuous **W**avelet **T**ransform
deoxyHb	**Deoxyh**emoglo**b**in
DNA	**D**eoxyribo**n**ucleic **A**cid
DWT	**D**iscrete **W**avelet **T**ransform
ECE	**E**mpirical **C**ross **E**ntropy
FP	**F**alse **P**ositives
FN	**F**alse **N**egatives
FT	**F**ourier **T**ransform
GA	**G**enetic **A**lgorithm
Hb	**H**emoglo**b**in
HC	**H**emi- and hemochromes
HS	**H**igh **S**pin
HSI	**H**yperspectral **I**maging
HSV	**H**ue**, S**aturation**, V**alue
KDE	**K**ernel **D**ensity **E**stimation
LDA	**L**inear **D**iscriminant **Analysis**
LR	**L**ikelihood **R**atio
LS	**L**ow **S**pin
LS-SVM	**L**east **S**quares **S**upport **V**ector **M**achines
metHb	**Meth**emoglo**b**in
MIR	**M**id-**I**nfra**r**ed
MLR	**M**ultiple **L**inear **R**egression
MSP	**M**icro**sp**ectrophotometry
NA	**N**umerical **A**perture
NIR	**N**ear-**I**nfra**r**ed
oxyHb	**Oxyh**emoglo**b**in
PAV	**P**ool **A**djacent **V**iolators
PBS	**P**hosphate-**b**uffered **S**aline

PCR	**P**olymerase **C**hain **R**eaction
PDF	**P**robability **D**ensity **F**unction
Phe	**Phe**nylalanine
PLS-DA	**P**artial **L**east-**S**quares **D**iscriminant **A**nalysis
PLSR	**P**artial **L**east **S**quares **R**egression
PQN	**P**robabilistic **Q**uotient **N**ormalization
QR	**Q**uantile **R**egression
RBE	**R**obust **B**aseline **E**stimation
RBCs	**R**ed **B**lood **C**ells
RH	**R**elative **H**umidity
rMANOVA	**r**egularized **M**ultivariate **A**nalysis of **V**ariance
RMSE	**R**oot **M**ean **S**quare **E**rror
RNA	**R**ibo**n**ucleic **a**cid
RT-PCR	**R**eal **T**ime **P**olymerase **C**hain **R**eaction
RS	**R**aman **S**pectroscopy
SNIP	**S**tatistics-sensitive **N**on-linear **I**terative **P**eak-clipping
SNV	**S**tandard **N**ormal **V**ariate
Trp	**T**ryptophane
TSD	**T**ime **S**ince **D**eposition
Tyr	**T**yrosine
UV	**U**ltra**v**iolet
Vis	**Vis**ible
WBCs	**W**hite **B**lood **C**ells

H_i	*i*-th hypothesis
t_E	age of the recovered evidence
t_{Ri}	age of the *i*-th set of reference bloodstains
$Pr(\cdot)$	probability
$Pr(\cdot\|\cdot)$	conditional probability
E	evidence data
m	number of samples
n	number of replicate measurements per sample
p	number of variables/parameters/features
W	within-sample variance-covariance matrix
B	between-sample variance-covariance matrix

THEORETICAL PART

| *CHAPTER 1*

INTRODUCTION

Wherever he steps, whatever he touches, whatever he leaves, even unconsciously, will serve as a silent witness against him. Not only his fingerprints or his footprints, but his hair, the fibers from his clothes, the glass he breaks, the tool mark he leaves, the paint he scratches, the ***blood*** *or semen he deposits or collects. All of these and more, bear mute witness against him. This is evidence that does not forget. It is not confused by the excitement of the moment. It is not absent because human witnesses are. It is factual evidence. Physical evidence cannot be wrong, it cannot perjure itself, it cannot be wholly absent.* ***Only human failure to find it, study and understand it, can diminish its value****.*

A famous quotation of Paul Kirk [1] – one of the most prominent criminalists in the history of the 20th century – on the Edmond Locard Exchange Principle, popularised with the sentence *every contact leaves a trace*, perfectly captures the essence of forensic science [2, 3]. Evidential materials found at the crime scene can be considered physical remains of human activity. That is the role of forensic scientists to extract – using the wide selection of modern analytical techniques – and interpret all possible information hidden in these remnants of a criminal act [4]. Typically, both of these phrases – the words of Locard as well as Kirk's quotation – are conceptually limited to trace evidence (also termed as microtraces due to their standard dimensions) [5, 6], which refers to small particulate matter that can be easily transferred between objects, people and places as a result of their interaction [7]. And indeed, analysis of these materials often provides exploratory leads in the course of investigations, usually by establishing a link at a so-called *source-level* between the recovered evidence and the control sample with known provenance [8]. However, it is a naïve mistake to think about trace evidence solely in terms of its size, as, in reality, most of the evidential materials should be regarded as trace evidence. All samples recovered at a crime scene, no matter whether it is microscopic gunshot residue deposited around a wound or blood trail on the floor, are evidence of potentially relevant connections, carrying a wealth of investigative information. It is also worth remembering that the English word *trace*, which derives from Latin *tractus* meaning "to pull along, to drag; to **lead**, to **direct**" [9], not only represents very small amounts but is also a sign that something has happened or existed [10]. This etymology gives us a broader and possibly a better understanding of the concept of trace evidence, indicating that the term should not always be reduced to the size-centered definition. After all, what provides better **exploratory leads** during forensic proceedings than blood evidence, which is often found at a crime scene in large quantities?

The increasing portrayal of forensic analytical methods in popular entertainment has resulted in society becoming more "forensically conscious". Consequently, for many, the first association with

body fluids found at the crime scene would probably be a cotton swab and DNA analysis. Considerably fewer people know, however, that even before the era of DNA typing, scientists could narrow down the field of suspects based on genetic characteristics found in blood cells. Findings of Landsteiner from the turn of the 20th century [11], which revealed that human blood could be classified into four types – according to antibodies present on the surface of erythrocyte membranes – allowed for at least a partial individualization of blood traces. However, a real serological revolution occurred a few decades later, along with the discovery of DNA profiling [12–14] and a technique called polymerase chain reaction (PCR), which enabled copying of a specific, small segment of DNA [15]. After the 1990s, DNA typing substituted all genetic tests that had previously been employed to analyze biological evidence, and thereby forensic experts were equipped with a potent tool for the individualization of bloodstains.

The development of DNA analysis was unquestionably one of the major milestones of 20th-century forensic science. However, despite the public accolades, DNA only answers the question *Who?* which is not fully exploiting the informative potential of blood evidence. It is also helpful to take into account of size, shape, and distribution of bloodstains. Falling or projected droplets of blood follow standard physical laws, which lay the groundwork for bloodstain pattern analysis methods (BPA) [16, 17]. Obviously, meticulous observation of blood patterns will never let us precisely reconstruct the blood-shed event. However, it can often give valuable clues about actions that gave rise to bloodstains origin. For example, BPA can indicate a mechanism(s) of bloodstain formation, minimum number of impacts, or their approximate point. This allows assessing whether analyzed traces are compatible with different versions of the same event presented by both parties to the proceedings [18, 19]. In other words, once bloodstains are associated with a person(s) based on DNA profiling, BPA can provide some interpretations on the ACTIVITY level [8, 20]. By doing so, much more information on the context of the event is delivered, as a forensic scientist not only determines who was the "donor" of blood but also verifies what activities (e.g., of a suspect) could have led to the pattern formation (Figure 1.1). And yet, this technique has only scratched the surface of its real potential. Until recently, BPA was treated with the reserve in many countries – like any new discipline – mainly due to some doubts concerning the method's objectivity [21, 22] and the shortage of BPA experts. Fortunately, due to forensic scientists' efforts to establish analytical standards and provide a sound scientific basis for these blood-based interpretations, BPA is becoming an increasingly important sub-specialty in forensics.

It could have therefore seemed that the blood-centered branch of forensic science requires no further research efforts. Nothing more mistaken! While the routine analysis can help address many relevant questions – such as *Is it possible that the blood originated from the victim?* or *How many people were bleeding at a scene* – there are fields in forensic science that still need some answers. Situating bloodstains in time is among these latter areas of knowledge [23–26]. An example from the history of forensic investigations should help to outline the importance of establishing the time since deposition (TSD) of bloodstains. The story is set in 1995, at the end of a sensational trial of an actor and a former football star – O. J. Simpson – who was accused of the brutal double murder of his ex-wife, Nicole

Brown Simpson, and her friend, Ronald Goldman [27, 28]. Despite a "mountain of evidence" implicating him as the murderer, including O. J. Simpson's blood traces revealed nearby victims, he was acquitted of all the charges. During the 252-day trial, Simpson's team of lawyers employed creative methods to convince jurors that the defendant's guilt had not been proved "beyond a reasonable doubt", undermining the credibility of numerous physical evidence, including bloodstains. The defense has cast doubt on the time of bloodstain formation, implying that Simpson's blood had been planted later on by the police in the critical areas of the murder scene. In such a way, the defendant's active involvement in the double homicide was called into question.

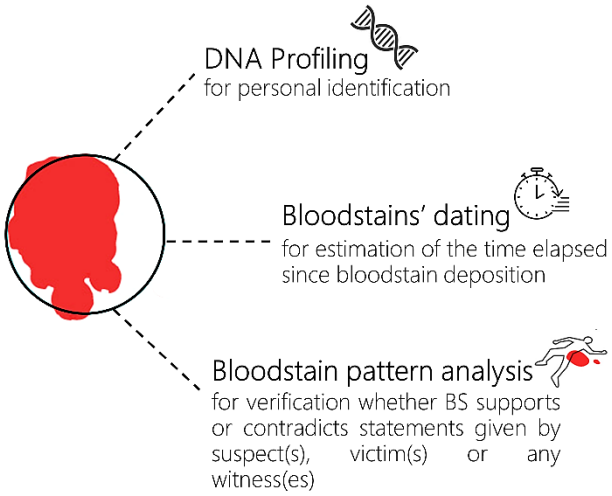

FIGURE 1.1.

Forensic relevance of bloodstains (BS).

The case mentioned above is just one of many examples demonstrating that the forensic arsenal of analytical methods is still incomplete. Modern forensic knowledge, which allows for such a comprehensive use of bloodstain patterns, does not make full use of the information "recorded" in them. This is because, in the era of DNA testing, it is frequently overlooked that verifying who was the donor of the trace is not always the critical issue. Results of DNA analysis, as yet, do not allow to verify whether the blood present at a scene is relevant to the crime. It is also impossible to determine the time of the suspect's activity based on genetic markers. Thus, in order to increase the evidential value of the trace, it is necessary to demonstrate **A UNITY OF TIME AND PLACE**, proving that a suspect was on the crime scene within a given time interval [29]. This can be done by providing the final piece of the forensic puzzle – **INFORMATION ABOUT BLOODSTAIN DEPOSITION TIME**.

Unfortunately, confrontation with the issue of time – regardless of the type of evidence being under evaluation – is probably one the most challenging tasks faced by experts. Therefore, it is no surprise that **A RELIABLE METHOD FOR BLOODSTAIN DATING, WHICH IS VIEWED AS THE HOLY GRAIL OF FORENSIC SCIENCE, STILL REMAINS BEYOND OUR REACH** [23–26]. Nevertheless, as elaborated in *Chapter 4*, due to changes in the physicochemical properties of blood, which occur during the trace degradation, an answer to the question of bloodstains' age may be considered achievable. This is

confirmed by a constantly growing body of research in the area of forensic dating. The great majority of already proposed tools fall under the category of the dynamic methods (see *Chapter 2*), aiming to correlate the time elapsed since trace deposition with aging processes of its unstable constituents, probed by adequate analytical methods. At first glance, it might seem that developing analytical tools themselves pose the most significant challenge. However, all studies conducted to date have established analytical procedures capable of monitoring bloodstains' time-dependent behavior, demonstrating physicochemical changes accompanying the degradation process. And yet, despite these advances, none of the proposed techniques have overcome the experimental research phase. Thus, it is reasonable to assume that the real problem lies elsewhere, namely in an **INABILITY TO TRANSLATE THESE DATING METHODS TO PRACTICAL PROCEEDINGS**.

The history of forensic science has witnessed many failed attempts to integrate seemingly powerful dating methods into its analytical armory [23–26]. Early approaches to establishing the TSD of bloodstains, consisting of visual comparison of blood color changes [30, 31], were initiated by an Italian assistant at the University of Genova – Louis Tomellini. His article from 1907 described the process of bloodstains degradation (from an hour up to one year elapsed since trace formation) by the set of 12 color figures. It was probably the earliest written mention of the blood dating tool developed for forensic purposes [30]. These vision-based methods have been shortly afterward replaced with more objective and advanced analytical techniques with the spectrophotometric- [32, 33], chromatographic- [34, 35], or spectroscopic-based methodologies [36–40]. Finally, during the past few years (2010–2020), the field has grown with some innovative solutions, among which methods of vibrational spectroscopy have earned the position of an unquestionable leader (a brief overview of spectroscopy-based dating methods can be found in *Chapter 5*). The growing popularity of spectroscopy, not only among forensic experts but also between chemists and physicists, is not surprising, mainly because these powerful instrumentations can produce vast amounts of data – usually in a non-invasive manner – within a short time. However, it should be recalled that a large body of data cannot be *a priori* equated with the valuable information contained within it. The produced spectrum of a bloodstain – or any other sample – should be regarded as a superimposition of all active components weighted for their concentration. Hence, spectroscopists' fundamental question is how to extract – from the body of recorded data – information relevant to the conducted research. In other words, a conversion from numerical data (e.g., spectra) into physicochemical information becomes essential [41].

The problem is that the average human brain is not adapted to process numbers efficiently. Across million years of primate evolution, our brain has been adapted to store and interpret only particular types of information – mainly immense quantities of botanical, zoological, topographical, or social data [42]. This mental limitation has triggered the need to develop methods capable of handling large amounts of numerical data, also in the chemical context. Fortunately, the initial skepticism about employing mathematical methods in the study of chemical questions, expressed very clearly by A. Comte: *If mathematical analysis should ever hold a prominent place in chemistry – an aberration*

which is happily almost impossible – it would occasion a rapid and widespread degeneration of that science (...) [43], has fallen on deaf ears. This "degeneration" of chemistry did occur in the 20th century. Nowadays, it is known as chemometrics, which, borrowing Svante Wold's words, might be explained as applying mathematical and statistical techniques *to extract chemical and physical information from complex data* [44]. However, it should be noted that the function of chemometric tools is merely to facilitate data analysis. One should always keep the purpose of the data modeling in focus, as a profound understanding of the nature of the problem – that determines the proper selection of the chemometric strategy – will always be the prerequisite of any adequate data treatment, which is often forgotten in the world of "push-the-button" automated data analysis [45].

Having looked into previous examples of bloodstains dating studies, it can be concluded that it is precisely the case. It is **THE FAILURE TO UNDERSTAND THE ESSENCE OF THE PROBLEM** and, consequently, **THE WRONG APPROACH FOR DATA ANALYSIS, WHICH SHOULD BE BLAMED FOR THE DELAYED EXPLOITATION OF ALREADY DEVELOPED DATING METHODS IN FORENSIC PRACTICE**. According to the universally adopted strategy, the majority of proposed methods have been guided by a simple principle – they have sought the dependency between some dynamic properties of degrading blood and time elapsed since deposition, usually through the employment of regression analysis [23, 24]. This approach, however, might not be entirely correct, as these models will always fit the aging behavior of samples used for their construction, namely bloodstains degrading under tightly controlled and usually stable laboratory conditions. But is the forensic reality that straightforward? In fact, no two crime scenes are ever precisely the same, and neither are the degradation pathways of blood deposits. Thus using dating models trained on the very limited datasets might lead to misestimations of TSD, depriving these conventional methods of almost entire practical value.

However, it does not mean that – because of these obstacles – questions about the time of trace formation should be silenced. It just means that these queries should be tackled differently to incorporate the uncertainty resulting from the factors influencing the aging process (e.g., environmental factors) into the dating approach. And precisely this endeavor – **THE QUEST FOR THE NOVEL FRAMEWORK FOR BLOODSTAINS DATING – IS THE SUBJECT OF THIS DISSERTATION**. It is hypothesized that impediments resulting from aging kinetics' variability could be addressed by substituting a case-suited comparison problem for the conventional dating approach. The critical aspect of this concept, based on estimating the (dis)similarity between the stage of evidence decomposition and sets of reference materials obtained through supervised aging, is elaborated in *2.2. The novel framework for evidence dating*.

The thesis's theoretical part consists of seven chapters intended for providing a potential reader with the background information needed to understand the presented study. The following three chapters, included in the second part of the dissertation, are devoted to the experimental and research results, completed with summarising conclusions.

| *CHAPTER 2*

DATING OF BLOOD TRACES: AN ATTAINABLE GOAL OR JUST A CHIMERA?

The construct of time has been accompanying every era of humanity. Its meaning is understood somehow instinctively. It allows us to express concepts that we use in our everyday lives – such as simultaneousness, duration, or succession – yet it is still hard to provide a clear, unequivocal explanation of the time itself. It is just like in the celebrated quote from Saint Augustine *What then is time? If no one asks me, I know what it is. If I wish to explain it to him who asks, I do not know.* That is probably why science, philosophy, art, or religion give their own, often very different time definitions. Nevertheless, everywhere – regardless of the scientific domain considered – this indefinable concept plays a distinct role. The situation is no different in forensic sciences. The ability to provide a reliable answer to the age of the trace could be a significant added value to the criminal inquiry, allowing the judicature to recreate a criminal situation *a posteriori,* which is one of the main objectives of forensic science [46, 47]. In the case of blood evidence, information on the temporal dimension may prove helpful in multiple ways, depending on the staging of the criminal procedure that usually consists of two phases – investigative and evaluative [48].

During the investigative phase, when circumstances of a crime remain unclear, information about the time of bloodstain(s) formation can contribute to establishing the timeline of events (e.g., sequence of bloodstains deposition) or verifying if the preserved trace has relevance to the case in question[*]. Due to large workloads, efficiency in forensics is of foremost importance. Hence particularly, the latter issue, an ability to select only pertinent blood traces, is the essential one, as it would significantly streamline the sampling procedure directly at the crime scene, not to mention a reduction in costs stemming from the subsequent DNA analysis. Obviously, prompt responses to these time-centered questions would require an on-site dating tool to deliver immediate and reliable answers. Unfortunately, despite all efforts made, practical application of technology providing TSD estimations directly at the crime scene – for example, smartphone-based methods [52, 53] – seems hardly possible, mainly because of the inability to model in advance varying aging rates of blood evidence, resulting from the multidimensionality of degradation process (*4.3 External factors influencing degradation process*). For that reason, **the present thesis focuses** rather **on the second phase of the criminal inquiry**. It should not be forgotten that questions of time emerging at **the evaluative stage** – which is usually concentrated around assessing the evidence in the light of two alternative hypotheses that represent the prosecutor's and defense's standpoints – is just as important. Questioning the validity of seized evidential material – as in the described case of O. J. Simpson – is a common practice followed

[*] The term *relevant trace* should be understood as a trace, which was left by the perpetrator during the criminal activity [49] or is somehow connected to the crime [50, 51].

by the suspect's representatives. In other words, information about the time of bloodstains formation becomes particularly relevant when the suspect does not question the identification of her/his blood traces but rather the time they were deposited. In this context, estimation of TSD could help dispel doubts regarding bloodstains' relevance by exposing anachronisms in courtroom scenarios.

Finally, it should be added that these kinds of time-centered questions are frequently asked not only in relation to blood deposits but also other forensic evidence such as fingerprints, ink entries, or gunshot residues [54–56]. Interestingly, forensic experts sometimes attempt to give reasonably accurate answers. But are such estimations acceptable? Can the age of the evidence be determined through available dating procedures?

2.1 General dating concepts in forensic science

In the forensic field, there are generally two distinct strategies for estimating the age of a questioned material (Figure 2.1). These concepts include the group of STATIC and DYNAMIC DATING METHODS [55].

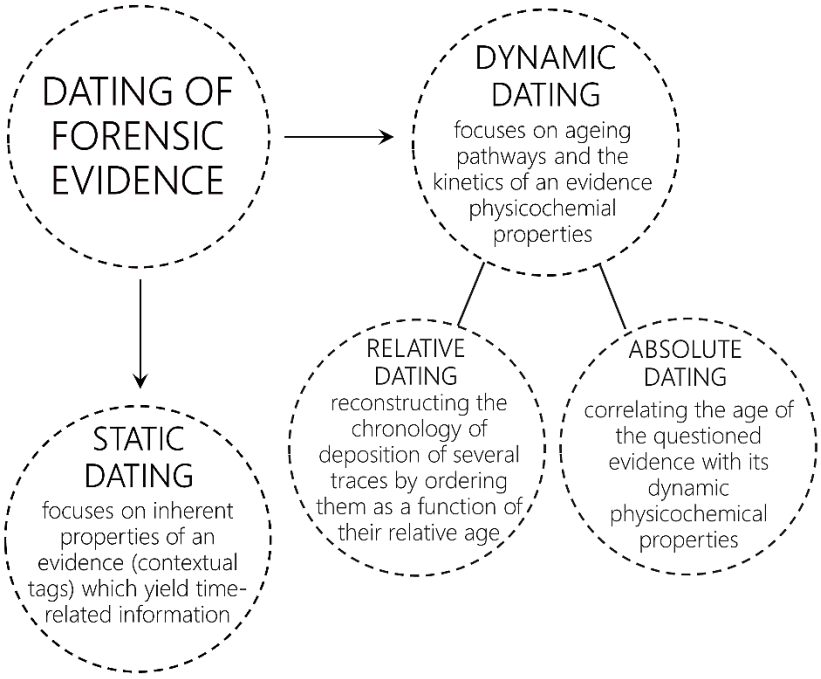

FIGURE 2.1.

General approaches for dating forensic evidence.

The first of these – the static approach – focuses on some inherent properties of examined materials, often referred to as contextual tags, which yield indirect time-related information, usually limited to a time interval defined by a date when the source object was put into circulation [29]. These contextual tags are supposed to be time-invariant, and their presence should be specific to certain time

frames, production periods, etc[†]. In other words, the static approach attempts to characterize the composition of evidence in order to identify some contextual tags to expose any of anachronistic features, and through that, verify claims for the authenticity of the questioned object. It is easy to conclude that this particular strategy is unsuitable for dating biological traces; hence it will not be discussed in great detail. Nevertheless, it is interesting to mention that the static approach is especially useful in examining documents and artworks. A well-known case of Hitler's diaries [57], a rehash of a previous fraud with written records of Mussolini [58], is probably one of the best self-explanatory examples of static dating. In 1983, the German magazine *Stern* announced that its editors acquired previously undiscovered diaries of Adolf Hitler [59], allegedly lost in the plane crash in 1945. This remarkable discovery was achieved at a relatively modest expansion at a total cost of approximately a few million dollars, provided to a reporter, Gerd Heidemann, involved in the "purchase procedure." The handwritten Hitler's biography – reportedly not particularly good one also from the literary standpoint – included everything: from descriptions of medical conditions such as halitosis (*Eva says I have bad breath*) to the confession that the Nazi dictator – surprisingly sensitive – was not aware of the wartime fate of the Jews [60]. It is no surprise then that this finding was greeted with experts' skepticism, giving rise to the question about the authenticity of newly surfaced documents. And indeed, the physicochemical examination of the diary established the presence of optical brighteners. This component was introduced into the paper manufacturing process in 1948, hence well after the alleged author's death. In this way, identifying contextual tags (optical brighteners) – and more precisely, demonstrating the discrepancy between them and dates written in the document – allowed to undermine the questioned object's authenticity.

It should be noted, however, that the above example represents the most optimistic scenario. When no contrary evidence is uncovered, static dating becomes a lot more complicated task, where giving a definite answer would be simply impossible. Finally, it should also be emphasized that in order to take full advantage of the static approach, profound knowledge of the variability in the composition of the examined object(s) throughout time is indispensable. It becomes evident when the forensic dating of art objects is considered, as substantial expertise in a particular painter's palette often allows for authentication of artworks [61–63]. On the other hand, though, it does not always guarantee total success in static dating. Times of high demand for masterpieces and rare auction objects created a whole host of counterfeiters with extensive knowledge of the field, adept at manufacturing forgeries that satisfy the market. Consequently, examiners should be very cautious when concluding investigated objects' authenticity, especially when no atypical components (as for example, synthetic pigments in Caravaggio's painting) are identified.

[†] Obviously – according to Heraclitus wisdom – physicochemical properties of any material undergo some variations over time. However, the pathways or kinetics of these changes do not constitute the backbone of the static dating approach. It is not the time-dependent alterations that we are interested in, but the presence of particular components characteristic to a given period of time.

The second approach for forensic dating, namely DYNAMIC DATING METHODS, focuses on degradation pathways and evidence properties' kinetics [29]. It is, therefore, the very opposite of the previously described concept of static dating. Properties of all objects, and thus also evidential materials, undergo continual transformations over time, which can be briefly termed as the aging process. In fact, it is the progression of events, which defines the passage of time. From change, our brains construct a sense of an "arrow" or direction of time. Needless to say, the base unit of time defined by the international system of units (SI) – the second – is tied to a particular alteration: the frequency associated with an electronic transition of the cesium-133 atom. A similar type of reasoning is used to evaluate the age of forensic traces through the dynamic approach. Owing to changes in the evidence characteristics, the answer to the question of time is considered possible. Encapsulation of these alterations (either physical or chemical) in some measurable parameters that reflect the extent of evidence degradation, followed by the determination of the relationship between these parameters and time, serves as the foundation for TSD estimations. Recognizing this possibility was unquestionably a great triumph of forensic scientists and the starting point for contemporary dating studies, which resulted in a continuously growing body of research geared towards age estimations of inks [55, 64], fingerprints [54], gunshot residues [56], and finally also blood traces [23–26]. Among these studies, regardless of the type of examined evidence, two different approaches can be further distinguished: RELATIVE and ABSOLUTE dynamic dating methods.

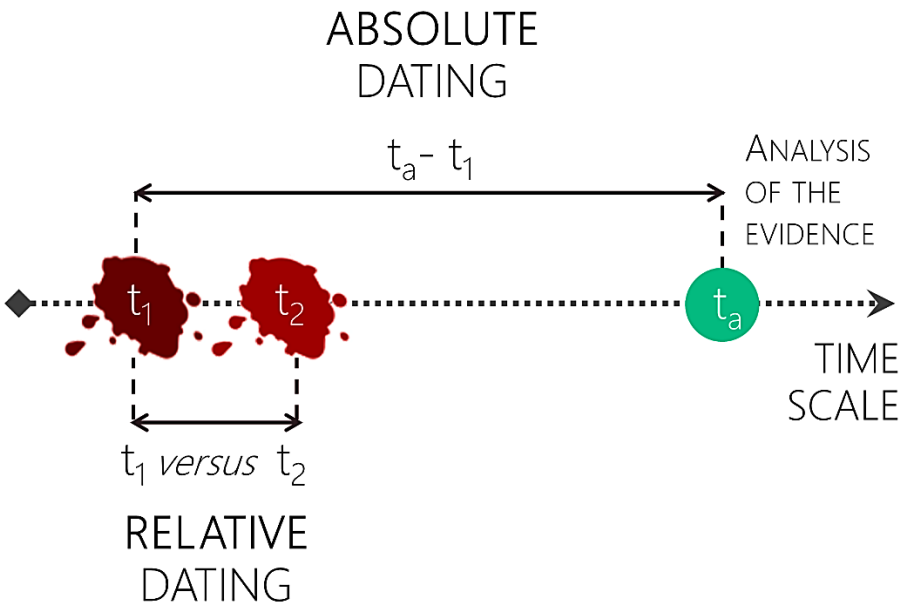

FIGURE 2.2.

Absolute and relative dynamic dating methods.

The relative dating approach's objective, which is illustrated with the example of bloodstains dating in Figure 2.2, is to estimate the age of the questioned trace in relation to other materials of the same nature (and possibly also originating from the same source). In other words, it attempts to order forensic traces as a function of their age, which is reflected in the stage of material decomposition, so as to establish the sequence of evidence deposition. This greatly simplifies the dating procedure since no calibration models intended for predicting the age of the trace (as in the case of absolute dating) have to be established. The general knowledge of the material's aging behavior and changes in previously identified aging parameters with time – e.g., solvent extraction rates used in relative dating of ink entries[‡] – are perfectly sufficient for reconstructing the trace formation's chronology. Nevertheless, the credibility of such estimations can be guaranteed only if compared traces followed the same aging kinetics. Therefore, the relative approach's applicability is limited to materials of the same initial composition, which were deposited at the same substrate and stored under the same conditions [29]. A good example of relative dating would be the already mentioned case of sequencing ink entries on documents such as checks or last wills and testimonies [66], which usually fulfills all these requirements. This situation, however, is not often met. And what is even more important, the relative approach, aimed at sequencing the formation of traces, in many cases, is not a suitable tool for addressing the time-related questions resulting from the context of the crime. Much more often, it is the absolute age of the evidence, lying at the heart of forensic investigations.

Contrary to the relative dating, the ABSOLUTE APPROACH (hereafter referred to as a conventional dating approach) – which is the most common method used during the ongoing studies on bloodstains dating [23–26] – does not require providing any reference samples, what at first sight might be perceived as a real asset. The idea of absolute age is understood as the time elapsed since the evidence's formation (a stain of body fluid, an ink entry, a fingerprint, etc.) until the forensic expertise (Figure 2.2). Hence, it would not be entirely incorrect to think of the concept of absolute age as an analogy to a person's chronological age, which is measured from birth to a given date. Unfortunately, upon its formation, the evidence is not equipped with any metrics that serve as an equivalent of our birth certificates. Consequently, forensic experts are forced to base their temporal estimations on the above-mentioned dependency between the TSD and some dynamic properties, previously identified as aging parameters, depicting the degradation process of a given object/material. Until now, in most cases, this task has been completed through the employment of regression analysis, where calibration models (mainly linear models), represented by equations relating measured values of the aging parameter (i.e., aging markers) and the absolute age of the evidence, are established [29]. However, it turns out that this conventional dating approach – as will be shown below – might not be entirely correct. It should be clearly stated that the current state of research allows only for monitoring the aging process of potential forensic traces but

[‡] As the ink ages, the polymerization and hardening of the resins take place, creating a kind of a trap for colourants, hindering the extraction of the ink from the substrate. Therefore, solvent extraction rate, which determines how efficiently an ink entry is extracted into a solvent, can be related to the time elapsed since ink deposition [65].

does not provide a valid, reliable method for estimating the age of a trace in practice; the best proof of which is lack of any official guidelines, published by acknowledged forensic institutions (e.g., European Network for Forensic Science Institutes, ENFSI) [67]. And as if this was not enough, no consensus on how to transfer the methods of absolute dating into forensic practice has been reached, also in the case of blood evidence.

Fortunately, the majority of researchers are at least in agreement with the theoretical basics of absolute dating, clearly specifying prerequisites for providing accurate TSD estimations. Whatever the examined material, the parameter(s) constituting the basis for the construction of aging models should be characterized by particular features [54, 68, 69], namely:

- they have to be predictable and persistent or, to put it another way, parameter(s) have to increase or decrease linearly with time (preferably over a large time scale);
- they should change over time in a reproducible manner;
- they should be adequate for the majority of samples within a particular category of forensic traces[§] [68];
- they should exhibit minimal variability caused by such external factors as storage conditions or substrates' properties.

Unfortunately, especially the last requirement is hardly ever met. It is not because of the shortcomings of selected aging parameters but due to the nature of the degradation process *per se*. It is necessary to realize that the aging of the questioned trace may follow different pathways at considerably different rates, depending on many external factors that affect the degradation process (see *4.3 External factors influencing the degradation process*). As a consequence, the absolute age of the evidence, which is revealed during the forensic expertise, does not correspond to the "chronological age" of the evidence understood as the time elapsed since deposition – the central concern of triers of fact – but rather to the ENVIRONMENTAL AGE, which – similarly to our biological age – represents the actual stage of material decomposition. Since an unlimited number of environmental factors can interfere with the evidence degradation process, it is not difficult to deduce that these two figures – the chronological and the environmental age – do not match up in most instances. And this brings us to the main reason for delayed exploitation of already developed bloodstains dating methods in routine caseworks.

As mentioned above, estimation of the absolute age is usually completed through the employment of regression analysis, where an equation relating measured values of the aging parameter (i.e., aging markers) and the absolute age of the evidential bloodstain is established [23, 24]. Unfortunately, it is often overlooked that equations underlying these calibration models are based on the

[§] As already proved in case of ink compositions [55], fingerprints [54, 70], and also hypothesized in case of blood traces (see *4.3.1. Initial blood composition*), the initial composition of the analysed material may directly affect the rate of degradation process, which may also follow different pathways. Thus, irrespective of the initial constitution of the deposited trace (which is always inferred with some degree of uncertainty), the relation between the ageing parameter(s) and the TSD should remain the same [68].

aging "behavior" of samples degrading under stable laboratory conditions, which hardly ever resembles the crime scene reality. The vicissitudes of external factors, mainly environment and blood biology, mean that no two degradation pathways are precisely alike. Thus, developing a universal dating model, which in no way incorporates the uncertainty deriving from the influence of factors altering the aging processes, seems an utterly failed idea. An idea, which, for whatever reason, has been reproduced by various research groups over the years. As a consequence, our discussion is back to square one. Admittedly, the absolute dating models are not devoid of any practical value, but their implementation is limited in a similar manner to relative dating methods – they may be found useful only for those bloodstains, which followed the same degradation pathways as training samples used for the model construction. Otherwise, application of such dating tools for predicting the age of the evidence – bloodstains characterized by different aging kinetics – might lead to significant misestimations of TSD, and thus the validity of such results as a form of legal evidence obviously should be questioned.

Given that situation, one might suggest – especially when focused on establishing an on-site dating tool – to develop in advance different variants of absolute dating models adapted to each possible scenario that could be encountered at a hypothetical crime scene. This solution, however, is somewhat unreasonable – if not wholly senseless – simply because it is virtually impossible to accomplish. It would require careful studies on the influence of all possible contributing factors (and their interactions) on the aging process (see *4.3 External factors influencing the degradation process*). It may therefore appear that forensic scientists are facing what seems like an impossible situation. After all, understanding the impact of external factors on bloodstains aging kinetics is indispensable to eventually translate the laboratory results to the forensic practice [71] – at least when the conventional approach to the dating issue is considered. So does it mean that, because of these difficulties, questions regarding the time aspect of bloodstains formation should be withdrawn from the courtroom scenario? Absolutely not[**]. It just means that the answer to the question of time should be sought elsewhere, perhaps by looking at the dating problem from an entirely different angle.

2.2 The novel framework for evidence dating

One of the possible ways of bringing forensic practitioners a step closer to reliable estimations of TSD may be establishing an entirely novel approach for TSD predictions based on a MODIFIED METHODOLOGY OF RELATIVE DATING, which constitutes the present thesis's backbone. The priorities of this strategy are explored below, while the technicalities will be introduced as appropriate throughout the upcoming chapters.

An essential starting point for establishing a reliable dating framework is realizing that external factors will always affect the degradation process, altering its rate to a lesser or greater extent, thus

[**] Otherwise, this dissertation should be terminated at this point.

having an important role in evidence dating. The uncertainty deriving from these influencing agents cannot be wholly eliminated either estimated in advance. Therefore it should be somehow incorporated into the dating strategy. The reasonable solution seems to be substituting a case-suited comparison problem for the conventional dating approach. The basis of this methodology would be to assess the (dis)similarity between the degree of the evidence degradation and the decomposition of comparative materials obtained during the process of supervised aging, which would, as precisely as possible, recreate the degradation of the evidence on site. This means that every dating procedure would be constructed on a case-by-case basis, being each time tailored to fit the examined traces. In such a way, the influence of external factors (donor characteristics, environmental conditions, nature of the substrate) on the analysis's validity should be considerably reduced.

To put that into perspective, let us use one more time an example of the murder case involving O. J. Simpson. Perhaps you remember that during the trial, the defense questioned the time of bloodstain formation – identified as Simpson's blood and revealed nearby the victims' bodies – implying that traces had been planted later on in the critical areas of the murder scene. In this case – as in most of the inquiries raised during the evaluative phase of the criminal procedure – it is not actually necessary to provide the absolute age of the evidence. The key point here is to verify whether the questioned bloodstain and more precisely the time of its formation, is in accordance with the scenario presented by the prosecution – claiming that the evidential bloodstain was formed at the time of the murder – or by the defense, which contradicted the above hypothesis, suggesting that the blood trace was significantly older. As a consequence, the question of time could be solved by comparing the degradation state of the evidential material with some reference bloodstains, created in such a way to match the scenario(s) representing the standpoint(s) of one (or both) parties to the proceedings. As mentioned above, these sets of reference materials should be obtained through the process of supervised aging, simulating – as closely as possible – the actual settings of evidence decomposition at the crime scene. In other words, a similar volume of blood, freshly drawn from the donor (if available – the same individual who was the donor of the questioned trace), deposited on an identical substrate and stored under similar conditions as those observed at the crime scene, should be subjected to the process of degradation for the time corresponding to the considered hypothesis (e.g., the prosecutor's). While estimating the approximate volume of deposited blood and determining the substrate type should not pose any severe difficulties, establishing the type of storage conditions a questioned bloodstain might have been exposed to for the alleged period of aging is a little bit more challenging. To reconstruct the weather events – more volatile than the indoors storage conditions – it often may be required to take advantage of forensic meteorology, which allows determining the weather conditions at a specific time and location on the basis of the historical atmospheric data [72]. If this measure fails and the aging conditions remain unknown, the different variants of supervised aging, selected based on contextual information, should be investigated.

Having both evidential and reference materials, the proposed dating procedure would enter into the next phase, namely the characterization of the state of blood traces degradation. Contrary to some

opinion, this examination cannot be performed based on the trace's visual quality, as the motto famous in certain forensic circles *the better it looks, the fresher it is* [70] has never been scientifically substantiated. The resulting conclusions have to be supported by more reliable tools. Hence, it becomes necessary to take advantage of an analytical method, which would enable representative and non-invasive probing of bloodstains' chemical composition (see *Chapter 5*). Finally, the resulting physicochemical data (e.g., spectral signatures) are supposed to be interpreted in the context of two perspectives – the prosecutor's and the defense's – and communicated understandably to the representatives of the justice system. As the determination of the exact TSD will never be possible, the presentation of these results should be based on probabilistic calculations.

In judicial practice, in order to report the evidential value of the observed similarities and differences in the registered physicochemical data, the evidence should be assessed in the context of two competing propositions that represent the prosecution's and defense's standpoints. To obtain a well-balanced evaluation, two different sets of reference materials (bloodstains aged in a supervised manner) should be created, producing – at best – results of two different comparisons. If possible, one of these reference sets should match the prosecution's version of events, and the other one should be aged according to the defense's scenario (see Figure 2.3). Thus, following this reasoning and referring once again – for the sake of the reader's convenience – to the discussed case of the O.J. Simpson, the first set of reference materials should be aged for the time corresponding to the absolute age of the evidential bloodstain (the time interval between the occurrence of the crime and the moment of the analysis of evidence, denoted as t_{R1}), so the scenario enforced by the prosecution. Similarly, the second set of reference materials, created in accordance with the opposite claim, should be subjected to the supervised aging for the time matching the absolute age of the evidential bloodstain proposed by the defense (denoted as t_{R2}). Subsequently, in the context of this atypical comparison problem, when the TSDs of two sets of reference materials match respectively the time elapsed since crime occurrence (t_{R1}) and the testimony of the suspect (t_{R2}), the considered hypotheses may be expressed as follows:

> **H_1**: the age of the recovered evidence (bloodstain(s) of questioned age, revealed at the crime scene; t_E) MATCHES the age of the reference material (bloodstains obtained during the process of supervised aging according to the prosecutor's or defense standpoint; t_{R1} or t_{R2}): $t_E = t_{R1}$ (first comparison) or $t_E = t_{R2}$ (second comparison).
>
> **H_2**: the age of the recovered evidence (bloodstain(s) of questioned age, revealed at the crime scene; t_E) DOES NOT MATCH the age of the reference material (bloodstains obtained during the process of supervised aging according to the prosecutor's or defense standpoint; t_{R1} or t_{R2}): $t_E \neq t_{R1}$ (first comparison) or $t_E \neq t_{R2}$ (second comparison).

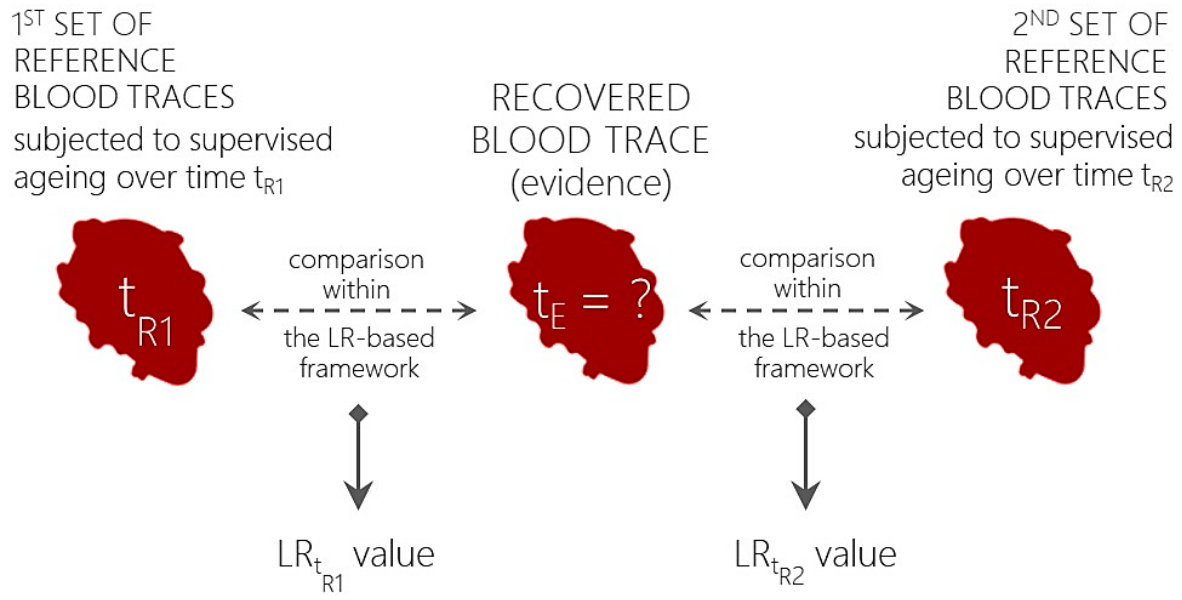

FIGURE 2.3.

Implementation of the comparison procedure within the LR framework aimed at estimating the TSD of a questioned bloodstain.

To indicate which of these hypotheses, considered within both comparisons, is supported by the evidence, conditional probabilities of registered data, given that any of the propositions is true, have to be delivered. This, in turn, can be expressed by the likelihood ratio (LR) approach – a recommended method for assessing the evidential value of the physicochemical data [8, 20, 73] – that will form the backbone of the comparative procedure proposed in the present thesis as a novel framework for blood evidence evaluation. A detailed description of the LR framework is beyond the scope of this chapter (it can be found in *Chapter 6*). At this point, for the sake of clarity, it should be briefly added that the LR is defined as:

$$LR = \frac{\Pr(E|H_1)}{\Pr(E|H_2)},$$

where E denotes the evidence obtained through the analysis (e.g., spectral data). The LR can have a value between zero and infinity, and its interpretation is the following: LR values above one support H_1, while LR values below one provide support for H_2. Moreover, the higher (lower) the LR value, the stronger the support for H_1 (H_2). For example, in the processes of comparing two sets of reference materials with the evidential trace within a considered case, two LR values (marked as $LR_{t_{R1}}$ and $LR_{t_{R2}}$ values in Figure 2.3) are obtained. Consequently, if the $LR_{t_{R1}}$ value is above 1, then the support toward the prosecutor's proposition would be provided (herein: the bloodstain revealed at the crime scene was deposited during the occurrence of crime), thereby contradicting the scenario presented by the suspect. At the same time,

the $LR_{t_{R2}}$ should not support the defense's proposition, and thus the value obtained within the second comparison is expected to be less than 1. Obviously, the results of comparisons might be reversed entirely; however, the obtained LRs should not contradict each other (hence if $LR_{t_{R1}} > 1$ then $LR_{t_{R2}} < 1$, and vice versa). In this way, it becomes clear that combining the results of these two parallel comparisons, based on the LR approach, provides another step toward a more reliable method of situating the questioned trace in time.

Obviously, despite indisputable advantages, the proposed dating strategy exhibits several drawbacks. The most serious of these is that the dating procedure could only occur after identifying the donor of the questioned bloodstain. This process, however, would be entirely in accordance with the current forensic practice since the questions of the bloodstain(s) age usually arise when the suspect was identified and claims that the trace had been left after or before the criminal act. Besides, it cannot be denied that the proposed protocol might be incredibly time-consuming. To a large extent, this depends on the efficient operation of the law enforcement agencies, the fact-finder's capability, and obviously time required for discovering the crime, which is beyond our control. And yet, despite its flaws, the proposed case-suited dating method appears to be the most promising way to proceed. Adopting such a strategy, which have been called a MODIFIED RELATIVE DATING APPROACH (as the age of the evidence is assessed in relation to the "artificially" created reference materials), may be the key we are searching for, as only by reducing the variability introduced by external factors, the comparable aging kinetics can be ensured, boosting the credibility of TSD estimations.

Finally, it should be once again clearly stressed that the forensic scientific literature continually claims that dating methods proposed by researchers are, at least for the time being, unsuitable for implementation into caseworks' reality. Nevertheless, numerous self-proclaimed "experts" offer services for situating forensic evidence in time, most often using debatable reliability methods or even basing their expertise on subjective opinions [54]. To make matters worse, the credibility of these testimonies is hardly ever questioned. This is because prosecutors, judges, and other representatives of justice, not being highly specialized with forensic methodologies, assume that forensic experts – as the name implies – *know what they are doing* [74] since they are trained within the particular field. As a consequence, the subjective, one-dimensional expert opinions are often considered by judicature during the decision-making process, even though *no one, no matter how well trained or well-intentioned, is completely immune to the confirmation bias and to his or her own cognitive blind spots (…)* [75, 76]. For that very reason, there is an urgent need for equipping forensic practitioners with reliable dating tools enabling the formulation of opinions going beyond *ipse dixit*. For that very reason, developing a novel approach for bloodstains dating is the main objective of the research presented in this thesis.

| *CHAPTER 3*

OBJECTIVES OF THE THESIS

The past years have witnessed numerous studies on bloodstains dating, and, as shown in *Chapter 5*, many of them have established methods effective in monitoring the aging process in laboratory settings. Unfortunately, the majority of the ongoing research focused solely on the technical aspects, completely ignoring the practical forensic context. Consequently, none of these conventional dating methods are suitable for casework application, which brings us to the main challenge addressed in the present thesis. The objective of this research was to overcome implementation difficulties by paving a new way in forensic dating studies, which eventually might bridge the gap between the laboratory benchtop and the courtroom. Furthermore, it is intended to provide the necessary machinery, which will enable this transition to be effected.

In order to further develop bloodstains dating research, the author proposes to consider the task of situating blood traces in time as a classical forensic comparison problem, solvable through the likelihood ratio approach. As already described in *2.2. The novel framework for evidence dating,* the basis of this concept is to estimate the (dis)similarity between the stage of evidence degradation and sets of reference materials, obtained through the process of supervised aging, simulating – as closely as possible – the actual settings of evidence decomposition at the crime scene (see *Modified relative dating* in Figure 3.1). Thus, every dating procedure would be adapted each time to the questioned blood traces. Obviously, to enable this comparison in the casework reality, it is necessary to establish and validate novel dating methodology in laboratory settings.

Establishing such a procedure should be considered a dual problem that requires addressing two distinct issues. **FIRST OF ALL, AN ANALYTICAL METHOD, SERVING AS A TOOL FOR CHARACTERIZING THE STATE OF BLOODSTAINS DEGRADATION, HAS TO BE DEVELOPED.** Given the characteristics of the examined trace (herein the bloodstain), the choice of Raman spectroscopy (RS) as a method capable of delivering information inherent to chemical changes accompanying the degradation process (*Chapter 5*) seemed a logical decision. It is coherent with RS's maturation as a powerful tool in investigating biological samples [77], especially heme-containing proteins [78]. As it has been revealed, the vast majority of bands comprising Raman spectra of Hb, isolated RBCs, and even whole blood originate from vibrational modes involving the C–C, C=C, and C–N bonds of the porphyrin ring within the heme structure [77–80], which are highly sensitive even to minute structural changes of the protein. Thus, this particular feature of hemoproteins' vibrational spectra holds promise for adapting RS to bloodstains dating studies, as it should give an insight into the formation of different Hb derivatives over time.

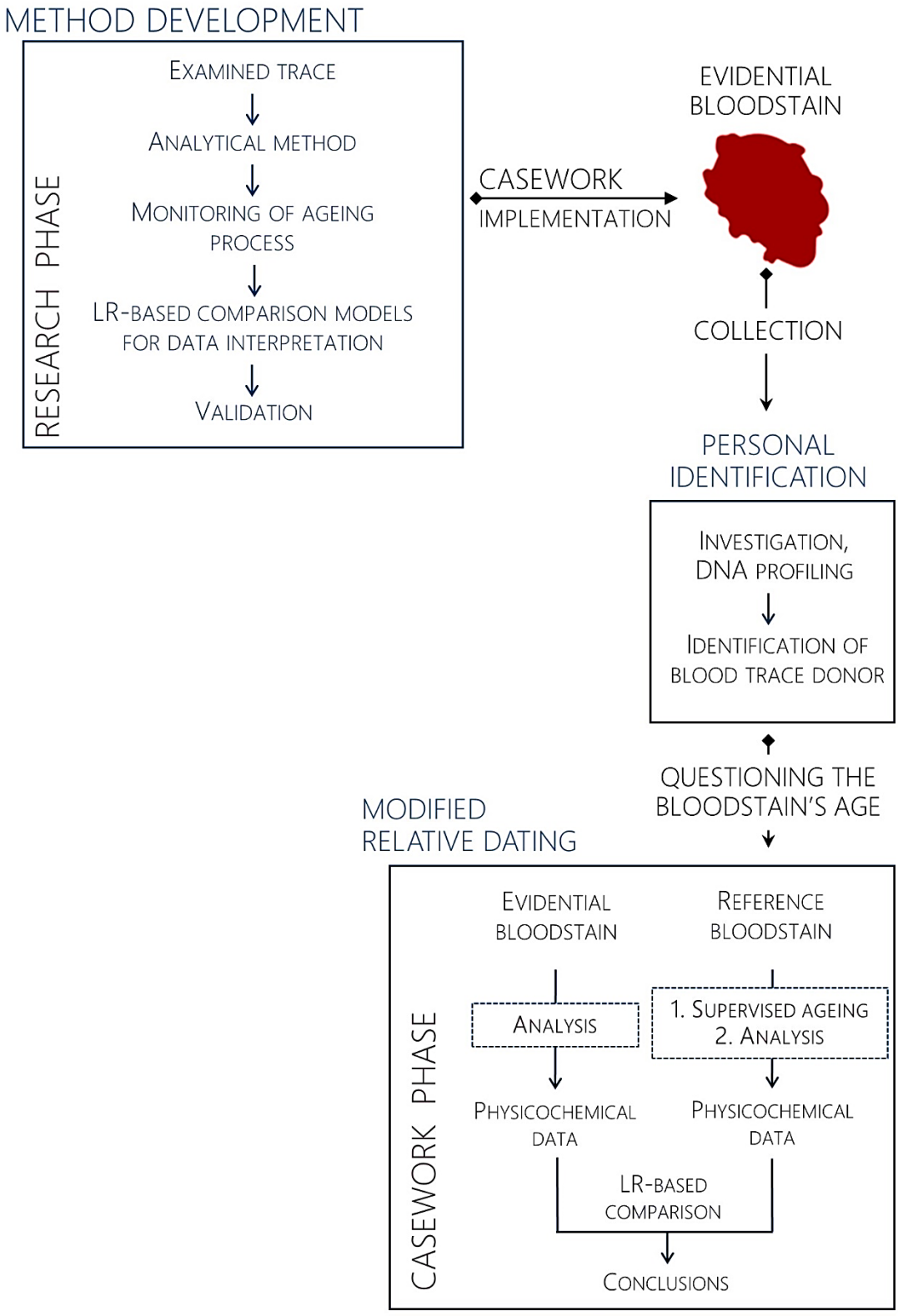

FIGURE 3.1.

A proposed procedure of modified relative dating of bloodstain evidence in forensic practice.

SECONDLY, EMPHASIS NEEDS TO BE PUT ON THE QUESTION 'WHAT DO THE ANALYTICAL RESULTS MEAN IN THE CONSIDERED CASE?'. Since the idea of absolute certainty has been abandoned by forensic scientists a long time ago [81], the evaluation of the evidence is best achieved through the application of the likelihood ratio approach (the justification for this is given in *Chapter 6*). As a consequence, answering the above question – in this particular case – boils down to the computation of LR models, designed for solving the comparison problem between two databases of Raman spectra of bloodstains, corresponding to the evidential and reference materials (possibly two sets of reference materials, as set out in detail in *2.2 The novel framework for evidence dating*). These probabilistic models should eventually allow assessing the (dis)similarity of obtained data, and through that, verify the stated hypotheses:

H_1: the age of the recovered evidence (bloodstain(s) of questioned age, revealed at the crime scene; t_E) MATCHES the age of the reference material (bloodstains obtained during the process of supervised aging according to the prosecutor's or defense standpoint; t_{R1} or t_{R2}): $t_E = t_{R1}$ (first comparison) or $t_E = t_{R2}$ (second comparison).

H_2: the age of the recovered evidence (bloodstain(s) of questioned age, revealed at the crime scene; t_E) DOES NOT MATCH the age of the reference material (bloodstains obtained during the process of supervised aging according to the prosecutor's or defense standpoint; t_{R1} or t_{R2}): $t_E \neq t_{R1}$ (first comparison) or $t_E \neq t_{R2}$ (second comparison).

It should be emphasized that studies reported in this thesis are confined to the so-called research phase of the proposed dating procedure (depicted as the *Method development* in Figure 3.1). In particular, they intend to verify the possibility of estimating the age of blood deposits – considered a comparison problem – through the LR-based approach.

All the research stages can be summarized in the following key elements:

1. Development of a Raman-based analytical method allowing for non-invasive and representative probing of the chemical composition of degrading bloodstains.
2. Collection of the spectral signatures of blood traces over the desired aging period.
3. Setting out a chemometric strategy for the pre-processing of obtained Raman spectra.
4. Designing the LR models for solving the comparison problem between the questioned bloodstain and the reference material(s) created "artificially."
5. Development of the LR models validation protocol.

Finally, it should be clearly stated that conducted studies, as yet, have not entered the casework phase. The modified relative dating suitability has not been tested in forensic reality; hence, the proposed approach – on no account – can be readily applied in practical proceedings.

| *CHAPTER 4*

EX VIVO DEGRADATION OF BLOOD

Approximately five liters of blood circulating inside the average human body serves two primary physiological functions – transport and defense – all of which are possible due to its steady flow to each body part through a system of arteries, veins, and capillaries. When these blood vessels are ruptured, causing external bleeding (e.g., a consequence of a criminal assault), blood loses its life-sustaining functions. Nevertheless, it continues to play a significant role – this time, however, supplying forensic investigations with crime-related information. In order to access a part thereof by answering the question of bloodstains age, the analyst should be familiar with a modicum of blood biochemistry and fundamentals of aging phenomena. An in-depth consideration of biological aspects is without a doubt out of the scope of this thesis and the reader's patience; nonetheless, a short overview of the subject is necessary to understand the essence of the problem and, most of all, the range of analytical methods available.

4.1 Composition of blood

Human blood is a liquid connective tissue, which comprises solid components, namely red blood cells (RBCs), white blood cells (WBCs), and platelets, suspended in straw-colored fluid, accounting for approximately 55% of the whole blood volume [82–84]. The liquid component – plasma – owes its form to the high water content (nearly 90% of plasma content). It acts as a carrying medium for the cellular elements and solutes such as lipids, salts, glucose, and series of dissolved proteins. Among the latter, one should distinguish clotting factors (numbered from I through XIII) involved in the coagulation cascade, which results in the formation of blood clots, consisting of all the cells entrapped in the mesh of fibrin threads [85]. The portion of blood, or more precisely, the remaining fraction of plasma, separated during clotting, is referred to as serum. It can be observed as a straw-yellow colored, watery fraction isolated above the dark red phase (the clot) in an undisturbed blood tube. In many cases, it can also be encountered at the crime scene, following a blood-shedding event, as pink-yellow fluid surrounding a coagulated pool of blood [85].

During the above-mentioned coagulation process, the clotting factors work in consort with the platelets (also called thrombocytes) involved in the initial phase of hemostasis. These nucleus-deprived, irregularly shaped cells are the smallest cellular components of blood with a diameter of no more than four microns. And while the prevention of excessive blood loss provided by platelets is undoubtedly important, the protection from infectious agents is no less crucial. The intracellular molecular mechanisms for fighting off infections are governed by WBCs (also known as leucocytes). Depending

on the apparent presence or absence of granules (sacs containing digestive enzymes or other chemical substances) in their cytoplasm, leucocytes are classified into two main categories: agranulocytes (lymphocytes and monocytes) and granulocytes (neutrophils, eosinophils, and basophils). Unlike the other cellular components of blood, all of WBCs are nucleated, which is especially important from the forensic perspective – since most DNA is found in the nucleus of a cell, WBCs are the primary source of DNA for forensic analysis of bloodstains [16, 17, 22]. Finally, apart from floating along in the bloodstream in search of infections, leucocytes are also responsible for other tasks such as removing particulate waste, small blood clots, and residues of the most abundant cellular blood component – erythrocytes – with an average life span of approximately 120 days [86]. Simplistically, while still functional, RBCs transport oxygen and carbon dioxide between cells and lungs [87]. In order to complete these functions, RBCs are "designed" in a highly well-thought-out manner. Their biconcave shape maximizes the efficiency of respiratory gas transport while simultaneously being small enough – the size of erythrocytes ranges from seven to eight microns – to make their way through the smallest of capillaries. In such a way, these two apparently contradictory requirements are satisfied, once again arousing our admiration for nature, which still beats the power of human imagination regarding the intelligence of its design.

Erythrocytes are not only the most numerous but – from our dating-oriented perspective – also the most important cells of the blood. Admittedly, normal RBCs counts fluctuate between 4.8 to 5.4 million cells per µl of fluid, making up about 45 percent of the whole blood volume. In the end, however, it is not the whole blood that we are interested in, but its residue – a bloodstain – which is created right after the completion of the water evaporation process. It should be underlined that **ERYTHROCYTES ARE** actually **THE MOST ABUNDANT COMPONENTS OF DRIED BLOODSTAINS**. For this reason, the vast number of proposed dating methods – including the one presented in this thesis – was focused on changing the properties of RBCs [23, 24]. In very few cases, these approaches were based on monitoring RBCs' time-dependent mechanical and morphological properties as a whole. As blood dries on the target surface, physical changes occur to the morphology of the cell – it becomes shrunken, loses its elasticity, and finally might even rupture and break apart [85]. These changes can be successfully monitored with atomic force microscopy (AFM), which has already been used to demonstrate alterations that occur to the elastic characteristics of RBCs [88–91]. Much more often, however, it was not even RBC that attracted the attention of researchers, but one of its major constituents, which resides in the cytoplasm, enclosed in a thin membrane of a highly organized structure.

Hemoglobin (Hb), referred to above, constitutes about 90–95 percent of the dry weight of RBCs. Its structure remained unresolved until the study of Max Pertuz, completed in 1959 [92], and it quickly became apparent that this Nobel-awarded discovery was indispensable to comprehend the spectacular role of Hb in medicine or biochemistry [93]. For example, the root cause of sickle cell disease – a blood disorder caused by a point mutation in the β-globin chain of Hb – would not be fully explained if not for the successful mapping of the protein structure [94]. What is possibly even more critical from a forensic

standpoint, Hb has been and continues to be of high investigative significance since it is a basis for many of the presumptive blood tests used at the crime scene. Some of the simplest and most frequently used methods (e.g., Leuchomalachite Green, Kastle–Meyer, or Hemastix® tests) rely on the peroxidase-like activity of Hb [95], which obviously results from its structural characteristics.

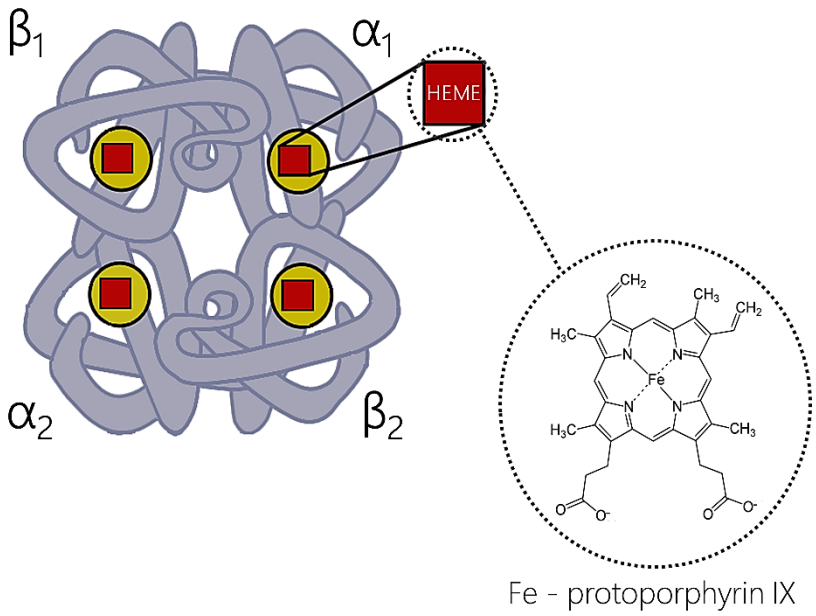

FIGURE 4.1.

A simplified structure of a hemoglobin molecule.

Hemoglobin consists of a protein part – the globin – and a prosthetic group – the heme [87], which is crucial for the above-mentioned capacity of Hb to act as a peroxidase in the presence of oxidizing equivalents (such as H_2O_2) [96]. The globin part is composed of four polypeptide chains, among which two pairs of subunits are distinguished. In human Hb, several different types of these subunits can be indicated – alpha (α), beta (β), gamma (γ), delta (δ) and epsilon (ε) – however, the normal adult hemoglobin (HbA) consists of globin containing mainly two pairs of polypeptide chains, α, and β, each having 141 and 146 amino acid residues respectively. A minor fraction of normal adult hemoglobin, referred to as HbA_2, apart from α- chains, also contains δ- subunits. As shown in Figure 4.1, within each of these chains, one heme molecule, composed of an organic component named protoporphyrin and a centrally placed iron ion, is located [87, 97]. The protoporphyrin structure is a nearly planar aromatic ring formed from four pyrrole-derived rings, joined together by methine bridges (=CH–), which creates a conjugated double bond system across the molecule [98]. This conjugation allows absorption of visible light, which gives heme – and eventually also blood – intensive red color. Depending on the substituents attached to the tetrapyrrole macrocycle, porphyrins encountered in natural systems possess an impressive variety of functional properties [99]. In the case of the heme protein, involved in oxygen transport and storage, catalysis, and gas sensing, the tetrapyrrole ring structure has

eight side chains – four methyl, two vinyl, and two propionate – attached to the C_β carbon atoms of the pyrrole rings (Figure 4.2).

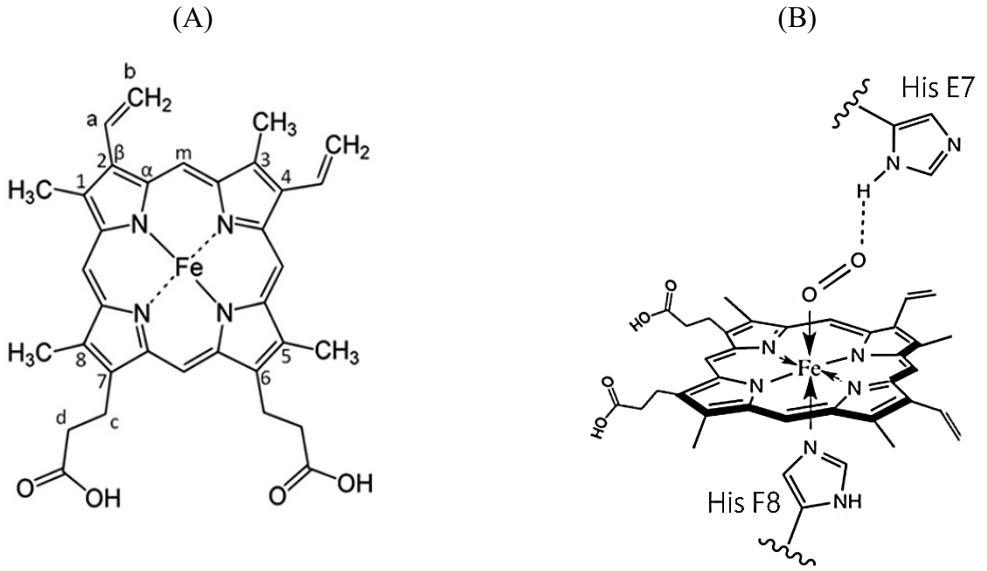

FIGURE 4.2.

A scheme of iron protoporphyrin IX (A); localization of proximal (His F8) and distal (His E7) histidines in relation to the plane of heme with the oxygen molecule bonded to the sixth coordination site of the ferric ion (B).

Finally, at the heart of the protoporphyrin ring of Hb, the iron ion is located, which can bind different types of ligands. It is attached to the organic moiety through pyrrole nitrogen atoms, which occupy four out of six of its coordination sites. Simultaneously, the remaining two can be employed to form additional bonds, one on each side of the macrocycle plane. The fifth coordination site of the central iron is invariably occupied by the nitrogen of the imidazole side chain in the proximal histidine (His F8), which originates from the protein part of Hb. In the proximity of the remaining sixth coordination site of the heme-embedded iron, there is another histidine residue – referred to as a distal histidine (His E7). This time, though, the amino acid is not attached to the iron (His E7 forms the Fe–N bond in the course of degradation – see *4.2 Chemistry of the aging process*), but it acts as a protective shield that isolates the iron from other Hb molecules. Such interaction might adversely affect the functionality of Hb, contributing to oxidation of the ferrous ion to its ferric form, which is incapable of binding oxygen. What is more, the distal histidine is also known to hamper access of carbon monoxide, which binds to the heme at the same site as oxygen, but approximately 210 times more tightly, leading to fatal consequences [87].

The heme-bound iron can exist in three different oxidation states [100]. It can be oxidized to the ferryl state (Fe(IV)=O) in the heme-containing oxygenases and peroxidases or to a more oxy-ferryl protoporphyrin IX radical during catalytic oxidation reactions. Nevertheless, for many of the *in vivo* functions of heme proteins, the ferrous (Fe^{2+}) and ferric (Fe^{3+}) oxidation states are sufficient. They

contain 24 or 23 electrons, respectively, including six or five valence electrons located on *3d* orbitals. If these electrons are located in orbitals of lower energy and coupled antiparallelly, then the iron ion is in a *low spin* (LS) state – in the case of Fe^{2+}, the spin number equals zero (S = 0), while for Fe^{3+} S = 1/2. In the *high spin* (HS) state of the iron ion, electrons are distributed parallelly, hence for the ferric ion, the spin number is 5/2, while for the ferrous – S = 2. It should also be emphasized that the electron configuration varies between different forms of Hb, as it changes upon binding of other ligands to the iron ion. And since the position of the iron ion in relation to the porphyrin plane is dependent on the spread of the electron cloud, alterations in the oxidation state of centrally placed iron, in a way, dictate the whole structure of Hb derivatives. This dependence, which becomes especially vital in dating studies, is well presented by the example of two major Hb species that can be recognized in the bloodstream of a healthy individual, namely five-coordinate ferrous deoxyhemoglobin (deoxyHb) – capable of binding oxygen – and oxyhemoglobin (oxyHb) with the oxygen molecule reversibly bonded to the sixth coordination site of the ferric ion (see Figure 4.4).

In the ferrous high-spin state of deoxyHb, the iron ion is simply too large to fit into the well-defined cavity within the porphyrin ring; hence it is placed approximately 4 nm out of the plane of the macrocycle, giving it a shape of a dome. In the ferric low-spin state characterizing the oxyHb, the macrocycle becomes more planar due to the movement of the iron ion toward the porphyrin plane. The explanation of this rearrangement –ridiculously simple yet beautiful – is as follows: binding of the oxygen molecule, which occupies the sixth coordination site of ferric ion, changes the distribution of electrons within the atom. Thus its dimension becomes small enough to fit in the crevice of the tetrapyrrole ring. The interaction between iron and oxygen is accompanied by the partial transfer of an electron from the ferrous ion of deoxyHb to the oxygen molecule; hence the superoxide anion (with the partial negative charge on the oxygen) is created. As a result, the structure is probably best described as the bond between the ferric cation (Fe^{3+}) and superoxide anion (O_2^-) [87, 101]. It is also important to mention that structural changes, which occur during ligand binding, are not strictly limited to the heme's plane. As the iron ion moves toward the porphyrin, the proximal histidine – coordinated to the iron in the fifth position – is also shifted, leading to the rupture of hydrogen bonds and some ionic interactions between α and β polypeptide chains [87, 97]. As a consequence, the conformational changes of the entire Hb molecule take place. Therefore, oxygen binding at one heme site is somehow communicated to neighboring sites of the molecule. Eventually, the resulting structure of oxyHb is referred to as the R form (*relaxed*) due to the greater mobility of its globin parts. In the case of deoxyHb, the α and β subunits are tighter; hence this particular Hb derivative is often called T form (*taut*).

However, the deoxyHb and oxyHb do not exhaust the list of Hb derivatives remaining in the bloodstream. Due to the position of the iron ion in a hydrophobic pocket within a Hb structure [102], oxyHb is considered a relatively stable protein. Oxidation, however, occurs either spontaneously at a rate of approximately 3% per day (this process is termed auto-oxidation) but also due to the influence of oxidative factors, to which Hb is exposed under physiological and non-physiological conditions. As

a consequence, superoxide radicals and methemoglobin (metHb) are formed. The latter product of oxyHb oxidation is defined as a derivative of Hb, containing a high-spin ferric heme [103]. The sixth coordination position of iron ion is occupied by water hydroxide anion [87, 104, 105]. As this particular form of Hb is no longer capable of binding and transporting oxygen, there should exist a protective mechanism that would somehow limit – as far as possible – this activity of the iron ion. And indeed, RBCs are not utterly defenseless against oxidation-induced deterioration. Erythrocytes have been equipped with proper enzymes (such as methemoglobin reductase and glutathione peroxidase), which reduce metHb to functional Hb and remove superoxide [106, 107]. Owing to this "recycling" process, less than 2% of total Hb species exists in the form of metHb [33, 103, 106, 108], simply because the rate of metHb reduction – taking place under physiological conditions – is far greater than oxyHb's oxidation.

In-vivo transformations of Hb, which were shortly described above, are accompanied by rearrangements of polypeptide chains, resulting in conformational changes of the protein molecule. In other words, one could say that Hb is an example of a protein in motion, which adapts to alterations in the electron distribution within the central iron ion, occurring upon its ligation. Finally, and perhaps most importantly, the structural dynamics of the Hb molecule is even more pronounced during the process of bloodstains degradation, and it can be indirectly monitored with suitable analytical techniques. As a consequence, this iron-rich protein has the potential to provide an insight into the enigmatic process of blood degradation.

4.2 Chemistry of the aging process

It is hard to deny that a continually growing body of blood-centered research is rather limited to the study of blood biochemistry, its functions, and diseases in living systems. At the same time, our knowledge about pathways of blood degradation occurring outside the human body remains superficial. On the first thought, it might appear that a thorough understanding of the aging chemistry is a *sine qua non* of answering the question of time elapsed since bloodstain deposition; hence some actions should be taken to fill this knowledge gap. On the other hand, though, when the forensic perspective is taken, one could ask if it is essential to describe the ex vivo transformations of blood exhaustively and identify all components of degrading traces. It is worth noticing that current dating approaches, usually based on vibrational spectroscopic data, could be compared to non-targeted methods. Due to their fingerprint character, spectral profiles are treated as snapshots representing the biomolecular composition of differently-aged samples. Variations therein are then exploited to recognize the changes that take place in degrading blood traces. On this basis – along with the support of chemometric methods – dating models can be established (more on this subject was already presented in *2.1. General dating concepts in forensic science*). However, it does not mean that the development of these models can be conducted mindlessly with a mere touch of a software button, with little or no knowledge of the subject.

Admittedly, examiners establishing multivariate dating tools usually are not concerned with naming individually each component, which gave rise to the observed signal. Nevertheless, they use biochemical knowledge to verify whether the variation observed in spectral features – correlated with the information of interest (herein, the age of the sample) – is consistent with possible degradation pathways. For this reason, at least a basic understanding of blood aging mechanisms – especially *ex vivo* transformations of Hb – should be gained.

When blood is deposited upon a surface, the cascade of physicochemical processes begins (Figure 4.3), which involves drying and coagulation of blood, accompanied by chemical transformations of its components.

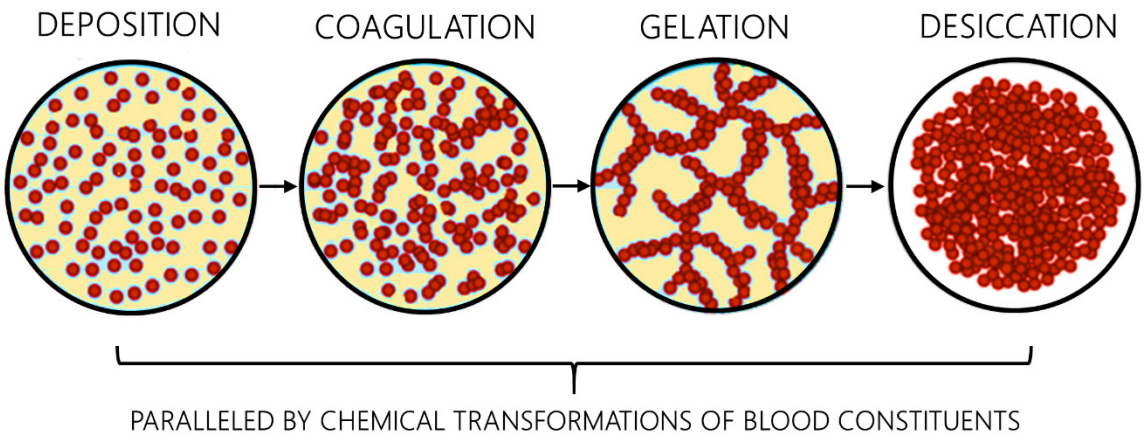

FIGURE 4.3.

An overview of the processes taking place after blood trace formation. The red dots represent the RBCs, while the yellowish areas correspond to the plasma [graphics modified from 109].

From a physical point of view, blood is often classified as a colloidal suspension, which can be described as a two-phase system composed of water as a liquid matrix and cellular elements – mainly RBCs – being the dispersed phase [109–111]. At the moment of bloodstain deposition, erythrocytes are homogenously distributed and move freely in the liquid plasma. Such a state, however, does not last long. During the coagulation process – initiated by aggregation of platelets in response to injured tissues – the network of fibrin polymer is formed, which leads to the gelation of blood [109–111]. Alongside the gelation stage, drying of watery fractions occurs, which follows different evaporation rates [109]. And precisely because of these two "competing" processes – evaporation and coagulation of blood – physical transformations of bloodstains encountered at the crime scene may proceed in different ways, depending on the amount of deposited fluid. As reported in practical forensic caseworks [16, 110, 112], separation of serum (the portion of plasma remaining after coagulation of blood) is observed exclusively in case of large blood deposits, where – due to the time taken for water to evaporate – the formation of blood clot can be completed. On the other hand, smaller bloodstains (just as those analyzed in the presented thesis) dry well before the time interval required for serum separation.

Once the desiccation process is completed, a pattern of self-organized blood particles (mainly RBCs) is created [113]. Interestingly – deviating slightly from the dating subject – the morphology of these blood residuals has also received scientific attention in the biomedical field. A few studies attempted to develop a cheap and rapid diagnostic tool [114, 115], assuming that blood residue arrangement depends on the composition of the liquid drop, which is obviously altered by certain diseases. Aside from that, the morphological changes of drying blood have also been studied by forensic scientists with the idea that cracking patterns of drying stains could reveal information concerning the time of their formation [109]. Thus, in order to calculate the age of bloodstains, originators of the described method have investigated the drying front – defined as an edge between dry and wet fluid, identified visually as a transition between the red and black color of drying trace – relating it to the evaporation rate of water and an approximative constant value of diffusion coefficient. And, of course, it is hard to deny that understanding mechanisms underlying the drying process, and correlating them to TSD, might be crucial for the correct assessment of case-specific time lapses. One need look no further than the famous case of Michael Peterson, an American writer convicted in 2003 of beating his wife to death at the bottom of the renowned staircase [116]. Among the key questions in understanding the timeline of events – described by Peterson as an unfortunate stairway accident – was the unknown timespan between the bleeding of the victim (formation of the blood pool) and the emergency call made by the grieving husband. Since the sizeable amount of blood was already dry on the arrival of paramedics and police forces, there were some reasonable suspicions concerning the chain of events given by Peterson. Therefore, during the trial, one of the most common inquiries addressed to forensic experts was the time required for bloodstains to dry – the question still easier asked than answered.

It should be remembered that the drying process is not only a function of blood volume but also temperature, humidity, air circulation, vapor pressure, and finally also the target surface [117, 118]. What is more, it is worth reflecting on whether it would not be better to monitor the drying process using more reliable tools than visual observation of bloodstains' morphology, such as near-infrared spectroscopy (NIR), which could be used for precise monitoring of moisture content. Not to mention the possibility of translating into the temporal information the chemical properties characterizing other blood constituents, which change during the progressive degradation of the trace. Hb and its derivatives play a unique role among these components.

4.2.1 Hemoglobin

The resulting bloodstain is formed mainly by cellular elements, the dominant part of which are erythrocytes filled with hemoglobin, which is why the vast majority of proposed dating methods boils down to pinpointing measurable parameters reflecting the degree of protein degradation [23, 24]. As previously mentioned, degrading blood traces contain at least several forms of Hb, depending on the oxidation state of iron ions and ligands bound to its sixth coordination site (see Figure 4.4). In

a bloodstream of a healthy individual, two main species of Hb can be distinguished – oxyHb and deoxyHb – which are also the predominant constituents (excluding water) of fresh blood deposits. However, as time proceeds, this initial population of Hb derivatives becomes more diverse, making it possible for forensic scientists to attempt to answer the question of time.

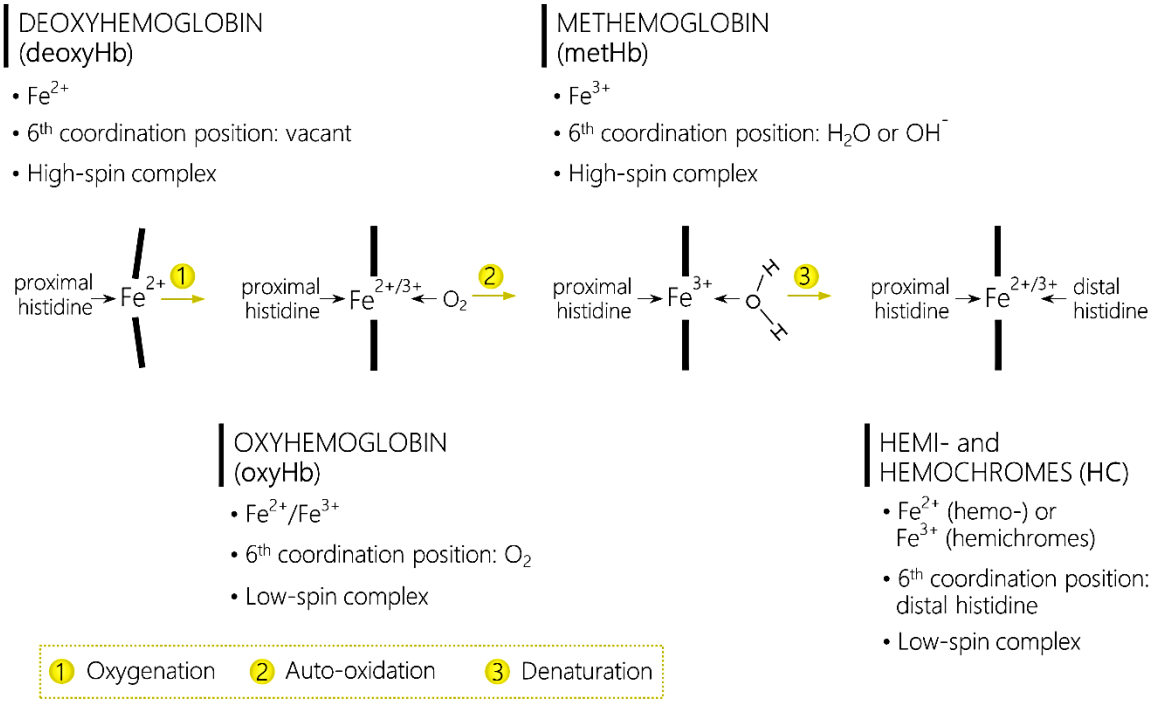

FIGURE 4.4.

Pathway of ex vivo hemoglobin degradation.

At the beginning of the Hb degradation process, aging changes may resemble the *in vivo* transformations. Upon exposure to ambient air, deoxyHb is transformed into oxyHb [101, 119–121]. This time, however, contrary to intravascular conversions, the fraction of deoxyHb is immediately saturated with oxygen in such a way that all oxygen-binding sites become occupied. Subsequently, as the oxyHb is continuously oxidized, a high spin ferric heme that cannot bind oxygen – namely metHb – is formed [105]. And that, in fact, is the point where some similarities between the *in vivo* and *ex vivo* transformations end, as – contrary to the metHb/deoxyHb redox cycle under physiological conditions – the formation of metHb, which takes place in degrading bloodstains, is irreversible. RBCs enzymes responsible for converting metHb back to deoxyHb are no longer functional outside of the cardiovascular system because they become inactivated due to denaturation during the drying process [122]. As a consequence, the degradation continues. Further spontaneous denaturation processes take place, producing irreversible and possibly reversible [123, 124] hemi- and hemochromes (HC), in which iron, either in the ferric (hemichrome) or the ferrous (hemochrome) low-spin state, coordinates endogenous amino acids – both proximal and distal His residues of globin chains [87, 106, 124]. To

enable the formation of these bis-His heme species, changes of the hydrophobic heme pocket geometry take place, resulting in conformational rearrangements in protein chains of Hb [125].

The aspect of oxyHb auto-oxidation and its subsequent denaturation was adequately addressed in the study of Bremmer et al. [126]. This particular research deviated from the standard dating studies, where empirical methods are employed to interpret the aging behavior of Hb, as it instead focused on understanding the conversion of oxyHb to metHb and HC, with particular attention given to the influence of environmental factors on these reaction rates. According to Bremmer et al. [126], the auto-oxidation of oxyHb should be described as a biphasic decay with a rapid first step, which slows down after approximately 10 hours since bloodstain formation. These oxidation rates can be classified as first-order reaction kinetics and have been proven to be severely affected by temperature. RH appeared to impact only the metHb-HC transition (a detailed description of the storage conditions' influence on the blood degradation can be found in *4.3 External factors influencing the degradation process*).

It has to be mentioned that according to the studies conducted on dried forms of Hb by Colombo and Sanches [124], some conformational changes occurring during the transition from metHb to HC are reversible upon rehydration. It cannot be excluded that in the drying process, a particular conformation of protein with the imidazole-N of distal histidine being sterically accessible for binding to the iron center is formed, which competes with other ligands (e.g., H_2O_2) for the sixth coordination position. The picture emerging from this study suggests that HC formed under drying conditions should not be considered as denatured species of Hb but their thermodynamically accessible derivatives. These conclusions – if factually accurate – are essential in terms of practical aspects of the dating procedure. Suppose the addition of water may somewhat “reverse” the aging of the bloodstain, inducing the transformation from HC to metHb [124, 127]. In that case, the traditional collection of blood traces with moistened cotton swabs should not be applied prior to the dating expertise. However, further research is definitely needed to verify these conclusions and eventually find a collection procedure, or preferably a non-invasive analytical method, which does not alter the chemical composition of bloodstains, leading to TSD misestimations.

Finally, it has also been established that HC, under certain physiological conditions, may be subjected to further oxidative deterioration, resulting in the release of the heme moiety due to dissociation of the polypeptide chains [104, 128]. Little is known, however, about subsequent transformations of denatured HC during the process of bloodstains degradation. Nevertheless, one thing is certain: the sixth coordination site of the iron atom is the place where all the action develops. The structural alterations of Hb, evolving during the oxidation and denaturation process, are accompanied by changes in its physicochemical properties (such as spin configuration, magnetic behavior, or optical absorption). Thus, tracking these changing Hb properties with suitable analytical tools may become an important way of deciphering the temporal information coded in evidential blood traces.

4.2.2 Other bloodstain constituents

It is abundantly clear – and if not, it should become clear upon reading the entire thesis – that the present research study was designed to reconstruct the issue of bloodstains dating, mainly through the examination of Hb degradation processes. However, it should be remembered that bloodstains' constituents are not limited solely to these heme-containing macromolecules. Apart from RBCs, there are other components – such as plasma with a whole range of proteins, enzymes, and WBCs containing both DNA and RNA – which undergo continual transformations. Therefore it is no surprise that degradation pathways of these remaining blood components have also attracted the attention of forensic scientists [23–26]. However, in these few cases, analytical methods of high sensitivity (e.g., fluorescence spectroscopy or biocatalytic assays) were precisely targeted at monitoring those specific molecules. Nevertheless, because of their low concentration, the contribution of these bloodstains' constituents to spectral signals examined within the present thesis is relatively negligible, and thus their application in dating studies is only briefly outlined.

Whole blood contains numerous endogenous fluorophores, including aromatic amino acids – Tryptophan (Trp), Tyrosine (Tyr), and Phenylalanine (Phe) – all of which are prone to time-triggered degradation. Therefore, it has been hypothesized that the conformational changes of blood Trp-containing proteins, mainly albumin and γ-globulin (two major plasma proteins), should be reflected throughout the process of bloodstains degradation in varying fluorescence lifetimes, corresponding to that particular aromatic amino acid. And indeed, these initial assumptions have been confirmed by studies of Guo et al. [129, 130] and later on by Shine et al. [131]. They demonstrated a non-linear decrease of fluorescence lifetimes of Trp over a degradation period. Additionally, besides the hypothesis about distortions of protein conformation, it has also been suggested that the origin of registered alterations in the monitored parameter might be the release of free amines or unbound iron ions, which are known for their quenching properties.

Apart from aromatic amino acids, there are also other plasma components appreciated for their age-dependent nature, which were used in monitoring the degradation process. A group of researchers led by Agudelo utilized natural denaturation processes of enzymes such as creatine kinase (CK) and alanine transaminase (ALT) [132] or alkaline phosphatase (ALP) [133] to determine the age of blood deposits. In those cases, the decay of enzymatic activity was monitored using biocatalytic assays designed to characterize the TSD of bloodstains and the age of the "source" of blood deposit.

Finally, some of the dating studies focused also on RNA [134–136]. While DNA appears to be a relatively stable component of dried blood deposits – at least as long as no bacterial growth occurs – RNA is subjected to more rapid degradation. For this reason, the process of RNA decomposition served as a basis for age determination of bloodstains in studies performed by Bauer et al. [134] and Anderson et al. [135, 136]. One could say that this RNA-based approach is somehow analogous to the Carbon-14 dating method, as in both cases, it is the ratio of different forms of the same "substance" that is used to

estimate the age of a sample. More specifically, RNA, known for its polymorphism, may exist in numerous forms (mRNA, tRNA, rRNA). These RNA species are characterized by different stability, leading to a change in ratios of RNA species over time. And precisely, this observation became the basis for estimating the age of bloodstains. In the Anderson et al. study from 2005 [135], real-time polymerase chain reaction (RT-PCR) was employed to monitor the ratio between mRNA versus rRNA. This approach was subsequently improved by targeting two distinct – although differently sized – regions on the same RNA strand, once again using RT-PCR assay [136]. It should be noted, however, that effectiveness of these methods depends on the quality of RNA, which can easily be compromised by storage conditions (e.g., temperature) during the bloodstain preservation period. Moreover, serological or biochemical techniques usually suffer from several fundamental issues – they are destructive, expensive, and time-consuming – which might successfully impede their application in practical proceedings.

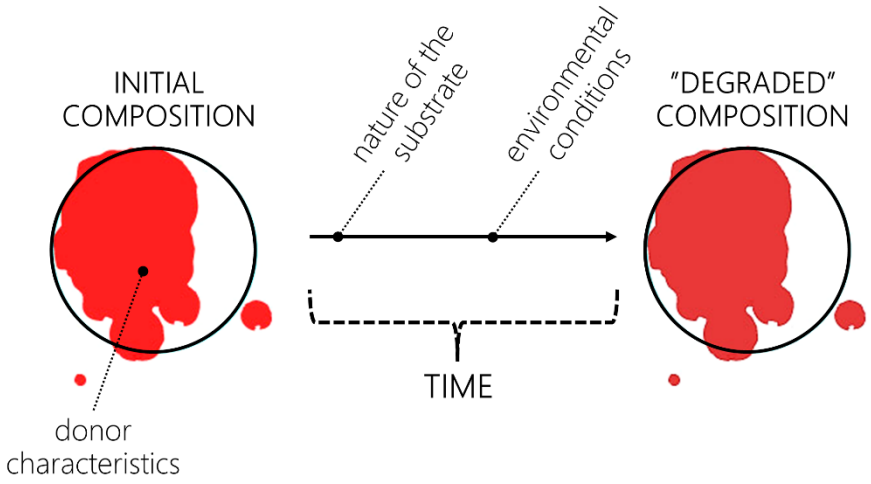

FIGURE 4.5.

A schematic representation of factors influencing the degradation of blood traces.

4.3 External factors influencing degradation process

Unfortunately, the aging process is not only a matter of time. Otherwise, the dating problem would probably have been solved long ago. Common to all forensic dating challenges, the core problem is that the world around us is a multifactorial system. It is not a vacuum neither a strictly controlled laboratory; hence evidence may degrade at different rates and possibly follow different decomposition pathways, depending on the wide range of external conditions to which it is exposed throughout the aging process. In the case of blood traces, among factors of potential importance, three groups can be indicated: the initial composition of blood (including between- but also within-person variations), the type of the substrate and, probably the most important of all of these, storage conditions (Figure 4.5).

Strangely enough, very few studies addressed the issue of the variability of bloodstains' aging kinetics, even though recognition of the above-mentioned dependencies is absolutely crucial when the practical implementation of proposed dating methodologies is taken into consideration. And to make matters worse, the already limited numbers of research investigating the influence of external factors on the degradation process of blood quite often reached contradictory conclusions, perhaps because the aging behavior was monitored with different analytical methods of varying sensitivity, aimed at characterizing other properties of blood traces. Above all, however, the impact of these external factors was usually studied in a univariate manner – changing one variable at a time – and therefore neglecting any potential interactions between them.

Finally, it should also be highlighted that the following subchapter considers only those factors, which may directly affect the process of Hb degradation (as the main component of bloodstains) itself. Other method-related effects, which may affect the aging process – such as a laser-induced degradation of bloodstains that can be sometimes observed in the case of Raman spectroscopy – will be discussed in forthcoming chapters.

4.3.1 Initial blood composition

In Larkin's Ph.D. dissertation from 2015, focused around bloodstain pattern analysis, it was stated *(...) blood can differ greatly from person to person; it is unknown what the significances of such changes in the components of blood will have on the drying bloodstains* [137]. Since then, little has changed, because the great majority of dating studies, in order to prevent introducing additional variability, was carried out using blood samples originating from a single donor or small, usually, undiversified groups of people, which included donor of the same race, biological sex, similar age, health conditions or even daily habits (e.g., smokers/non-smokers). And even if the sample's population was more varied, in a way that it consisted of blood collected from different individuals [38, 52, 53, 131, 138–140, 144], the number of examined blood traces was still insufficient for complete capture of biological variation and comprehensive evaluation of its influence on the process of degradation. Consequently, the current scientific knowledge on dependencies between the aging of bloodstains and their initial composition is actually no different from what it was five years ago – it is still opaque, often to the point of profound obscurity.

Blood is a medium, which - in addition to performing "housekeeping" functions – transfers vast amounts of information between different structures and compartments of the human body, mainly in the form of chemical signals. Thus it is not unusual when that blood-encoded information is used to characterize changes in cells, tissues, organs, and the body as a whole. To extract that biochemical information, researchers often reach for spectroscopic methods, such as Raman spectroscopy [78]. Spectral signatures of blood, but not only, have already been used to monitor the chemistry behind processes involved in ailments such as particular types of cancer, diabetes, or malaria. What is of

potential importance from the dating point of view, a few studies – such as those conducted by Lekka et al. [142] and Bryszewska [143] – established that some of the investigated conditions, for example, diabetes or hypertension, can alter the chemical composition of erythrocytes' membranes. As a result, differences in the RBCs stiffness between healthy donors and those suffering from the diseases mentioned above were reported. Now apply these observations to forensic reality and – more precisely – dating issues. In case when the progress of bloodstains' degradation is expressed through the alterations in the elastic properties of erythrocytes [88, 89], it would be highly unreasonable to underestimate the possible influence of these aberrations on the aging phenomenon, observed through the prism of atomic force spectroscopy (AFM).

Needless to say, that dependency between the chemical makeup of blood and its degradation may become even more important once disorders that directly affect the composition of blood – and especially Hb species – are considered. A perfect illustration of such a state is methemoglobinemia, a condition in which an abnormal amount of metHb is produced [103]. At this point, it should be recalled that once leaving the cardiovascular system of a healthy individual, blood should maintain metHb levels at no more than approximately 2% of total Hb species [33, 106, 108, 144]. In some instances, however, this particular form of Hb, incapable of binding oxygen, may be produced under physiological conditions in excessive amounts due to the genetic defect in the RBCs metabolism and the exposure to toxins and oxidant drugs [103, 104, 108].

When looking closely at Figure 4.4, we can only theorize that since successive transformations of Hb derivatives are, in fact, the basis of the blood aging process, then its degradation may proceed at different rates depending on the initial composition of the trace – e.g., the level of metHb or other biological components that vary in concentration throughout the day [145]. Nevertheless, all these hypotheses have no scientific value until verified based on extensive population studies, which ideally should take into account not only the aforementioned blood disorders but also other sources of biological variabilities, such as:

- different biological sexes, age, and race of donors [141];
- intake of medication, in particular, blood thinners such as aspirin, which interfere with blood clotting action [38, 146];
- levels of carboxyhemoglobin, which may be abnormally high in case of smokers, victims of carbon monoxide poisoning or fire [147–151];
- diet [103, 152–160].

In other words, if the health condition, lifestyle, or even dietary factors have an established impact on the blood composition, one cannot simply assume that the process of blood degradation will always follow the same pathways, irrespective of the donor and the time of bloodshed event. Thus, if anyone actually considers rendering dating methodologies from the laboratory bench to the crime scene (e.g., through the implementation of the modified relative dating approach), there is no question that the

issue of blood variability requires further research efforts [141, 147]. This will allow us to verify whether the reference bloodstain should be deposited using the blood drawn from the individual who was the "donor" of the bloodstain evidence.

4.3.2 Substrate properties

Until now, researchers have given little priority to the influence of the underlying substrate on the bloodstains' aging processes, marginalizing it in favor of the examination of other factors, especially the effect of storage conditions. It seems reasonable to assume that the interactions between the blood and the material on which the evidence was deposited should not significantly affect biochemical alterations of degrading blood traces [141], contrary to, for example, morphological properties of RBCs [88]. And indeed, this hypothesis was partially proven true owing to the study of Hanson et al. [161], which showed no noticeable effect of underlying substrate on the so-called blue spectral shift (hypsochromic shift) of the Hb Soret band, which was previously identified as a parameter correlated with TSD. However, finding Hanson's study comprehensive would be a tremendous understatement, as the research involved analysis of blood deposited on cotton, polyester, printer paper, and denim. In other words, researchers' attention was focused solely on absorbing materials; hence these results can constitute only partial evidence in support of the investigated hypothesis. After all, it is well known that properties of impacted surface – besides forces acting upon blood volume and composition of the fluid – affect the shape, size, and, what is even more important, the thickness of the bloodstain [137], which – in turn – determines the drying time of blood deposit. As already established, the time needed for the drying process to complete is not only important in the context of blood coagulation but also the rate of Hb transformations. According to another Hanson's investigation [123], autooxidation of oxyHb progresses faster in dried rather than liquid states of blood traces, which may be explained by the lack of activity of RBCs enzymes responsible for reducing metHb observed upon samples dehydration. That is why the investigation on blood-substrate interactions should be continued with the primary aim of comparing the rate of aging processes observed for bloodstains formed on porous and non-porous materials to verify whether the variations in drying periods of blood deposits may eventually affect the TSD estimations.

4.3.3 Environmental factors

Finally, it will not be an overstatement to say that the impact of initial blood composition or substrates' properties on the process of blood degradation almost pales into insignificance once compared with the influence of environmental factors. Bloodshed events may occur in varying humidity, light exposure, and temperatures, creating a multitude of aging scenarios, meaning that establishing a universal approach for bloodstains dating may be troublesome, if not impossible, to accomplish.

The first person to report the close link between the storage conditions of blood trace – namely temperature, light exposure, and relative humidity (RH) – and the rate of its aging, characterized by the blood color changes monitored with reflectance spectroscopy, probably was Patterson [32]. However, that particular branch of dating studies, focusing on the susceptibility of the decomposition process to environmental disturbances, for a long time did not attract the scientists' attention. In fact, the effect of evidence storage conditions has only recently become the center of intensive investigations, once the implementation of spectroscopic dating methods in practical proceedings became some kind of *idée fixe* of forensic examiners.

The transformations between different Hb species, including autooxidation of oxyHb to metHb with subsequent formation of HC, and thus also blood degradation process, are certainly temperature dependent [162]. For this reason, the influence of temperature is definitely the most exhaustively investigated factor that affects the aging of blood traces. Irrespective of the analytical method applied to track blood degradation, the conclusions of these studies unequivocally stated that an increase in the storage temperature accelerates the bloodstains' aging [52, 71, 123, 132, 161, 163–165]. According to the already mentioned study of Bremmer et al. [71], which may be the most comprehensive study in its field, temperature affects not only the transition rates of biphasic conversion of oxyHb to metHb (Eq. 4.1), corresponding to slow oxidation of β chains of Hb (designated as k_s) and fast oxidation of α chains (designated as k_f) but also the rate of metHb-HC transformation, marked as k_2.

$$oxyHb \xrightarrow{k_1=k_s+k_f} metHb \xrightarrow{k_2} HC \tag{4.1}$$

A substantial increase in the fast and slow oxidation rates (respectively, 6- and 18-fold) was observed over the temperature range, which might be encountered in real case scenarios, namely from −20°C to 37°C. What is more, according to Hanson et al. [123, 161], it is not only the rate of Hb transformations that is altered by temperature but also the extent of these conversions. As it has been established, elevated temperature contributed to a greater hypsochromic shift of the Soret band of Hb (λ_{max}=412 nm), which in the case of Hanson's method served as an aging marker, depicting the degree of bloodstains degradation. It should also be noted that based on Thanakiatkrai et al. [52] and Hanson et al. [123] studies, a significant slow-down in the degradation rate of bloodstains stored at low temperature was demonstrated. In the course of experiments, bloodstains were kept at −20°C, and – despite elapsing time – no substantial alterations in properties indicative of bloodstains' degradation were recorded. These independent findings can be of great importance in practice since they may allow the development of a sample preservation method before the analysis in real-world settings. Although, storage of bloodstains in deep-freeze conditions cannot be regarded as an entirely non-invasive method of sample preservation [127], halting the post-collection degradation changes – even if quasi-destructive – still

seems more reasonable than running the considerable risk of reaching a stage of advanced degradation, when observation of alterations in time-dependent properties of bloodstains is no longer possible.

Along with the temperature and time, the process of bloodstains aging is also a function of relative humidity [52, 71, 123]. The decrease in the rate of degradation with increasing RH levels was reported in the study of Hanson and Ballantyne [123] and subsequently confirmed by Thanakiatkrai et al. [52]. Group of Hanson, which investigated the aging behavior of bloodstains kept under varying RH ranges at two different temperature levels (22°C and 30°C), concluded that the scale of the RH impact on blood degradation could also depend on temperature, implying that both of these factors – RH and temperature – may alleviate or enhance each other. And, in fact, the authors of the above-mentioned paper, either consciously or unconsciously, suggested a significant venue for future research, which, as yet, has not been followed. It needs to be realized that discussed factors (temperature, RH, etc.) should not be considered as independent variables but rather as a system of interdependent factors. Interactions between them do occur. Hence, to get a whole picture, experiments that manipulate only a single factor at a time should be replaced by methods – such as techniques of factorial designs – which enable examination of their interactions [166].

But sadly, despite these premises, researchers followed the univariate way of proceeding. Bremmer et al. [71], who investigated solely the impact of RH using reflectance spectroscopy, established that the auto-oxidation of oxyHb – so the first stage of Hb conversion – was not affected by the RH. However, the situation is different as far as the conversion of metHb to HC is considered, which was described as a process highly dependent on the RH. Additionally, it was evidenced that the k_2 reaction rate constant (Eq. 4.1) tends to zero when the RH approximates 100%. It means that the high humidity conditions may inhibit the formation of HC, which is entirely in line with previous findings of Tsuruga et al. [167]. Finally, the link between the RH and the transformation from metHb to HC has also been demonstrated by Colombo and Sanches [124]. As already mentioned in *2.2.1 Hemoglobin*, some of the conformational changes of Hb chains that take place during the metHb-HC conversion might be reversible upon rehydration, which once again focuses our attention on the need to reconsider the concept of extracting bloodstains from the interfering substrate or collecting blood specimens with a moistened cotton swab before dating studies.

The impact of electromagnetic radiation is also not without significance. However, its effect on blood decomposition appears to be even more complicated, as several examinations performed to date led to somewhat contradictory results. In order to investigate the influence of light exposure, the way of proceeding has been common to all studies: blood samples were stored under different lighting conditions – exposed to sunlight or fluorescent light – and subsequently compared with degradation of traces, which were protected from any light sources. Research carried out by groups of Miki and Ikeya [163], Fuijta [165], and Thanakiatkrai [52] all evidenced that the rate of *ex vivo* blood degradation accelerated when the sample was exposed to sunlight. At roughly the same time, completely different

conclusions have been reached by Bauer et al. [134]. The experiment found no difference in the aging of bloodstains exposed to sunlight and those kept away from natural light sources.

Apart from the effect of the sunlight, scientists did not fail (or did they?) to shed some light on the impact of radiation emitted by fluorescent lamps – which are the most common type of artificial household lightning – on the aging process. In this case, similar aging patterns were reported for samples protected from artificial light and those kept under irradiation at room temperature, indicating that the fluorescent lamp has little [35] or no influence [52, 163] on the rate of bloodstain decomposition. However, as noted by Inoue [35], some differences are observed with increased temperature – storage of samples under the fluorescent light at 37°C, resulted in acceleration of aging changes in comparison to degradation processes involving bloodstains protected from the irradiation. Taking these results into consideration, it seems that it is an interaction of light exposure and temperature, which plays a decisive role in the aging processes. Conflicting conclusions drawn by researchers may have arisen because of differences in the storage temperature of bloodstains. Hence, once again – as it was already concluded in the case of studies involving the influence of RH – instead of investigating one variable at a time, methods enabling investigation of interactions between different factors – in other words, the multivariate approach – should be incorporated into degradation-directed studies. Another explanation, albeit more unlikely, was also pointed out by Bremmer et al. [23]. They suggested that these contradictory conclusions might arise from the fact that the ability to observe the influence of light exposure on the rate of bloodstains degradation is method-specific.

Lastly, it should be borne in mind that the degradation of bloodstains deposited in closed spaces represents possibly the most straightforward aging scenario. The evidential blood traces may be often exposed to the outdoor environment, subjected to hardly ever controlled fluctuations of weather conditions, soil, air pollution, or even bacterial growth [123]. In other words, no two crime scenes are ever precisely the same, and neither is the aging kinetics of blood traces. Precisely for this reason, as was already explained in *Chapter 2*, establishing a universal method for TSD estimations is impossible to accomplish. The overwhelming vicissitudes of environment and blood biology also mean that developing in advance a variety of conventional dating models, corresponding to each possible scenario that could be encountered at a hypothetical crime scene, will be a Sisyphean job. Eventually, once again, everything combines to prove that the solution should be instead sought elsewhere, perhaps by approaching the dating problem from an entirely different angle. One such solution is a previously introduced concept based on a modified methodology of relative dating, which constitutes the backbone of the present thesis, and which can eventually reshape our notion of what is achievable in terms of evidence dating. In order to do so, an analytical method for characterizing bloodstain degradation has to be developed.

| *CHAPTER 5*

AN ANALYTICAL METHOD FOR MONITORING BLOODSTAINS DEGRADATION

To establish any approach for estimating the TSD of blood traces, the information inherent to changes accompanying the process of blood degradation has to be delivered. In other words, developing an analytical method for probing the state of bloodstains decomposition becomes necessary. It is well understood that this particular phase is a core element of dating strategy, decisive in the entire venture's success. Because of that, it is also the point of intersection between all forensic quests for bloodstains age determination. Whatever dating approach is chosen, any strategy proposed to date has been initiated by developing analytical tools for monitoring bloodstains degradation. It will be no different with the present thesis.

Over the last decades, researchers specializing in the time-related examination of bloodstains have focused chiefly on spectroscopic techniques, which – due to the wealth of provided information and the nature of these analytical methods – should be an understandable tactic. For many years, spectroscopic methods have been primarily considered tools for molecular structure and organic matter studies, classified as primary research. However, the immense development of spectroscopic instrumentation combined with non-destructiveness and, often, user-friendly advantages of these techniques have expanded the application of spectroscopy to many other areas, contributing significantly to the development of the forensic research of body fluids [168]. In blood dating studies, approaches based on the visible range of the electromagnetic spectrum have received the greatest attention (approximately 60% of the articles published between 2011 and 2020). The remaining investigations have benefited from fluorescence and vibrational spectroscopy (NIR, FT-MIR, and Raman spectroscopy). The latter group is particularly noteworthy, as, during the previous years, their position has strengthened significantly. Should we be surprised? Not necessarily. After all, the scattering and absorption (within the wavelength range of 250–1100 nm) of whole blood are predominated by erythrocytes – they surpass scattering and absorption of other blood components by two to three orders of magnitude [169–171]. When moving beyond 1100 nm toward the NIR range of the electromagnetic spectrum, blood absorption becomes dominated by water molecules' absorption, which may create a (misleading) impression of a problem[††]. However, as soon as water evaporation completes, small absorption peaks, between 1690 and 2400 nm, assigned to more specific blood components such as Hb, albumin, and globulin [140], can be identified. In essence, if the main contributor to each of the above-mentioned phenomena is RBC and Hb molecules – the main constituents of degrading blood traces (as explained in *Chapter 4*) – then spectroscopic techniques, founded on monitoring these phenomena,

[††] Even though water absorption bands obscure other blood's spectral features, tracking the degree of water evaporation may actually provide some valuable time-dependent information, indicative of the bloodstains' age.

appear to be adequate tools to characterize the aging bloodstains. Table 1 summarizes papers focused on the estimation of TSD of bloodstains by spectroscopic techniques.

Interactions between electromagnetic radiation and matter – which constitutes the backbone of any spectroscopic method – are an effective way of probing the chemical composition of samples and their physical properties. According to its wave nature, electromagnetic radiation can be characterized by the wavelength λ (the distance between two points on the wave of the same phase, given in nm), its frequency ν (the number of oscillations per unit time, given in Hz), and its wavenumber (the number of waves per unit length, in cm^{-1})‡‡. However, in many phenomena (e.g., in molecular transitions), radiation reveals its particle nature, where it should be treated as discrete "packets" of energy called photons. According to this (quantum) interpretation, one photon's energy is proportional to its frequency and wavenumber. The Planck equation gives the relationship between these scales:

$$E = h\nu = \frac{hc}{\lambda}, \tag{5.1}$$

where h is Planck's constant (6.626×10^{-34} J·s) and c corresponds to the velocity of light in a vacuum (2.998×10^{10} cm/s).

According to Eq. 5.1, the energy of radiation increases with its frequency. Thus, depending on the electromagnetic radiation's wavelength, various kinds of light-matter interactions might occur [172]. What is more, these interactions are also determined by the properties of the investigated materials. The energy possessed by a molecule at any given moment is defined as the combination of the contributing energy components: electronic, vibrational, rotational, and translational. Translational energy relates to the displacement of molecules in space as a function of the normal thermal motions of matter. Rotational energy is observed as a molecule's tumbling motion resulting from energy absorption in the microwave region. Vibrational energy corresponds to the absorption of energy by a molecule as the component atoms vibrate around the mean center of their chemical bonds. And finally, the electronic energy is linked to electrons' transitions while they are distributed throughout the molecule, either localized within specific bonds or delocalized over structures. In essence, the interaction of electromagnetic radiation with a molecule might lead to absorption that then induces an electronic, vibrational, or rotational transition, depending on this radiation's energy, which serves as a foundation for different spectroscopy methods. To examine these interactions, spectrometers are employed, which monitor the dependence between wavelength/wavenumber and the intensity of radiation absorbed (e.g., infrared spectroscopy), emitted (e.g., fluorescence spectroscopy), or scattered (e.g., Raman spectroscopy) by the system [173]. Such a dependence is called a spectrum, often considered the "fingerprint" of the studied material.

‡‡ In Raman spectroscopy, where the vibrational states are being considered, it is usually much more convenient to discuss the scattered radiation in terms of energy. Consequently, it is preferable to use frequency or wavenumber – instead of wavelength – which are linearly related to energy.

On a more macroscopic level, when the beam of incident radiation strikes the sample, a portion of the radiation undergoes specular reflection, which is determined by the refractive index – a measure of bending a ray of the incident light, resulting from the difference between optical densities of interfacing media [127]. Since the radiation does not penetrate the sample, its interaction with electrons of atoms and molecules of the material is somewhat limited. This phenomenon simply cannot offer rich chemical information. On the contrary, it frequently constitutes an obstacle to spectral measurements – manifested, among other things, in baseline vertical shifts and global intensity amplifications – which quite often can be effectively removed using different pre-processing methods (*Chapter 7.1*). The situation is entirely different when the incident radiation penetrates deeper into the sample's interior, leading to SCATTERING and ABSORPTION of the photons, yielding valuable insights into the specimen's chemical characteristics.

Suppose an incident photon's energy matches the energy gap between the ground and excited state of a molecule. In that case, the photon may be absorbed, resulting in the molecule being promoted to a higher energy state. Precisely this loss of the radiation's energy, which is used on the molecule excitation, is measured in absorption spectroscopy. When the incident radiation corresponds to the UV–Vis range of the electromagnetic spectrum, its absorption triggers the excitation of the outer electrons of the molecule (electronic transition), whereas absorption of infrared radiation brings about changes in molecular vibrations within molecules (vibrational transition). Upon irradiation, however, a photon may penetrate deeper into the matter, distort (polarize) the cloud of electrons around the nuclei, inducing some nuclear motions as well, and be immediately SCATTERED in all directions. In this case, there is no need for the photon to correspond to the energy gap between the ground and the excited VIBRATIONAL STATE of the molecule. Nevertheless, it still enables determining the molecule's vibrational frequencies (for details, see *5.1.1 Fundamentals of the technique*). And precisely, this type of light-matter interaction, known as the RAMAN EFFECT, will be placed at the core of the present thesis. The following subchapter outlines the theory behind the technique applied herein to probe the chemical composition of degrading bloodstains.

5.1 Raman spectroscopy

Within this work scope, a method hypothesized as a suitable tool for monitoring the bloodstains degradation is RAMAN SPECTROSCOPY (RS). The choice of RS was coherent with its maturation as a powerful technique in the analysis of biosamples [77], especially heme-containing proteins [78]. Furthermore, it has been revealed that the vast majority of bands comprising Raman spectra of Hb, isolated erythrocytes, and even whole blood originate from vibrational modes involving the C–C, C=C, and C–N bonds of the porphyrin ring within the heme structure [78–80], which are highly sensitive even to minute structural changes of the protein.

TABLE 5.1. Recent spectroscopic techniques (2011–2020) applied in the bloodstains dating.

Technique	Monitored characteristics of aging bloodstains	Type of the substrate	Sample preparation for the analysis	Results	The time scale of the method	Ref.
Microspectrophotometry (MSP)	Variables extracted from the Vis reflectance spectra (442–585 nm) with feature selection methods (Fisher weight's and an approach based on Fourier Transform)	Glazed white tile	None; non-destructive analysis	Most distinctive changes appeared in the region of the α and β absorption bands of Hb, with the bands decreasing in intensity, broadening and merging into one band with increasing TSD; LDA model developed to estimate the TSD between 1 and 37 days, allowed to obtain up to 99.2% CCR when training and test set spectra were registered for the same bloodstain; For separate bloodstains serving as training and test sets, the LDA model was characterized by a CCR of 54.7%, with an average error of ca. 17 hours (for estimations up to 19 days since deposition)	–	[174]
Reflectance Spectroscopy in visible (VIS) range	Fractions of bloodstain chromophores oxyHb, met-Hb, and HC determined by quantitative analysis of reflectance spectra (350–1050 nm)	White cotton substrate	None; non-destructive analysis	Fractions of Hb derivatives (oxyHb, metHb, and HC) in bloodstains demonstrated a distinct temporal behavior; OxyHb underwent a biphasic auto-oxidation process, rate of oxidation decreased as bloodstains aged	Up to 60 days since deposition	[37]

(continued on next page)

TABLE 5.1. (continued)

Technique	Monitored characteristics of aging bloodstains	Type of the substrate	Sample preparation for the analysis	Results	The time scale of the method	Ref.
				The sum of the monitored Hb fractions remained approx. constant during the aging period, indicating that the whole content of oxyHb is transformed to metHb and HC		[37]
Reflectance Spectroscopy in visible (VIS) range	Fractions of oxyHb, metHb, and HC determined by quantitative analysis of reflectance spectra (450–800 nm)	White cotton	None; non-destructive analysis	Transformation of oxyHb followed biphasic oxidation - initially rapid process slowed down after ten hours; Rates of oxidation processes were strongly temperature-dependent; The transition from oxyHb to metHb did not depend on RH, contrary to the subsequent metHb to HC transformation, which was affected by RH (for the RH→100%, no HC is formed)	–	[126]
Reflectance Spectroscopy in visible (VIS) range	Visible reflectance spectra recorded in range 400–1000 nm (multivariate analysis)	Glass slides	None; non-destructive analysis	PLSR, PCR, and LS-SVM models, established on three different periods (from 2 to 24 h, 1 to 7 days, and 7 to 45 days since bloodstain formation), were developed; The best predictive ability was obtained for the models based on the region of 500–780 nm of Vis spectrum;	Up to 45 days since deposition	[139]

(continued on next page)

TABLE 5.1. (continued)

Technique	Monitored characteristics of aging bloodstains	Type of the substrate	Sample preparation for the analysis	Results	The time scale of the method	Ref.
				LS-SVM models outperformed the PLSR and PCR models, achieving an RMSEP of 42.7920 hours		[139]
Hyperspectral imaging (HSI)	Fractions of oxyHb, metHb, and HC - values extracted from visible reflectance images of bloodstains	White cotton	None; non-destructive analysis	Fraction of oxyHb decreased with time, while the content of metHb increased within the three weeks since deposition, with subsequent decrease of its value; a fraction of HC increased with time; Owing to the comparison with bloodstains within the reference database, TSD of the samples, mimicking evidence found at crime scenes, could have been estimated (absolute dating); Accuracy of estimation decreased with age from 0.9 days of absolute error, corresponding to the bloodstain of 0.1 days old, to 6.0 days of error for the sample analyzed 40 days after deposition; Order of deposition of bloodstains (relative dating), stored under unknown conditions, was established without comparison with database samples	Up to 200 days since deposition with the median relative error equal to 13.4% of the actual age	[151]

(continued on next page)

TABLE 5.1. (continued)

Technique	Monitored characteristics of aging bloodstains	Type of the substrate	Sample preparation for the analysis	Results	The time scale of the method	Ref.
Hyperspectral imaging (HSI)	Reflectance spectra (Vis range, between 505 nm and 600 nm) - four (for 30 days study) and eight (for one day study) variables corresponding to intensities at spectral wavelengths, selected with feature selection method (Fisher test combined with analysis of the correlation between variables)	White photocopier paper (80 g/m2)	None; non-destructive analysis	Conversion of oxyHb to HC, monitored by the relative intensity of the readings at 550 nm to 520 nm as a function of time, revealed exponential decay, which corresponds to fast oxidation of oxyHb to metHb (complete within three days), followed by slow formation of HC (continuing up to 30 days); LDA model based on selected variables allowed to estimate the TSD of test samples with an average error of ±0.27 days for the first seven days and an average overall mistake of ±1.17 days up to 30 days	Up to 30 days since deposition	[162]
Digital image analysis	Color analysis: color values (CMYK) extracted from the digital images	Filter paper; Mock case: 24 bloodstains deposited on household objects and stored under uncontrolled conditions	None; non-destructive analysis	Magenta color value (M) was chosen as a parameter for developing a dating model due to its high correlation with TSD (R^2 = 0.966); Magenta values decreased exponentially with increasing time;	Up to 42 days since deposition	[52]

(continued on next page)

TABLE 5.1. (continued)

Technique	Monitored characteristics of aging bloodstains	Type of the substrate	Sample preparation for the analysis	Results	The time scale of the method	Ref.
				Within- and between-person variations were not observed ($p > 0.05$); Smartphone camera, temperature, humidity, and substrate color influence the dating analysis itself, but also the process of bloodstain degradation (T and RH); Machine learning classification algorithm Random Forests™ for age estimation allowed for 100% accurate predictions during the blind test (samples stored under controlled conditions) and 83% correct classifications of mock casework samples		[52]
Digital image analysis	Color analysis: RGB values per pixel of bloodstain image converted into the V value of HSV (hue, saturation, and brightness)	Wood, slide glass, wallpaper, fabric, and A4 paper at 0°, 15°, 30°, 45°, and 60°	None; non-destructive analysis	Changes in the color of bloodstains were detectable on five different materials up to 42 hours elapsed since bloodstain formation; No significant difference was observed in color intensity values of the bloodstains under the following conditions: 5 °C and 23 °C; 10, 25, 40, and 55% RH;	Up to 42 hours since deposition	[53]

(continued on next page)

TABLE 5.1. (continued)

Technique	Monitored characteristics of aging bloodstains	Type of the substrate	Sample preparation for the analysis	Results	The time scale of the method	Ref.
				Storage temperature influenced the degradation process: differences between V values for bloodstains stored in 10 °C and 37 °C were detected		[53]
Fluorescence spectroscopy (λ_{ex}: 295 nm, λ_{em}: 350 nm)	The fluorescence lifetime of tryptophan, an endogenous fluorophore of blood proteins	Plastic Petri dishes	Dried scratches of blood dissolved in PBS buffer and centrifuged; plasma was subjected to analysis	Non-linear decrease of fluorescence lifetimes from 4.0 ns for blood analyzed immediately after deposition to 2.5 ns, corresponding to two-month-old bloodstains, was observed; Most rapid changes occurred within the first 150 hours since bloodstain creation, with plateau being reached after approx. 300 hours	Up to seven days since deposition	[129]
Solid-state fluorescence spectroscopy (λ_{ex}: 405 nm, λ_{em} > 435 nm)	Fluorescence lifetime images of tryptophan	Non-specified	None; non-destructive analysis	Images of solid-state bloodstains demonstrated heterogeneity of the lifetime distributions within the sample surface; Correlation of the intensity of fluorescence and its lifetime values, corresponding to the different points of bloodstains (fluorescence mapping), with TSD may serve as a more reliable method of bloodstain dating	–	[130]

(continued on next page)

TABLE 5.1. (continued)

Technique	Monitored characteristics of aging bloodstains	Type of the substrate	Sample preparation for the analysis	Results	The time scale of the method	Ref.
Fluorescence Spectroscopy (λ_{ex}: 281 nm, λ_{em}: 330 nm)	The fluorescence life-time of tryptophan and tyrosine	Plastic Petri dishes	Bloodstains fragments of uncontro-lled sizes dissolved in 1 ml of PBS; The supernatant, obtained after vorte-xing, sonica-tion, and centrifuga-tion of sam-ples, was subjected to analysis	Non-linear decrease of fluorescence lifetimes over time from approx. 3.0 ns for samples analyzed 19 hours after deposition, to approx. 2.0 ns after 50 days of aging was observed; The decrease was statistically significant ($p < 0.05$) within the first 91 hours of the blood being deposited; A certain degree of inter-donor variation was revealed	Up to 91 hours since deposition; Suitable for distinguishing freshly deposited and older bloodstains	[131]
Near-infrared Spectroscopy	Vibrational reflectance spectra of whole dried bloodstains recorded in 1100–2500 nm (multivariate signature of blood components)	Porous (gauze) and non-porous (glass) substrates	None; non-destructive analysis	Vibrational bands originating from water molecules (~1400 nm and ~1900 nm) were the main contributor of fresh bloodstains; Substrate affected the rate of bloodstain drying ;	Up to 590 hours since deposition	[138]

(continued on next page)

TABLE 5.1. (continued)

Technique	Monitored characteristics of aging bloodstains	Type of the substrate	Sample preparation for the analysis	Results	The time scale of the method	Ref.
				After an hour, bands due to proteins appeared within the range 1800-2500 nm, and a new band, corresponding to the formation of metHb, appeared in the 1460–1860 nm; Standard error of prediction for a model based on the area of 1460 - 1860 nm band, fitted with a least-squares regression, equaled 2.3 hours over a total time of 590 hours		[138]
Near-infrared Spectroscopy	Vibrational reflectance spectra (800–2778 nm) of whole dried bloodstains (multi-variate signature of blood components, mainly Hb derivatives)	White, black, red, green, and blue cotton	None; non-destructive analysis	PLS model created for estimating the TSD, separately for each colored background, allowed to predict the age of the bloodstain up to one month, with RMSE of prediction varying from 6.8% to 8.9%; Accuracy of estimation decreased with age	Up to one month since deposition	[140]

(continued on next page)

TABLE 5.1. (continued)

Technique	Monitored characteristics of aging bloodstains	Type of the substrate	Sample preparation for the analysis	Results	The time scale of the method	Ref.
Attenuated total reflectance (ATR) Fourier transform infrared spectroscopy (FT-IR)	Spectra recorded using ATR mode in the range 900–1800 cm^{-1}	Glass slides	Bloodstain dissolved in normal saline deposited on the ATR crystal and dried with an air dryer	Vibrational bands at 1649 cm^{-1} (α-helix structure of Hb) and 1533 cm^{-1} (amide II) varied with TSD; Two PLSR models – for indoor and outdoor aged samples – exhibited RMSEP of 7.24 and 6.43 days, respectively, for the entire degradation period (0.25–107 days); Discrimination between fresh (TSD≤1 day) and old (TSD> 1 day) was possible owing to PLS-DA models (accuracy corresponding to outdoor samples equaled to 0.98 and indoor samples – 0.99)	Up to 107 days since deposition; Suitable for distinguishing freshly deposited and older bloodstains	[175]
Attenuated total reflectance (ATR) Fourier transform infrared spectroscopy (FT-IR)	Spectra recorded using ATR mode in the range 400-4000 cm^{-1}	Glass slides	None; non-destructive analysis	Bands at 1535 cm^{-1} (amide II) and 1647 cm^{-1} (α-helix structure of Hb) varied with the age of bloodstains; Regression-based statistical methods (curve estimation, MLR, and PLSR) were developed for age estimations based on variables (25 peaks) selected using peak analyzer method in *Origin* software within spectra subjected to 1st derivative transform;	Up to 175 days old bloodstains; MLR and PLSR models represent an error of ~3 ± 1 days and ~4 ± 1 days, respectively	[176]

(continued on next page)

TABLE 5.1. (continued)

Technique	Monitored characteristics of aging bloodstains	Type of the substrate	Sample preparation for the analysis	Results	The time scale of the method	Ref.
Raman Spectroscopy (laser wavelength: 785 nm)	Raman spectra of whole dried blood-stains (multivariate signature of blood components)	A silicon wafer	None; non-destructive analysis	After two weeks elapsed since bloodstains formation, new bands at 667, 747, and 1248 cm^{-1} materialized, whereas markers of Fe-O_2 at bands at 419, 570, and 1638 cm^{-1} disappeared; The spectrum of a two-week dried bloodstain exhibited the same vibrational features as those observed at high laser powers	–	[177]
Raman Spectroscopy (laser wavelength: 785 nm)	Raman spectra of whole dried blood-stains (multivariate signature of blood components, mainly Hb derivatives)	Glass slide covered with aluminum foil	None; non-destructive analysis	Several spectral features changed with time: 1) intensification of fluorescence background toward the low-frequency spectral range during the aging, possibly due to formation of metHb and HC, 2) 377 cm^{-1} band, identified as a metHb marker, increased its intensity in relation to 420 cm^{-1} (oxyHb marker); 3) intensity of the band at 1252 cm^{-1} (part of the amide III spectral region, assigned to the random coil) increased,	Up to 168 hours (seven days) since deposition; Suitable for differ-frentiating between "new" (1 hour) and "old" (1 week) bloodstains	[38]

(continued on next page)

TABLE 5.1. (continued)

Technique	Monitored characteristics of aging bloodstains	Type of the substrate	Sample preparation for the analysis	Results	The time scale of the method	Ref.
				4) intensity of bands at 1637 (O_2 marker band) and 1224 cm^{-1} (part of the amide III spectral region, assigned to β-sheet) decreased; PLSR analysis with four latent variables was used for developing a predictive model for TSD estimation with cross-validated RMSE and R^2 values of 0.13 and 0.97, respectively		[38]
Raman Spectroscopy (laser wavelength: 785 nm)	Raman spectra of whole dried bloodstains (chemical signature of blood components, mainly Hb derivatives)	Aluminum foil-covered microscope slide	None; non-destructive analysis	Spectral changes observed with aging: 1) increase of the fluorescence background toward the low-frequency spectral range, 2) decrease of the 1224 cm^{-1} band and increase of the 1252 cm^{-1} band, corresponding to transformation from β-sheet into a random coil (continue up to one month since bloodstain deposition); 3) increase of the 970 cm^{-1} band's intensity, reflecting Hb aggregation;	Up to 2 years	[141]

(continued on next page)

TABLE 5.1. (continued)

Technique	Monitored characteristics of aging bloodstains	Type of the substrate	Sample preparation for the analysis	Results	The time scale of the method	Ref.
				4) redshift of the band at 520 cm^{-1} to 500 cm^{-1} (after one month elapsed since deposition) with subsequent increase of its intensity, 5) red shift of 676 cm^{-1} and 754 cm^{-1} bands to 660 cm^{-1} and 746 cm^{-1} (after one month elapsed since deposition), 6) diminishing of following bands over time (non-existent in 1-year-old sample's spectrum): 345, 419, 1562, 1600, 1619, 1637 and 1653 cm^{-1}, 7) increase of the intensity of 440 cm^{-1} (novel spectral feature, non-existing in spectra for 1-month-old stains); Minimal variances between results obtained for different donors; Minor differences observed between spectra registered for one-year-old and two-year-old bloodstains; For TSD predictions PLSR and PCR calibration models based on 126 bloodstain spectra of the male donor were developed ($RMSE_{PLSR}$=0.29, $RMSE_{PCR}$=0.31, accuracy TSD estimations ~70%)		[141]

This particular feature of hemoproteins' vibrational spectra holds promise for adapting RS to bloodstains dating studies, as it should give an insight into the formation of different Hb derivatives over time. What is more, water molecules, which severely contribute to IR absorption bands, are weak Raman scatterers. This gives researchers a perfect opportunity to look directly into body fluids' chemical characteristics without water interference. As a result, inelastic scattering provides direct insight into the state of Hb, and hence RS has been repeatedly applied in blood-related investigations ranging from the understanding of Hb oxygenation [101, 178–183] to monitoring heme aggregation during disorders associated with erythrocytes [184–186], and, most importantly, in the forensic examinations [187, 188].

5.1.1 Fundamentals of the technique

Raman spectroscopy is based on transitions between vibrational and rotational levels of molecules resulting from inelastic light scattering. This effect was described theoretically by A. Smekal in 1923 [189] and confirmed experimentally by an Indian physicist C. V. Raman in 1928 [190].

It is interesting to note that the same effect of light scattering is, in fact, observed in the macro- and microscopic world. It can be imagined as a scattering of light by a colloidal solution when the particle size is similar to the incident light wavelength. Light scattering is also observed on the energy levels of molecules and can be explained by the vibrational levels. When a substance is irradiated with intense monochromatic light of frequency ν_0, three distinct mechanisms of the "molecule-electromagnetic wave" interactions can be observed (Figure 5.1):

- The elastic scattering, known as RAYLEIGH SCATTERING, where precisely the same frequency characterizes the scattered light as the incident radiation. According to the basic principles of quantum mechanics, in this case, the molecule is promoted into a much higher state called the virtual state, after which it immediately returns to the same ground-state (ν=0). Consequently, no energy changes occur.
- The inelastic scattering termed ANTI-STOKES RAMAN SCATTERING ($\nu_0+\nu_{osc}$). Here, an interaction between a photon and an excited molecule (ν=1) occurs, and subsequently, it returns to the ground state (ν=1). As a result, the radiation of increased frequency is scattered.
- The inelastic scattering referred to as STOKES RAMAN SCATTERING ($\nu_0-\nu_{osc}$). After the interaction with the photon, the molecule does not return to the ground state but to the excited level. Since the molecule retains some energy, then the frequency of the scattered radiation is reduced.

Differences in energy between scattered and incident radiation correspond to the investigated molecule's vibrational states [191–193], and precisely these varying frequencies of scattered light constitute a Raman spectrum. It consists of lines evenly located around the most intense Rayleigh band with frequencies $\nu_0 \pm \nu_{osc}$, where ν_{osc} corresponds to the transition frequency between vibrational levels.

The magnitude of the Raman shift from the Rayleigh band is independent of the excitation radiation frequency – it results solely from scattering molecules' properties. In theory, the Raman spectrum should comprise bands appearing at frequencies both lower and higher than ν_0. However, due to the lower intensity of the anti-Stokes bands ($\nu_0+\nu_{osc}$), resulting from the fact that oscillating excited states are poorly occupied at the room temperature (according to the Boltzmann distribution), typically, only the Stokes lines are recorded.

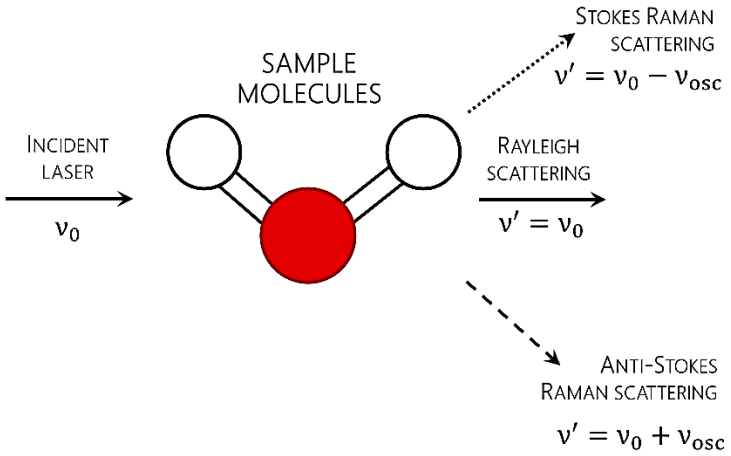

FIGURE 5.1.

Schematic representation of Rayleigh and Raman scattering.

The classical theory proposed by Placzek may explain the observed scattering mechanism. It is based on the concept that scattered light is generated by oscillating electric dipoles induced by the electric field of exciting radiation. In other words, it is accepted that upon the light-molecule interaction, the distribution of electrons in the molecule is deformed relative to the positively charged nuclei. As a result, an induced dipole moment is generated in the molecule (when linear Raman scattering is considered):

$$\mu_{ind} = \alpha E_0, \tag{5.2}$$

where α is polarizability tensor, E_0 is an electric vector of an electromagnetic wave. The polarizability represents the tendency of electrons of molecules to be distorted by an external electric field. It depends on the structure and type, and direction of chemical bonds in the molecule and is responsible for scattering exciting radiation in all directions.

As mentioned above, the scattering of light by a molecule is associated with oscillations of an induced electric dipole. Electric dipoles may be induced in a molecule by external electric fields. The electrical component of the electromagnetic radiation varies according to the following equation:

$$E = E_0 cos 2\pi \nu_0 t, \tag{5.3}$$

where E_0 corresponds to the amplitude, ν_0 to the frequency, and t is the time.

When radiation interacts with a vibrating molecule, the value of the induced dipole moment will vary with the same frequency so that the excited molecule will become the source of its own radiation:

$$\mu_{ind} = \alpha E_0 cos 2\pi \nu_0 t, \tag{5.4}$$

However, as has been already mentioned, the molecule scatters not only the ν_0 radiation, but also additional waves with different frequencies (Raman scattering). To adequately describe the scattered radiation distribution, more information on the polarizability should be provided. Each molecule possesses the non-zero polarizability, which is a 3×3 rank two tensor:

$$\alpha = \begin{pmatrix} \alpha_{XX} & \alpha_{XY} & \alpha_{XZ} \\ \alpha_{YX} & \alpha_{YY} & \alpha_{YZ} \\ \alpha_{ZX} & \alpha_{ZY} & \alpha_{ZZ} \end{pmatrix}. \tag{5.5}$$

In the case of isotropic molecules, all the components of a given tensor are identical. In turn, when at least one tensor value is different from the others (e.g. $\alpha_{XX} \neq \alpha_{XZ}$), then the molecule is anisotropic.

When oscillating, the molecule changes its shape according to its structural characteristics; hence each component of the polarizability tensor can be represented as:

$$\alpha_{ij} = (\alpha_{ij})_0 + (\frac{\delta \alpha_{ij}}{\delta q})_0 q, \tag{5.6}$$

where $(\frac{\delta \alpha_{ij}}{\delta q})_0$ describes the modification of the α_{ij} during the vibration described by coordinate q. This coordinate, characterizing the displacement of the atom's nuclei of the molecule around their equilibrium during the oscillations, can be defined according to the formula:

$$q = Q cos 2\pi \nu t, \tag{5.7}$$

where Q denotes the amplitude of given vibration of frequency ν. Combining this with the Eq. 5.6 results in an expression for the polarizability tensor:

$$\alpha_{ij} = (\alpha_{ij})_0 + (\frac{\delta \alpha_{ij}}{\delta q})_0 Q cos 2\pi \nu t, \tag{5.8}$$

which inserted into the formula for the induced dipole moment, finally leads us to the most important equation:

$$\mu_{ind} = \alpha_0 E_0 cos2\pi\nu_0 t + \frac{1}{2}(\frac{\delta\alpha}{\delta q})_0 Q_{osc} E_0 \times [cos2\pi(\nu_0 + \nu_{osc})t + cos2\pi(\nu_0 - \nu_{osc})t]. \quad (5.9)$$

This expression explains how – according to the classical theory of Raman scattering – the induced and also oscillating dipole moment simultaneously generates electromagnetic radiation of three frequencies, corresponding to Rayleigh (in red), Stokes (in green), and anti-Stokes (in blue) Raman scattering. The schematic diagram of energy levels illustrates the formation of three frequency components (Figure 5.2). This theory also evidences that the Raman shift is, in fact, independent of the excitation's wavelength. And thus, the obtained spectrum is expected to demonstrate the same wavenumber pattern (but not necessarily the same relative intensities), no matter what kind of laser line is chosen.

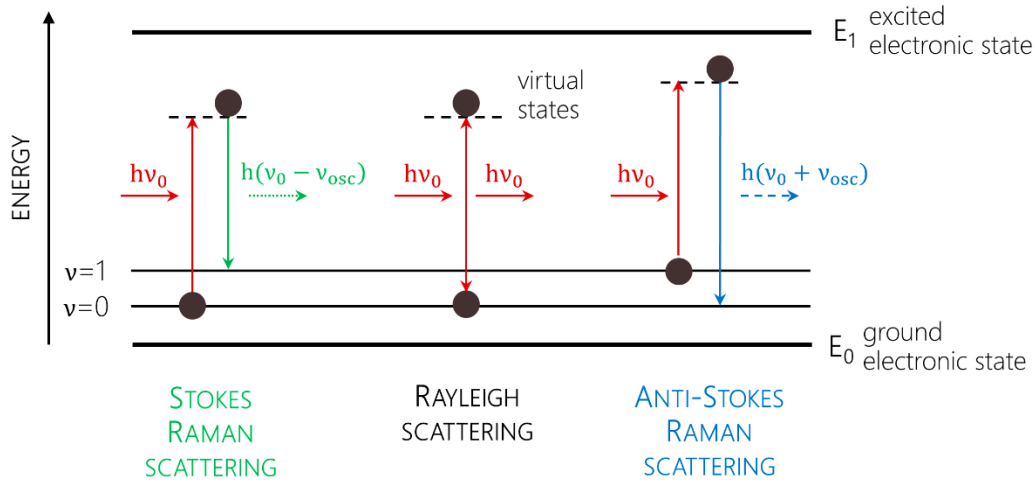

FIGURE 5.2.

A schematic representation of Rayleigh and Raman scattering energy transitions.

The energy diagram in Figure 5.2 shows the two-photon nature of Rayleigh and Raman scattering, which brings us to the partial quantum mechanical interpretation of the scattering process. In contrast to the IR absorption, which is a one-photon phenomenon, both Raman and Rayleigh scattering can be described as two simultaneous transitions via virtual states of the molecule. Firstly, a photon of the incident radiation is annihilated (once excited to the virtual state). Subsequently – after ca. 10-14 s – another photon either of the same energy (Rayleigh scattering), lower energy (Stokes Raman), or higher energy (anti-Stokes Raman) is created.

Any direct transitions between two energy levels accompanied by the scattering process (Raman transitions) are allowed when their transition moment is non-zero, and the change of polarizability due to transition from *n* to *m* vibrational state occurs:

$$\alpha_{nm} = \langle \Psi_n | \hat{\alpha} | \Psi_m \rangle. \tag{5.10}$$

It should also be mentioned that this quantum description, as the only one, properly describes the intensity of the scattered radiation for a given $n \rightarrow m$ transition, which will be determined by the properties of the transition polarizability tensor. Hence, it is necessary to investigate the dependence of the transition polarizabilities on the normal vibrational coordinates. The integral intensity of the Raman radiation (I_{Raman}) depends on the intensity of incident light (I_0), the fourth power of the frequency of the excitation light (if there is no absorption from any electronic transition of energy similar to the incident light), and on the square of transition moment of α_{nm}:

$$I_{Raman} \propto I_0 \cdot (\nu_0 \pm \nu_{osc})^4 \cdot |\alpha_{nm}|^2. \tag{5.11}$$

The intensity of Raman active vibrations is dependent on the incident light polarization, and the depolarization ratio ρ expresses this:

$$\rho = \frac{3\beta^2}{45\alpha^2 + 4\beta^2} = \frac{I_{90^\circ}}{I_{0^\circ}}, \tag{5.12}$$

where β corresponds to the anisotropy of the polarisability tensor.

The depolarization ratio is determined by recording the intensity of scattered light polarized perpendicularly (I_{90°) and the intensity of scattered light polarized parallelly (I_{0°). The depolarization ratio allows determining the symmetry of normal mode (vibration), and its value varies from 0 to 0.75. For ρ=0, a vibration is entirely symmetric (e.g., A_1), and its band is very intensive and called a totally polarized band. In turn, when ρ is 0.75, then vibration is totally asymmetric or degenerated (e.g., B_2, T). The corresponding bands are generally of low intensity and are called depolarized bands.

5.1.2 Instrumentation for Raman spectroscopy

Before any analysis, Raman spectroscopists face a series of choices in deciding how to investigate a questioned material to register a spectrum of sufficient quality. Given the sample's chemical characteristics, answers to all emerging questions are usually determined by choosing the excitation source, which dictates the type of instrument used. This choice, however, is not always straightforward. As previously described (Eq. 5.11), Raman scattering's intensity depends on the frequency of the exciting laser, its power, and the polarizability of the analyzed molecule. In other words, two adjustable parameters will decide on the quality of the registered spectrum – namely the wavelength and the power of the incident laser – among which the former one is far more significant because the scattering depends

on the fourth power of the frequency. And truth to be told, selecting the measurement parameters often revolves around improving the intensity of the weak Raman phenomena.

Given that information, the most intuitive way of significant signal enhancement would be working with the UV excitation, as it is the highest frequency available. Simultaneously, it should allow eliminating the undesired fluorescence background that often overlaps the entire Raman spectrum when the visible light is used. However, despite these advantages, excitation in the UV region is not a common choice. Why is that? Since many materials absorb UV radiation (such as bloodstains or biospecimens in general), high frequency does not only mean higher scattering intensity but also implies a higher risk of sample degradation through burning and photodecomposition. Looking at the other end of the available spectrum of excitation sources – namely the NIR incident lasers – the tables are turning. While the intensity of Raman scattering is significantly reduced – and hence also the quality of the spectrum – the risk of sample degradation is decreased as well. Thus, it becomes clear that it is nothing but the trade-off between signal strength, fluorescence background, and photodamage risk (particularly relevant in the case of biological samples) that often dominates excitation wavelength choice for Raman spectroscopy and consequently also the entire measuring system. And there is a lot to choose from.

TABLE 5.2. A comparison of interferometric and dispersive Raman spectrometers (modified from [191]).

	INTERFEROMETRIC SPECTROMETER	**DISPERSIVE SPECTROMETER**
Incident laser	NIR (usually the 1064 nm wavelength)	UV, Vis, NIR (wavelength up to 830 nm)
Sample compartment	Microscope stage; x, y, z – stage; macro chamber	Microscope stage; x, y, z – stage; macro chamber
Optical element splitting light	Interferometer	Monochromator (diffraction grating)
Detector	Semiconductor detector	CCD camera

Current Raman spectrometers can be generally divided into two major classes: systems consisting of a dispersive monochromator with a charge-coupled device (CCD) detector and interferometric instruments using a Fourier Transform (FT). As shown in Table 5.2, both of these systems operate on different laser excitation frequencies.

A closer examination of the above table should reveal the main difference between the dispersive and interferometric spectrometers regarding an optical element/setup, whose function is to split light scattered by a sample. And it is the wavelength of the excitation source that dictates the choice of these optical components. The crucial parts of the Raman spectrometer are described below, with a particular focus on the dispersive system (see Figure 5.3), which has been employed in the present study.

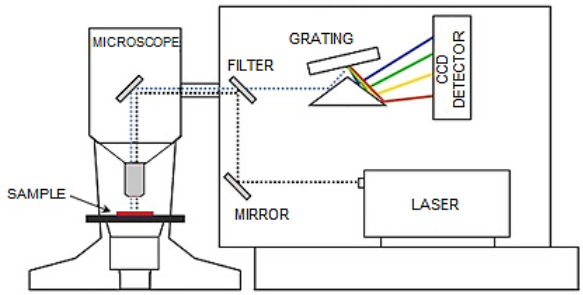

FIGURE 5.3.

A schematic diagram of a dispersive Raman microscope.

5.1.2.1 Laser

The type of laser used usually depends on the analyzed material. Dispersive Raman spectrometers, which take center stage in our considerations, are typically equipped with lasers ranging from UV through Vis to NIR light (up to 830 nm). For the already outlined reasons, UV sources are not the most common choice. However, UV scattering can provide some unique information (especially when protein-rich matrices are under examination [193, 194]). The most frequently used Raman systems are fitted with visible excitation lasers, typically an argon ion laser with excitation wavelengths at 488 and 514.5 nm or a helium-neon laser with the 632.8 nm excitation line. There has also been an overwhelming trend toward using NIR excitation (diode lasers with an excitation at 785 nm) in recent years. This drift stems from an interference source and frustration among Raman spectroscopists – the fluorescence phenomenon. Since considerably fewer molecules absorb in the NIR region than the Vis light, the main advantage of using NIR laser compared to lasers emitting UV-Vis light lies in minimizing (or even eliminating) the fluorescence background in Raman spectra. From the technical perspective, it is also possible to reduce the fluorescence even more by going further into the NIR (e.g., using the 1064 nm Nd/YAG lasers). However, it has to be borne in mind that these lasers carry an increased risk of sample damage due to heating effects. Since scattering decreases along with the increase of incident light wavelength (as shown in Eq. 5.11), the loss in signal intensity has to be compensated by much higher laser powers and longer exposure times. In effect, the final laser choice is always the compromise offered between fluorescence suppression and Raman scattering intensity.

5.1.2.2 Filters

To prevent an intense laser beam from reaching the detector and drowning out the relatively weak Raman scattering, the spectrometer has to be equipped with optical filters. Among these optical

elements, there are two basic types available – namely notch and edge filters. In both cases, they are placed in the beam path to block the Rayleigh scatter (laser line) and, at the same time, to allow the Raman scattered light (either Stokes or both Stokes and anti-Stokes components depending on the type of filter used) to reach the detector.

- NOTCH FILTERS have a sharp, discrete absorption, which coincides with a laser wavelength. In other words, this type of filter removes radiation solely at the laser's frequency and in a region on either side of it (ca. 200 cm^{-1} on both sides). As a result, measurements for both the Stokes and anti-Stokes Raman scattering become possible. However, the main disadvantage is the notch filter's finite lifetime, which will degrade in time.
- EDGE FILTERS are long-pass filters that absorb all wavelengths up to a certain frequency and transmit all wavelengths above this frequency with high efficiency. Consequently, only Stokes scattering (as well as any other lower energy radiation, e.g., fluorescence background) is transmitted to the detector. This type of filter allows for the laser line's excellent blocking since they are characterized by a very steep edge between the absorbing and transmitting spectral region. Clearly, registering anti-Stokes scattering becomes impossible. However, the advantage of edge filters is that they are cheaper and also environmentally stable with a near-infinite lifetime.

The main disadvantage of those filters is that they are coupled with only one excitation wavelength. If one desires to work with many laser sources, tunable filters might prove a good solution. However, this type of instrumentation is rarely considered for routine analysis since it requires a lot of experience to operate. Therefore, if one wishes to apply different excitation sources within the single Raman spectrometer, the simplest solution in technical terms still involves replacing the optical filter for the one adapted to the kind of laser used.

5.1.2.3 Spectrograph and detector

After filtering out the Rayleigh scattering, Raman light can be further processed using the optical system to separate the radiation into different frequencies. Subsequently, the so dispersed radiation reaches the CCD device (since FT-Raman is no longer our sole focus, the semiconductor detectors – which are usually used in interferometric spectrometers – will not be addressed in any way throughout this thesis). In order to split the beam of the inelastically scattered radiation, most modern Raman instruments employ spectrographs – with the Czerny-Turner spectrograph being particularly widely used – which direct various Raman wavelengths to different elements of the detector. An essential part of the spectrograph is the diffraction grating, which is a regularly spaced set of parallel slits that is intended to split the beam of Raman scattering. The dispersion of the radiation depends on the wavelength at which scattering is most efficient (the blaze wavelength) and the number of lines per centimeter (the dispersion

increases with the groove density). Given the sharp characteristics of Raman bands, it is preferred to use high groove density, which guarantees a broader dispersion of Raman scattering, and hence a higher resolution. A typical number of slits per 1 mm used in Raman spectrometers varies from 300–2000 for UV-Vis light and 10–200 for NIR, while the choice of the grating is obviously adjusted to the CCD detector.

The CCD detectors are dominant detectors for dispersive Raman spectrometers. In essence, the CCD is a two-dimensional array of silicon photovoltaic detectors. Each sector is separately connected to the computer, which "reads" each component (intensity and wavelength) of the previously spectrally splitted light. These sectored silicon sections are usually arranged in arrays of 200 × 200 up to 2048 × 1024 detector elements, which exhibit a high quantum yield in the range of 300–900 nm.

5.1.2.4 Sample preparation and handling

Generally, Raman spectra collection usually does not require complicated sample preparation procedures or a particular mounting type. The sample presentation is rarely an issue for bulk samples and other materials such as polymers, compressed pellets, or thin films. These types of materials, in most cases, are mounted on a three-axis translation stage directly under the laser beam, allowing *in situ* measurements. However, suppose the investigated material (e.g., bodily fluids or tissues) cannot be placed directly on the translation stage. In this case, samples have to be manipulated differently, often by depositing on Al-coated glass slides [38, 141, 177], which provide low and almost featureless background and enable the acquisition of high-quality Raman signals without substrate interference or losing important fingerprint information of biomedical specimen [195]. In some cases, however, the presentation of the investigated object may not be that straightforward, and the sample itself may require some form of gentle manipulation, as well, even when the non-destructive analysis should be preferred.

It should be clearly emphasized that the sample's morphology often dictates the quality of a registered spectrum. For example, a fine powder of a given material may yield a signal exhibiting a broad background, which is commonly ascribed to the sample's intrinsic fluorescence. However, as already demonstrated [196], this phenomenon is not always fluorescence-related, as the hampering background can be reduced once the material is prepared differently. Signals of better quality, with sufficiently defined spectral features, can usually be obtained when performing measurements of water-immersed samples[§§] [196] or simply by compression or homogenization material. This misinterpretation often arises when Raman spectra of biological specimens are considered. Nevertheless, it should be realized that the spectral background is not always correlated with the chemical composition of the sample (or its impurities) but with its morphology. Therefore, a proper preparation of the sample,

[§§] The important advantage of Raman spectroscopy is the possibility to record vibrational spectrum of aqueous solutions because of the low polarizability of water (contrary to its dipole moment, which hinders IR-based measurements).

providing – for example – a compact surface, may contribute to the limitation of stray light (reaching the CCD array), and through that, result in substantially reduced background. Obviously, this is not always possible, especially in forensic practice.

When working with biological specimens, other factors may hamper the process of spectral acquisition as well. In the case of highly absorbing materials, there is a substantial risk of sample decomposition. This sample damage can often be visually spotted as a change in color or a black spot on the sample's surface. However, in some cases, the damage is occurring solely on the molecular level. The best example of this is the subject of the present research, namely the heme-containing samples. As will be discussed later (see *Experimental part*), in this case, laser beam focused on the sample can result in changes of heme's conformation and its bonding in the protein, without destroying it, but resulting in subtle alterations of the spectral features. To minimize this effect, some unique strategies have to be developed. One possible method to reduce photodecomposition is to introduce a sampling method, in which the probed material does not remain irradiated throughout the whole time of the analysis but constantly moves, passing through the laser beam. With solid samples – like bloodstains – this can be done by spinning the specimen during the spectrum's acquisition, for example, by using specially designed rotating stages. By doing so, the photodamage minimized and indeed averaged spectral characteristics of a heterogeneous sample can be provided.

Finally, it should be mentioned that nowadays, a wide variety of Raman spectrometers is readily available, not only in research but also in forensic laboratories. One can choose from handheld spectrometers (which may be employed directly at the crime scene to perform the analysis as the investigation unfolds) or benchtop microscope systems, where the Raman spectroscopy is coupled with the conventional light microscopy. This combination offers the possibility to chemically investigate small-scale objects (e.g., > 0.5 μm), making it incredibly attractive when it comes to trace evidence analysis for forensic purposes. On the other hand, though, the Raman microscope's employment may pose some serious difficulties when faced with analyzing highly heterogeneous materials, as it carries a particular risk of subsampling errors, leading to non-representative Raman signatures. This obstacle can usually be overcome by acquiring a few single-point measurements within different sample areas [38, 141, 177]. This solution, however, is clearly impossible when the probed feature is time-dependent, and hence the acquisition of spectra should be performed within the shortest possible time. Fortunately, the challenge of representative sampling and interconnected time resolution can be mitigated by a relatively simple solution applied in this study – implementation of already mentioned rotating stage – which is exhaustively studied in the experimental part of the thesis (*Chapter 9*).

5.1.3 Raman spectra of hemoproteins

Before describing how Raman spectroscopy has been applied to the investigation of bloodstains for dating purposes, it seems reasonable to provide a short overview of information encoded in vibrational

spectra of proteins [197]. In particular, hemoglobin – the main component of degrading blood traces. Simply put, to justify the choice of Raman spectroscopy for monitoring bloodstains degradation, the origin and the general localization of bands, characteristics of molecular groups in hemoproteins should be at least briefly discussed.

With Raman spectroscopy, several vibrational modes can be employed for the analysis of protein structure. Most of them may fall into one of three categories:

- vibrations related to the secondary structure of proteins,
- vibrations originating from the amino-acid side chains,
- vibrations associated with prosthetic groups of proteins and other molecules interacting with them.

A short description of the first two groups will be provided in the following subchapters in general terms, while the last group of vibrations – being too diverse to be discussed comprehensively – will be limited exclusively to considerations about the hemoglobin derivatives.

5.1.3.1 Vibrations related to the secondary structure of proteins

As already briefly mentioned, even though water exhibits three Raman active vibrations, it is a weak Raman scatterer, and thus it rarely interferes with Raman spectra of other constituents (although the impact of water cannot be entirely excluded). What is more, based on the previous theoretical considerations, it can be concluded that stretching vibrations involving C=O and C–N bonds are expected to yield high Raman intensities because of the large polarizability changes associated with their vibrations. Given the above background, it becomes clear that Raman signatures of protein samples should give an insight into several amide bands, even without their resonance enhancement. These spectral features originate from atoms making up the peptide bond (CONH group) that vibrates with several frequencies. In total, nine amide modes can be distinguished referred to as amide A (NH stretching, about 3500cm^{-1}), amide B (NH stretching, about 3100 cm^{-1}), and amide I to VII (I: 1600–1690 cm^{-1}, II: 1480–1580 cm^{-1}, III: 1230– 1300cm^{-1}, IV: 625–770 cm^{-1}, V: 640–800cm^{-1}, VI: 540–600 cm^{-1}, VII: 200 cm^{-1}) [197]. However, when Raman spectra excited in the Vis spectral region are investigated, amide bands usually overlap with more intense side-chain bands [198–200], which prevents the registration of amide spectral features. As a consequence, only three of these signals are sufficiently well-resolved to provide any insight into the overall structure of the polypeptides, namely amide I, amide II (although a little less frequently), and finally amide III. The amide I mode is dominated by C=O stretching vibrations (with small contributions of N–H bending and C_{α}–H bending vibrations), while both amide II and III are associated with coupled C–N stretching and N–H bending vibrations of the peptide group.

In most biomolecular studies, a particular interest is usually devoted to the secondary structure of proteins, among which the α-helix and the β-sheet structures represent the most significant groups. Typical wavenumbers for α-helix and β-sheet structures are 1662–1655 and 1272–1264cm^{-1} (α), 1674–1672 and 1242–1227cm^{-1} (β), respectively, for amide I and amide III modes [201]. Most importantly for us, the shapes and positions of amide bands are sensitive to arrangements of amino acid residues in a polypeptide chain, which are hypothesized to change during bloodstains degradation. Therefore, a careful investigation of amide bands may contribute to the identification of different protein backbone confirmations. For example, when proteins undergo denaturation – e.g., during the aging of bloodstains – some conformational changes in which the natural ordered structure is converted into a disordered one should occur. This, in turn, is expected to contribute to changes in the Raman signatures, often assignable to amide III modes, but also vibrations of amino acid residues.

On the other hand, however, it is important to note that in order to investigate conformational changes of hemoproteins, e.g., in bloodstains, the UV or the NIR laser line (1064 nm) has to be employed [197, 202]. That is because bands due to amide modes of proteins are entirely missing in the Raman spectra excited within the visible range of the electromagnetic spectrum or even with the 785-nm laser line, which is fairly easy to explain when examining the electronic absorption spectrum of porphyrin-containing specimens (Figure 5.4), dominated by intense $\pi \rightarrow \pi^*$ transitions. Excitation in resonance with these transitions leads to an enhancement (even by a factor of 10^3 to 10^5) of the Raman-active modes of a porphyrin, producing spectra with features exclusive to the heme chromophore [197].

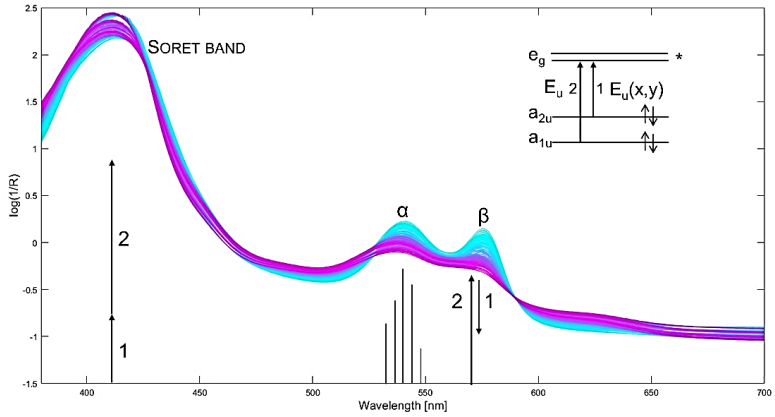

FIGURE 5.4.

Electronic absorption spectra of a heme-containing sample (degrading bloodstains) with a Soret band (at around 420 nm) and Q band (consisting of α and β components at ca. 530 and 575 nm, respectively).

5.1.3.2 | Vibrations originating from the amino-acid side chains

Besides the amide bands, Raman spectra of proteins also exhibit some additional features that allow investigation of the environment of amino acid chains. These include the amino acid side-chain modes originating from aromatic amino acids such as tyrosine, tryptophan, phenylalanine, and histidine – known as important structural stabilizing factors in peptides and proteins – as well as cysteine, which

forms sulfide bridges [203]. Previously identified Raman bands characteristic of aromatic amino acid vibrations are summarized in table 5.3.

TABLE 5.3. Raman features of aromatic amino acids in proteins.

AMINO ACID	FREQUENCIES [cm^{-1}]
Tyrosine	1620, 1210, 1183, **850**[a], **830**, **645**
Tryptophan	1582, 1552, 1417, **1360**, **1340**, 1011, 881, 757, 570
Phenylalanine	1605, 1585, 1207, 1183, 1035, 1005, 622
Histidine	**1282** or **1265**, 1204, 985, 623

[a] Bolded values indicate features sensitive to conformational changes.

TYROSINE is known to generate a pair of relatively intense Raman bands at 850 and 830 cm^{-1} [204], which may be employed for establishing the degree of the unfolding of a polypeptide chain in water, for example, during denaturation. These two bands result from the Fermi resonance phenomenon involving the in-plane fundamental mode expected to near 840 cm^{-1} and the first overtone of the out-of-plane bending vibration of atoms of the ring, substituted in the *para* position near 420 cm^{-1} [205, 206]. Studies of numerous proteins revealed the correlation between the ratio of intensities of the tyrosyl doublet (I_{850}/I_{830}) and the hydrogen-bonding state of the phenolic OH group. Consequently, as demonstrated by Siamwiza and co-workers [205], investigation of the ratio I_{850}/I_{830} reflects the OH hydrogen-bonding state, which, in turn, is indicative of the unfolding of the protein chain.

TRYPTOPHAN, as indicated in table 5.3, generates many prominent spectral features, which have been linked to the local environment and geometry of the tryptophan side chain in proteins. Among these, one should mention – once again – a Fermi doublet with components at 1360 and 1340 cm^{-1}. The intensity ratio of these two bands (I_{1360}/I_{1340}) serves as an indicator of local hydropathy since – as established by [206] – it increases with increasing hydrophobicity of the indole ring environment. Furthermore, the position of a sharp feature present within 1540 to 1560 cm^{-1} is indicative of the absolute value of the side chain torsion angle $\chi_{2,1}$ ($C_{\delta 1}$ –C_{γ} –C_{β} –C_{α}) [207]; the frequency of a Raman band near 880 cm^{-1} is sensitive to indole N–H hydrogen-bond donation [206]; while the 755 cm^{-1} band intensity, originating from an indole ring-breathing vibration, increases with decreasing hydrophobicity of the ring environment [208].

PHENYLALANINE, when it exceeds 1% of the protein composition, produces a band at approximately 1005 cm^{-1} – the most intense Raman line of phenylalanine – corresponding to the breathing vibration of the aromatic ring, which is also present in Raman signatures of bloodstains [38, 141, 177]. More detailed information about the origin of other spectral bands can be found in the work of Hernández et al. [209].

HISTIDINE in aqueous solutions exhibits relatively weak Raman features. However, when dissolved in D_2O, histidine generates a moderately intense Raman band near 1408 cm^{-1}, assigned to an

in-plane vibration of the N-deuterated imidazole ring [210]. This band is particularly useful for monitoring histidine H/D exchange dynamics as well as imidazole ring geometry [211].

CYSTEINE'S sulfhydryl bond (S–H) stretching vibration produces a Raman band, which has been evidenced to serve as a unique probe of local SH structure and dynamics [208, 212, 213]. This sulfhydryl marker is observed in a spectrum region (2500 to 2600 cm^{-1}) lacking interference from other protein Raman bands. The correlation between sulfhydryl hydrogen bonding and the S–H stretching frequency is well documented.

5.1.3.3 Vibrations associated with prosthetic groups of proteins – iron protoporphyrin IX

Nevertheless, given the current state of knowledge, it is somewhat unrealistic to expect a host of vibrations from amino acid side-chains or those related to secondary structures of proteins in the Raman signatures of bloodstains [214, 215]. It is well known that Raman spectra of protoporphyrin-based molecules, as multidentate complexes, are incredibly complicated, dominated with bands in the region 100−2000 cm^{-1}, both from the porphyrin ring and the iron's ligands. Vibrational frequencies for the C–C and C–N lie mainly in the region 200 to 1700 cm^{-1}, while the vibrations related to the metal atom (e.g., Fe–N, Fe–O_2, Fe–CO) occur solely between 200 and 800 cm^{-1}. This gives us the perfect opportunity to study heme protein structures, especially with the aid of resonance Raman spectroscopy (RRS), where a signal's enhancement is obtained once the laser excitation wavelength coincides with the porphyrin ring's absorption band [216].

The 1970s studies on Hb's structural characteristics initiated the exploitation of RS within the field of blood examination [101, 178, 179, 180, 181]. A comprehensive investigation of the normal vibrations of porphyrin systems has been performed by Abe *et al.* [217] and Spiro [101, 120]. The notion that Raman spectra of Hb reflect the oxidation and spin state of iron atoms and the degree of Hb oxygenation laid the foundation for future studies [218]. Subsequent research revealed that the vast majority of Raman peaks derive from the vibrations of C−C, C=C, and C=N bonds of the heme's porphyrin ring (see Figure 5.5) [80, 180, 217], and that – in fact – all of the present spectral features come exclusively from the heme. Examples of the specific peaks that correspond to vibrational modes of heme proteins are listed in Table 5.4.

Among the Raman bands listed in Table 5.4, some of the high-frequency vibrational modes are especially sensitive to the protoporphyrin's electron density and structural properties. For example, the features within the range 1400−1300 cm^{-1}, consisting of breathing modes of porphyrin macrocycle, reflect changes of the electron density in the π heme's orbitals. During the oxidation-reduction reactions of the central iron, the population of these orbitals changes significantly; thus, this spectral region is also known as the oxidation state marker line [80]. Raman bands in the high wavenumber region − 1650−1500 cm^{-1} − comprising mainly of porphyrin in-plane vibrational modes, are sensitized to

porphyrin distortions accompanying alternations in the size of the central porphyrin-core and the spin state of the iron atom. Hence this particular line was named the core-size marker line [80, 183].

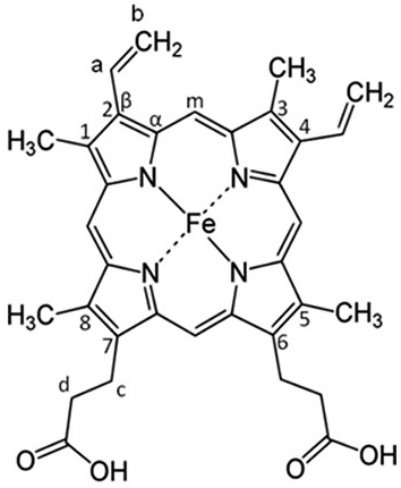

FIGURE 5.5.
Labeling scheme of iron protoporphyrin IX [219].

What is more, some of these porphyrin vibrations may be selectively enhanced, enabling precise analysis of heme dynamics. The symmetry and electronic structure of heme molecules result in their capability of absorbing Vis light. By tuning the incident laser wavelength to the vicinity of an electronic transition, the resonance Raman effect can be obtained and investigated, ranging from UV to NIR frequencies [210]. In fact, the current state of knowledge about Hb geometry and its dynamics is primarily derived from these rich resources of resonance Raman data [78]. As demonstrated in Figure 5.4, the electronic absorption spectrum of porphyrins is characterized with a Soret band around 420 nm and a Q band (consisting of α and β components at ca. 530 and 575 nm, respectively) [192, 220, 221]. When excited with a laser wavelength within the Soret maxima, a substantial enhancement of the ν_4 band (ca. 1360 cm^{-1}) is provided [220, 221]. When shifting towards 488 nm, apart from the 1360 cm^{-1}, a strong band is also observed at 1585 cm^{-1} (ν_{19} mode). In turn, the use of the 532 nm laser excitation enhances 1585, 1131, and 751 cm^{-1} Raman bands [101, 222], which are corresponding to ν_{19}, ν_{22}, and ν_{15} modes, respectively.

5.1.4 Probing degradation processes of bloodstains with Raman spectroscopy – an overview

Given that Hb's Raman spectra depend on the oxidation state and the spin state of the central iron atom, as well as on the nature of ligands and protein environment, it can be presumed that this particular analytical tool is an appropriate candidate for characterizing blood *ex vivo* transformations. And of course, the author is not the first to notice that Raman spectroscopy may provide molecular insight into Hb's degradation pathways.

TABLE 5.4. Band positions and corresponding coordinates/assignments for hemoglobin. Coordinates are based on Hu et al. [219], and assignments are based on a porphyrin labeling scheme created by Abe et al. [212]. Data is collected from Wood et al. [223] and Wood and McNaughton [210]. Positions vary slightly with excitation wavelength, and some modes are specific to the oxygenation state. The intensities of bands depend on resonance enhancement mechanisms.

OBSERVED BAND [cm^{-1}]	ASSIGNMENT	SYMMETRY TERM	LOCAL COORDINATE[a]
1653	Amide I		$\nu(C{=}O)+\nu(C{-}N)+\delta(NH_2)$
1639	ν_{10}	B_{1g}	$\nu(C_\alpha C_m)_{asym}$
1620			$\nu(C_a{=}C_b)$
1582	ν_{37}	E_u	$\nu(C_\alpha C_m)_{asym}$
1566	ν_{19}	B_{1g}	$\nu(C_\beta C_\beta)$
1547	ν_{11}	B_{1g}	$\nu(C_\beta C_\beta)$
1526	ν_{38}	E_u	ν(pyrrole breathing)
1448			$\delta(CH_2/CH_3)$
1371	ν_4	A_{1g}	ν(pyrrole half-ring)$_{sym}$
1356	ν_{41}	A_{1g}	ν(pyrrole half-ring)$_{sym}$
1222	ν_{13} or ν_{42}	B_{1g} or E_u	$\delta(C_mH)$
1207	$\nu_5 + \nu_{18}$	$A_{1g} + B_{1g}$	$\delta(C_mH)$
1174	ν_{30}	B_{2g}	ν(pyrrole half-ring)$_{asym}$
1156	ν_{44}	E_u	ν(pyrrole half-ring)$_{asym}$
1127	ν_5	B_{1g}	$\nu(C_{\beta}$–methyl)
1082			$\delta(=C_bH_2)_4$
1002			Phenylalanine
993	ν_{45}	E_u	$\nu(C_\beta C_1)$asym
975			$\nu(C_aH{=})$
827	γ_{10}	B_{1u}	$\gamma(C_mH)$
789	ν_6	A_{1g}	ν(pyrrole breathing)
754	ν_{15}	B_{1g}	ν(pyrrole breathing)
673	γ_5	A_{1g}	δ(pyrrole deform)$_{sym}$
576		A_{1g}	$\delta(Fe{-}O_2)$
419			$\delta(Fe{-}O{-}O)$

ν, in-plane stretch; *δ*, deformation mode; *γ*, out-of-plane stretch; sym, symmetric; asym, asymmetric; deform, deformation;
[a]Subscripts *α*, *β*, *m* represent the carbon atoms at the alpha, beta, and *meso* positions of porphyrins; a and b correspond to vinyl group carbons. For a detailed scheme of iron protoporphyrin macrocycle labeling, see Figure 5.5.

In a 2011 paper on the application of Raman spectroscopy in forensic analysis of blood [224], Boyd with co-workers noticed that the relative intensities of scattering peaks depend on the sample's age. This was presumably the first mention of the time-dependent behavior of the Raman spectra of bloodstains. It was tempting to associate these variations with Hb's structural changes resulting from its

ex vivo degradation. This finding put forensic scientists on the path leading to the question of what can be accomplished with Raman spectroscopy in terms of bloodstain dating.

Three years later, Lemler et al. [177] followed the direction indicated by Boyd's group. A two-week investigation of dried stains of whole blood revealed distinct changes in NIR Raman spectra, which were interpreted as the effect of blood aging, triggered by the exposure to ambient conditions. The consequences of this naturally occurring degradation process, reflected in spectral signatures, have been presented in Table 5.5. Lemler has also managed to remove ambiguities concerning the origin of bands contributing to the spectrum of whole blood, challenging the previous studies reporting the presence of vibrational features corresponding to proteins [225–227] and other blood components [228, 229]. In agreement with earlier findings of Sato et al. [trac154], it was demonstrated that the Raman spectrum of blood, acquired with 785 nm laser, did not provide information about any other constituent of this multi-component body fluid but Hb protein. The bands previously assigned to other blood constituents, in turn, were just spectral symptoms of the heme aggregation process.

And since 2016, the leading provider of development in Raman-based bloodstains dating research remains the group of Igor Lednev [230]. In their first study [38], scientists led by Doty combined Raman spectroscopy with statistical modeling to estimate the TSD of a bloodstain up to one week old. Several spectral features (summarized in Table 5.5) were observed to change with time, and their interdependence was investigated in-depth with two-dimensional correlation spectroscopy (2D CoS). The 2D CoS, employed to interpret the dynamics within the region of most prominent spectral alterations (1210−1260 cm^{-1}), revealed a negative correlation between two peaks located at 1252 and 1224 cm^{-1}, with the decrease of the 1224 cm^{-1} peak as a first stage, followed by the increase of the intensity at 1252 cm^{-1}. Authors assigned these features to frequencies of amide III band − random coil (1252 cm^{-1}) and β-sheet (1224 cm^{-1}) − concluding that the process of Hb denaturation preceded aggregation. However, this reasoning might not be correct since the numerous RBC studies [177, 183, 184, 209, 223, 231, 232] have assigned the band at ~1225 cm^{-1} to the C_m−H methine in-plane bending vibration within protoporphyrin IX moiety (Figure 5.5). And indeed, it might be hard to escape the conclusion that the time-dependent features within 1210−1260 cm^{-1} are the results of peptide bond vibrations. As already explained in *5.1.3.1 Vibrations related to the secondary structure of proteins*, the region of amide III vibration, which has been defined within 1260−1310 cm^{-1}, 1235−1242 cm^{-1}, and 1240−1250 cm^{-1} for α-helix, β-sheet and random coil structure, respectively [197, 223, 234], indeed serves as a sensitive probe of peptide conformation.

Therefore, it might be tempting to interpret the band at 1252 cm^{-1} as the amide III mode. However, according to Wood et al. [183], the absence of amide I mode (~1650 cm^{-1}) should exclude this assignment from consideration. Instead, several Monash group studies [183–186, 209, 223] suggest that the whole spectral range between 1200 and 1300 cm^{-1} should be instead interpreted as the signatures of methine vibrations, which also can be severely affected by heme stacking and protein interactions.

TABLE 5.5. Positions, assignments, and local coordinates of bands observed during aging of bloodstains using 785 nm excitation [177]. Assignments based on [212, 219, 223, 231].

OBSERVED BAND (CM^{-1})	VIBRATIONAL ASSIGNMENT	LOCAL COORDINATES[a]	DRIED "FRESH" BLOOD TRACE (TSD ~ 1H)	AGED BLOOD TRACE (TSD ~ 2 WEEKS)
347	ν_8	$\nu(Fe{-}N)$	medium intensity	
377		$\delta(C_\beta C_c C_d)$	weak intensity	increase of intensity
417		$\delta(Fe{-}O{-}O)$	medium intensity	absent
570		$\nu(Fe{-}O_2)$	weak intensity	absent
621	ν_{12}		weak intensity	
667			absent	increase of intensity
677	ν_7	$\delta(\text{pyr deform})_{sym}$	medium intensity	decrease of intensity
716	γ_5	$\delta(\text{pyr fold})_{sym}$	weak intensity	
747			absent	increase of intensity
754	ν_{15}	$\nu(\text{pyr breathing})$	strong intensity	
788	ν_6	$\nu(\text{pyr breathing})$	weak intensity	
856			weak intensity	
900		p: C−C skeletal	weak intensity	
937	ν_{37}		medium intensity	
970	ν_{46}	$\delta(\text{pyr deform})_{asym}$ or $\gamma(=C_bH_2)_{sym}$	absent	increase of intensity
1003		phenylalanine	strong intensity	
1030		$\delta(=C_bH_2)_{asym}$	weak intensity	
1054		$\delta(=C_bH_2)_{asym}$	weak intensity	
1127	ν_5		medium intensity	
	ν_{22}	$\nu(\text{pyrrole half-ring})_{asym}$		
1173	ν_{30}	$\nu(\text{pyrrole half-ring})_{asym}$	weak intensity	
1224	ν_{13} or ν_{42}	$\delta(C_mH)$ prop $\delta(CH_2)$ twisting	medium intensity	
1248	ν_{13}	$\delta(C_mH)$	absent	increase of intensity
1311	ν_{21}	$\delta(C_mH)_{asym}$	weak intensity	
1341	ν_{41}	$\nu(\text{pyr half-ring})_{sym}$	medium intensity	
1374	ν_4	$\nu(\text{pyr half-ring})_{sym}$	medium intensity	
1398	ν_{20}	$\nu(\text{pyr quarter-ring})$	medium intensity	
1450		$\delta(CH_2/CH_3)$	strong intensity	
1563	ν_2 or ν_{11}	$\nu(C_\beta C_\beta)$	strong intensity	
1582	ν_{37}	$\nu(C_\alpha C_m)_{asym}$	medium intensity	
1603	ν_{19}	$\nu(C_\alpha C_m)_{asym}$	medium intensity	
1621		$\nu(C_a{=}C_b)$	strong intensity	
1638	ν_{10}	$\nu(C_\alpha C_m)_{asym}$	medium intensity	absent
1654		Amide I	weak intensity	

ν, stretch; δ, in-plane deformation; γ, out-of-plane deformation; sym, symmetric; asym, asymmetric; p, protein; prop, propionate; pyr, pyrrole; deform, deformation.

[a] Subscripts *α*, *β*, *m* represent the carbon atoms at the alpha, beta, and *meso* positions of porphyrins; a and b correspond to vinyl group carbons, while c and d to propionate carbons. For a detailed scheme of heme labeling, adopted by Hu et al. [219], see Figure 5.5.

Nevertheless, ambiguities concerning the root causes of those dynamic spectral changes should not affect the performance of PLSR models developed for time estimations, which eventually allowed to determine the age of bloodstains up to one week since deposition (for details, see Table 5.1). What is

even more important, it was demonstrated that the monitored dynamic features did not reach a plateau in the logarithmic time scale. Hence, it might be presumed that Raman-based estimation of TSD can be performed on a scale of hours and over more extended periods.

Fortunately, Doty et al. did not keep us too long in a state of suspense. The results of a long-term study [141] evidenced the changes in Raman spectra up to two years elapsed since bloodstain formation (Table 5.1). However, the differences between the spectra corresponding to one- and two-year-old samples were minor. To estimate the TSD of a bloodstain, two regression models (PLSR and PCR) were developed. As could have been expected, the accuracy of predictions decreased as bloodstains aged, simply because spectral signatures of severely degraded stains changed only subtly with time progression. Long-term forecasts of the models were also worsened due to poor spectra quality, resulting primarily from increased fluorescence, which often impedes the Raman analysis of body fluids.

However, this powerful Raman-based temporal information can only be achieved at the cost of intense work devoted to a selection of an adequate analytical setup (e.g., laser line, laser power, number of accumulations, time of exposure, etc.), which would allow avoiding an artificial, and therefore undesired, degradation of bloodstains. The exceptional susceptibility of Hb to laser irradiation was established by several researchers [177, 213, 235, 236]. Therefore care should be taken to prevent the photoinduced chemistry of Hb molecules. Unfortunately, ensuring this is not a straightforward task. And that is because the spectrum of the aging bloodstain exhibits the same features as those observed at high laser powers [177]. For this reason, it might be impossible to differentiate between the photoinduced effects caused by the laser irradiation and the non-accelerated Hb transformations, especially when the rate of natural blood degradation remains unknown. Groups of Ramser [218] and Ahlawat [236], who investigated the effects of laser power in Raman spectroscopy of RBC, have observed three spectral symptoms attributed to the laser-induced processes. It should be reiterated that all of these changes were also noted during the natural aging of bloodstains:

1. A decrease in Raman intensity, which might indicate cytoplasm leakage through the RBC membrane.
2. A change in Raman spectra indicative of initial deoxygenation of oxyHb, followed by the formation of HC [236] or conversion of oxyHb to metHb [213].
3. An enhancement of fluorescence intensity.

Since both of these studies were performed with 532 nm or 514.5 nm laser lines, which fall within the Q-band region of Hb absorption, there was a possibility that the observed spectral changes resulted from thermal processes initiated by light absorption. Ramser et al. [218] carried out calculations of heat transport in RBC to verify this assumption. An estimated rise of the temperature at the laser focus equaled ~2.3°C (for initial laser power 0.7 mW). Hence, the thermal degradation was excluded to explain the observed spectral changes because the actual cell temperature remained well below

physiological conditions (~37°C). Consequently, photo-induced chemical reactions (e.g., photo-oxidation) were blamed for the observed spectral alterations. In the second of the mentioned studies, Ahlawat et al. [236] noticed that even a few 10-second accumulations at low laser powers (mW) triggered spectral changes implying the transformation of oxyHb toward deoxyHb, which increased with laser power. The effect of power-dependent deoxygenation has been evidenced to be reversible at short (~5 seconds) exposure to the laser irradiation, however for extended exposure durations, an irreversible derivative of Hb with ferric iron in the low spin state − possibly corresponding to HC − was formed. None of these changes were observed in the spectra registered for entirely deoxygenated Hb exposed to the same laser powers as oxygenated species. Thus, it was reasonable to conclude that the role of the oxidizing agent, contributing to oxidative damage of erythrocytes, was played by the free oxygen, which was formed due to laser-induced photo-dissociation. However, these results contradicted the earlier findings of Ramser et al. [218], which suggested the formation of metHb as the final product of the photo-induced changes.

Further evidence supporting the influence of laser irradiation on the Hb chemistry was delivered by Dasgupta et al. [235] and Lemler et al. [177]. Despite employing the laser corresponding to the non-electronically resonant NIR region of Hb, namely the 785 nm line, also in these studies, Raman spectra of whole blood were proven to be a function of the incident laser power. Along with the increased intensities of heme aggregation marker bands (972 cm^{-1}, 1248 cm^{-1}, and 1366 cm^{-1}), among the symptoms of a photo-damage, Dasgupta et al. [235] also suggested the formation of HC, thereby partly supporting the results mentioned above of Ahlawat et al. [236]. These bands were also consistent with subsequent observations of the Monash [185, 223] and Ziegler group [177, 232], which attributed the observed Raman signatures to Hb existing in the aggregated form (Table 5.6). These differences between the results of the aforementioned studies might suggest that mechanisms of laser-induced damage to Hb, occurring at 532/514.5 nm [213, 236] and 785 nm [177, 235], follow separate pathways. Even though the source of these discrepancies remains undiscovered, one thing is obvious – photo-induced denaturation can appear even within the nominally non-resonant region of Hb. Therefore it is essential to choose the experimental setup carefully. Lemler et al. [177] suggested that to avoid the photo-damage of RBC, long acquisition times with low excitation power should be preferred over high excitation power coupled with low acquisition times.

Another possible solution to decrease the absorption, hence reducing the risk of resulting photodamage, is to collect the Raman spectrum while the sample is circulated. This method of analyzing exceptionally sensitive specimens has already been proven effective by Woodruff and Spiro [237]. And, in fact, this particular sampling method may also have the added advantage of providing a representative Raman signature of a highly heterogeneous, constantly evolving sample.

TABLE 5.6. Vibrational bands of whole blood and red blood cells affected by high laser fluence. Data from [177].

HIGH POWER SPECTRUM (cm^{-1})[a]	LOW POWER SPECTRUM (cm^{-1})[a]	VIBRATIONAL ASSIGNMENT	LOCAL COORDINATE
–	419	$\delta(Fe–O_2)$	$Fe–O_2$ bend
–	570	$\nu(Fe–O_2)$	$Fe–O_2$ stretch
667	677	ν_7	$\nu(\text{pyr deform})_{sym}$
747	754	ν_{15}	ν(pyr breathing)
970	–		$\gamma(C_\alpha H=)$?
1123	1128	ν_5	$\nu(C_\beta\text{-methyl})$
1248	–	ν_{13} or ν_{42}	$\delta(C_mH)$
–	1311	ν_{21}	$\delta(C_mH)$
1370	1374	ν_4	$\nu(\text{pyr half-ring})_{sym}$
1392	1398	ν_{20}	ν(pyr quarter-ring)
1543	1549	ν_{11}	$\nu(C_\beta C_\beta)$
1576	1582	ν_{37}	$\nu(C_\beta C_m)_{asym}$
1629	1638	ν_{10}	$\nu(C_\beta C_m)_{asym}$

C_α, *C_β*, *C_m* correspond to the carbon atoms at the alpha, beta, and *meso* positions of porphyrins, respectively, whilst the *pyr* represents the pyrrole ring (see Figure 5.5)

[a] The estimated peak frequency precision is ±1 cm^{-1}.

Despite valuable progress in Raman-based dating studies, some challenges continually hamper the implementation of these methodologies in legal proceedings. One of these obstacles might be representative probing of the chemical composition of degrading bloodstains, usually pursued by acquiring a few single-point measurements within different sample areas [38, 141, 177]. The problem is that dried deposits of body fluids are not only physically but also chemically heterogeneous; hence this sampling mode might result in poor reproducibility of measurements and, in the long term, misestimations of TSD. Given the above, the study presented in this thesis intended to expand the current Raman-based approaches primarily by eradicating the risk of the laser-induced degradation of bloodstains [24, 177, 235] subsampling errors (for details, see *Chapter 8 Materials and methods*).

| *CHAPTER 6*

COMPUTATIONAL METHODS FOR ASSESSING THE (DIS)SIMILARITY BETWEEN THE DEGREE OF BLOODSTAINS DEGRADATION

As described in *2.2. The novel framework for evidence dating*, all attempts to implement already developed tools for monitoring bloodstains degradation in the forensic dating practice, has miserably failed, hardly ever going beyond pages of scientific journals. Although it may seem that this stagnation derives from the multidimensionality of the aging process, that is only partly true. The influence of external factors cannot be alleviated or eliminated; hence this obstacle will always stand in our way. Consequently, in order to defeat this impediment, the current course of action has to be diverted, as the problem here is not the absence of technically advanced analytical methods – continually pursued by scientists – but the lack of an adequate approach, which would embrace the uncertainty deriving from the external factors. In today's situation, it is much more important to ask the right question, as the problem is the wrong way to address the problem. We are all aware of its existence, but do we see it right?

The measure proposed under this dissertation aims to substitute the case-suited comparison problem for the conventional dating strategy. As the critical aspect of this novel concept is based on estimating the (dis)similarity between the decomposition of evidence and reference bloodstains, hence apart from physicochemical patterns characterizing the samples of interest (*Chapter 5. An analytical method for monitoring bloodstains degradation*), a tool enabling comparison of those in the forensic context is also required. It may appear – especially to researchers deprived of any forensic-related experience – that this task could be completed solely by applying chemometric techniques, which allow for catching possible (dis)similarities among samples or visualizing the data group structures. At this point, however, it should be reminded that an adequately performed forensic expertise also involves the interpretation and communication of findings to assist fact finders (e.g., judges or prosecutors) in their decision making, since they usually lack any form of chemical knowledge or technological understanding of employed methods. Therefore, the evidence evaluation step is not fully completed by applying chemometric tools, as these techniques cannot interpret the evidence in light of two perspectives (H_1 and H_2), as required among the forensic community. And this requirement brings us to the use of STATISTICS in FORENSIC SCIENCE.

It appears perfectly natural that both of these fields should come together. And indeed, the symbiosis of statistics and forensics has been inaugurated over 40 years ago as a response to strong criticism of the widespread practice of evidence interpretations deficient in any mathematical foundations. Kirk and Kingston briefly commented on this somewhat natural order of things with the following words: *It can be fairly stated that there is no form of evidence whose interpretation is so*

definite that statistical treatment is not needed or desirable [73]. In this regard, nothing has changed: any categorical conclusions are not allowed – unless the compared samples present completely different physicochemical profiles or the results of the so-called jigsaw fitting procedure are considered – as 100% certainty can never be guaranteed. Consequently, perceiving results as categorical and simultaneously neglecting the "fuzziness of boundaries" may lead to forensic misconduct. Therefore, according to the acknowledged standards, the communication of results should be expressed in a probabilistic manner. With that in mind, forensic experts implemented different statistical approaches to evidence assessment. The high number of cases involving so-called objective comparison methods of forensic evidence used the frequentists approach with significance tests [73]. It is well known that applying a simple Student's t-test allows to compare the means of two groups of measurements (herein corresponding to the recovered and control samples) and assess how significant the differences between those samples are. In other words, the classical approach lets you know whether those differences (measured in means) could have happened by chance. But this is not enough. Note that for the forensic evaluation of evidence within a comparison problem, it is not only the SIMILARITY that is important but also the RARITY of the compared patterns in the relevant population. Thus, emphasis has to be put on the importance of posing the question: what does this similarity mean in this particular case? In order to do so, apart from the similarity of compared samples[***], several factors have to be taken into consideration once expressing the opinions about the forensic evidence –which are not included when using frequency tests – namely:

- the uniqueness of chemical patterns,
- possible sources of uncertainty (sources of error) including the within- and between-object (sample) variability in the relevant population of samples,
- correlation between the measured features/variables.

To overcome deficiencies of the classical approach, so that it could be applied in the forensic context anyway, the so-called TWO-STAGE APPROACH comprising of the comparison- and the rarity-stage should be introduced [8, 73, 283]. In the first stage, as described above, the evidence is compared with the reference sample through the application of frequency tests (e.g., Student's t-test for univariate data or Hotelling's T^2-test for multivariate data), which take into account only information about within-sample variation and the similarity of the compared samples. If the first stage fails to reject the null hypothesis assuming the equality of compared means (for univariate data) or vectors of mean values (for multivariate data), and hence the samples are deemed similar, the comparison has to be followed by the evaluation of rarity of the evidence. Needless to say, when observing a similarity between compared materials, the strength of the evidence increases with the uniqueness of the measured features. Therefore, in many cases, the most valuable tool in forensic research is not a microscope or a spectrometer, but an

[***] That requirement is valid only when studying the comparison problem, which is the subject of our discussion throughout this thesis. The classification task understood in a forensic context (where the recovered sample is ascribed to one of a number of previously determined categories) is not taken into consideration.

adequately designed database, which should characterize in a representative manner the relevant population so as to provide information about the rarity of the physicochemical data, as well as the within- and between-sample variability. Nonetheless, despite this measure, the two-stage approach is still plagued with several problems.

First of all, the application of significance tests requires a cut-off point represented by the significance level *α,* chosen arbitrarily – in this case – by the person performing the expertise. This, in turn, leads to another problem, which may be referred to as the *falling off the cliff* effect [239], where a slight difference in significance probability values can substantially impact the person of interest. For example, consider the difference between the comparison results, which is significant at the $p = 0.052$, and a difference which is significant at the $p = 0.048$ level for $\alpha = 0.05$. In the first scenario, the evidence and reference material are deemed similar (fail to reject the null hypothesis, $p > \alpha$), hence the evaluation process is taken to the second stage – the rarity assessment. In the second, the procedure is discontinued because of the lack of similarity (rejection of the null hypothesis, $p \leq \alpha$) between compared materials. In other words, a minimal difference in measured feature(s) characterizing the samples of interest may very often decide to discount the evidence against the suspect entirely. And finally, the two-step approach violates in a way the *presumption of innocence*, placing the burden of proof on the shoulders of the defense instead of the prosecution. This is because the starting point of significance tests usually assumes that the evidence from the crime scene and the reference material obtained from the suspect's environment derive from the same source (as the H_0 states, the equality of compared means or vectors of mean values). Consequently, the suspect is a priori associated with the crime (viewed as guilty), and it is the concern of the defense to demonstrate that the possible difference is significant at the subjectively pre-specified significance level. It could be said then that in this configuration, the *presumption of innocence* turns into the *presumption of guilt*, which according to specific sources [240], infringes Article 11(1) of the *Universal Declaration of Human Rights* and Article 6(2) of *the Convention for the Protection of Human Rights and Fundamental Freedoms*. Fortunately, the described two-step strategy is not the only approach to evidence assessment.

6.1 Likelihood ratio-based evaluation of evidence

The limitations mentioned above, combined with the errors in evidence reporting within some well-established forensic fields, have revealed a major need for a *paradigm shift* [241] in an interpretation and evaluation in a courtroom scenario. The urgency of increasing transparency and reliability of forensic assessment methods was unequivocally stressed not only by forensic experts [242–244] but also by statisticians [8, 73, 238] and even lawyers [241, 245]. Moreover, the ongoing debate about acceptance of expert testimony was fuelled by the continually followed practice of experience-based opinions expressed in the court in the form of match/non-match statements, which was deprived of any

scientific rigor. To cope with these requirements, the LIKELIHOOD RATIO (LR) APPROACH for assessing the weight of evidence in a probabilistic manner has been advocated by the forensic community [20].

One of the main advantages of the LR-based approach over other methods is that the evidence is analyzed both in light of the prosecution's hypothesis and its alternative. Thus, it can be said that the LR expresses the degree of support of the evidence to the relevant propositions considered in a given case. It leads us away from subjective thresholds, as the LR theory is free of assuming any significance level α representing the probability of rejecting the null hypothesis given that it is true. Its attractiveness also lies in the fact that it allows for more efficient use of available knowledge about the case, as several kinds of evidence can often be integrated into a single evidential value. Finally, the LR-based methodology takes into account all those factors, which were missing once the classical approach was considered. It means that apart from the similarity of the features, their rarity and the between-sample variability are incorporated into a single calculation run. No wonder then that the LR approach is being slowly brought to the forefront of forensic evidence evaluation methods, being also recommended by the European Network of Forensic Science Institutes (ENFSI) – an organization responsible for maintaining high-quality standards among forensic institutes within Europe [20].

To better understand the LR-based evaluation of evidence, let us look at the example of a comparison problem transferred into dating studies. As already mentioned, the evidence (herein the bloodstain of a questioned age) should be interpreted in the context of two competing hypotheses, defined at the source level[†††] [246]:

H_1: the TSD of the evidence (recovered) bloodstain (t_R) is consistent with the TSD of the reference (control) bloodstain (t_C), hence $t_R = t_C$;

H_2: the TSD of the evidence (recovered) bloodstain (t_R) is **not** consistent with the TSD of the reference (control) bloodstain (t_C), hence $t_R \neq t_C$.

To indicate the correct hypothesis, the decision-makers should base their final verdict on the *a posteriori* probabilities in favor of any of the hypothesis $\frac{\Pr(H_1|E,I)}{\Pr(H_2|E,I)}$ derived from the background information (I) about the case, as well as the assessed forensic evidence (E), which might be represented by the physicochemical data [darboux 1908]. The Bayes' theorem expresses the connection between all of these elements:

$$\frac{\Pr(H_1|I)}{\Pr(H_2|I)} \cdot \frac{\Pr(E,I|H_1)}{\Pr(E,I|H_2)} = \frac{\Pr(H_1|I)}{\Pr(H_2|I)} \cdot LR = \frac{\Pr(H_1|E,I)}{\Pr(H_2|E,I)}. \quad (6.1)$$

[†††] At this point, it has to be clearly pointed out that, in this particular case, the *source* ought to be understood as a group of bloodstains corresponding to the same TSD.

The role of the forensic expert, in turn, involves the estimation of conditional probabilities of observing obtained data, given that any of the hypotheses is true. The ratio of these conditional probabilities is defined as a likelihood ratio in the following manner: *If the probability that evidence (E) expressed as variable X takes the value x if H_1 is true is denoted Pr(X = x|H_1) and Pr(X = x|H_2) refers to the probability that X takes the value x when H_2 is true, the likelihood ratio is expressed as a measure that compares the probability that X = x when H_1 is true with the probability that X = x when H_2 is true*:

$$LR = \frac{\Pr(X = x|H_1)}{\Pr(X = x|H_2)} = \frac{\Pr(E|H_1)}{\Pr(E|H_2)}^{‡‡‡}. \tag{6.2}$$

For continuous type data, the probabilities should be replaced by probability densities:

$$LR = \frac{f(X = x|H_1)}{f(X = x|H_2)} = \frac{f(E|H_1)}{f(E|H_2)}. \tag{6.3}$$

The LR can be viewed as a measure of the strength of the evidence in favor of H_1 compared with H_2 when X = x. It can take values between zero and infinity and is interpreted as follows: LR values above one support H_1, while LR values below one provide support for H_2. Additionally, the strength of support towards each of the hypotheses is determined by the magnitude of LR value: the higher (lower) the value of the LR, the stronger the support towards H_1 (H_2) [8]. Therefore, LR is a qualitative and quantitative measure of the strength of the support for one of the hypotheses, which is its highly desirable feature.

Given Equation 6.1, it becomes clear that the LR – and hence also the forensic expert – acts as a bridge between the prior and posterior odds[§§§] in Bayes' theorem. According to the theorem, after consideration of the evidence, the hypothesis's prior odds are updated to posterior odds by multiplying the former ones by the LR value provided by the forensic expert. And that is precisely where the great merit of the LR approach, considered as a quantitative measure of evidence strength, manifests itself, as – in fact – it determines whether the prior odds are updated in a way that strengthens (the LR value is above 1) or weakens (the LR is below 1) the evidence for the main hypothesis. Consequently, forensic experts should be regarded as playing an ancillary function [8, 247, 248], providing vital assistance (in the form of the weight of findings estimated after the evidence examination) to the fact finders.

And this role of the LR models for extensive evidence evaluation, embedded within the Bayes theory (Equation 6.1), was already recognized in the early 1900s in the context of the Alfred Dreyfus affair from 1894 [73, 249]. This 35-year-old Alsatian French artillery officer was accused of communicating French military secrets to the Germans and subsequently sentenced to life imprisonment

‡‡‡ From here onwards, the background information about the case *I* is removed from the notation for the sake of simplicity. It is assumed, though, that the probabilities are conditioned to *I*.
§§§ The quotient of complementary probabilities in Equation 6.1.

based on document analysis. During the first of many trials, the forensic expert employed probabilistic reasoning to determine that the probability of Dreyfus's guilt equaled 0.9984 [250]. This conclusion, however, was not correct due to a probability inference error. During the retrial, among other reports, an opinion of mathematicians – Appell, Darboux, and Poincaré – exposed a fundamental fact: a probability of identification cannot be established solely based on evidence examination, because of other *prior* information, which should be taken into account, and which is not always accessible to forensic experts. As explained by Darboux et al. [250] *(...) since it is absolutely impossible for us [the forensic experts] to know the a priori probability, we cannot say: this coincidence proves that the ratio of the forgery's probability to the inverse probability is a real value.* ***We can only say:*** *following the observation of this coincidence, this* ***ratio becomes X times greater than before the observation****.* This idea, perfectly illustrating a legal trial course, initiated a process leading to the increasing application of the LR approach for evidence evaluation. Consequently, due to its universality, the LR framework has been proposed for solving both comparison and classification problems raised in many forensic disciplines, as presented in Table 6.1.

6.2 Construction of likelihood ratio models – a comparison problem

The employment of the LR framework in forensic sciences has been extensively influenced by DNA profiling [73, 251, 252]. DNA profiles, however, constitute the records of discrete values of short-tandem repetitions at given places (*loci*) in the chain. As this thesis, just like the majority of disciplines focused on source-level comparison problems, deals with CONTINUOUSLY valued measurements of features (e.g., Raman spectra) obtained from the evidence and the reference sample, a description of techniques applied in DISCRETE LR calculations will not be provided (the reader is referred to the literature covering this topic [73, 239, 251, 252]). If the scale of available data is continuous, then the LR computation boils down to establishing the ratio of the probability density function (PDF) valid under H_1 evaluated at the evidence (E) to the PDF valid under H_2 considered at the evidence (E), as denoted in Eq. 6.3. Therefore, in order to calculate the LR, the PDFs under the two hypotheses have to be estimated. Thus it becomes clear that the proper evaluation of the evidential value cannot be based solely on measurements of the samples of interest (the evidence and the reference material). All of the LR models are embedded in the statistical distributions of the underlying data.

6.2.1 Computation of model parameters

The reliable evaluation of evidence should consider the similarity and the rarity of physicochemical characteristics, not to mention the possible levels of variation (within- and between-sample variability).

TABLE 6.1. Exemplary applications of the LR framework within the forensic disciplines [based on 5, 250].

FORENSIC FIELD OF APPLICATION	REFERENCES
Fingerprints	[242, 253, 254]
Microtraces (glass)	[256–262]
Microtraces (paint)	[263–265]
Microtraces (polymers)	[264, 265]
Microtraces (fibers)	[257]
Microtraces (hair)	[266]
Earmarks	[267]
Fire debris	[268]
Explosives	[269]
Tool marks	[270]
Documents, inks	[271]
Drugs	[272, 273]
DNA profiling	[252]
Handwriting	[73]
Biometrics	[274]
Phonetic-acoustic speaker recognition	[244, 250]
Image recognition	[275]

For this reason, the forensic expert has to be provided with adequate background databases of the recorded features, which should exhaustively characterize the whole relevant population of samples so that the distributional parameters (e.g., means, variances, covariances) could be credibly estimated. Each of the m objects within the background database is characterized similarly to the recovered and the control sample, resulting in p-dimensional vectors $x_{ij} = (x_{ij1} \dots x_{ijp})^T$ where $i = 1, \dots m$ and $j = 1, \dots n$, with n corresponding to the number of measurements performed per sample (m samples, each measured n times). Ultimately, the background dataset is arranged in a matrix of size $(m \cdot n) \times p$.

The within-object variance estimate is denoted as $\mathbf{W}$ and is assumed equal for all samples. Its estimate takes into consideration the sum of squares ($\mathbf{S_w}$) of deviations of each measurement $\boldsymbol{x_{ij}}$ from the m object means $\bar{\boldsymbol{x}}_{\boldsymbol{i}}$. It is calculated in the following manner:

$$\boldsymbol{W} = \frac{\boldsymbol{S_w}}{m(n-1)}, \tag{6.4}$$

where

$$\boldsymbol{S_w} = \sum_{i=1}^{m}\sum_{j=1}^{n}(\boldsymbol{x_{ij}} - \overline{\boldsymbol{x}}_{\boldsymbol{i}})(\boldsymbol{x_{ij}} - \overline{\boldsymbol{x}}_{\boldsymbol{i}})^T,$$

where $\boldsymbol{x_{ij}}$ is a vector of the values of the p variables obtained in the j-th measurement for the i-th object. The $\overline{\boldsymbol{x}}_{\boldsymbol{i}}$ is a vector of the means of the p-variables describing each of the i-th samples in the database, which is given as $\overline{\boldsymbol{x}}_{\boldsymbol{i}} = \frac{1}{n}\sum_{j=1}^{n}\boldsymbol{x_{ij}}$.

The between-object variance estimate, in turn, involves the sum of squares ($\mathbf{S}^*$) of the mean deviations of the object means ($\overline{\boldsymbol{x}}_{\boldsymbol{i}}$) from the overall mean ($\overline{\boldsymbol{x}}$) reduced by the within-object variance estimate ($\boldsymbol{S_w}$) and normalized by the relevant number of degrees of freedom. Ultimately, the between-sample variance-covariance estimate (**B**) is expressed as:

$$\boldsymbol{B} = \frac{\boldsymbol{S^*}}{m-1} - \frac{\boldsymbol{S_w}}{mn(n-1)}, \tag{6.5}$$

where

$$\boldsymbol{S^*} = \sum_{i=1}^{m}(\overline{\boldsymbol{x}}_{\boldsymbol{i}} - \overline{\boldsymbol{x}})(\overline{\boldsymbol{x}}_{\boldsymbol{i}} - \overline{\boldsymbol{x}})^T,$$

and $\overline{\boldsymbol{x}} = \frac{1}{mn}\sum_{i=1}^{m}\sum_{j=1}^{n}\boldsymbol{x_{ij}}$.

The data are assumed normally distributed. However, when the shape of the PDFs cannot be considered normal and cannot be transformed to normality, data distribution is modeled in a non-parametrical manner, usually using the kernel density estimation (KDE) method [276].

6.2.1.1 Kernel density estimation

KDE can be described as a "smoothing histogram", which estimates the underlying distribution by averaging over all objects means instead of the general mean as adopted in Gaussian distribution. Instead of averaging over all data points by calculating general parameters as, e.g., only mean and variance characterizing the normal distribution, the KDE procedure models the distribution concerning each single data point separately. Consequently, the estimated probability density function depends upon all the considered data points, and its shape is not arbitrarily fixed but adjusted to the data distribution.

KDE places a function (so-called kernel) with the shape of, e.g., the normal distribution centered at each considered data point, x_i. Gaussian kernels represent the normal distribution functions $N(\mu, \sigma^2) = N(x_i, h^2)$, located on each data point x_i with smoothing/bandwidth parameters h adjusting

their widths (note that other kernels are also available [276]). The function is expressed in the following way:

$$K(\theta|\bar{\boldsymbol{x}}_{\boldsymbol{i}}, \boldsymbol{H}) = (2\pi)^{-\frac{p}{2}}|\boldsymbol{H}|^{-\frac{1}{2}}\exp\left\{-\frac{1}{2}(\theta - \bar{\boldsymbol{x}}_{\boldsymbol{i}})^T\boldsymbol{H}^{-1}(\theta - \bar{\boldsymbol{x}}_{\boldsymbol{i}})\right\}, \tag{6.6}$$

with H being kernel bandwidth matrix. In the case of univariate data, Equation 6.6 simplifies:

$$K(\theta|\bar{x}_i, h) = \frac{1}{\sqrt{2\pi h}}\exp\left(-\frac{1}{2}\left(\frac{\theta-\bar{x}_i}{h}\right)^2\right).$$

Ultimately, the KDE curve is obtained by placing the Gaussian kernels on each of the considered data points and averaging them so that it integrates to the unit area:

$$f(x) = \frac{1}{m}\sum_{i=1}^{m} K(\theta|\bar{x}_i, h). \tag{6.7}$$

Special consideration should also be given to the appropriate amount of smoothing, in other words, to adjusting the *h* parameter. The information about the actual distribution and some subtle features of the data under analysis might be lost when its value is too high. Simultaneously, when *h* is set too low, the probability density curve might get too spiky, leading to difficulties in interpreting the distribution. For this reason, many methods for optimizing the value of *h* have been proposed to date [276]. In the case of LR estimations, the *h* parameter is given by the expression $h = h_{opt} = \left(\frac{4}{m(2p+1)}\right)^{\frac{1}{p+4}}$ where *p* corresponds to the number of variables describing the *m* samples in the background database.

Nowadays, the KDE is often applied to univariate data in forensic science as well as multivariate data [8]. It should also be mentioned that the KDE procedure can be considered a reliable method in cases where the training data (consisting of simulated or real observations) for the studied hypotheses features many observations and few variables (e.g., low-dimensional data).

6.2.2 Construction of the LR model

Having estimated the parameters described above from the background database, LR models can be constructed and subsequently used for answering the question about the common origin of two samples – defined as the recovered (evidence) and reference (control) materials – captured in the considered hypotheses H_1 and H_2. The reference sample $\mathbf{y}_1$ is described by k_1-observations of the *p* variables (the set of variables is in accordance with the one corresponding to database samples):

$$\boldsymbol{y_{1j}} = (y_{1j1}, \cdots, y_{1jp})^T$$

with the mean vector $\bar{\boldsymbol{y}}_{\boldsymbol{1}} = \frac{1}{k_1}\sum_{j=1}^{k_1} \boldsymbol{y}_{\boldsymbol{1j}}$, originating from the normal distribution $(\bar{\boldsymbol{y}}_{\boldsymbol{1}} \mid \mu, \boldsymbol{W}, \boldsymbol{B}) \sim N\left(\mu, \frac{\boldsymbol{W}}{k_1} + \boldsymbol{B}\right)$. By analogy, the recovered sample $\mathbf{y_2}$ is characterized by the k_2 replicate observations of the p variables:

$$\boldsymbol{y}_{\boldsymbol{2j}} = (y_{2j1}, \ldots, y_{2jp})^T$$

with the mean vector $\bar{\boldsymbol{y}}_{\boldsymbol{2}} = \frac{1}{k_2}\sum_{j=1}^{k_2} \boldsymbol{y}_{\boldsymbol{2j}}$, originating from the normal distribution $(\bar{\boldsymbol{y}}_{\boldsymbol{2}} \mid \mu, \boldsymbol{W}, \boldsymbol{B}) \sim N\left(\mu, \frac{\boldsymbol{W}}{k_2} + \boldsymbol{B}\right)$.

According to Equation 6.3, the LR numerator evaluates the support towards the H_1. It can be shown that the numerator of this equation can be expressed by taking into account the (dis)similarity of physicochemical data between compared samples, as well as their rarity, measured by the distance of the weighted mean – given as $\bar{\boldsymbol{y}}^* = \frac{k_1\bar{\boldsymbol{y}}_{\boldsymbol{1}} + k_2\bar{\boldsymbol{y}}_{\boldsymbol{2}}}{k_1 + k_2}$ (coming from the normal distribution $(\bar{\boldsymbol{y}}^* \mid \mu, \boldsymbol{W}, \boldsymbol{B}) \sim N\left(\mu, \frac{\boldsymbol{W}}{k_1+k_2} + \boldsymbol{B}\right)$) – from the overall mean $\bar{\boldsymbol{x}}$. The denominator of the LR formula, in turn, corresponds with H_2.

If the between-sample distribution can be assumed normal, then – as already mentioned – the LR expression is given as in [73]. When the data cannot be considered normally distributed, which is often the case, the KDE procedure is applied to estimate the underlying distributions. Consequently, the numerator is formulated as follows [5]:

$$\begin{aligned} f(\bar{\boldsymbol{y}}_{\boldsymbol{1}}, \bar{\boldsymbol{y}}_{\boldsymbol{2}} \mid \boldsymbol{W}, \boldsymbol{B}, \bar{\boldsymbol{x}}, H_1) &= f(\bar{\boldsymbol{y}}_{\boldsymbol{1}} - \bar{\boldsymbol{y}}_{\boldsymbol{2}} \mid \boldsymbol{W}, H_1) \times \frac{1}{m}\sum_{i=1}^{m} K(\bar{\boldsymbol{y}}^* \mid \bar{\boldsymbol{x}}_{\boldsymbol{i}}, \boldsymbol{W}, \boldsymbol{B}, h, H_1) = \\ &= (2\pi)^{-\frac{p}{2}} \left|\frac{\boldsymbol{W}}{k_1} + \frac{\boldsymbol{W}}{k_2}\right|^{-\frac{1}{2}} \exp\left\{-\frac{1}{2}(\bar{\boldsymbol{y}}_{\boldsymbol{1}} - \bar{\boldsymbol{y}}_{\boldsymbol{2}})^T \left(\frac{\boldsymbol{W}}{k_1} + \frac{\boldsymbol{W}}{k_2}\right)^{-1} (\bar{\boldsymbol{y}}_{\boldsymbol{1}} - \bar{\boldsymbol{y}}_{\boldsymbol{2}})\right\} \times \\ &\times (2\pi)^{-\frac{p}{2}} \left|\frac{\boldsymbol{W}}{k_1 + k_2} + h^2\boldsymbol{B}\right|^{-\frac{1}{2}} \frac{1}{m}\sum_{i=1}^{m} exp\left\{-\frac{1}{2}(\bar{\boldsymbol{y}}^* - \bar{\boldsymbol{x}}_{\boldsymbol{i}})^T \left(\frac{\boldsymbol{W}}{k_1 + k_2} + h^2\boldsymbol{B}\right)^{-1} (\bar{\boldsymbol{y}}^* - \bar{\boldsymbol{x}}_{\boldsymbol{i}})\right\}. \end{aligned} \tag{6.8}$$

Then the denominator takes the form [5]:

$$\begin{aligned} f(\bar{\boldsymbol{y}}_{\boldsymbol{1}}, \bar{\boldsymbol{y}}_{\boldsymbol{2}} \mid \boldsymbol{W}, \boldsymbol{B}, \bar{\boldsymbol{x}}, H_2) &= \frac{1}{m}\sum_{i=1}^{m} K(\bar{\boldsymbol{y}}_{\boldsymbol{1}} \mid \bar{\boldsymbol{x}}_{\boldsymbol{i}}, \boldsymbol{W}, \boldsymbol{B}, h, H_2) \times \frac{1}{m}\sum_{i=1}^{m} K(\bar{\boldsymbol{y}}_{\boldsymbol{2}} \mid \bar{\boldsymbol{x}}_{\boldsymbol{i}}, \boldsymbol{W}, \boldsymbol{B}, h, H_2) = \\ &= (2\pi)^{-\frac{p}{2}} \left|\frac{\boldsymbol{W}}{k_1} + h^2\boldsymbol{B}\right|^{-\frac{1}{2}} \frac{1}{m}\sum_{i=1}^{m} exp\left\{-\frac{1}{2}(\bar{\boldsymbol{y}}_{\boldsymbol{1}} - \bar{\boldsymbol{x}}_{\boldsymbol{i}})^T \left(\frac{\boldsymbol{W}}{k_1} + h^2\boldsymbol{B}\right)^{-1} (\bar{\boldsymbol{y}}_{\boldsymbol{1}} - \bar{\boldsymbol{x}}_{\boldsymbol{i}})\right\} \times \\ &\times (2\pi)^{-\frac{p}{2}} \left|\frac{\boldsymbol{W}}{k_2} + h^2\boldsymbol{B}\right|^{-\frac{1}{2}} \frac{1}{m}\sum_{i=1}^{m} exp\left\{-\frac{1}{2}(\bar{\boldsymbol{y}}_{\boldsymbol{2}} - \bar{\boldsymbol{x}}_{\boldsymbol{i}})^T \left(\frac{\boldsymbol{W}}{k_2} + h^2\boldsymbol{B}\right)^{-1} (\bar{\boldsymbol{y}}_{\boldsymbol{2}} - \bar{\boldsymbol{x}}_{\boldsymbol{i}})\right\}. \end{aligned} \tag{6.9}$$

Finally, for univariate data (p = 1), all matrices or vectors become scalars, e.g., variance-covariance matrix **W** becomes variance w^2 and $\overline{\boldsymbol{x}}$ is reduced to $\bar{x}$.

6.3 Performance assessment

To claim that forensic experts are expected to draw impartial conclusions based on the available data is stating the obvious. It may also seem obvious that they are well prepared for this task, as, in terms of technological possibilities, the very best standard has been achieved. The analytical methods have substantially changed over time, evolving from highly subjective assessments of information-poor data to multivariate signals (e.g., Raman spectra). Never before, throughout forensics' history, experts had more powerful computational devices at their disposal, which – combined with accomplishments of chemometrics and statistics – continually allow to morph the vast arrays of data into information and ultimately also into knowledge. Nevertheless, despite this analytical progress, it should be remembered that forensic science is primarily a "human construct" (especially at the culmination of the examination process). Hence, it still is – and always will be – error-prone. As a consequence, questioning the "scientificity" of forensics resources is inevitable. It has been witnessed in recent years, when the validity and reliability of the information provided by forensic experts, its ability to discriminate between defense and prosecution standpoints, has been questioned and challenged as never before [278, 279].

For this reason, instead of focusing solely on the validation of the analytical method itself, as if it existed in isolation from the results evaluation process, it appears imperative to turn the focus onto the credibility of the examination process at its finale, namely the interpretation and communication of the findings. This means that, before implementing any new forensic technique, specific steps must be taken to demonstrate objectively that each stage of the proposed methodology – and therefore also the interpretation of the results – is suitable for its intended use [20]. This also means that, even though the LR methodology is a recommended tool for establishing a framework for the forensic evaluation of evidence, its application does not automatically guarantee the quality of the evaluation process. In other words, each of the newly developed statistical tools, and hence also LR models, requires proper validation.

Faced with verifying the LR model's performance – or any other method, regardless of its type – one should answer the fundamental question: what is the function of the given model?; what should be expected from it? To respond to these, think back to the *6.1 Likelihood ratio models*, where the expert's task in forensic practice was discussed. In the light of Bayesian theory, forensic experts should be regarded as playing an ancillary function [8, 247, 248], modifying the knowledge of fact-finders with the results of the physicochemical analysis (Eq. 6.1), expressed in the form of LR values. Given the above background, it becomes clear that to be considered effective, the LR model – developed for solving the COMPARISON task – should comply with three essential criteria. First, the model should

differentiate between two contrasting hypotheses and hence be characterized by HIGH DISCRIMINATING CAPABILITIES. In other words, it is expected to provide support for the correct hypothesis (i.e., LR>1 and LR<1 when, respectively, H_1 and H_2 are correct). It is also desired that the model's support toward the correct proposition is as strong as possible (i.e., $LR \gg 1$ when H_1 is correct, and $LR \ll 1$ when H_2 is true). On the other hand, if the support is given to the incorrect hypothesis, an effective model is expected to provide LR values concentrating around unity, delivering only weak misleading evidence. Such a situation would correspond to the WELL-CALIBRATED model, supporting the true proposition to a higher degree (and vice-versa). In fact, only when all of these conditions are fulfilled, the effectiveness of the given LR model – considered both in terms of qualitative and quantitative aspects of its functioning, can be termed as its ACCURACY – can be confirmed.

The decision on whether the LR model meets the above-mentioned criteria, and hence whether it may be implemented in future forensic caseworks, is usually based on empirical tests, which take into account the results of simulated experiments. Each simulated case requires a validation database composed of samples with known *ground-truth* labels (in this case, bloodstains of the known age), which allow us to assess the model's performance, given the generated LR values. It is also worth highlighting the difference between the background and the validation databases. As it was explained in *6.1. Likelihood ratio-based evaluation of evidence*, the background database is always used to model the variation of the evidential materials in a relevant population in order to calculate the LR. The validation database, in turn, is composed of hypothetical recovered and control materials that are employed to simulate a potential case under conditions similar to those in which the evidence evaluation method is expected to be used. In the considered blood dating studies, the validation database should comprise blood traces stored under (possibly) the same conditions as the questioned bloodstain(s), and their aging period should be long enough to encompass the TSD proposed in both hypotheses – H_1 and H_2. Once a validation database has been indicated, a range of LR values can be computed for hypothetical cases, which constitute a so-called *validation set of LR values*. This validation set is subsequently used to calculate different measures of the LR model's performance. In the COMPARISON problem, typically, two different performance metrics can be distinguished: levels of false responses and empirical cross entropy (ECE).

6.3.1 False positive and false negative rates

The most straightforward and perhaps also the most common method for commenting on LR models' effectiveness in forensic sciences is assessing the levels of incorrect responses provided by the given model [8]. In the context of the comparison problem, rates of false positive (FP) and false negative (FN) answers are estimated, which may be considered as a measure of the discriminating power (DP) of LR values, associated with the ability to distinguish cases where H_1 and H_2 are respectively true. The FN response occurs when the model falsely supports the incorrect proposition – in this case, H_2 – hence the

obtained LR value is lower than unity for a *true*-H_1. Conversely, the FP answer is obtained when LR is higher than one (LR>1) for *true*-H_2. To estimate those rates, the following experiments are designed:

- To assess the rate of FALSE NEGATIVE answers, the comparison of two samples (the recovered and control) that genuinely originate from the same source has to be performed. In other words, in the case of the given dating studies, bloodstains of the same age should be compared with each other. For this purpose, the comparison procedure of each bloodstain sample gathered in the first database was repeated for recovered samples stored in the validation database. In this way, the number of experiments to assess the false negative responses equals $N_1 = m$, concerning comparisons of m samples of the same age (i.e., $t_R = t_E$). Since measurements obtained for the equally-aged bloodstains are compared, the model's desired response is LR > 1. Therefore, each value of LR < 1 is then a FALSE NEGATIVE answer.
- To estimate the FALSE POSITIVE rates, LR values should be calculated for two bloodstains characterized by different times since deposition, assuming that H_2 is the correct hypothesis. Since compared samples are of different ages, the expected values of the LRs should be less than one (LR < 1), hence each value supporting the H_1 (LR > 1) is considered as the FALSE POSITIVE answer. The total number of calculations in this experiment is given by $N_2 = m^2 - m$, as it involves comparing differently-aged samples originating from two different m-object databases after eliminating a single bloodstain (serving as so-called reference material).

It is also worth mentioning that even though from the purely theoretical point of view, the importance of each type of these errors may be the same – in the sense that both of them are equally undesired – in reality, this is not the case. This is because false positives may have far more dramatic consequences than false negative responses, as in the courtroom scenario, they may ultimately result in providing false evidence against the suspect, who – according to the law – has the right to be presumed innocent until proven guilty.

It is hard to argue that the simplicity of estimating the rates of false positive and false negative responses and ease of its interpretation are unquestionable advantages of performance evaluation. Nonetheless, validation of LR models solely through the prism of false answers cannot be considered the complete measure of performance, simply because, in this way, we focus only on the qualitative aspect of the model functioning without knowing anything about the strength of support towards the hypotheses. As it was stressed repeatedly, the ability to discriminate between samples, however important, is not the only required characteristic of the LR values set. Apart from supporting the correct hypothesis, it is desired that this support's strength be as high as possible for that particular proposition. In turn, when the true hypothesis is rejected, the obtained LR value must provide only weak support for the false proposition. To better understand that, imagine the situation where false negative answers of LR = 0.01 and LR = 0.98 are obtained for *true*-H_1. Both of them provide misleading support for H_2, and therefore when taking into account solely the FN rates, one might conclude that both of these models

are characterized by the same performance. Nothing more mistaken! Since the strength of the support toward the incorrect proposition is significantly different, there will be a difference in model performance. The second scenario is more favorable, or rather less unfavorable, because even if the model happens to support the incorrect hypothesis, it will deceive the judicature (in the light of the Bayesian theorem) only to a minor extent. Concerning the false positives, similar dependency works – misleading LR values are desired to be close to unity (LR ≈ 1).

Now, it should become clear that information on the rate of false responses is not sufficient for an extensive and credible portrayal of the LR model's performance. What is worse, negligence in validating the quantitative aspect of models' functioning may, in fact, turn their great advantage into a defect with potentially dangerous consequences. Numerous problems can lead to LR values providing support, in some cases strong support, for the incorrect hypothesis. These may include the heterogeneity of the evidence – particularly problematic in the case of biological samples – which often leads to flawed LR models developed from a population that does not characterize the control or recovered samples in a representative manner, or the sparsity of the data, which, again, may result in poor models, providing that robustness of these models to data sparsity is insufficient [280]. Nevertheless, whatever the cause of improper models' functioning, a procedure allowing to evaluate their effectiveness comprehensively must be implemented. How exactly can it be done? Through the employment of the accuracy metric named the EMPIRICAL CROSS ENTROPY (ECE).

6.3.2 Empirical cross entropy – combining discriminating power and calibration

In the context of the Bayes decision theory, the effective discrimination between two propositions is simply not enough. This is because, as already signaled above, in order to be useful, the LR models should also be well-calibrated. Before we go any further, it should not go unmentioned that in terms of statistics, the idea of the calibration itself is understood differently than in a conventional, analytical context. Herein, it is defined as performance characteristics referring to the *validation set of LR values*. Calibration relates to the desired behavior of the LRs, which should be considered a constituent of a Bayesian inference procedure [280]. If the LRs are well-calibrated, then the support towards the correct proposition increases with the discrimination power, significantly influencing the judicature's final decisions. On the other hand, poorly discriminating LR models' outcomes would only slightly modify prior probabilities, and therefore the risk of drawing wrong conclusions during the trial due to misleading evidence would be minimized. Simply put, a better-calibrated model would yield more reliable LR values, which should eventually contribute to better decisions taken by the fact finder.

In order to assess the global performance of LR models, an approach that takes into account both the qualitative and quantitative aspects of their functioning is required. It is considered that an adequate tool for thoroughly assessing models is empirical cross entropy [8, 280, 281], founded on the information theory, which captures information on both discriminating power and calibration of

a validation set of LR values. Therefore, one can say that ECE is basically a metric of the model's ACCURACY[****], which should be understood as a degree of agreement between the calculated LR and the ground truth label of a particular proposition.

In order to model the importance of errors, the ECE procedure estimates the model's performance, assigning a penalty (or cost) to each LR value in favor of the wrong hypothesis. This penalizing system is controlled by the logarithmic strictly proper scoring rules [8, 282], where for each value of the evidence *E*, the scoring rule takes the following values:

$$H_1\ true\colon\ -log_2 Pr(H_1|E)$$
$$H_2\ true\colon\ -log_2 Pr(H_2|E)$$

Consequently, the higher the support for the wrong hypothesis, the more severe the given error is because, the greater penalty is assigned to the evaluated LR model.

The overall penalty rate (*LS*) is defined as the average value of assigned penalties over many different LR model's responses, for which the actual values of the H_1 and H_2 are known:

$$LS = \frac{1}{N_1}\sum_{i=1}^{N_1}\log_2\left[1+\frac{\Pr(H_2)}{LR_i\ \Pr(H_1)}\right]+\frac{1}{N_2}\sum_{j=1}^{N_2}\log_2\left[1+\frac{LR_j\ \Pr(H_1)}{\Pr(H_2)}\right], \tag{6.10}$$

where N_1 and N_2 correspond to the number of experiments performed under H_1 and H_1 hypotheses.

Following this procedure (Eq. 6.10), the metrics of accuracy can be expressed as a function of prior probability in the form of the ECE, calculated through the following formula:

$$ECE = \frac{\Pr(H_1)}{N_1}\sum_{i=1}^{N_1}\log_2\left[1+\frac{\Pr(H_2)}{LR_i\ \Pr(H_1)}\right]+\frac{\Pr(H_2)}{N_2}\sum_{j=1}^{N_2}\log_2\left[1+\frac{LR_j\ \Pr(H_1)}{\Pr(H_2)}\right], \tag{6.11}$$

where N_1 denotes the number of experiments performed to estimate false negative rates (when H_1 is a true hypothesis), and N_2 corresponds to the number of simulated cases where false positive rates were calculated (considered under H_2). The LR_i and LR_j, in turn, denote a particular LR value obtained for the validation set for which H_1 and H_2 are respectively correct.

[****] Once again, the discrepancy between the accuracy considered within the purely analytical and the LR context has to be emphasized. In the first case, accuracy refers to the closeness of agreement between a measured quantity value and a true quantity value of a measure. In turn, when the LR context is considered, no quantitative ground truth exists, because the LR is a "product" of a probabilistic inference (which is not a technical measurement), and hence it is virtually impossible to estimate univocal relation between a computed LR value and a pair of compared specimens. Consequently, a given LR value is considered as more accurate if it supports the true (known) hypothesis to a higher degree, and vice-versa.

When comparing the LS and ECE expressions, it can be immediately seen that the ECE is, in fact, the average of the logarithmic scoring rule, weighted by the relevant prior probabilities [8, 281]. Unfortunately, some difficulties might be encountered when the above-mentioned approach is to be applied in forensic practice. As shown in Eq 6.11, ECE is a function of both LR values and prior probabilities. While the LR values (denoted as LR_i and LR_j) are provided by the model being under assessment. The prior probabilities are not readily available since the forensic expert is in no way empowered to estimate them. In such a case, the prior possibilities are always the province of the fact-finder. Therefore, in order to overcome the lack of the forensic expert's knowledge about the prior odds, an alternative method of presenting $Pr(H_1)$ and $Pr(H_2)$ has to be introduced. This aim is achieved by computing and representing ECE for a wide range of prior probability quotients $Pr(H_1)/Pr(H_2)$ – usually referred to as prior odds – which are eventually presented in a graphical form (Figure 6.1). Ultimately, the ECE calculated for the particular LR value can be represented in a prior-dependent way and expressed as their logarithm with base 10 (as they are usually used for evidence evaluation).

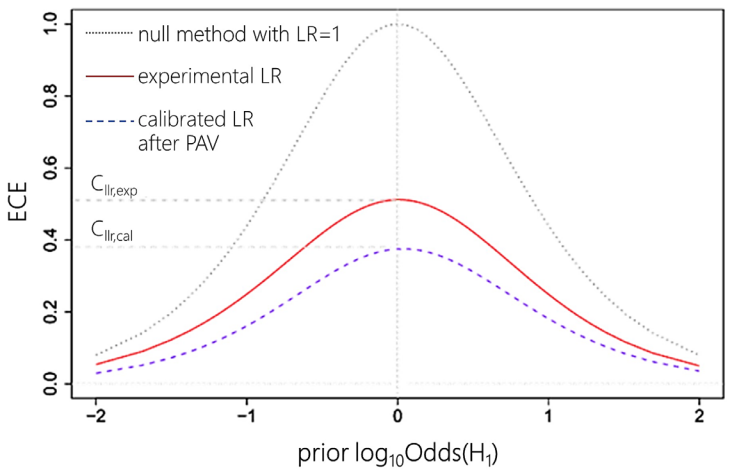

FIGURE 6.1.

Empirical cross entropy (ECE) plot.

To clearly illustrate not only the accuracy itself but also the calibration of LRs and additionally give some insight into the possibility of improvement of the model, the ECE plot is usually comprised of three performance curves [5, 8]:

- The red curve (named *experimental*) represents the ECE of the LR values generated by the model under assessment, reflecting the method's accuracy – the closeness of the calculated LR value and the ground truth label of the hypothesis being under consideration. The lower the solid curve, the more accurate the method since less information is needed than the ground truth state of knowledge.

- The black curve (named *null* or *neutral*) refers to the model that always delivers LR=1, which means it does not support any propositions, and therefore it is called a neutral method. This particular performance curve is treated as a boundary that the experimental LR should not exceed. Otherwise, it would mean that the forensic examination results, expressed in the form of an LR value, would introduce more misleading information than assuming the evidence's neutrality.
- The blue curve (named *calibrated*) corresponds to ECE computed for an optimally calibrated set of LR values that is expressing strong support for correct propositions and delivering insignificant support for the wrong ones. In order to achieve this perfect calibration, LRs, provided by the model under evaluation, are transformed using an algorithm named Pool Adjacent Violators (PAV) [8, 283]. Since the ground truth labels are known during this modification, the calibrated curve establishes a reference of performance, which can never be obtained in practice. As a result, the only difference between the experimental and calibrated model outcomes lies actually in the calibration. Precisely this difference, expressed by the distance between the red and blue curves, represents the possibility of any further refinement of the model's performance.

It is also interesting to mention that under the information-theoretical framework, the entropy itself (which is a function of a given probability distribution) should be interpreted as a measure used to quantify the uncertainty about the unknown variable – herein the actual value of the considered hypotheses – in the light of available knowledge. This general knowledge includes the background information gathered by the fact-finders (denoted as I in Eq. 6.1) and the evidence analysis results. In other words, any additional knowledge about the issue under examination should provide additional information, and through that, reduce entropy. The correctly performed evaluation of evidence should therefore be regarded as the "supplier" of the information. The results of this examination, expressed in the form of the LR values, are desired to reduce the uncertainty (the entropy) about the fact finders' conclusions, hence facilitating the decision-making process embedded in the courtroom scenario. Consequently, ECE, in fact, represents the mean additional information, computed as an average over the validation set of LRs, that is still required (after examination of the evidence) to uncover the actual value of the given proposition.

The easiest way to interpret the resulting ECE plot is to study the ECE curve's relative location obtained during the model's evaluation (solid red curve). If we consider the situation before the evidence examination (represented as a dotted black curve), additionally assuming that the background information does not provide support for any of the hypotheses – $Pr(H_1) = Pr(H_2)$ – then the uncertainty about the correct hypothesis equals 100%. Once the evidence is analyzed, the calculated LR values may or may not reduce uncertainty concerning the neutral case (before the evidence analysis, the uncertainty equals 100%). The effect of the evidence examination, whether beneficial or not, is portrayed on the

ECE plot. The higher the experimental ECE curve, the more information needs to be provided to identify the correct hypothesis and vice-versa. Therefore, one should always aim to develop a model, which would deliver LRs characterized by low values of ECE, with the experimental plot lying below the neutral curve. Only in this case, the reduction of information loss is observed. For clarity, examples of ECE plots exhibiting different performances are presented in Figure 6.2.

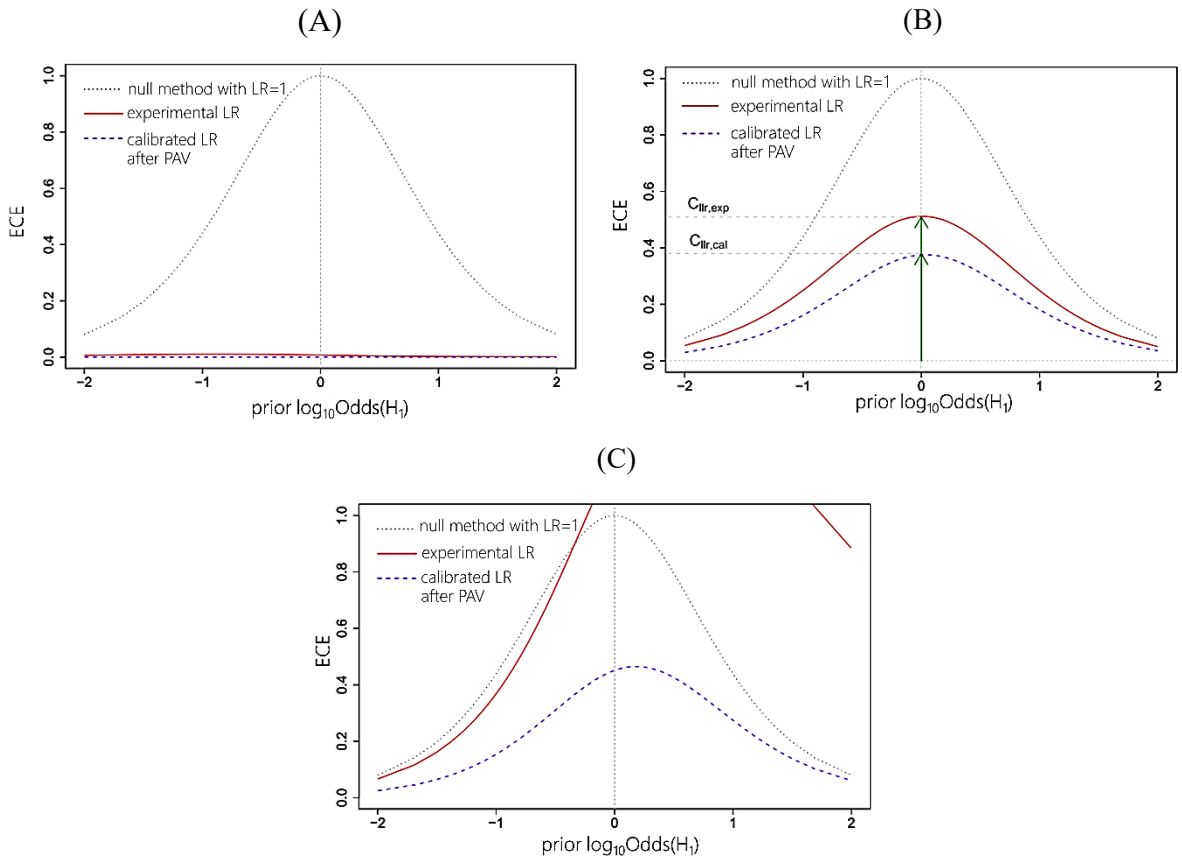

FIGURE 6.2.

Empirical cross entropy (ECE) plots characterized by (A) ideal, (B) acceptable, (C) unacceptable performance [graphics from 5].

In practical terms, representing the ECE plot in a wide range of prior probabilities has an additional benefit. No one actually expects the fact finder to estimate in advance the prior odds. As a result of a detailed evaluation of the applied LR model, the forensic expert entering the courtroom is prepared for a broad spectrum of possible scenarios. On the other hand, the presentation of the ECE results in a graphical form can be troublesome, especially during the comparison of the methods. For this reason, single numerical measures, summarizing the ECE for a chosen value of prior probabilities such as $C_{llr,exp,}$ and $C_{llr,cal}$ corresponding to the point of *prior* $log_{10}Odds(H_1)=0$ for *experimental* and *calibrated* ECE curve respectively, were introduced.

Finally, it should also be mentioned that despite all of the aforementioned merits of the ECE, this methodology still cannot be considered a flawless measure of model performance. It might be said that the ECE approach somewhat lacks robustness, as it is susceptible to even a single LR value, providing strong support for the incorrect hypothesis. In particular, when small databases are considered, the penalty assigned to a misleading LR value might outweigh the award given for the LRs supporting the correct hypothesis. Therefore, examiners dealing with scarce databases should be urged to investigate the ECE results with caution, especially when accompanied by the low rates of false negative and false positive answers.

| *CHAPTER 7*

TOWARD HYBRID LIKELIHOOD RATIO MODELS – COMBINING CHEMOMETRICS AND LIKELIHOOD RATIO FRAMEWORK FOR EVALUATING SPECTRAL DATA

Early approaches to measuring the strength of evidence using LR were focused on data consisting of a small number of variables, with the interpretation of glass fragments' elemental composition being probably the most prominent example [258, 284]. And indeed, the construction of LR models based on low-dimensionality data should not pose any severe difficulties. This is because for datasets containing fewer variables than samples they describe, a reliable estimation of the LR model parameters, such as means, variances, and covariances, does not pose problems. Unfortunately, difficulties in calculating those parameters arise as the number of variables needed for a complete description of all samples increases. Consequently, the conventional LR approach is not well-adjusted to deal with high-dimensionality data [8], where the number of variables exceeds the sample population's size. An example of this is, of course, Raman-based datasets, and thus LR models developed in this thesis simply cannot be founded on the recorded data just "as they are". Registered signals require engaging some specific measures that would compress the spectra (often with hundreds or thousands of variables) down to just a few variables that will serve as the basis for developing the LR models.

A remedy for the above-mentioned *curse of dimensionality* is a form of symbiosis between the LR approach and chemometrics known as HYBRID LR MODELS, introduced by Martyna et al. [264], which have already proven their effectiveness through years of use in forensic studies [262, 263, 265, 285]. Reduction of data dimensionality and extraction of informative features (with regard to the purpose of the study) are carried out through the implementation of chemometrics. Whereas the subsequent construction of LR models, based on a limited number of new latent variables summarizing the data and exposing their desired characteristics, makes up deficiencies that arise when the data evaluation process is restricted solely to chemometric methods[††††].

However, to apply the analytical signals to work optimally within the LR approach, it is often necessary to take some additional steps prior to data modeling. Multivariate data – such as Raman spectra – consist of numerical vectors containing the experimental variable's intensities measured. These signals usually contain some unwanted variation, which may undermine the variation of interest. Hence, the undesired contributions should be minimized mathematically by applying suitable signal pre-processing methods before further analysis.

[††††] It is worth recalling that chemometric tools do not take into account some aspects essential from the forensic perspective – e.g., information regarding the rarity of the physicochemical features.

7.1 Signal pre-processing

No matter how dazzling the computational methods may be, the "garbage in, garbage out" paradigm will always apply to the data they process. No chemometric tools can spin straw into gold, and thus there is no substitute for optimal data collection. And indeed, many undesired signal variations can be minimized to some extent or even avoided through a suitable selection of sample presentation methods (as already briefly discussed in *5.1.2.4. Sample preparation and handling*) and experimental conditions. Nevertheless, spectral data pre-processing can still significantly improve the subsequent multivariate analysis even after proper data collection.

As the name implies, signal pre-processing involves processing the raw to "clean" data by removing the undesired variation so as to highlight the features chemically relevant for further analysis, e.g., discrimination (by discrimination, we mean herein judging whether the features of the questioned sample resemble the characteristics of a reference sample of known age so much that they can be considered as originating from the same source[‡‡‡‡]). The presence of such variation, which is unrelated to the goal for which data was collected, can be ascribed to instrumental drifts, sample state, or some external physical contributions [286]. These deteriorating effects are usually observed in vibrational spectroscopy as noise, baseline vertical shifts, and global intensity effects, which typically arise from light scattering phenomena [287] that can become quite severe, especially in the case of biospecimens. Various pre-processing methods have been developed to compensate for these differences in spectral signals [288]. However, because of their diversity that generates a multitude of possible choices, the pre-processing stage is often seen as more of a burden than a blessing. What is the reason for this?

The employment of different pre-processing methods can be termed a pre-processing strategy, consisting of various steps (e.g., denoising and smoothing, baseline correction, normalization) that are often already implemented in the software systems. This, in turn, makes the pre-processing readily available even for inexperienced users. However, several different normalization methods, smoothing, etc., can be applied in each of these steps. The problem is that there are no clear rules, no explicit directions on how to compose the pre-processing strategy to improve the data analysis outcome. Consequently, questions like *When to use the specific pre-processing technique? Is the single method enough? If not, which techniques should be combined, and in what order?* [287, 289] are often left unanswered, and the combination of pre-processing methods may be blindly selected from the rich reservoir of available tools. In other cases, the decision is made through visual inspection of the signal graphical representation. The pre-processing strategy is considered satisfactory if unwanted artifacts are effectively eliminated and the signal appears more transparent (in the sense that certain features, e.g., unique for the groups, are more evident). This tactic, again, is not entirely correct because of its

[‡‡‡‡] Here, the *source* ought to be understood as a group of bloodstains corresponding to the same time since deposition (TSD).

subjectivity and absence of any guarantee that the most appealing results will provide effective statistical models. Another selection procedure, and perhaps the most common one, can be summarized as a "fit-for-use" approach [289]. Here, a few pre-processing strategies are implemented, often based on personal experience. The ultimately chosen sub-optimal strategy is producing the data yielding best performing statistical models. And even though it is hardly possible that the globally optimal solution will be among these few tested combinations, it does not mean that such a procedure will not lead to the model of acceptable performance. Nevertheless, the question still arises – is it possible, in any way, to propose an optimal pre-processing strategy, which on the one hand, is more automated, and on the other is suited for distortions observed in the registered data and the purpose of the study? After all, we all agree that pre-processing can either make or break subsequent data analysis, and hence its significance is undeniable.

To date, some suggestions on how to tackle that issue were proposed [290]. One of the possible ways to solve that problem is developing quality parameters considered indicators that evaluate the pre-processing strategy effectiveness, according to the purpose of further analysis. The optimal preprocessing strategy is found when quality parameters take their best values [291], for example, by using the genetic algorithms (*7.2. Genetic algorithms*). In the case of this study, which is aimed at the discrimination between differently-aged samples, the quality parameter may be defined as a ratio of the between-source and within-source variation (b^2/w^2) for the preprocessed data (*7.3. Regularised MANOVA*), obtained through the regularised MANOVA (rMANOVA) procedure. It should be emphasized that rMANOVA not only contributes to the pre-processing optimization but also has the added advantage of solving the dimensionality problem, which occurs during the construction of LR models using multivariate data. This is because it reduces data dimensionality in a beneficial way for optimal sources separation – by maximizing differences between differently-aged samples and simultaneously minimizing differences within samples of the same TSD – and also highlights their specific features.

The following subchapter summarizes the pre-processing methods employed in the study, together with the chemometric tools of data compression required for developing hybrid LR models. It does not aim to review these chemometric practices but only provides sufficient basics and bibliography positions for the readers who might not be familiar with them.

7.1.1 Denoising and smoothing

Minimization of noise, an inherent component of any measured signal, aims to increase the signal-to-noise ratio of the data, making it more legible and visually pleasing. To date, various methods have been proposed for smoothing and denoising data sets. However, a line of demarcation between those two procedures is rarely established. It should be reminded that denoising and smoothing are applied to handle different noise types. While smoothing removes components (of the transformed signal)

occurring in the high end of the transformed domain regardless of amplitude, denoising eliminates small-amplitude components appearing in the transformed domain irrespective of position.

MOVING POLYNOMIAL FITTING consists of identifying a low degree polynomial for a subset of signal points in a window of a given width, centered on the point to be treated. The fitted polynomial value is then substituted for a central point of the window. Subsequently, the window is then shifted by one point, and the calculation is repeated for the new point. The procedure is continued until the window reaches the end of the signal, and obviously, it cannot be applied to the edge points of the spectrum. The moving polynomial fitting corresponds to the Savitzky-Golay algorithm used with a differentiation order of zero in practice [292].

DISCRETE WAVELET TRANSFORM (DWT), just like Fourier transform (FT), is one of the available tools for performing filtering in the frequency domain. Their general principle assumes that the signal can be decomposed into a weighted sum of a signal of different frequencies. Because noise, baseline, and actual signal components are well separated in the frequency domain (baseline varies at the lowest rates, while the signal noise frequency is the highest), the unwanted components can be removed. Depending on the eliminated parts, low-pass, high-pass, or band-pass filters can be applied, after which the filtered signal can be restored through the reverse transform.

Perhaps the most popular method for filtering in the frequency domain is the Fourier Transform, representing the signal only as a linear combination of sinusoids and cosinusoids. Thus, it is not well adapted for representing non-stationary signals – as spectra – that are not continuously repeated. It is possible to overcome this limitation using wavelet functions [293–297], which are localized in both space and frequency. They may be employed to represent the signal at different resolution scales and to varying proportions in different signal regions. WT proceeds by the recursive application of a matrix of wavelet coefficients to a signal while changing its location (by translation, determined by localization parameter) and frequency (controlled by scaling parameter).

The WT-based denoising procedure consists of three primary steps: decomposition of the signal, elimination of small coefficients (thresholding), and signal reconstruction. Usually, two different approaches can be employed in order to remove small coefficients – hard thresholding or soft thresholding. The hard thresholding method boils down to assigning all the wavelet coefficients below a given threshold value equal to zero. In turn, in soft thresholding, the wavelet coefficients are reduced by the threshold value. Apart from that, the noise level has to be estimated, which can be performed differently. The most popular approach, known as the universal thresholding, is founded on the statistical properties of white Gaussian noise. The standard deviation of the detail coefficients of the first level of decomposition is used to calculate the threshold level. However, this definition can lead to overestimating the noise level; therefore, to address this problem, the cross-validation CV procedure can be introduced.

The theory of wavelets, together with mathematical formulas, will not be discussed in great detail, as this is beyond the scope of the present thesis. However, it is necessary to mention, because of

potential users, other parameters that determine the quality of the WT-based signal denoising, namely the type of wavelet function, i.e., the filter used to decompose the signal and the level of DWT decomposition. For reference, see [298].

7.1.2 Baseline correction

Analytical signals (like spectra) may contain structured backgrounds that are called baselines. They are supposed to be continuous, low-frequency signals of different types (e.g., constant, linear, polynomial). Thus, there are many baseline correction methods, and the choice of the best ones is strongly dependent on the particular application [299].

Raman signals are often accompanied by broad and intense fluorescence, a competing process to the relatively weak Raman scattering effect. It is often the case that the fluorescence is so intense that it obscures the Raman peaks. At a time like this, some experimental techniques applied during signal collection are engaged, which aim to enhance the Raman scattering (RRS, SERS, CARS, or SRS) or take advantage of physical differences in both phenomena (e.g., time-gated Raman spectroscopy). The photobleaching process or simply changing the laser source can also be effective [300]. Finally, the problem of baseline effects that do not entirely cover the actual Raman signal, which may arise, among others, from the sample's fluorescence, can be addressed after signal collection, using computational methods of baseline corrections.

In the most elemental form, POLYNOMIAL METHODS fit the polynomial curve to the baseline points defined by the analyst using the least-squares method. As can be easily imagined, this basic approach was subjective and highly time-consuming; hence it was advanced by the automated methods such as modified polyfit (ModPoly) [301] and improved modified polyfit (IModPoly) [302]. In the first of the above-mentioned procedures, the polynomial (**w**) of a fixed but adaptable degree is initially fitted to the raw signal in a least-squares manner. Since this procedure requires eliminating the actual peaks from the fit, they are removed in an iterative process. In each turn, polynomial fitting is applied to a newly-obtained signal generated as the minimum between the polynomial fitted in the previous round and the raw signal.

With the signals of high noise level, the outcome of ModPoly may appear insufficient as noise may be interpreted as the signal itself. Besides, a few major peaks can often determine the entire polynomial fitting. To solve these issues, the IModPoly algorithm was proposed [303], which takes into account signal noise distortion and the impact of large Raman bands on the fitting procedure. During the first iteration of this procedure, the major peaks are identified, and the corresponding spectral ranges are removed from the following rounds of the fitting. The process starts with a single polynomial fitting using the original Raman signal, followed by the calculation of residual and its standard deviation (DEV), which is considered a measure of the noise level. Each iteration fits a polynomial to the signal (being the minimum of the signal to which the polynomial was fitted in the previous round) and this

polynomial plus the value of DEV. Values greater than the sum of fitting function and DEV are treated as Raman signal. When the procedure converges, the baseline is interpolated in the major peak regions and subtracted from the untreated signal.

ASYMMETRIC PENALIZED LEAST SQUARES METHODS propose identifying the baseline of a spectrum with a penalized least squares regression. The raw signal is smoothed by monitoring the balance between the roughness and the fidelity of the smoothed curve to the signal [304]. The fidelity is understood as a lack of fit measured as the sum of squared differences between the smoothed curve (**z**) and the signal (**s**):

$$F = \sum_{i=1}^{J} (s_i - z_i)^2.$$

The squared sum of differences between adjacent points is used to estimate the roughness of the curve:

$$R = \sum_{i=1}^{J-1} (z_i - z_{i+1})^2 = \sum_{i=1}^{J-1} (\Delta z_i)^2.$$

Most often, however, squared second differences are applied. In its most general form for *m*-th differences, Equation (6) becomes $R = \sum_{i=1}^{J-1} (\Delta^2 z_i)^2$.

The expression $Q = F + \lambda R$ is minimized using penalized least squares to determine **z**. The analyst arbitrarily assigns the tuning parameter λ, which – as can be seen from the equation – controls the contribution of the roughness to the entire expression (Q).

To estimate the baseline, the signal peaks have to be removed so as to establish **z** fitting only the baseline regions. In order to do so, asymmetric weights, w_i, are employed with a role in weighing the positive deviations from the baseline much less than the negative deviations. Subsequently, the fidelity expression is then modified accordingly:

$$F = \sum_{i=1}^{J} w_i (s_i - z_i)^2 = (\boldsymbol{s} - \boldsymbol{z})^T \boldsymbol{W} (\boldsymbol{s} - \boldsymbol{z}),$$

where **W** is a diagonal *J x J* matrix with **w** on the diagonal. For the system of equations:

$$(\boldsymbol{W} - \lambda \boldsymbol{D}^T \boldsymbol{D})\boldsymbol{z} = \boldsymbol{W}\boldsymbol{s},$$

the solution is found using initial weights, which then can be updated. The entire procedure is carried out until convergence when the change in weights is no longer observed, and the baseline estimate does not improve anymore. The final baseline is computed from

$$\boldsymbol{z} = (\boldsymbol{W} - \lambda \boldsymbol{D}^T \boldsymbol{D})^{-1} \boldsymbol{W}\boldsymbol{s}$$

and then subtracted from the signal.

There are different variates of asymmetric least-squares methods depending on the way of assigning the weights. The most straightforward variation gives small *p* or large $1-p$ weights for peak regions ($s_i > z_i$) and baseline segments ($s_i \leq z_i$) respectively. In another approach [305], an automatic

weights assignment in an adaptive iteratively reweighted penalized least squares (airPLS) algorithm was proposed. Informative peak regions have also been indicated with continuous wavelet transform (CWT), where the Haar wavelet proved to be effective in determining the position and width of the peaks [306].

Another representative of ALS methods referred to as doubly weighted spline [307] assumes that the roughness term should contribute more to the baseline estimation in peak regions instead of baseline segments. Therefore, minimum stiffness γ_{min} is assigned to baseline regions while takes maximum γ_{max} for peak regions.

And finally, the asymmetric penalized least squares algorithm [308] for baseline estimation should be mentioned. Its attractiveness derives from the ability to diminish between-replicate variations observed in signals after the baseline correction. The fundamental idea of this approach relies on introducing an additional penalty assigned to already corrected replicate signals to "punish" significant differences between spectra, which should be as similar as possible.

STATISTICS-SENSITIVE NON-LINEAR ITERATIVE PEAK-CLIPPING (SNIP) proved to be an efficient method for dealing with baseline variations for other signals, even though initially it was proposed for correcting baseline effects in PIXE spectra of geological samples [309]. The algorithm is initialized with a low statistics digital filter that takes into account significant differences in signal magnitude and transforms each signal intensity according to the equation $y_i = \log\left(\log(s_i + 1) + 1\right)$ Subsequently, the baseline is estimated from 1 to W in an iterative manner, where W is the size of the clipping window. In the w-th iteration, each intensity point, y_i, becomes a central $2w + 1$-length interval point substituted by a minimum of the mean intensities at both interval ends and the point intensity itself. Finally, the baseline is estimated using inverse transform $g_i = \min\left(y_i, \frac{1}{2} \cdot y_{i+w} - y_{i-w}\right)$ and subtracted from the spectrum.

QUANTILE REGRESSION-BASED METHODS, including polynomial or spline quantile regression (QR) methods, fit the baseline when small quantiles are assumed (e.g., 0.01) [310]. They can also be advanced in weighted quantile regression models with weights automatically and iteratively assigned.

ROBUST BASELINE ESTIMATION (RBE), in the simplest sense, refers to techniques of baseline estimation that are less sensitive to outliers (extreme observations) than the conventional least-squares approach. It classifies points within the peak regions as outliers (regarding the signal ranges that belong to baseline sections) and assumes that the baseline, with an undefined functional shape, can only be estimated locally, in small fragments, using, e.g., linear models [311]. In order to fulfill these requirements, RBE methods are most appropriate that will robustly estimate the baseline only in small-signal fractions while discounting the peak region points. Kernel functions specify these signal fractions. The residuals of the local regression models are then used for establishing small weights for signal points with large residuals (peaks) and unit weights for baseline region points according to an equation:

$$\begin{cases} w_i = \max\left(1 - \left(\frac{s_i - z_i}{\sigma b)^2}, 0\right)\right)^2, & if\ \frac{s_i - z_i}{\sigma} \geq 0 \\ w_i = 1, & if\ \frac{s_i - z_i}{\sigma} < 0, \end{cases}$$

where σ is the scale parameter, estimated as median absolute deviation: $\sigma = 1.4826 \cdot median(|s_i - -z_i|)$. B, in turn, is the robustness parameter that controls the influence outliers and ordinary points have on baseline estimation. Subsequently, the baseline is recalculated in an iterative manner using weighted least squares regression models.

7.1.3 Normalization

A measured signal **x** may also be influenced by multiplicative effects, meaning that instead of **x**, the a**x** is registered (with $a \neq 1$). In the field of vibrational spectroscopy, these effects can be observed due to the particle size of the analyzed sample, the geometry of the measuring device, or even unstable conditions such as fluctuating laser power (in Raman spectroscopy). Therefore, in order to make samples comparable, it may be necessary to normalize signals characterizing those samples. In most cases, normalization consists of multiplying the signal by a scaling value to make the corresponding intensities comparable across spectra, which should not theoretically pose any differences. Although spectral normalization methods are applied to each spectrum, it should be remembered that some of them require the whole dataset to estimate the correction factors. Hence the attention should be paid when splitting data into training and test sets is performed.

STANDARD NORMAL VARIATE (SNV) was introduced by Barnes et al. [312] to reduce differences in the spectra' global intensities and alleviate multiplicative effects of scattering and particle size. In order to correct those unwanted variations, each spectrum has its mean value subtracted and subsequently is divided by its standard deviation, leading to the elimination of the constant offset and multiplicative differences between spectra. However, despite its evident advantages, SNV produces spectra that are different from the physical signals in the sense that SNV-treated signals contain negative values, and the spectral information is spread along the whole spectral range. In other words, the price to pay for removing unwanted variation using SNV may be the loss of information related to original variables [287, 313].

PROBABILISTIC QUOTIENT NORMALIZATION (PQN) was initially developed to avoid the diluting effect of urine samples measured by NMR [314]. It proposes to estimate the factor d affecting the signal $\boldsymbol{x}$ using only a part of its variables. This approach calculates a normalization coefficient as the median quotient between the untreated and reference signals [314, 315]. For normalization, each i-th signal intensity is divided by the defined quotient as a normalization factor. However, it should be noted that PQN-treated spectra might be affected by the so-called information shift, where information in one wavelength region tends to be shifted elsewhere or simply smeared across the entire spectral range [287]. Consequently, this pre-treatment method, along with others that shift or rescale spectra (e.g., SNV), poses a risk of erroneous interpretations.

7.2 Genetic algorithm

Given the personal experience and some familiarity with the problem at hand, the spectroscopist may attempt to decide on the most reasonable pre-processing strategy. However, having looked at the previous subchapters, which actually present only a tiny fraction of all possible pre-processing methods, there is no dispute that the plethora of available algorithms (requiring selection of various input variables) makes the process of educated guesses inherently flawed. This "informed trial and error" approach is usually a sub-optimal solution, as it is virtually impossible that the analyst exhaustively explores all pre-processing methods and their combinations [290]. Theoretically, it would be possible to perform a grid search to find the optimal strategy, providing the most desirable model's performance, but this approach is computationally expensive and far too time-consuming. Fortunately, with the development of chemometrics and greater computing processing powers, various methods for optimizing pre-processing strategies have been suggested (as detailed in [290]). One possible solution is to employ a heuristic search algorithm such as a genetic algorithm (GA).

Genetic algorithms (GAs), proposed by Holland in the 1970s, are a computing technique that can efficiently solve problems with many possible solutions [316]. They are founded on the Darwinian evolution theory of the "survival of the fittest," where nature determines the survivability of individuals based on their adaptation to life. In other words, GA can be considered an optimization technique because it allows choosing the best solution by mimicking the evolution of a species in a specific environment. More detailed information on genetic algorithms can be found in references [317–322].

In the paper on the application of genetic algorithms in chemometrics, Lucasius and Kateman stated that their eventual impact probably *relies in their ability to support and supplement the techniques that are already established in the area, rather than to make any of these redundant* [323]. For large-scale optimizations, this conclusion is not necessarily true, as GAs could be one of the few ways to find a reasonable solution, producing significantly better results than those obtained by the standard techniques. The first encountered problem to be addressed is coding the information in a way comprehensible for the computer to mirror the pattern of what occurs in nature. It can be said that the result of an optimization procedure is a function of the experimental conditions, some input variables, just as the fitness to the environment is a function of the genetic material.

When transferring the GA concept to the chemometric field, the following correspondences can be distinguished [324]:

- a response function indicates adaptation to the environment;
- genes define genetic material in the same manner as the experimental conditions are determined by variables involved in the given optimization procedure (the gene-variables correspondence);
- a sequence of nitrogenated bases defines the information written in each gene. Similarly, the binary code can be applied to transform variables' value in a word written in bits.

In the GA-based optimization procedure, the initial step is to generate the original population (array) by random selection of a specified number of individuals (rows) described by their genetic material (variables corresponding to the array's columns). Thus, each individual represents a subset of the original variables within the larger superset of data under analysis. Subsequently, analogously to Darwinian evolution, individuals with the best fit for the environment are selected, mated, and their genes are shuffled in the crossover process. In this way, the desired genetic material is preserved for the next generation, whereby the weak one is eliminated according to the survival of the fittest rule. This procedure is continued until a particular stopping criterion has been reached.

In its simplest form, the evolutionary stage of a GA proceeds in the following manner [325]:

(1) a proportion of the fittest individuals from the parent population is extracted,

(2) the selected offspring are recombined (crossover),

(3) the mated population is subjected to mutation (changing the values of the variables),

(4) the fitness of newly evolved offspring is assessed,

(5) a proportion of the offspring is reinserted into the population, replacing the worst parents (mixing the variables and changing their values slightly to receive better solutions than previously),

(6) the process is repeated until a stopping criterion is reached.

It is worth noting that several fittest individuals are always kept and propagated to the next generation to avoid losing their most profitable genetic material. This is because it may happen that despite the average response of the new set is improved, in some cases, new best solutions do not always outperform the fittest ones in the previous selection [291]. Consequently, a specified number of solutions derived from each set is preserved as the most optimal solutions.

The GA, just like any other algorithm, is not objective in the sense that it is optimized to some definition of success. In chemometrics, this success may be equaled to the pre-processing strategy leading to the best performance model, assessed through some quality parameters desired to take their extremes (maximum or minimum). Therefore, the fittest individuals (herein, the best pre-processing tactics) are characterized by the lowest/highest quality parameter. In this study, when the discrimination of the highly multidimensional data is the problem at hand, the criterium for selecting the most appropriate signal preprocessing strategy is based on the rMANOVA first latent variable.

7.3 Regularised MANOVA

The choice of this particular quality parameter, indicative of the effectiveness of the pre-processing strategy, is obviously not accidental. It results from the necessity of combining the signal pre-processing with reduction of data dimensionality in a way that contributes further data analysis for forensic purposes [263, 264], in this particular case – discriminating between differently-aged samples. The prerequisite

for any successful discrimination is that the average variance of the replicate measurements within each group is much lower than the variance of group averages. If this condition is not satisfied, distributions of variables characterizing the compared groups will overlap, preventing successful discrimination. That also applies to LR models designed for distinguishing between bloodstains of different TSD.

Among methods of variance analysis offered by contemporary chemometrics, several tools are suited for studying highly correlated multivariate data sets. One of them is a regularized multivariate analysis of variance (rMANOVA), which – unlike its prototype (MANOVA) – is suitable for data populations containing more variables than samples [326]. rMANOVA was introduced in the literature as a weighted average of the ASCA (ANOVA simultaneous component analysis) and MANOVA models to address the problems encountered with both of these methods – deal with datasets containing more variables than samples (MANOVA's limitation) and take into account correlation between variables (restriction of ASCA).

The main goal of this method is to define new directions (eigenvectors) that boost the between-group variance (denoted as **B**) while minimizing the within-group variance (denoted as **W**). Its objective is to find the eigenvectors of the matrix, along which the between-samples variance is the highest and the within-samples variance the lowest, according to the following formula:

$$\mathbf{J^*} = ((1-\delta)\mathbf{W}+\delta\mathbf{T})^{-1}\mathbf{B}. \quad (7.1)$$

T is the target matrix, which is either $\boldsymbol{T} = \frac{1}{p} tr(\boldsymbol{W})$ when the variances of p variables for each sample are equal or **T**=diag (**W**) when the variances for each sample are unique. δ is dependent on the chosen target and expresses the variance of the **W** matrix components, and its optimal value is calculated according to the Ledoit–Wolf theorem [326, 327]. The importance of the studied variables can be determined based on the eigenvectors of **J*** [327]. Subsequently, these new latent variables, derived from rMANOVA and owing to that characterized by least variability within each source and maximal variability between sources, can serve as input variables for the construction of LR models for solving the considered comparison problem.

Once investigating the equation 7.1, it is also worth noting that the rMANOVA model turns into a MANOVA model when δ=0, whereas rMANOVA becomes ASCA for δ=1 and **T**=I [285].

EXPERIMENTAL PART

CHAPTER 8

PRELUDE TO EXPERIMENTAL RESEARCH

As a preliminary remark, it will be helpful to briefly outline the construction of the experimental part of the thesis (shown graphically in Figure 8.1), which stems from the dual nature of the dating problem discussed in the theoretical section. Specifically, the first part described in *Chapter 9* is dedicated to developing a Raman procedure for monitoring bloodstains degradation processes. Whereas the second one, addressed in *Chapter 10,* discusses the construction of likelihood ratio-based comparison models for data interpretation. These two parts combined constitute the title procedure of the present dissertation, namely, A NOVEL FRAMEWORK FOR BLOOD EVIDENCE EVALUATION.

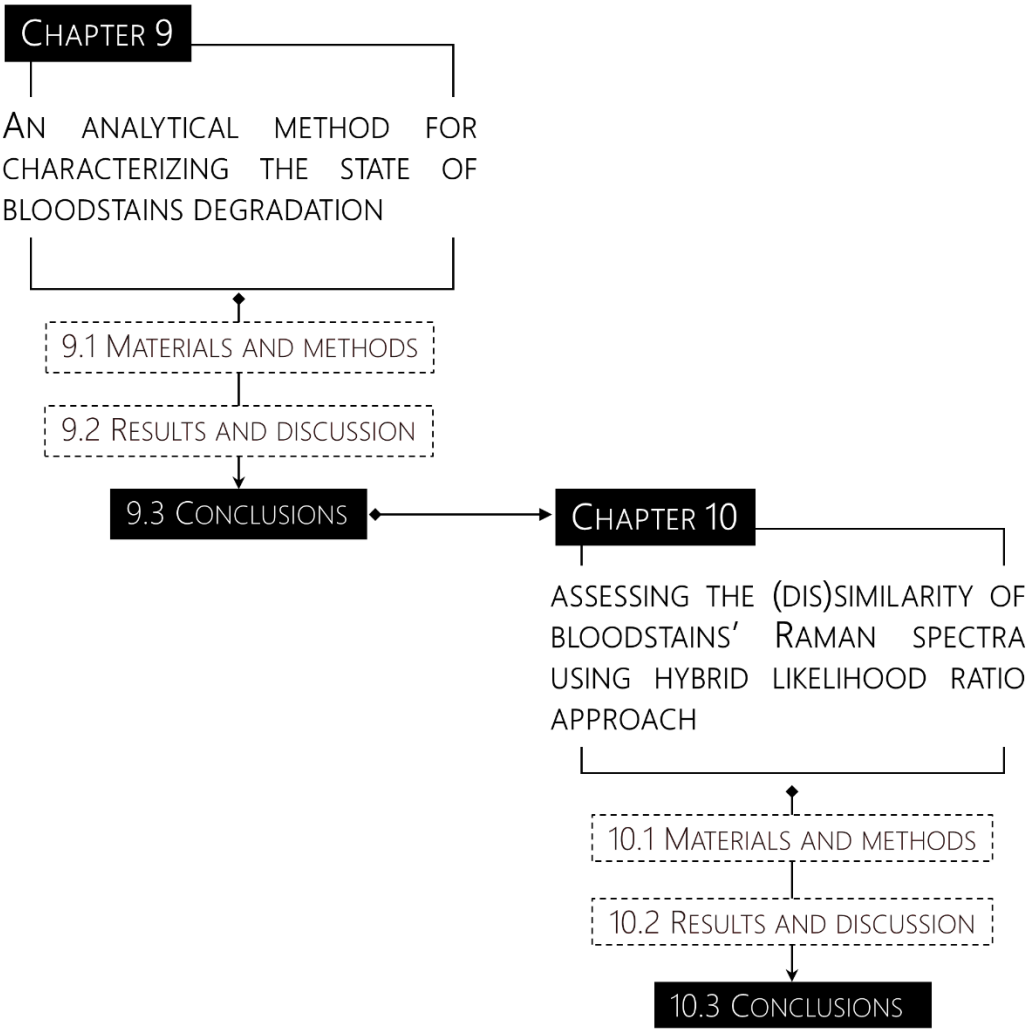

FIGURE 8.1.

An outline of the thesis's experimental part.

| *CHAPTER 9*

AN ANALYTICAL METHOD FOR CHARACTERIZING THE STATE OF BLOODSTAINS DEGRADATION

Vibrational features of hemoproteins (especially hemoglobin), discussed in *Chapter 5,* seemed a reasonable amount of information to form a hypothesis about the efficacy of Raman spectroscopy (RS) in characterizing different Hb derivatives formed in degrading bloodstains. This, in turn, held a promise for adapting it to the present age estimation studies. However, the hypothesis about representing the time-dependent bloodstains' behavior in Raman spectra has already been proposed by Boyd and co-workers [224] and confirmed later by independent studies [38, 141, 177]. In other words, it quickly turned out that implementing RS in dating approaches *per se* was not an essential novelty from an analytical point of view. Fortunately, the development of such a procedure was not the main focus of the present research but only a necessary step towards achieving the assumed goal, namely establishing the novel dating approach.

Nevertheless, despite its relatively wide application, the standard way of proceeding when using Raman-based methods for dating purposes still exhibits some challenges that may hamper its application in forensic practice. One of these difficulties results from representative probing of the chemical composition of aging bloodstains in the shortest possible time. A conventional procedure is to carry out such an analysis by acquiring a few single-point measurements within different areas of the degrading trace [38, 141, 177]. However, dried deposits of body fluids are highly heterogeneous, both in terms of their physical and chemical characteristics. Thus, this sampling mode is highly probable to produce spectra of poor reproducibility (especially at the initial stage of degradation) and, in the long term, result in misestimations of TSD. Consequently, an analytical procedure itself is still in need of some improvements.

Given the above, the first part of the research intended to expand the current Raman-based approaches primarily by reducing the risk of subsampling errors. In order to do so, the rotating measurement mode that involved spinning the bloodstain sample during the spectral acquisition utilizing a magnetic-driven sample-holder [328, 329] was established and subsequently employed for characterizing the behavior of bloodstains during the three-week degradation period.

9.1 Materials and methods

9.1.1 Samples preparation

The main aim of this phase of the research was a verification of Raman's feasibility to monitor the variability in spectral responses, which arises solely from the blood degradation processes. Therefore,

to mitigate the possible influence of inter-individual factors such as health condition, diet, medication intake, or age on the initial composition of blood, which contribute to the spectra' variability, and associated aging kinetics, the analysis was carried out on blood drawn from a single donor. Twenty µL aliquots of capillary blood, obtained by finger puncture, were transferred into aluminum sample pans (Figure 9.1) – yielding an almost featureless background that did not interfere with Raman scattering – and then allowed to dry for two hours before spectrum collection. All analyzed blood samples were preservatives- and anticoagulants-free to imitate the potential evidence as closely as possible. The first drop of blood was always discarded because of cell debris and tissue fluid at the puncture site.

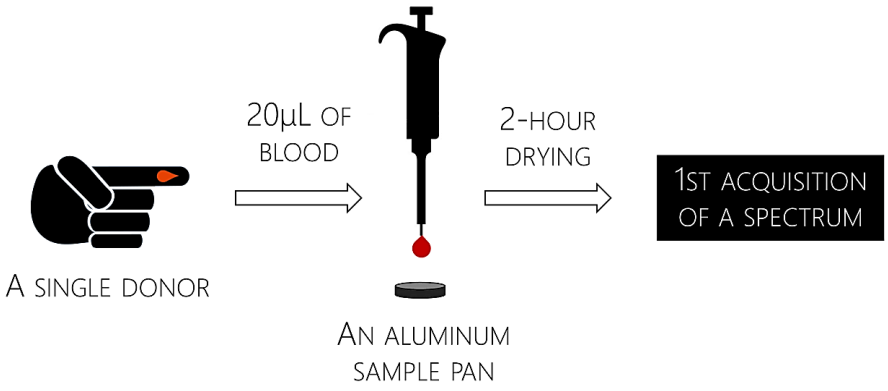

FIGURE 9.1.
A scheme of the sample preparation procedure.

Within the first part of the study, discussed in this chapter, two classes of bloodstains were used. The first class was used for performing experiments designed for choosing the setup of spectral acquisition. It consisted of four groups of six bloodstains, each of which served to test different laser power levels (see *9.1.2 Raman instrumentation and sample presentation*). The second class of bloodstains, namely the population of samples used for monitoring the trace degradation, comprised two separate sets with six bloodstains, each created for rotating and static measurement modes, respectively. It also should be highlighted that due to the continuous transformation of bloodstains, exceptionally dynamic at the initial degradation, repeated acquisitions of spectra carried out consecutively on the same specimen might have produced Raman signatures characterizing bloodstains of slightly different age. Therefore, to perform repeated measurements of blood traces corresponding to the same age, each of the six samples mentioned above was created at time intervals (10 minutes for the rotating and 20 minutes for the static mode) estimated with regard to the duration of spectral acquisition beforehand. Consequently, they should be treated as repeated measurements of blood traces corresponding to the same time since deposition (TSD) rather than separate bloodstain samples.

Finally, bloodstains employed for dating purposes (the second class) were stored, protected from any light sources, for three weeks under laboratory conditions (temperature: 23.6 ± 2.0 °C, relative humidity: 30 ± 4%).

9.1.2 Raman instrumentation and sample presentation

All of the spectral measurements presented in this dissertation were possible through the courtesy of *Università degli Studi di Torino*, which made its facilities available for the sake of this research project. The measurements have been performed exploiting a Renishaw *inVia Raman Microscope* spectrometer, equipped with a CCD detector, a 5× objective (with the NA value of 0.1), and a 785-nm laser line (Figure 9.2 A). All of the spectra were registered in the range 300–1800 cm^{-1}, which was chosen based strictly on previously reported Hb's spectral features.

(A)

(B)

FIGURE 9.2.

A Renishaw *inVia Raman Microscope* spectrometer utilized for conducting analyses in the Interdepartmental Center *Nanostructured surfaces and interfaces* (NIS), Università di Torino (A); a modified sample's stage with an element providing an external magnetic field (B). Photographs were taken by Alessandro Damin (Department of Chemistry, NIS Interdepartmental Centre, Università di Torino).

Investigation of subtle spectral changes without damaging the sample often requires an unconventional measurement setting. When dealing with a specimen of an exceptional vulnerability to laser irradiation – just like Hb [24, 177, 235] – a smart-and-simple strategy is to exploit the sample movement that reduces the laser-induced damages while increasing the representativeness of measurements. Several examples of such solutions have already been reported in the literature [330–333], and a similar technology, called herein the ROTATING MEASUREMENT MODE, was implemented during the present thesis.

The concept of the used device, designed by [329] and presented in Figure 9.3, is pretty straightforward: the analyzed material is attached to the specially constructed holder, and the measurement is performed during its rotation. The mechanical force needed to set the sample in a rotary motion is provided due to a standard magnetic stirrer, i.e., applying an external rotating magnetic field. As shown in Figure 9.3, a permanent magnet is built in the sample holder, which by aligning to the applied field, forces the sample movement. Concerning previous examples [332, 333], the unquestionable benefit of this configuration is that all large mechanical parts are positioned away from the sample holder. What is more, the motion is transmitted in a contactless way, and hence, the sample holder can be placed in closed containers whilst still being movable.

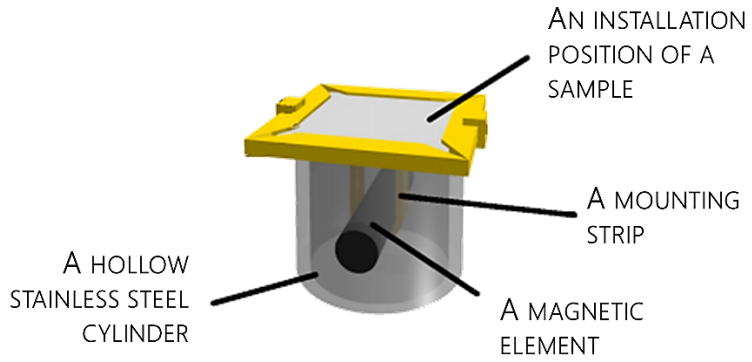

FIGURE 9.3.

A scheme of the rotating sample holder and its main components (graphics modified from [328]).

The body of the sample holder constitutes a hollow stainless steel cylinder that contains the magnetic element (AlNiCo-5 bar) mounted inside of it. The choice of this particular magnetic alloy was dictated by its high Curie temperature (above 800 °C), which enables high-temperature treatment without losing the magnetization and its magnetic coercivity (about 50 kA m^{-1}). The sample is integrated with the sample holder – it is installed on the upper part of the cylinder – and thus, when the latter rotates due to the external magnetic field, the former is set in motion. It is also worth adding that the sample holder has been designed to enable a certain degree of miniaturization – it can be built with a diameter lower than 1 cm. This patent-granted setup [329] has already been successfully applied in some studies, which required fast and reliable Raman measurements, also with the UV-excitation [334–336].

Nonetheless, bearing in mind that introducing the magnetic-driven rotation of the sample might be, in fact, an unnecessary effort, the rotating mode has been confronted with the standard single-point measurements, referred to later on as a STATIC MODE. To establish parameters allowing for non-invasive spectral acquisition, both for the rotating and static measurement modes, applied later on during the aging studies, a spectral indicator of bloodstain degradation has been defined. The role of this indicator has been fulfilled by the ratio between the band at 1227 cm^{-1} and one of the previously identified Hb aggregation markers [24, 235] – a spectral feature at 1248 cm^{-1}. The 1227/1248 ratio was monitored for four groups of bloodstains, created independently for the static and rotating measurements (as described in *9.1.1 Samples preparation*). Each of these groups was analyzed with the increasing power of the excitation source to verify whether, upon increasing the power, any of the monitored ratios significantly decreased, which would be indicative of laser-induced detrimental effects. The laser beam was focused to a diameter ~72 μm^2 and its power equalled to 0.6 mW ($7.98 \cdot 10^{-3}$ mW/μm^2), 1.2 mW (0.02 mW/μm^2), 5.8 mW (0.08 mW/ μm^2) and 11.5 mW (0.16 mW/μm^2) measured at the sample, which corresponded to 0.5%, 1%, 5% and 10% of the initial power of excitation source (~103 mW on the sample), respectively. Throughout this power test, the exposure time and the number of accumulations were adapted separately for each excitation power to maintain the comparable number of counts, thereby providing Raman spectra of a similar signal-to-noise ratio.

9.1.3 Tracking time-dependent changes in bloodstains composition

Subsequently, to monitor the time-dependent behavior of blood traces, Raman spectra of samples were recorded every two hours (from two up to eight hours elapsed since bloodstain formation) and then once per day for three weeks (excluding the weekends). All measurements were performed using both measurement modes.

9.1.4 Signals pre-processing

Before proceeding to any forms of signal pre-processing, the original spectra were truncated to omit the range 300–600 cm^{-1}, which was severely affected by the noise and increasing baseline. Consequently, each spectrum covered the range 600–1800 cm^{-1}, which included crucial Raman bands connected to the spectral features assigned to analytes of interest (Hb and its derivatives).

SPECTRAL AXIS ALIGNMENT AND COSMIC RAYS ELIMINATION

As spectra of the same bloodstains have been recorded over several days, it was virtually impossible to precisely calibrate the Raman instrument to obtain an equally spaced Raman shift axis, which is an essential requirement for interpreting the spectra similarity using various statistical or chemometric methods. Therefore, before applying any pre-processing methods, Raman spectra had to be aligned to

a common axis so that they represent the signal intensities recorded for equally spaced Raman shift points, which is consistent between profiles. This problem was sorted out using spline functions with cubic polynomials [337], which allowed interpolating the signal and finding the intensities for the new set of equally spaced points. Apart from spectral alignment, Raman spectra should also be corrected for Cosmic rays, which are generated when high-energy particles pass through the CCD detector, generating many electrons interpreted as a signal. These appear as totally random, very sharp emission lines, usually affecting only one pixel at a time. To remove these features from spectra, the *Cosmic Ray Remover* option in Renishaw's WiRE™ software was activated during spectra registration. The median filtering option implies the acquisition of two additional accumulations for each desired spectrum. Subsequently, for each Raman frequency, the median of the three values is taken. This procedure allows for automatic rejection of all shapes and sizes of cosmic rays as they will always be an extreme value rather than the median.

Background correction

Various phenomena, like fluorescence, discussed briefly in the previous chapters of the theoretical part, induce uneven amplitude shifts across different wavenumbers. This effect has to be compensated prior to proceeding with further data analysis. As already mentioned, many such techniques are at the disposal of researchers. One of those approaches, namely an adaptive iteratively reweighted penalized least squares (airPLS) fitting procedure (introduced by Zhang et al. [305]), was employed in the first part of the study to mitigate the effect of fluorescence, which quite severely affected bloodstains' Raman signatures (especially at an advanced stage of degradation). In this technique, no user intervention (e.g., band detection) is required, and the baseline itself is gradually approximated by the weighted penalized least squares method. Weighting is provided to the sum of squared differences between the original spectrum and the estimated baseline to eliminate the bands and focus only on baseline points during the approximation procedure.

Smoothing

Baseline removal eliminates the effects of broad bands or low-frequency components present in the Raman spectra. However, the high-frequency part of the Raman signal, which typically has much lower FWHM (full width half maximum) compared with genuine Raman bands, also needs to be eliminated. What is more, the performance of baseline correction methods might be negatively affected by noise factors. Therefore, smoothing should be employed before baseline removal, and precisely this was the approach that was followed in this study. Before the airPLS procedure, the Savitzky-Golay filtering with the polynomial of the third degree – using 21-point and 17-point windows in case of the static and rotating modes, respectively – was implemented, followed by the logarithmic transformation and mean-centering, aimed at ensuring the homogeneity of data variance.

NORMALIZATION

Finally, to alleviate unwanted inter-spectra distortions and reveal the actual temporal behavior of Raman features, the smoothed and background-corrected Raman spectra were subjected to the probabilistic quotient normalization (PQN) [314]. During this procedure, the normalization factor for each spectrum was indicated as a median of quotients, which were obtained by dividing the acquired spectrum by a reference (the median signal).

The final effect of signals pre-processing is presented in Figures 9.4 and 9.5 for the static and rotating measurement modes.

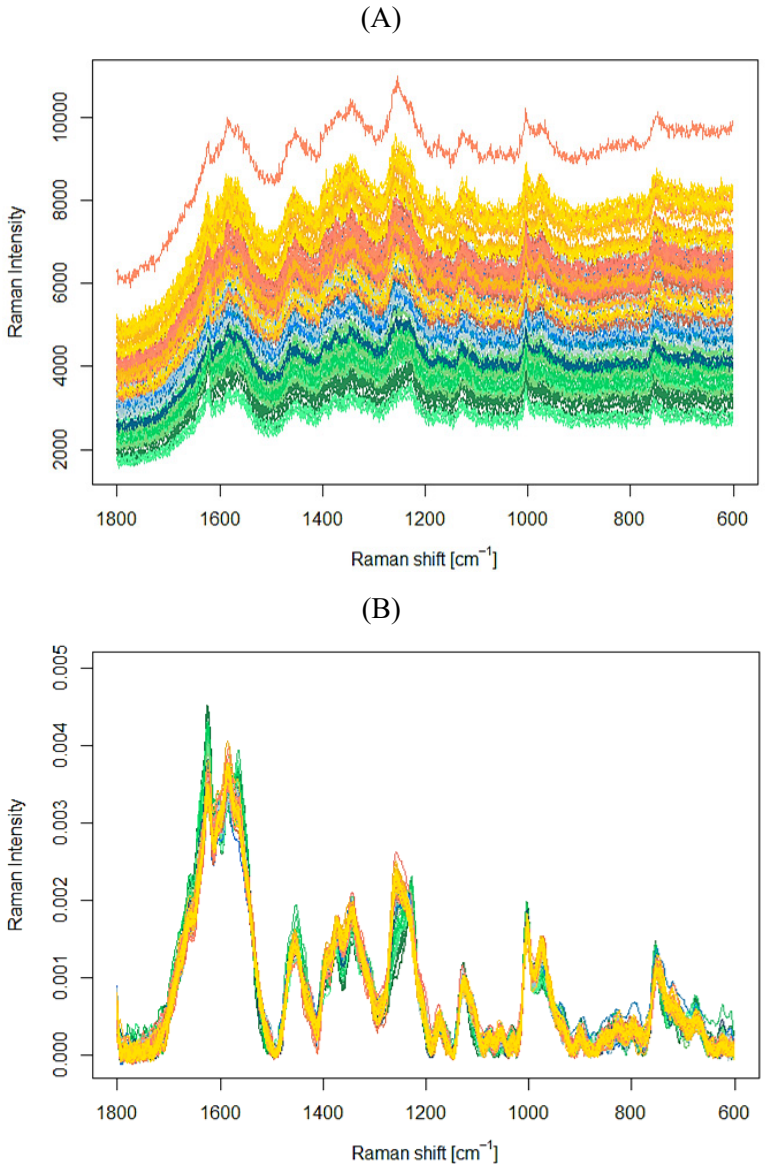

FIGURE 9.4.

Raman spectra of degrading bloodstains registered in static mode before (A) and after pre-processing (B). Spectra depicted with the same color represent bloodstains of the same age.

(A)

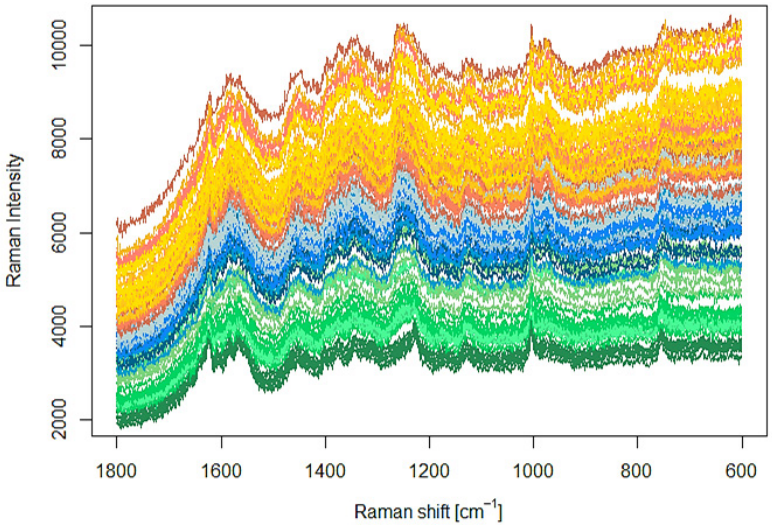

(B)

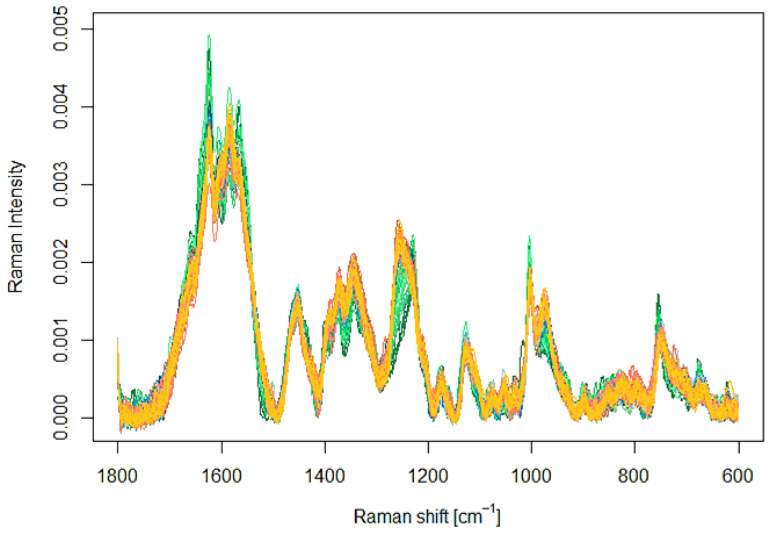

FIGURE 9.5.

Raman spectra of degrading bloodstains registered in rotating mode before (A) and after pre-processing (B). Spectra depicted with the same color represent bloodstains of the same age.

In the light of the previous discussion regarding the optimization of the spectral pre-processing using genetic algorithms (*7.1. Signal pre-processing*), it must be made clear that the choice of the pre-processing strategy applied herein was based on the thorough visual inspection of corrected signals. However, this subjective way of proceeding was implemented solely in the present part of the study, in which the considered issue was a development of a Raman-based procedure for characterizing aging bloodstains, and above all, the choice between the static and rotating measurement modes. The problem of optimizing the spectral pre-processing was the subject of further work (*Chapter 10*), where the discrimination between differently-aged bloodstains was attempted; and hence the proper preparation of spectral signatures, serving as a basis for this discrimination, was of utmost importance.

9.1.5 Comparison between the static and rotating sampling modes using rMANOVA

The prerequisite for any successful discrimination of samples is that the variance between groups' averages is much higher than the average variance of the replicate measurements within each group. If this requirement is not met, distributions of variables characterizing the compared groups will overlap, preventing effective discrimination. That also applies to LR models designed to distinguish between bloodstains characterized by different deposition times.

Several tools are suited for studying highly correlated multivariate data sets among variance analysis methods offered by chemometrics. One of them is a regularized multivariate analysis of variance (rMANOVA), which – unlike its prototype (MANOVA) – is suitable for data populations containing more variables than samples [326]. The main goal of this method is to define new directions (eigenvectors) that boost the between-group variance (denoted as **B**) while minimizing the within-group variance (denoted as **W**).

Within the present study, a single group consisted of Raman signatures registered for bloodstains of the same age (characterized by the same TSD values). Hence the variation within measurements of equally-aged blood traces equaled to the within-group variance **W**. The between-group variance **B**, in turn, corresponded to the variation of the averages of blood traces deposited at different times. To assess the ability of both measurement modes to produce data that allowed for effective discrimination of bloodstains in terms of the time of their formation, and by doing so to verify which of those two methods (static or rotating measurement modes) should be implemented in future LR-based dating procedure, rMANOVA was employed to compare the variance structure of registered Raman spectra. Considering that for univariate data, all matrices are substituted by scalars (e.g., **W** becomes w^2), the b^2 to w^2 ratio was investigated on the first eigenvector (first canonical variate, CV1), which is the pursued direction maximizing the b^2/w^2.

What is more, in order to initially investigate the changes in the performance of both modes with the passage of time, static and rotating datasets comprising spectra registered over the entire degradation period (three weeks) were divided into three subgroups, corresponding to spectra acquired within the first seven, 14, and 21 days of aging. For each of these subgroups, the b^2/w^2 ratios were calculated.

All the mathematical background of the research was carried out in R software [338] using home-written scripts authored by A. Martyna and available R packages (version 3.3.1).

9.2 Results and discussion

9.2.1 A selection of Raman spectra acquisition setup

In Raman spectroscopy studies, laser excitation choice is one of the most important considerations. The chosen wavelength impacts Raman intensity, spatial resolution, background fluorescence, and also acquisition time. Different wavelength regions offer numerous advantages and disadvantages; hence the final laser selection is primarily dictated by the sample under investigation. With all the influencing aspects taken into account (*5.1.2.1 Laser*), the most commonly used wavelength in Raman spectroscopy is perhaps 785 nm. This is because it often offers the best equilibrium between scattering efficiency, fluorescence interference, and detector efficiency. In the case of the present study, the motivation for choosing the 785 nm excitation was threefold. First of all, according to the previous studies of Lemler's group [177] and Sato et al. [202], the Raman spectrum of whole blood acquired with 785 nm laser line encapsulate information solely about the main component of degrading bloodstains, namely Hb protein and its derivatives. Secondly, the excitation wavelength distant from the electronic absorption region of blood fluorescent components should allow to avoid overlapping the informative Raman scattering with the photoluminescence phenomenon. Finally, and most importantly, the primary focus was to ensure that the process of spectral acquisition did not interfere in the state of Hb, which has been already reported as a molecule highly prone to photodegradation [177, 218, 235]. Therefore, it was advisable to excite the sample using the laser source away from the range of electronic transitions of Hb derivatives, including weak Q-band (α and β) between 490 and 650 nm, and the most intense Soret band in the region of 400–436 nm [23, 24]. By this operation, the risk of the increased absorption of the electromagnetic radiation by the sample and its consequent heating, which might result in the formation of undesirable laser-induced heme aggregation products [218, 235], has been considerably alleviated.

Nevertheless, suppose the power of laser irradiation would be too high. In that case, the precautions mentioned above against laser-triggered degradation of blood samples will not be sufficient to prevent the photoinduced changes, which can appear within the nominally non-resonant region of Hb [177, 235]. An example of such an undesired effect was presented in Figure 9.6 using Raman spectra registered in a static mode at two different laser power levels (0.5% and 10%)[§§§§]. As can be easily seen, spectral symptoms attributed to the laser-triggered degradation are present even when measurements are conducted with the 785 nm excitation. The sudden change of spectral features, especially within the 1200–1300 cm^{-1}, can be readily indicated for signal characterizing static bloodstains registered with 0.16 $mW/\mu m^2$ (10% of initial laser power). The Raman signature of photodegraded bloodstain consists of increased background counts (which obviously cannot be observed in Figure 9.6 due to the implemented

[§§§§] For ease of visualization, Figure 9.6 compares just two extreme laser powers, 0.5%, and 10%. Description of all tested laser's parameters can be found on the following pages and figures.

background correction) and broader bands in comparison to that registered with a lower level of laser power, namely $7.98 \cdot 10^{-3}$ mW/μm^2 (0.5% of initial laser power). Moreover, alterations in the relative intensity of several spectral components occurred. In this respect, the increase of spectral features at 1366 cm^{-1}, 1248 cm^{-1}, and 974 cm^{-1} seems particularly interesting. Considering the structure of Hb, a few possible hypotheses regarding the mechanism behind laser-induced degradation have been suggested.

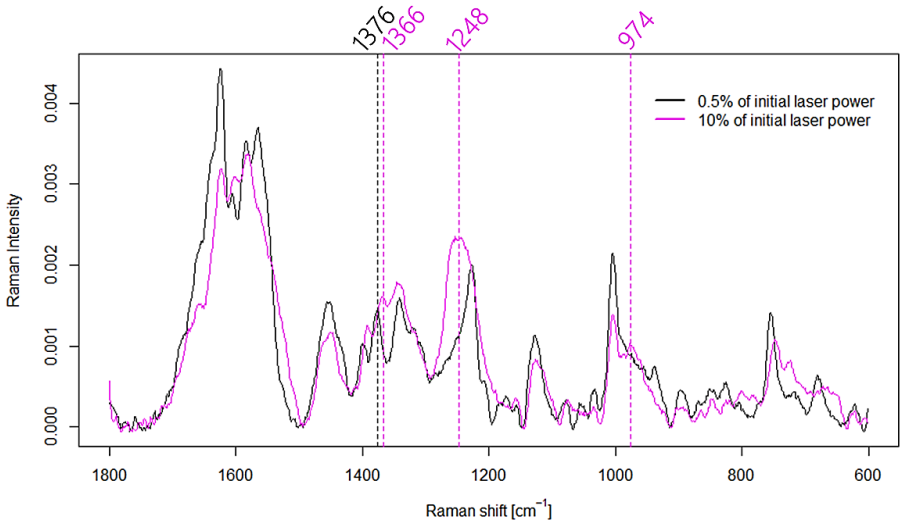

FIGURE 9.6.

Laser-induced changes in Raman spectra of 2-hour blood traces registered with 785 nm excitation laser in a static mode. Bands indicated in black and magenta correspond to spectra recorded with 0.5% and 10% of initial laser power, respectively. Signals were processed according to the procedure outlined in *9.1.4 Signals pre-processing.*

In the study of Black et al. [339, 340], who investigated chemical changes in blood undergoing laser photocoagulation, it has been suggested that the oxygen (initially present in the oxyHb, see Figure 4.4), became irreversibly chemically bound in Fe^{3+} metHb complexes. This conclusion was based on the grounds that no free oxygen was released from the blood samples. Ramser et al. [218] presented similar reasoning, suggesting the formation of metHb as the final step of the photoinduced changes. Firstly, however, heat transfer calculations in red blood cells (RBCs) were conducted to verify whether the observed spectral changes could have resulted from light absorption-triggered thermal processes. An estimated increase of the temperature at the laser focus equaled ~2.3 °C (for initial laser power 0.7 mW); thus – according to these calculations – the actual cell temperature remained well below physiological conditions (~37 °C). Consequently, thermal degradation of RBCs was excluded as an explanation of changes observed in spectra features. However, Ramser's computations considered the water as a main absorbing component of blood and, at the same time, entirely underestimated the contribution of Hb. It should be remembered that the absorption coefficient of Hb, highly concentrated in dried bloodstains, is much higher than that of water.

Unfortunately, the above conclusions concerning the formation of metHb complexes cannot be fully resolved based on our observations. As shown in Figure 9.6, the spectrum recorded at a lower laser power (indicated in black) is characterized by the position of the band ν_4 at 1376 cm^{-1}. The ν_4 mode, assigned to the half-ring stretching vibration, is described as a vibration that stretches the entire ring of the protoporphyrin IX; therefore, it is often referred to as the ring's "breathing" motions. Most importantly, however, it should be reminded that this particular band is considered to be characteristic of the oxidation state of the iron atom embedded in the heme moiety. In the case of Hb complexes containing a Fe^{2+} cation (e.g., deoxyHb), the ν_4 band is located at the lower values of Raman shift (ca. 1360 cm^{-1}), while in complexes with the Fe^{3+} cation (e.g., oxyHb), it is shifted to higher values (ca. 1376 cm^{-1}). Therefore, the spectral feature at 1376 cm^{-1} in the Raman signature of the bloodstain registered using lower laser power, presented in Figure 9.6, indicates the presence of Fe^{3+} ions (and through that possible occurrence of oxyHb, which is expected to be a dominating Hb's species in a freshly formed blood trace). With increasing laser power (a Raman spectrum plotted in magenta), the band characteristic of the oxidation state shifts from position 1376 cm^{-1} to 1366 cm^{-1}, most likely due to a gradual change in the oxidation state of the iron ion ($Fe^{3+} \rightarrow Fe^{2+}$). This observation, in turn, supports the hypothesis that the laser-induced degradation mechanism leads to the dissociation of oxygen from oxyHb as described in [153], giving rise to partially deoxygenated Hb Fe^{2+}/Fe^{3+} (Figure 4.4). At the same time, the conclusions presented by Black et al. [339, 340] and Ramser et al. [218] about the formation of metHb cannot be entirely excluded, as its ν_4 vibration falls somewhere between 1376 cm^{-1} (Fe^{3+}) and 1360 cm^{-1} (Fe^{2+}). In this case, observation of the stretching bands assigned to $\nu(Fe{-}O_2)$ at ~ 571 cm^{-1}, characteristic for oxyHb, and $\nu(Fe{-}OH_2)$, emerging in the Raman spectra metHb at ~ 508 cm^{-1}, would help dispel doubts. Unfortunately, as already mentioned, in this study, the spectral region below 600 cm^{-1} was highly distorted due to increased baseline, which made it impossible to infer from $\nu(Fe{-}O_2)$ and $\nu(Fe{-}OH_2)$ modes. It should also be added that in the case of the present study, where the spectra were recorded with the 785 nm laser, the precise observation of ν_4 vibrations was difficult because of their relatively low intensities. In order to obtain a strong resonant enhancement of the symmetric A_{1g} mode (which includes ν_4 vibrations), a laser line near the Soret band should be used, for example, 488 nm[*****].

Given these between-studies inaccuracies, the hypothesis about the potential mechanism behind the laser-triggered degradation should be reverified again, possibly by resorting to the previous findings of the Monash group [185, 223]. This time, the increased intensities of bands at 972 cm^{-1}, 1248 cm^{-1}, and 1366 cm^{-1}, observable also in the "damaged" bloodstain's spectrum in Figure 9.6, were attributed to the formation of Hb aggregates stemming from photoinduced Hb denaturation. The enhanced background, in turn, was interpreted as a result of the migration of energy, in the form of an exciton,

[*****] Perhaps it should be added that at the beginning of the present study, initial screening of different laser lines and resultant Raman spectra of bloodstains has been performed. This pilot study has revealed a strong fluorescence overlapping signals registered with Vis excitation sources. As a consquence, employment of the laser lines such as 488 nm has been discarded.

throughout the closely packed protoporphyrin moieties in aggregated heme structures [185, 223]. Since these spectral characteristics were also consistent symptoms of laser-induced degradation observed in the present study, it might be reasonable to postulate the possible involvement of protein denaturation in laser-triggered degradation of bloodstains.

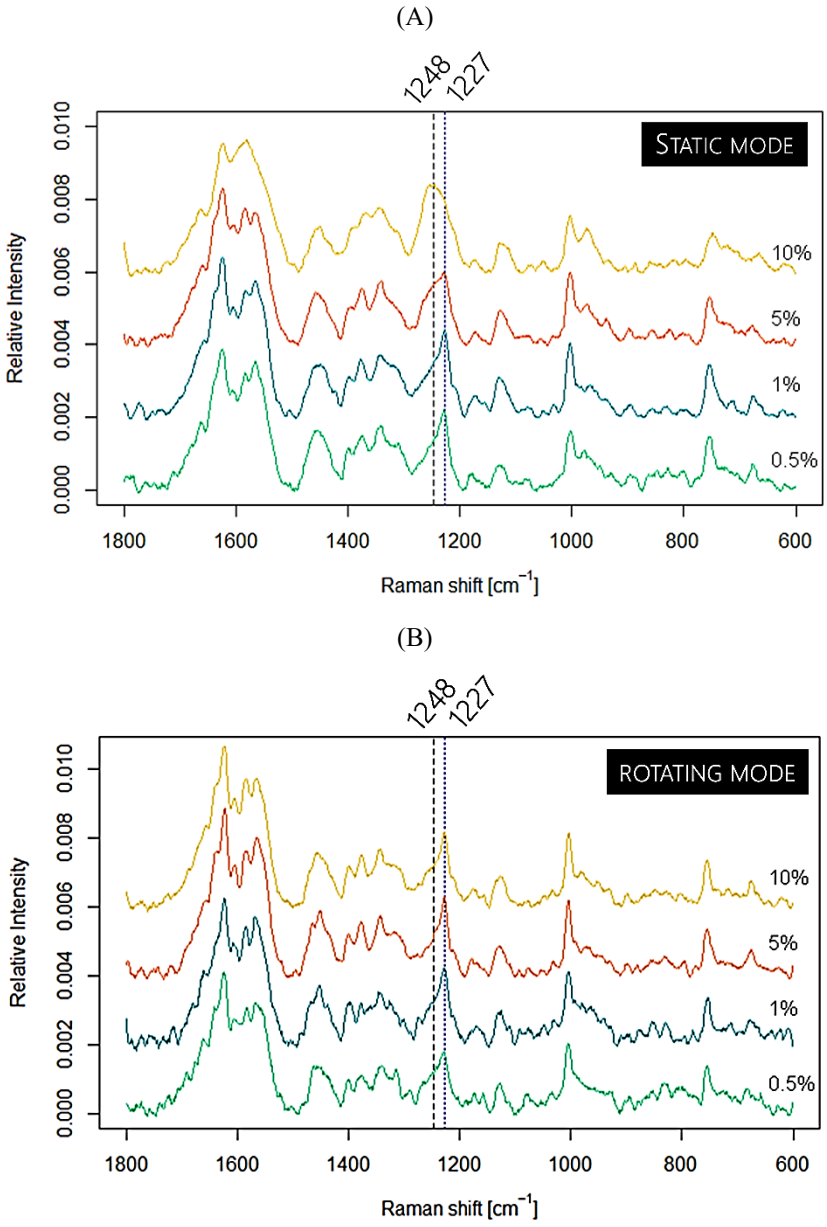

FIGURE 9.7.

Influence of the laser power on Raman spectra of 2-hour blood traces registered with 785 nm excitation laser in the static (A) and rotating mode (B). The ratio between the intensity of the heme aggregation marker at 1248 cm^{-1} (dashed line) and a non-altering band at 1227 cm^{-1} (dotted line) served as an indicator of Hb photodegradation while deciding on non-invasive measurement parameters. Signals were processed according to the procedure outlined in *9.1.4 Signals pre-processing* and shifted for better visualization.

It should also be emphasized that registered Raman signals do not allow unambiguously identifying which degradation products dominate the composition of photo-damaged bloodstains. It rather indicates the trends in the populations of Fe^{2+} and Fe^{3+}. Consequently, the exact mechanism behind laser-induced degradation is only hypothesized and needs to be examined further.

To get a (more) complete picture, it should be beneficial to facilitate the reasoning process with other analytical techniques, which are well-recognized techniques capable of characterizing the Hb derivatives (e.g., UV–Vis spectroscopy). Nonetheless, there are few cast-iron certainties among all of those questions, and one of them is that care must be taken to prevent the photoinduced chemistry of Hb.

Before proceeding, it also should be reiterated that the study presented in this dissertation was never intended to investigate the laser-induced degradation of blood but to develop a non-invasive Raman-based procedure for bloodstains dating. Therefore, it was not attempted to explain these laser-triggered mechanisms at all costs[†††††], just to minimize the laser exposure. This is why greater emphasis was given to selecting appropriate – in other words, non-interfering with Hb structure – measurement conditions, as already described in *9.1.2 Raman instrumentation and sample presentation*. *Ad rem*, the decision on non-invasive spectral acquisition parameters was adopted based on information encoded in the signal at 1248 cm^{-1}, serving as a marker of laser-induced degradation. The changing characteristics of this band with increasing laser powers can be observed in Figure 9.7 for the static (A) spectra, contrary to the signals acquired with the rotating (B) measurement mode. Besides the evident power-dependent behavior of the 1248 cm^{-1} band, the choice of this particular degradation indicator was also justified by the chemistry underlying its occurrence. In recent studies of Lednev's group [38, 141], this spectral feature was assigned to the frequency of amide III band – interpreted as indicative of random coil conformation of Hb protein. That interpretation resulted in the conclusion that the process of Hb denaturation preceded aggregation. And indeed, the region of amide III vibration, as already discussed in *5.1.3.1 Vibrations related to the secondary structure of proteins*, serves as a sensitive peptide conformation probe. Its occurrence depends on the secondary structure, and it has been defined within 1260–1310 cm^{-1}, 1235–1242 cm^{-1}, and 1240–1250 cm^{-1} for α-helix, β-sheet, and random coil structure, respectively [197, 233, 234]. Therefore, it is not surprising to interpret the band at ~1248 cm^{-1} as the amide III mode. This reasoning, however, most likely is a misguided attempt since the protein spectral features are not always observed in the Raman signatures of RBCs or whole blood. Why is that? It is well known that the obtained spectrum is the superimposition of all vibrationally active constituents. However, specific Raman intensities may be significantly enhanced in some cases – depending on the applied excitation source – due to the resonance Raman effect mentioned repeatedly. It should be borne in mind that because of the resonant enhancement of hemoporphyrin modes, the bands originating from proteins do not appear in the spectra recorded at 488, 514, 568, and 633 nm, contrary to the signals

[†††††] However, it does not mean that this question does not keep the author awake at night.

registered with 1064 nm lasers that give insight into the secondary structure of proteins [341]. And in fact, the assignment of the ~1248 cm^{-1} band proposed by Doty et al. [38, 141] was based on the spectral characteristics of proteins acquired with 1064 nm [197] and not a 785-nm laser, which authors employed during the dating studies of bloodstains [38, 141]. Comparing to the NIR (1064 nm) laser source, the situation is somewhat different in the case of 785-nm excitation, where a few proteinaceous bands appear, such as the amide I (1650 cm^{-1}), the CH_2/CH_3 deformation modes originating from the amino acid side chains at 1446 cm^{-1}, and the phenylalanine band at 1003 cm^{-1}. However, the whole spectral range between 1200 and 1300 cm^{-1} – and thus also the 1248 cm^{-1} degradation marker – which indeed overlays with the region of amide III modes, have also been assigned to the C_m–H methine vibrations within protoporphyrin IX moiety of heme [177, 184, 185, 223, 231], which are of B_{1g} and E_u symmetry type. As demonstrated in the study of Wood et al. [223], these bands are strongly enhanced – along with A_{1g}, A_{2g}, B_{2g}, and vinyl modes (see Table 5.4) – once the Raman signal is acquired using 785-nm laser excitation. Since the enhancement mechanism within heme groups has a more significant impact on the Raman spectrum than the contribution of protein bands such as amide III, hence in this case (and also in the case of Lednev's group studies [38, 141]), the spectral feature observed at ~1248 cm^{-1} is associated with the C_m–H in-plane vibrations of methine hydrogen in porphyrin macrocycle.

Given the above, the employment of the 1248 cm^{-1} band as a sensitive molecular probe of Hb perturbations in response to the laser power seemed a perfectly reasonable choice. After all, it cannot be denied that heme stacking and protein interactions occurring during its degradation may influence the C_m–H methine vibrations within the protoporphyrin structure. Investigation of spectra registered in the static mode (Figure 9.7A), and in particular the 1248 cm^{-1} band, reveals that if one aims at obtaining good-quality Raman signatures while avoiding the photo-damage of Hb, low excitation power combined with long acquisition times should be preferred over high power coupled with short acquisitions. Precisely for this reason, applying conventional static mode, when monitoring the time-dependent behavior of heterogeneous materials might pose some technical difficulties. And that is because providing a representative Raman signature, which in the case of single-point measurements can only be obtained by performing multiple measurements across the sample, is hardly possible within a short time. Fortunately, the problem of laser power and interconnected time resolution can be alleviated using a relatively simple solution applied herein – the implementation of rotating measurement mode [328, 329]. Since the irradiated point of the rotating bloodstain is constantly refreshed, the excitation energy is distributed over a larger area. As a consequence, the risk of sample damaging can be significantly reduced. And indeed, the visual examination of Raman spectra registered for rotating bloodstains (Figure 9.7B) revealed that, contrary to static measurements, even the signals acquired with 10% of initial laser power (0.16 $mW/\mu m^2$) were deprived of spectral features typical of decomposed bloodstains.

(A)

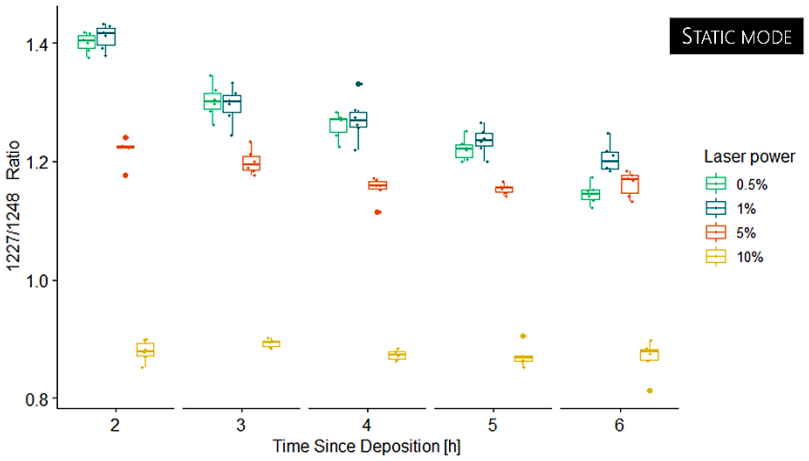

(B)

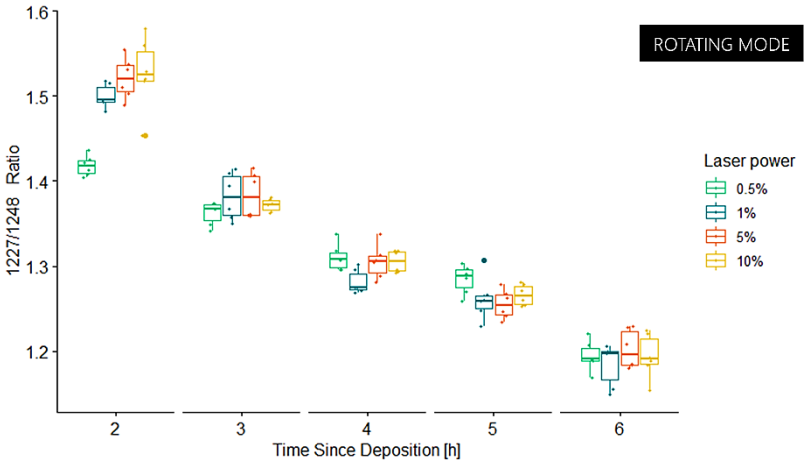

FIGURE 9.8.

Boxplots depicting the distribution of intensity ratios between peaks located at 1227 cm^{-1} and 1248 cm^{-1}, serving as markers of Hb photo-damage, observed for Raman spectra of bloodstains registered using different levels of laser power – $7.98 \cdot 10^{-3}$ $mW/\mu m^2$, 0.02 $mW/\mu m^2$, 0.08 $mW/\mu m^2$ and 0.16 $mW/\mu m^2$ corresponding to 0.5%, 1%, 5%, 10% of initial power – in the (A) static and (B) rotating measurement mode.

The difference in the trends, qualitatively determined by direct inspection of sets of data as those in the panels of Figure 9.7, were fully confirmed by calculating the ratio between the band at 1227 cm^{-1} and the aforementioned modification marker at 1248 cm^{-1} for all sets of measurements. The results of these calculations are depicted as ratios distribution (boxplots) presented in Figure 9.8. Therefore, the signal acquisition in the static mode was eventually performed using ten 20-s accumulations with 1% (0.02 $mW/\mu m^2$). In the rotating mode – two 20-s accumulations with 10% of initial excitation laser power (0.16 $mW/\mu m^2$) were employed (see Figure 9.9). Both of these setups allowed to reduce to a minimum duration of spectral acquisition while mitigating the detrimental influence of the laser.

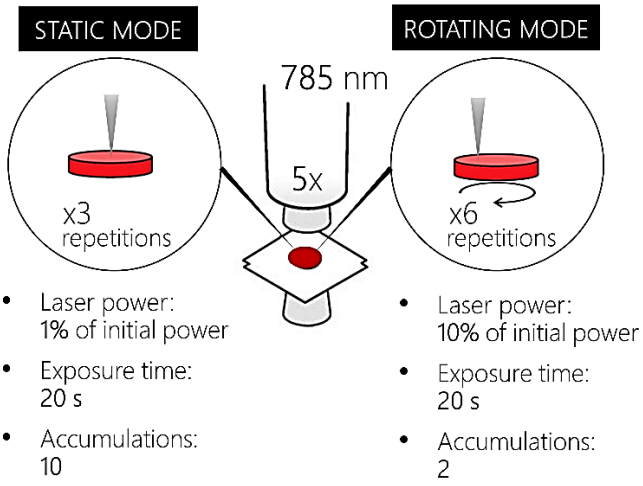

FIGURE 9.9.

Acquisition parameters of Raman spectra applied for the static and rotating modes of measurement.

9.2.2 A time-dependency of bloodstains Raman signals – a visual inspection

Once the parameters of static and rotating sampling methods have been decided, the research entered the key phase, which was solely focused on tracking the aging transformations of blood traces considered on the spectral level. Immediately noticeable among obtained Raman signals, the most profound degradation symptom was a baseline intensity increasing with bloodstains age (Figures 9.4A and 9.5A). Unfortunately, the root cause of this phenomenon as yet has not been fully explained, and – as it usually happens with complex biomolecular systems – there are several possible interpretations for the observed substantial background.

As already demonstrated, oxyhemoglobin (oxyHb) – or rather heme embedded within its structure – could not have been blamed for observed fluorescence [342]. Even though porphyrins (and thus also a precursor of heme – protoporphyrin IX) show fluorescence when excited with the NIR source, the iron ions bound to the tetrapyrrole ring significantly quench this emission [24]. As a consequence, fresh whole blood dominated by oxyHb species does not exhibit NIR autofluorescence [343], contrary to aged blood traces [38, 129–131, 141, 177]. The fluorescence enhancement of bloodstains, demonstrated in this research, was constantly progressing over time. This observation implied that one possible source of this phenomenon was a gradual increase of Hb degradation products showing higher intrinsic fluorescence than oxyHb. According to the previous research [343–345], it was evidenced that one of those Hb species – exhibiting strong fluorescence emission [235] – are hemichromes (Figure 4.4), which were indicated among products of laser-induced [235] as well as the natural degradation of blood. And perhaps they are not the only dysfunctional forms of Hb generated during the aging process. At the moment, it cannot be entirely excluded that the Hb transformations do not continue, resulting in the formation of other dysfunctional species. One of the possible decomposition pathways leading to Hb fluorescent properties may be the dissociation of Hb subunits followed by the release of iron ions, as reported in [343–345]. To complete the picture, it is worth emphasizing that the electron spin resonance studies of degrading bloodstains have also suggested

a similar conclusion, revealing a signal allegedly originating from non-heme iron, which was increasing with degradation time [163]. Considering that, it is hard to resist the impression that, in this case, the degradation pathway would bear a resemblance to the blood recycling process occurring *in vivo*, where Hb protein is metabolized to globin chains and heme [163, 343–345]. As a result of this heme breakdown, iron is released from the protoporphyrin plane, giving rise to Hb metabolites of significant fluorescence. So far, however, this type of *ex vivo* decomposition has never been substantiated or refuted because the issue of whether heme degradation is solely enzymatic or non-enzymatic remains unanswered [163, 346].

On the other hand, the observed increase of the background signal does not necessarily have to be associated with the intrinsic fluorescence of degradation products. A probable alternative explanation can be found in numerous studies of Wood et al. [184, 185, 223], who established that the same effect of marked increased background counts could also occur due to excitonic interactions throughout the network of heme aggregates. Admittedly, this reasoning was made during somewhat invasive measurements designed to study the effect of temperature and laser power on RBCs' Raman spectra. However, it was already established that Raman signatures of laser-deteriorated bloodstains bore more than a passing resemblance to naturally aged samples [177], implying that both degradation mechanisms result in the formation of similar dysfunctional Hb species. If that is indeed so, then the aging of bloodstains may trigger aggregation of similar Hb decomposition products, increasing the probability of excitonic interactions between the metalloporphyrins, which contribute to a gradual increase of baseline. Another hypothesis – somewhat similar to the reasoning given above, as once again related to the aggregation process – was proposed by Marzec et al. [347]. It was reasoned that such substantial background might originate from the photothermal signal [348]. Photons absorbed by hemoproteins can be converted into heat, which ultimately might be responsible for increasing the baseline. In other words, the older the bloodstain, the more advanced the process of Hb aggregation and, through that, the increase of baseline intensity. All these taken together leave no doubt that further studies to recognize the origin of background influence would be beneficial. At the moment, however, it appears rational to postulate that the observed trend is a combination of the above-mentioned phenomena. The intrinsic fluorescence of degradation products (e.g., hemichromes) may be paralleled by the aggregation of Hb species, leading to excitonic interactions and a more profound photothermal effect resulting from the increased absorption of photons. Finally, it should be clearly stated that estimating the bloodstains TSD solely from the fluorescence signal, increasingly dominating the Raman scattering, is a somewhat risky solution. Simply because variation in the baseline may also originate from other factors (e.g., sampling geometry as discussed in *5.1.2.4 Sample preparation and handling*) and not necessarily degradation products. That is precisely why, before proceeding with further data analysis, Raman signals were baseline corrected to expose variations within Raman bands, which co-evolved with the fluorescence enhancement. The effects of this correction procedure were already presented in Figures 9.4 and 9.5.

(A)

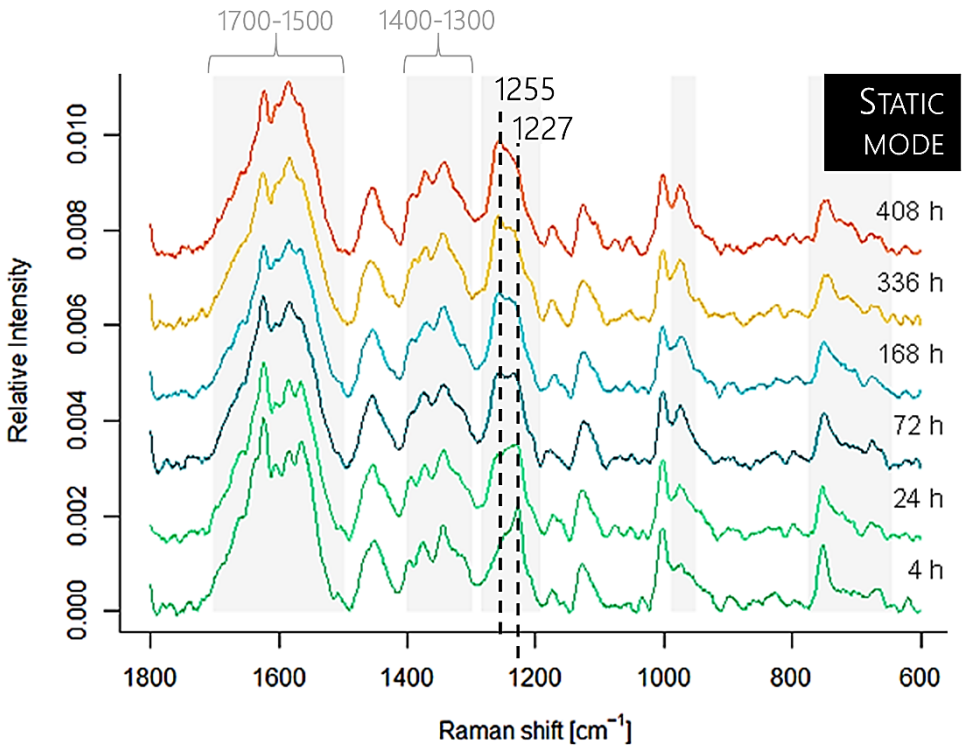

(B)

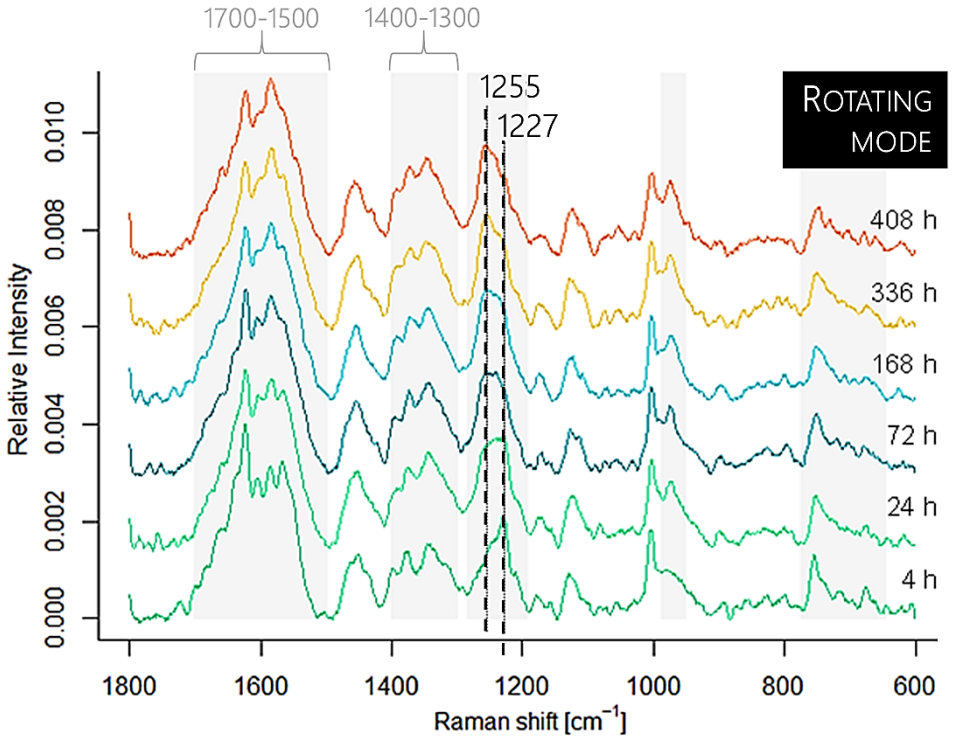

FIGURE 9.10.

Exemplary Raman signatures of aging bloodstains registered with 785 nm excitation laser in the rotating and static mode. Time-dependent bands are highlighted in grey. Spectra were treated according to the procedure outlined in *9.1.4 Signals pre-processing* and shifted for better visualization.

A graphic presentation of the background-corrected Raman spectra (Figure 9.10) exposed subtle but noticeable time-dependent changes in bands pattern. And once again, the author's attention was drawn mainly to variations in the range of 1220–1300 cm^{-1}, which were reminiscent of laser-induced spectral distortions (compare with Figure 9.7 A). A characteristic and relatively sharp band at about 1227 cm^{-1} was broadening with time progression, moving through maximum reached ca. 1248 $cm^{-1,}$ ultimately forming a band at 1255 cm^{-1}. As already debated in *9.2. A selection of Raman spectra acquisition setup*, the source of this dynamic behavior should be ascribed to modifications of C_m–H methine vibrations within heme moiety [185, 223]. By presenting the ratios of bands at 1227 cm^{-1} and 1255 cm^{-1}, referred later to as a1227/1255 ratio, in a function of time (Figure 9.11), it can be noticed that rapid decline of their value at the initial stage of degradation would enable discriminating differently-aged bloodstains. This differentiation would be more effective for spectra registered in the rotating mode, as no overlap between distributions of ratios equivalent to different time points was observed. Contrary to values characterizing static bloodstains (see, for instance, pairs of data at 4 and 6 h, and 6 and 8 h).

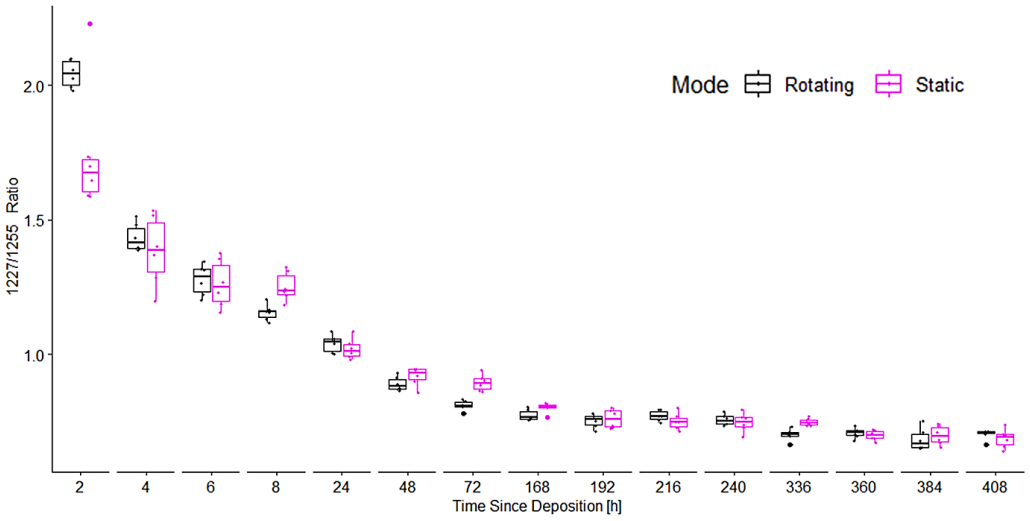

FIGURE 9.11.

Boxplots representing intensity ratios of Raman bands at 1227 cm^{-1} and 1255 cm^{-1} against the aging time of static and rotating bloodstains (given in hours).

9.2.3 Comparison between the static and rotating mode – analysis of variance

Despite the potential applicability of the 1227/1255 ratio as the aging marker, it is not difficult to conclude why its adoption in the dating task has some obvious limitations. First of all, it is not feasible to manually estimate the TSD of blood traces at long time scales using this particular spectral feature. This is because its values quickly reach a plateau – in the case of this experiment after ca. 168 h (seven days) of natural degradation (Figure 9.11). But most importantly, concluding the bloodstains' age from the 1227/1255 ratio changes limits the dating capabilities of the method. Consideration of a single

spectral feature while ignoring the interactive effects of other potentially informative dynamic variables is nothing but a severe waste of information encoded in Raman signatures and almost a blasphemy against chemometrics. The usefulness of the method simply cannot be deduced from a single variable.

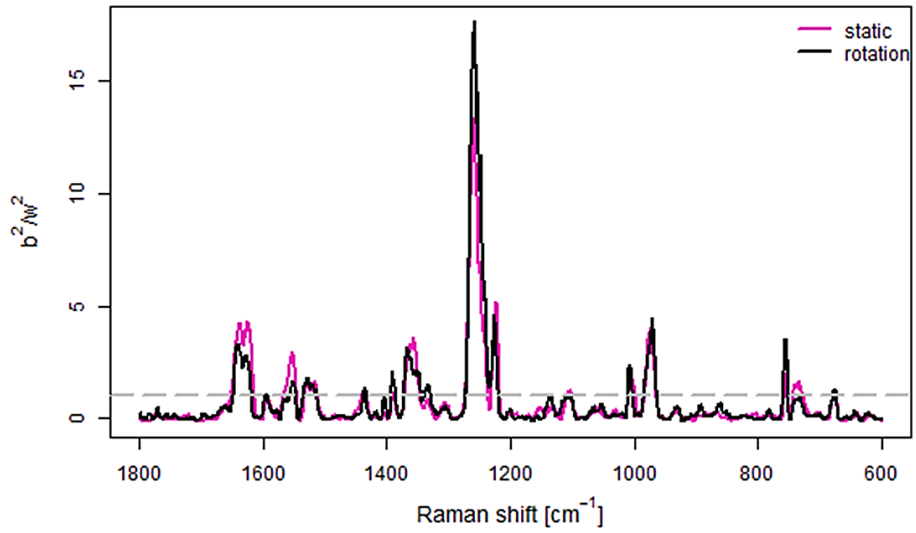

FIGURE 9.12.

The b^2/w^2 values corresponding to each value of Raman shift. The grey dashed line indicates $b^2 = w^2$.

To identify any other time-related changes in recorded Raman spectra, and through that, establish whether a further differentiation between similarly-aged blood traces would be attainable, the analysis of b^2/w^2 values corresponding to each Raman shift value was conducted (Figure 9.12). A summary of all time-dependent spectral features, characterized by values of b^2/w^2 above one (meaning that the variance between differently-aged bloodstains was higher than within groups of bloodstains characterized by the same age), can be found below in Table 9.1.

The b^2/w^2 values in positions typical of bands assigned to Hb constituents not related to the heme motif – such as CH_2/CH_3 amino acid deformation modes (1450 cm^{-1}) – are usually close to zero, indicating that these parts of the Hb structure remained relatively unaltered during bloodstains aging. For the remaining part of Raman spectra, excluding the already discussed 1220–1300 cm^{-1} region, the variation between spectra of bloodstains characterized by different TSDs seemed to result mainly from alterations observed at higher Raman shifts. This relates primarily to the ranges 1700–1500 cm^{-1} and 1400–1300 cm^{-1} (indicated in Figure 9.10) which were recognized as spectral regions containing so-called core-size and oxidation markers of Hb [80]. The first group of mentioned Raman bands gives an insight into porphyrin distortions that accompany changes of the central porphyrin-core size and the spin state of iron ions. The second is sensitized to alterations in the electron density in the π heme's orbitals [80]. For instance, the intensities of such a spectral feature as a characteristic band of Fe^{2+}–O_2 at 1638 cm^{-1} [$\nu(C_\alpha C_m)_{asym}$], initially visible as a shoulder-type band, disappeared over time.

TABLE 9.1. Positions and local coordinates of spectral features exhibiting time-dependent behavior identified owing to the analysis of Figure 9.12.

RAMAN SHIFT [cm^{-1}]	LOCAL COORDINATE[a]	OBSERVED CHANGE
677	δ(pyr deform)$_{sym}$	decrease of intensity
747		increase of intensity
754	ν(pyr breathing)	decrease of intensity
974	δ(pyr deform)$_{asym}$ or $\gamma(=C_bH_2)_{sym}$	increase of intensity
1227	$\delta(C_mH)$	decrease of intensity
1242	$\delta(C_mH)$	increase of intensity
1255	$\delta(C_mH)$	increase of intensity
1312	$\delta(C_mH)_{asym}$	disappearance
1344	ν(pyr half-ring)$_{sym}$	increase of intensity, broadening
1376	ν(pyr half-ring)$_{sym}$	redshift (band at 1370 cm^{-1})
1398	ν(pyr quarter-ring)	disappearance
1566	$\nu(C_\beta C_\beta)$	decrease of intensity
1584	$\nu(C_\alpha C_m)_{asym}$	increase of intensity
1604	$\nu(C_\alpha C_m)_{asym}$	disappearance
1623	$\nu(C_a=C_b)$	decrease of intensity
1638	$\nu(C_\alpha C_m)_{asym}$	disappearance

ν, stretch; δ, in-plane deformation; γ, out-of-plane deformation; sym, symmetric; asym, asymmetric; pyr, pyrrole; deform, deformation

[a] Subscripts α, β, m represent the carbon atoms at the alpha, beta, and meso positions of porphyrins; a and b correspond to vinyl group carbons. For a detailed scheme of heme labeling, see Figure 5.5.

As the degradation progresses, the aforementioned spectral range is becoming dominated by the band located at 1586 cm^{-1} resulting from in-plane asymmetric stretching $\nu(C_\alpha C_m)_{asym}$. It is a vibration of E_u symmetry that appears in high-spin complexes, which is often used as an indication for the identification of five-coordination complexes. Another important feature is the vibration located at 1623 cm^{-1}, i.e., the band of strong intensity derived from the vibrations $\nu(C_a=C_b)$ of the vinyl group, typical for the forms of meth-hemoproteins. These two features combined could indicate the presence of five-coordinated metHb, in which, due to the solid-state of investigated bloodstains, the substituent (H_2O) in the sixth coordination position was missing. The above observations should lead to the conclusion that the Hb forms, in which oxygen binds to the sixth vertical coordination position of the iron ion of heme (oxyHb), initially present in the 2-hour bloodstains (first acquisition of a bloodstain's spectrum), were disappearing during the decomposition process (according to the scheme presented Figure 4.4). By contrast, already mentioned heme aggregation markers (974 cm^{-1}, 1255 cm^{-1}) increased over degradation time. At the initial stage of aging, they were present on the spectra along with the Fe^{2+}–O_2 marker band at 1638 cm^{-1}, indicating that the bloodstains contained a mixture of aggregated heme and oxyHb. Furthermore, having looked at the range of so-called oxidation markers (1400–1300 cm^{-1}), it can be observed that ferric-heme species initially dominated the composition of relatively fresh

bloodstains (e.g., oxyHb), as evidenced by the band at 1376 cm^{-1} – the marker of oxidation state corresponding to Fe^{3+}. Upon aging, however, the position of the ν_4 vibration slightly shifted toward lower Raman shit values (~1370 cm^{-1}). This suggested that the population of Hb species was gradually enriched with metHb forms, which only supported the conclusions based on the spectral alterations observed in the 1700–1500 cm^{-1} region. All these factors combined are strong indicators that the aging of blood traces boils down primarily – though not necessarily exclusively – to the conversion of oxyHb to metHb and HC, followed by the aggregation of heme species. It should also be noted that at an advanced stage of natural degradation, the spectra of whole blood demonstrate remarkably similar vibrational features as those observed for the dried fresh whole blood exposed to high laser powers (λ_{ex}: 785 nm). This conclusion is in full accordance with previous reports of Lemler et al. [177], which evidenced that the natural and laser-induced deterioration of blood gives rise to similarly structured degradation products.

However, it cannot be denied that an exhaustive characterization of the ongoing degradation mechanisms and resulting decomposition products based solely on the near-infrared Raman spectra is rather problematic. The partial cause of this problem is that the aging process of blood led to increased background counts. This, in turn, made it difficult to detect some minor spectral changes in incredibly complex signals that may be vital for comprehending the role of other possible pathways of the *ex vivo* degradation of bloodstains. A potential solution might be applying more advanced mathematical modeling methods, such as multivariate curve resolution-alternating least squares (MCR-ALS) proposed by [349], which performs deconvolution of Raman spectra to enhance identification of significant spectral components responsible for the aging process. Nonetheless, it is essential to realize that a detailed investigation of aging pathways was never the main inspiration behind this research at this point of this study. Instead, the central concept was to found a non-invasive analytical method capable of providing an insight into the stage of blood evidence degradation in a relatively quick and highly representative way. The takeaway message here is that **RAMAN SPECTRA EXHIBIT CLEAR TIME-DEPENDENCY**. Consequently, **THESE ALTERATIONS IN SPECTRAL CHARACTERISTICS**, well-recognized symptoms of Hb degradation products formation [38, 141, 177, 235], **CAN BE MATHEMATICALLY CORRELATED WITH THE ELAPSED TIME** and subsequently **EMPLOYED IN FORENSIC DATING** studies.

Having proved that Raman signatures of degrading blood traces are a source of chemical information contained in spectral features other than the 1227/1255 ratio, the next step was to assess the discrimination capabilities of both measurement modes using rMANOVA, which took into account correlation among time-dependent variables. According to the results presented in Figure 9.12, and more precisely the calculated b^2/w^2, it could be concluded that the rotating mode of spectral acquisition outperformed the conventional static procedure when it comes to its potential discriminating capabilities. Furthermore, as shown in Figure 9.13, higher values of b^2/w^2 were obtained, and the differences between the groups of bloodstains varying in TSD were most distinct on the scale of the first

week. During the first few days of aging, the highest b^2/w^2 values were observed for both measurement modes when the ongoing degradation changes were most pronounced. However, the reduction of within-group variability in the novel sampling mode was more effective, as the ratios corresponding to rotating measurements were almost twice as high as those characterizing the static dataset. And, indeed, it is perfectly understandable. The sample movement allowed to provide, at a given time-point, truly averaged spectral characteristics of chemically heterogeneous blood trace. This, in turn, was reflected in low rates of w^2, which characterized dispersion of measurements of the bloodstains of the same TSD. Thus it is clear that the employment of rotating mode should be the most beneficial, especially in the early stage of aging, when the static single-point measurements are particularly susceptible to subsampling errors. As time progressed and degradation slowed down considerably, a steady decline in b^2/w^2 values was observed. It should also be noted that variances between ratios obtained for static and rotating modes were fading. The possible and most reasonable reason for this observation is the unification of degradation product distribution along bloodstains' surface. Nonetheless, even though the aging rate significantly ceased, it was established that discriminating between differently-aged bloodstains should still be possible ($b^2>w^2$) at more advanced stages of degradation. What is even more critical, **THE SUPERIORITY OF ROTATING MODE IN TERMS OF THIS DISCRIMINATING CAPABILITY WAS DEMONSTRATED** within the entire degradation period (Figure 9.13). And this, in turn, may very well become a promise of successful implementation of newly developed Raman-based procedure in the LR-based comparison approach for estimating the age of bloodstains (*Chapter 10*).

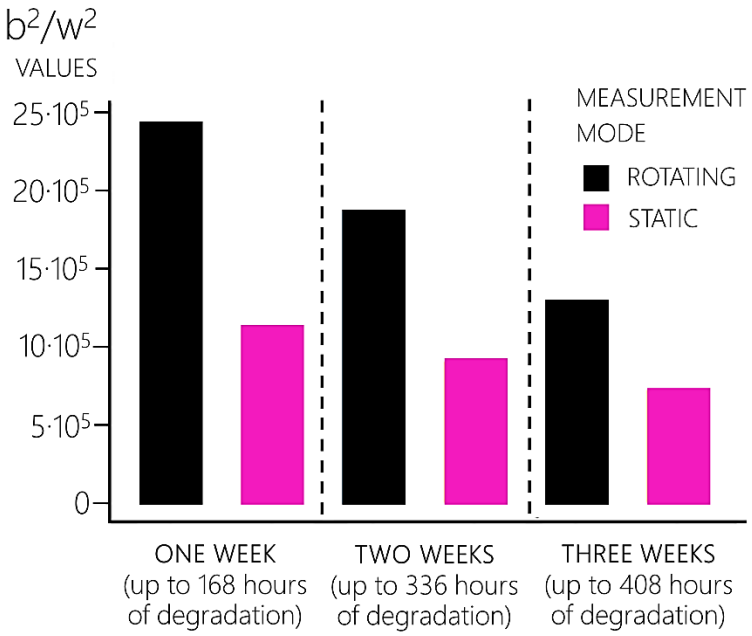

FIGURE 9.13.

Comparison of b^2/w^2 values (on the first eigenvector, CV1) characterizing data sets obtained in rotating and static mode after one, two, and three weeks of bloodstains degradation.

9.3 Conclusions

The present chapter summarized the attempt to establish an analytical procedure, serving as a tool for characterizing the state of bloodstains degradation. In other words, it addressed the first of the thesis objectives set out in *Chapter 3*:

All the research stages can be summarized in the following key elements:

1. Development of a Raman-based analytical method allowing for non-invasive and representative probing of the chemical composition of degrading bloodstains.
2. Collection of the spectral signatures of blood traces over the desired aging period.
3. Setting out a chemometric strategy for the pre-processing of obtained Raman spectra.
4. Designing the LR models for solving the comparison problem between the questioned bloodstain and the reference material(s) created "artificially."
5. Development of the LR models validation protocol.

Given the characteristics of the studied materials, it was hypothesized that the right candidate for this task would be Raman spectroscopy (RS). And, indeed, the discussed results proved the effectiveness of RS as a method capable of delivering information inherent to chemical changes accompanying the degradation process of blood traces.

It has been also demonstrated that the newly proposed rotating sampling method should be preferred over the conventional static measurements for at least two reasons. Regarding the reproducibility of registered Raman signatures, the rotating mode reduced the risk of subsampling errors, which was established by analyzing data variance using rMANOVA. It was revealed that the variance between Raman spectra registered for bloodstains deposited at the same time (w^2) was significantly lower than the variance observed between spectral signatures of differently-aged blood traces (b^2) when the sample was rotated during the spectral acquisition. The novel probing method provided an averaged signature of an inhomogenous sample, thereby facilitating bloodstains' discrimination varying in their ages. This level of representativeness simply could not have been achieved through the performance of repeated static measurements in different areas of the sample. Especially if it is highly desired to perform the analysis in the shortest possible time, as is the case with characterizing the composition of the blood trace at the initial stage of its aging process. And this brings us to another motive behind promoting the rotating mode, namely the measurement duration. Since the application of the rotor system enabled a constant renewal of the irradiated area of bloodstains, the risk of laser-induced detrimental effects has been reduced to a negligible extent. Consequently, it became possible to register the Raman spectra

using higher laser power, leading to shortened measurements, down to six minutes compared to 15 minutes of the conventional static approach.

All these factors combined allowed positioning the rotating mode of Raman spectroscopy among front-line analytical tools capable of providing chemical insight into the time-dependent behavior of bloodstains. However, it cannot be denied that there is more to forensic dating of evidence than simply registering informative data. And even though establishing an analytical method is far from being straightforward, an adaptation of the proposed methodology in the field of practical forensic proceedings is way more challenging.

| *CHAPTER 10*

ASSESSING THE (DIS)SIMILARITY OF BLOODSTAINS' RAMAN SPECTRA USING HYBRID LIKELIHOOD RATIO APPROACH

The results presented in the previous chapter clearly demonstrate that the Raman characteristics of bloodstains do indeed change with time. However, as repeatedly mentioned throughout the thesis, an application of Raman spectroscopy is nothing new in the field of blood dating studies. What is more, the technique's potential has already been well documented [38, 141, 177]. Thus, the real challenge and novelty remain in developing a method with acceptable precision and reproducibility to allow its implementation into the forensic scenario. In other words, the Raman-based approach, correspondingly to other proposed analytical tools (see Table 5.1), still requires to evolve beyond the research phase.

The great majority of published dating struggles utilized idealized environmental conditions and substrates, which is perfectly understandable given that the purpose of these studies was to track changes in the aging of bloodstains and understand the inherent variations of defined aging markers. Consequently, this relative "conservatism" concerning the environmental factors, characteristics of a donor, or even type of substrate usually resulted in dating models of excellent predictability obtained at the research phase. It is not difficult to foresee, though, that attempt to transfer these models to forensic caseworks – as yet utterly unsuccessful – would result in misestimations of bloodstains age, depriving these conventional methods of almost entire practical value. This is evidenced by the fact that in none of the forensic organizations working according to *ISO/IEC 17025* international quality standards, the absolute dating of bloodstains (or any other forensic trace) is performed on a daily analytical basis.

As with all forensic tasks, an elastic dating approach that considers all factors influencing the validity of the evidence evaluation is the key to success. Unfortunately, no two crime scenes are ever precisely the same, and neither is the aging kinetics of blood traces. Precisely for this reason, establishing a universal framework for estimations of time of deposition may be impossible to accomplish. So, despite technological advances, the question remains – how to incorporate the uncertainty deriving from the influence of factors affecting the aging processes into the dating approach? Perhaps by looking at the dating problem from an entirely different perspective, outlined in *2.2. The novel framework for evidence dating*. Therefore, the second part of the study, presented in this chapter, focuses on reframing evidence dating by substituting the likelihood ratio-based comparison procedure for conventional calibration models. Presumably, such an attitude change may eventually re-shape our notion of what is achievable in the field of forensic dating.

10.1 Materials and methods

10.1.1 Samples preparation

The sample preparation procedure itself was analogous to the methodology used during the first stage of the research (*9.1.1. Samples preparation*). Bloodstains were obtained by depositing 20 µl aliquots of capillary blood on aluminum sample pans, providing low and almost featureless background signals. In order to mimic the real forensic scenario, samples were preservative-free and originated from the same individual. Before the first spectrum collection, bloodstains were left to dry for two hours under ambient laboratory conditions and subsequently analyzed every two hours (up to eight hours elapsed since bloodstain formation) during the first day of degradation. For the next three weeks, when the degradation process was remarkably slower, bloodstains were analyzed daily (excluding weekends). Eventually, the measurement scheme applied in this part of the thesis resulted in 18 time-points, assumed to constitute 18 different evidence time-related sources. Each of the time-point was characterized by six bloodstains (which served as replicate measurements of samples at a given time-point) created one after another at appropriate time intervals, according to the procedure already described in the previous chapter. Between measurements, the samples were degrading under relatively stable conditions – stored in darkness, exposed to temperature (T) and relative humidity (RH) controlled by the laboratory air-conditioning system (for details, see Figure 10.1).

For the research phase of the study (see Figure 3.1), a single database of bloodstains' samples was obviously insufficient. It should be reminded that the task undertaken was to verify whether the features of the recovered bloodstain (evidence) were similar enough to the features of a bloodstain of known age (time-related source), created according to the prosecutor's/defence hypothesis. In order to assess whether considered samples were of the same TSD, their spectral signatures were compared through likelihood ratio models. Thus, at least two datasets of bloodstains were required – one set working as the source of data for training the model and deriving the reference sample of bloodstain (the product of the so-called supervised aging process), and the second set from which the recovered bloodstain (the evidence) was selected. In this study, three separate databases (termed as set °1–°3) were prepared, according to the scheme presented in Figure 10.1. Each of the databases consisted of six Raman signals recorded for each 18 time points during the three-week degradation period.

The aging of bloodstains within each of these datasets was performed in a supervised manner so as to reduce the influence of external factors and, through that, normalize the aging kinetics between each of the datasets as much as possible. Only in this way, the assessment of the (dis)similarity between the degree of the evidence degradation and the decomposition of comparative materials would be meaningful. But first, the question had to be asked: which of the external factors influencing the aging process (donor characteristics, environmental conditions, nature of the substrate) could be actually controlled? Would it be possible to fix all of them on the "level" corresponding to the conditions during

the criminal act? From the practical perspective, when considering an actual forensic workflow, it would be possible to ensure the same substrate and environmental conditions (in some cases, within a certain error). However, providing blood of precisely the same composition as body fluid deposited during the alleged participation in the crime is simply impossible. Even if the reference bloodstains would be created using the blood of the potential suspect – the donor of the questioned evidence – the initial composition of blood may still exhibit some biochemical differences of potential importance.

In the present study, the construction of three databases was performed to reflect the possible forensic workflow. Namely, all bloodstains were deposited on the same substrates and stored under nearly the same environmental conditions. However, as shown in Figure 10.1, these three databases differed in deposition time – the samples were collected in three consecutive months – and hence they reflected the instability of initial blood composition resulting from dietary and health condition-related factors. Precisely as it would be in an actual proceeding when differences in biochemical composition of evidence and reference materials are anticipated. At this point, it should also be noted that even though the average temperature and relative humidity were similar in the case of all three sets, the temperature conditions varied during the first day of aging. While in the case of bloodstains' sets °1 and °2, the temperature was 23.5 °C and 22.8°C, respectively, bloodstains constituting the set °3 were deposited whilst the temperature in the laboratory was significantly higher: 30.8 °C. In turn, knowing that it is the first hours from the moment of deposition that are crucial for the entire degradation process, this temperature difference should be borne in mind when interpreting the performance of obtained LR models.

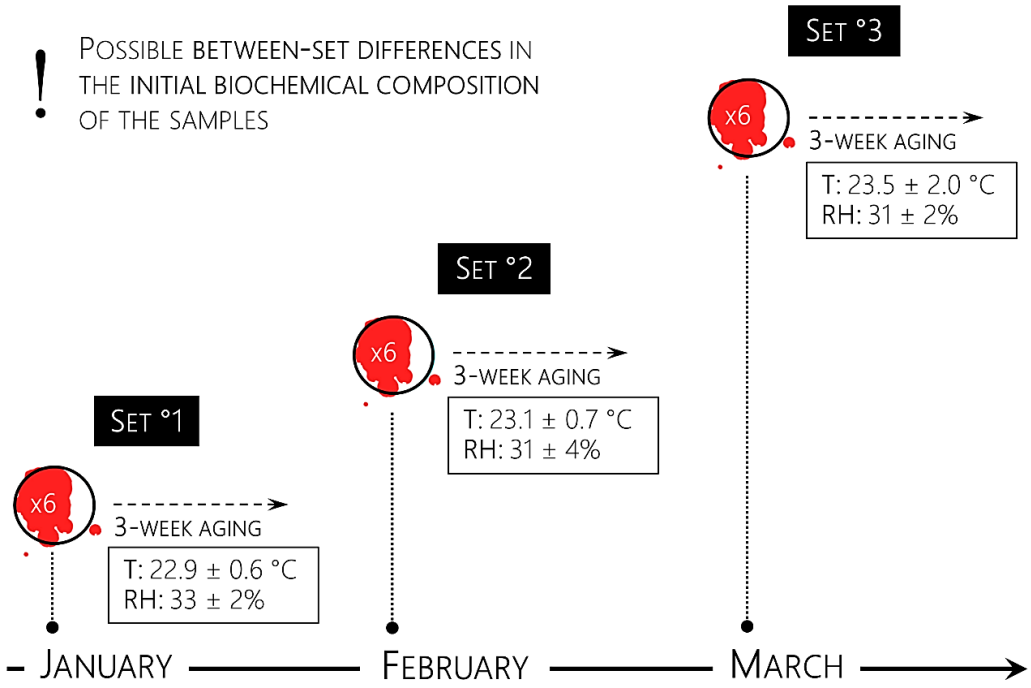

FIGURE 10.1.

The general scheme of the supervised aging process of three different bloodstains sets, which served for the development and subsequent validation of likelihood ratio models.

10.1.2 Acquisition of bloodstains' Raman signatures

Raman signatures of degrading blood traces were obtained following the procedure described in *Chapter 9* using a Renishaw *inVia Raman Microscope* spectrometer. In order to prevent sample damage resulting from the excessive point laser irradiation, all spectra were registered using the ROTATING MODE. Detailed experimental conditions used in the present part of the study are presented in Table 10.1.

TABLE 10.1. The rotating mode experimental conditions used during the spectral characterization of bloodstains sets °1–°3.

EXPERIMENTAL CONDITIONS	
Detector	Peltier-cooled charge-coupled device (CCD)
Laser excitation source [nm]	785
Laser density [mW/μm^2]	ca. 0.16 (10% of total laser power)
Spectral range [cm^{-1}]	600–1800
Objective	5x NIR optimized objective (N.A. = 0.1)
Accumulations	2
Time of acquisition [s]	20
Sample holder	Aluminum sample pans
Cosmic Ray removal	ON

Thus, at this stage of the research, another – the second – point of the thesis' objectives was achieved:

1. Development of a Raman-based analytical method allowing for non-invasive and representative probing of the chemical composition of degrading bloodstains.
2. Collection of the spectral signatures of blood traces over the desired aging period.
3. Setting out a chemometric strategy for the pre-processing of obtained Raman spectra.
4. Designing the LR models for solving the comparison problem between the questioned bloodstain and the reference material(s) created "artificially."
5. Development of the LR models validation protocol.

10.1.3 Development of the likelihood ratio procedure for bloodstains discrimination

As already discussed, selecting an adequate approach to the dating problem and, consequently, developing a reliable model to interpret data is an essential step of age estimation methods, which should not be underestimated. After identifying the person of interest (who usually becomes a suspect at a later stage of the proceedings), alternative hypotheses about the course of events are forwarded. For this reason, rather than directly estimating a time since deposition (TSD), the preferred approach should be the interpretation of the analytical findings in the light of these hypotheses, which basically boils down to assignment to the findings an evidential value.

Since the present study suggested considering the dating task as a comparative procedure, it addressed the issue of discrimination between differently-aged bloodstains, where the evidence (and more precisely its physicochemical characteristics – in this case, Raman signatures) is weighted against some reference materials. To achieve this goal, a probabilistic approach founded on the calculation of likelihood ratio (LR) is currently indicated as the most reliable tactic [20], which was also applied herein. However, the conventional LR models fail when comparing samples characterized by many variables (e.g., Raman spectra) because of the singularity of the variance-covariance matrices. The solution is to apply hybrid LR models [264], founded upon a restricted number of new latent variables derived from chemometric tools, instead of employing all signal variables. As in any other discrimination problem, well-performing LR models are expected when each source data (herein, the "source" should be considered a group of bloodstains of given TSD, e.g., two-hour-old bloodstains) are as unique as possible. What is more, the means of the features characterizing different sources are desired to be much more distant than the data within the sources. In other words, effective LR models are those defined for a few latent variables that maximize the between source variation, **B**, while minimizing the variation of the data within each source, **W**.

The estimation of these new latent variables is rarely attempted using the "raw" instrumental signals, as the discrimination of differently-aged samples usually benefits from appropriately performed pre-processing of the registered data. As described in *Chapter 7*, in the case of this study, the optimization of the pre-processing protocol was combined with the reduction of data dimensionality through rMANOVA to maximize differences between sources and minimize differences within them. This tactic has been recently developed by Martyna *et al.* [291], where the quality parameter for the genetic algorithm-based selection of the most suitable pre-processing strategy for discrimination purposes was defined as a ratio of the between-source and within-source variation (b^2/w^2). An argument in favor of applying this particular method of variance analysis was that it enabled the reduction of data dimensionality in a way that is beneficial for optimal sources separation and also highlighted their individual features. Given these reasons, the LR models proposed for the novel procedure of bloodstains

dating were constructed for the first latent variable, LV1, from rMANOVA, which has already proved reasonably effective in separating the sources [326].

10.1.3.1 The chemometric tactic of data treatment

Instead of a time-consuming and labor-intensive grid search among all available preprocessing strategies, an adequate pre-processing procedure, consisting of a sequence of methods aimed at denoising, baseline correction, and normalization of signals, was established using the genetic algorithm (GA) developed by Martyna in [291]. Since no single pre-processing method is individual, and the end result depends largely on their mutual interactions, the optimization procedure applied herein concerned the entire sequence of above-mentioned preprocessing steps.

The preprocessing strategy was initialized with denoising/smoothing, followed by the baseline correction and normalization. Additionally, to compensate heteroscedastic noise [350] that grows with signal intensity and thus affects the covariance structure of the variables, denoised/smoothed signals, $a = [a_1, \ldots, a_J]$ were subjected to the log-centered transform in the following manner:

$$s = log_{10} a - \frac{1}{J} \sum_{i=1}^{J} log_{10} a_i.$$

The most optimal preprocessing strategy was indicated using GA-based procedure from among chromosomes, each described by three genes referring to denoising, baseline correction, and normalization steps. The tested denoising strategies involved 16 different methods based on discrete wavelet transform [294] and Savitzky-Golay filter [292]. The baseline correction methods summed up to 64 various tools using asymmetric penalized least squares [304–308], robust baseline estimation [311], statistics-sensitive non-linear iterative peak-clipping [309], polynomials fitting [301–303], and quantile regression [310]. And finally, standard normal variate and probabilistic quotient normalization [312, 314] were introduced among the available options of normalization methods. The groups of parameters, which characterize the considered preprocessing techniques, were roughly selected for optimization after a visual examination of the pre-processed signals. Table 10.2 summarises all preprocessing methods implemented in the GA optimization procedure.

A ratio of the between-source to within-source variance (b^2/w^2) on the first rMANOVA latent variable, LV1, served here as a quality parameter assessing the effectiveness of preprocessing strategies. The initial generation in GA entailed 50 randomly selected preprocessing strategies. The chance of mutations was 0.1, the elitism level was set at 5%, and the algorithm converged when five subsequent solutions were identical. All calculations were performed in R software [338] using scripts home-written by A. Martyna and available R packages.

TABLE 10.2. Parameters of pre-processing methods tested during the GA-based optimization.

CLASS OF METHODS	METHOD	PARAMETER	PARAMETER VALUE	REF.
Denoising/smoothing				
Savitzky-Golay (SG)	–	*p*-polynomial degree *w*-window size	*p*: 3, 4, 5, 6 *w*: 17	[292]
discrete wavelet transform (DWT)	–	*W*-wavelet type *d*-decomposition level for denoising *t*-threshold estimation *c*-thresholding policy *sd*-dispersion estimate	*W*: Daubechies least-asymmetric wavelet (4, 8), Coiflets (1, 5) *d*: 10 *t*: universal, SURE *c*: hard, soft *sd*: MAD	[293–297]
Baseline correction				
asymmetric penalized least squares methods				
	pWAsPLS	*m*- order of differnces λ- penalty *w*- weights	*m*: 2 *λ:* $6\cdot10^5$, $8\cdot10^5$, $1\cdot10^6$ *w*: 0.001, 0.005	
	CWTAsWPLS	*m*- order of differnces λ- penalty	*m*: 2 *λ:* $1\cdot10^6$, $7\cdot10^7$, $8\cdot10^7$, $9\cdot10^7$, $1\cdot10^8$, $2\cdot10^8$	[306]
	airPLS	*m*- order of differnces λ- penalty	*m*: 2 *λ:*$5\cdot10^4$, $6\cdot10^4$, $7\cdot10^4$, $8\cdot10^4$, $9\cdot10^4$, $1\cdot10^5$	[305]
	doublyWAsPLS	*m*- order of differnces γ_{max}-penalty $r = \gamma_{min}/\gamma_{max}$ – penalties ratio	*m*: 2 γ_{maz}: $6\cdot10^4$, $8\cdot10^4$, $1\cdot10^5$ *r*: 0.7, 0.9	[307]
	multiWAsPLS	*m*- order of differnces λ- penalty *μ*- penalty term	*m*: 2 *λ:* 10, 100 *μ:* $1\cdot10^7$, $1\cdot10^8$, $1\cdot10^9$	[308]

TABLE 20.2. *(continued)*

CLASS OF METHODS	METHOD	PARAMETER	PARAMETER VALUE	REF.
robust baseline estimation (RBE)	–	*b*- robustness parameter *h*- the proportion of signal points for local regression	*b:* 2, 2.2, 2.5 *h:* 0.3, 0.4	[311]
statistics-sensitive non-linear iterative peak-clipping (SNIP)	–	*w*- clipping window	*w:* 20, 22, 24, 26, 28, 30	[309]
polynomial methods				
	modified polynomial (ModPoly)	*p*- polynomial degree	*p*: 3, 4, 5, 6, 7, 8	[301]
quantile regression methods				
	polynomial quantile regression (polyQR)	*p*- polynomial degree *q*- quantile	*p*: 4, 5, 6 *q*: 0.01, 0.05	[310]
	spline quantile regression (splineQR)	*q*- quantile λ- penalty	*q*: 0.001, 0.01, 0.05, 0.1 λ: 0	[310]
	reweighted quantile regression (reweightedQR)	*p*- polynomial degree *q*- quantile	*p*: 5, 6 *q*: 0.01, 0.05, 0.1	[310]
<u>Normalization</u>				
standard normal variate (SNV)	–	–	–	[312]
probabilistic quotient normalisation (PQN)	–	–	–	[314]

10.1.3.2 The development and validation of hybrid likelihood ratio models

An LR-based approach requires the formulation of at least two contrasting hypotheses on the course of the events, which generally reflect the position of the prosecutor and the defense. To better understand this methodology, let us turn one last time to the O.J. Simpson case presented at the very beginning of the dissertation (*Chapter 1*). In the aforementioned case, one of the traces secured was bloodstains left at the crime scene by the suspect, O.J. Simpson. However, the relevance of this evidence to the case at hand was questioned by casting doubt on the timing of the bloodstains' deposition. Thus, the critical information for establishing the suspect's connection to the murder turned out to be the age of the traces.

In such a case, when the time since bloodstains deposition is contested and the time elapsed since the incident is known (t_R), possible hypotheses could be:

H_1: the age of the recovered evidence (bloodstain(s) of questioned age, revealed at the crime scene, t_E) WAS DEPOSITED during the commission of the crime, $t_R = t_E$.

H_2: the age of the recovered evidence (bloodstain(s) of questioned age, revealed at the crime scene, t_E) WAS NOT DEPOSITED during the commission of the crime, $t_E \neq t_R$.

However, the possible age of the bloodstains corresponding to H_2 usually cannot be indicated by the suspect. Also, in the aforementioned case, O. J. Simpson did not provide an alternative scenario. He simply denied the one presented by the prosecution. Thus, in order to reach the most reliable conclusions, it is obligatory to provide several groups of reference bloodstains (if possible, originating from the suspect) for the purpose of supervised dating. These reference materials should be aged over different times (t_R), depending on the investigated timeframes, covering not only the time of the commission of the crime (t_E) but also any other time the suspect may specify in his defense. A few replicate measurements of the blood samples should be collected at each time point (here, six replicates) to establish an appropriate database (termed earlier as set °1) of bloodstains' Raman signatures to trace the degradation pattern over time. It should also be reiterated that the variability of data is expected to be relatively high. Namely, even if the reference samples are submitted to the same storage conditions as those expected to have been experienced by the questioned evidence, it is virtually impossible to provide a genuine replica of the evidential bloodstains. It must be noted that the chemical composition of blood samples included in the first database (set °1), determined, for example, by dietary habits or health condition of the donor, may be drastically different from the composition of the evidence left at the crime scene. Unfortunately, the initial composition of bloodstains is a factor whose influence cannot be wholly eliminated. And precisely for this reason, its impact should be studied in a particularly thorough manner.

Consequently, the task is to compare the characteristics of the recovered bloodstains (evidence) and each time-related reference sample derived from the first database (set °1) to assess whether they

can be of the same age. And this poses a conventional forensic comparison problem, solvable using the LR approach [8]. Hence, performed comparisons consider the following hypotheses:

H_1: the recovered bloodstain age (t_E) is consistent with the age of a reference bloodstain (t_R), i.e., $t_R = t_E$.

H_2: the recovered bloodstain age (t_E) is different from the age of a reference bloodstain (t_R), i.e., $t_E \neq t_R$.

The following procedure was proposed for each comparison between two bloodstains, the recovered sample, and one of the reference materials from the first database (set °1). The first database (set °1), containing six Raman spectra recorded for 18 time-related bloodstains (6×18 signals), was divided into two parts. Three signals corresponding to 18 time-related points (3×18 signals) were randomly selected to constitute a sub-database (set °1a), and the remaining created the second equally-sized sub-database (set °1b). The set °1a was used for summarising the case-specific data to find the new LV1 direction from rMANOVA. The data from set °1b, along with the spectra measured for the recovered bloodstains (constituting the set °2), were then mean-centered (using the mean of set °1a) and projected on LV1. Finally, the projections for the recovered sample, defined by the mean of $k_1 = 3$ data $\bar{y}_1 = \sum_{i=1}^{k_1} y_{1i}/k_1$ and one of the reference bloodstains, defined by a mean of $k_2 = 3$ data $\bar{y}_2 = \sum_{i=1}^{k_2} y_{2i}/k_2$ were compared. In order to define the relevant distributions, the remaining $M = 17$ samples with $n = 3$ data each, described by their means $\bar{x}_m = \sum_{j=1}^{n} x_{mj}/n$, were used as a background population. The within-source variance was defined as:

$$w^2 = \frac{\sum_{m=1}^{M}\sum_{j=1}^{n}(x_{mj}-\bar{x}_m)^2}{M(n-1)},$$

while the between-source variance is expressed as:

$$b^2 = \frac{\sum_{m=1}^{M}(\bar{x}_m-\bar{x})^2}{M(n-1)} - \frac{w^2}{n},$$

where $\bar{x} = \frac{1}{Mn}\sum_{m=1}^{M}\sum_{j=1}^{n} x_{mj}$.

The LR formula consists of four components, as shown in Figure 10.2. The first part of the formula expresses the probability density of the distribution with a mean equal to zero and variance equal to $\frac{w^2}{k_1} + \frac{w^2}{k_2}$ at $\bar{y}_1 - \bar{y}_2$. The second component estimates the probability density of the distribution estimated with Gaussian kernels positioned at each $\bar{x}_m$with variance equal to $\frac{w^2}{k_1+k_2} + h^2b^2$ at $\bar{y}^* = \frac{\bar{y}_1k_1-\bar{y}_2k_2}{k_1+k_2}$. The h is expressed as $\left(\frac{4}{M(2p+1)}\right)^{\frac{1}{p+4}}$, where p is the number of the considered variables. In the case of this study, the p equals one. The final density curve is obtained by averaging Gaussian kernels (see *6.2.1.1 Kernel density estimation*) so that it integrates to unit area. It should also be emphasized that

the appropriate amount of smoothing, denoted as *h*, must be selected carefully. If it is set too high, the information about the actual distribution and some subtle features of the data under analysis will be lost. When *h* is set too low, the probability density curve might become too spiky, making the distribution ragged and challenging to interpret.

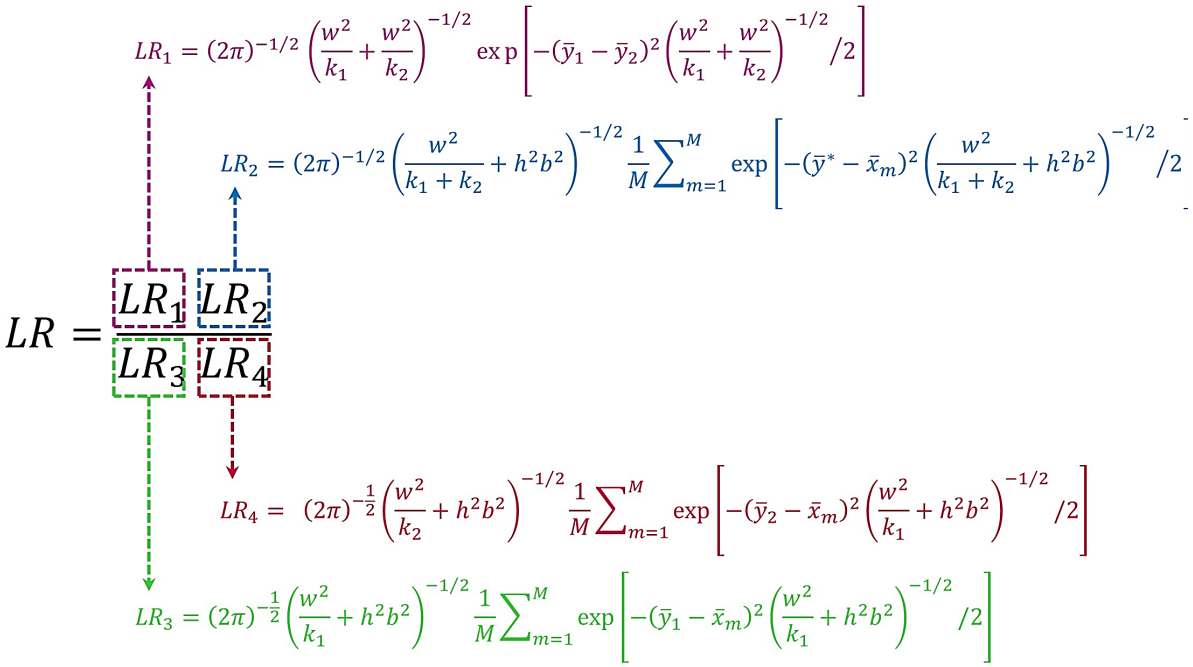

FIGURE 10.2.

The expression for the likelihood ratio (LR) applied in the study.

In contrast to the first two components, which assume that H_1 is true, the remaining two expressions in the denominator of the LR formula assume the opposite, so they are independent. They both estimate the probability density of the distribution estimated with Gaussian kernels positioned at each $\bar{x}_m$ with variance equal to $\frac{w^2}{k_1}+h^2b^2$ (or $\frac{w^2}{k_2}+h^2b^2$) at $\bar{y}_1$ or $\bar{y}_2$, respectively. The final LR is given in Figure 10.2.

Obviously, such a procedure in which each of the bloodstain samples from the first database (set °1) is compared with a single recovered sample from the second database is insufficient for research purposes. Therefore, in order to validate the LR model (see *6.2 Performance assessment*), the procedure was repeated for various recovered samples stored in the second database (set °2). In this way, there will be *m* experiments to assess the false negative responses, which will concern comparing *m* samples of the same age (i.e., $t_R = t_E$). Since the H_1 hypothesis should be supported in this case, and the expected LR value is above one, false negatives will appear when LR<1. To estimate the false positive answers, where the H_2 should be supported (LR<1), $m^2 - m$ will concern comparing samples of different ages (i.e., $t_R \neq t_E$), thus each LR>1 will be classified as the answer providing incorrect support for the H_1 (false positive). All three databases (sets °1–°3) were used to test the LR models' performance. According to

the above protocol, the experiments were carried out for pairs of these databases, storing the reference and the recovered samples. Moreover, the experiments for false positives and false negatives were carried out ten times, each time generating a set to train and test the LR model. The final error rates will therefore be presented as an average of these partial results.

At the very end, it should also be added that the LR models were not developed based on the whole spectral range but on the regions previously indicated thanks to rMANOVA as those characterized by b^2/w^2 above zero (Figure 9.12). As a consequence, seven different combinations were tested, as shown in Figure 10.3.

10.2 Results and discussion

10.2.1 Development of likelihood ratio models

10.2.1.1 Pre-processing of Raman signatures using genetic algorithm (GA)

Considering the mentioned difference in temperature occurring during the first day of the aging process of the third set of bloodstains deposited in March, the verification of the usefulness of the proposed approach for bloodstains dating began with the comparison of sets °1 and °2. In this case, the degradation conditions were most similar to each other, and thus the assumptions of the supervised aging procedure were achieved in the fullest way. As described in the previous subsection, initially, the first database (set °1) was used to train the models, while the second database (set °2) was the source of the recovered sample (evidence). Subsequently, this division was reversed, with the second database being used to train the models and the first database providing the evidence samples for the comparison procedure. Models were constructed based on seven different ranges of the Raman spectrum (Figure 10.3), which ultimately resulted in 14 different LR models.

In this study, the strategy based on applying the genetic algorithm (GA) to indicate the optimal combination of pre-processing tools was implemented, following the study of Martyna [291]. Table 10.3 collects all the pre-processing solutions suggested by the GA as the most effective combinations in yielding the highest ratio of the between-source and within-source variation (b^2/w^2) for the first latent variable computed from rMANOVA as a quality parameter. The suitability of the proposed methodology was ultimately verified by the performance of developed LR models built for the first rMANOVA's eigenvector, which were reflected in – among others – the levels of false positive and false negative rates shown as boxplots in Figure 10.4 and summarized in Table 10.4.

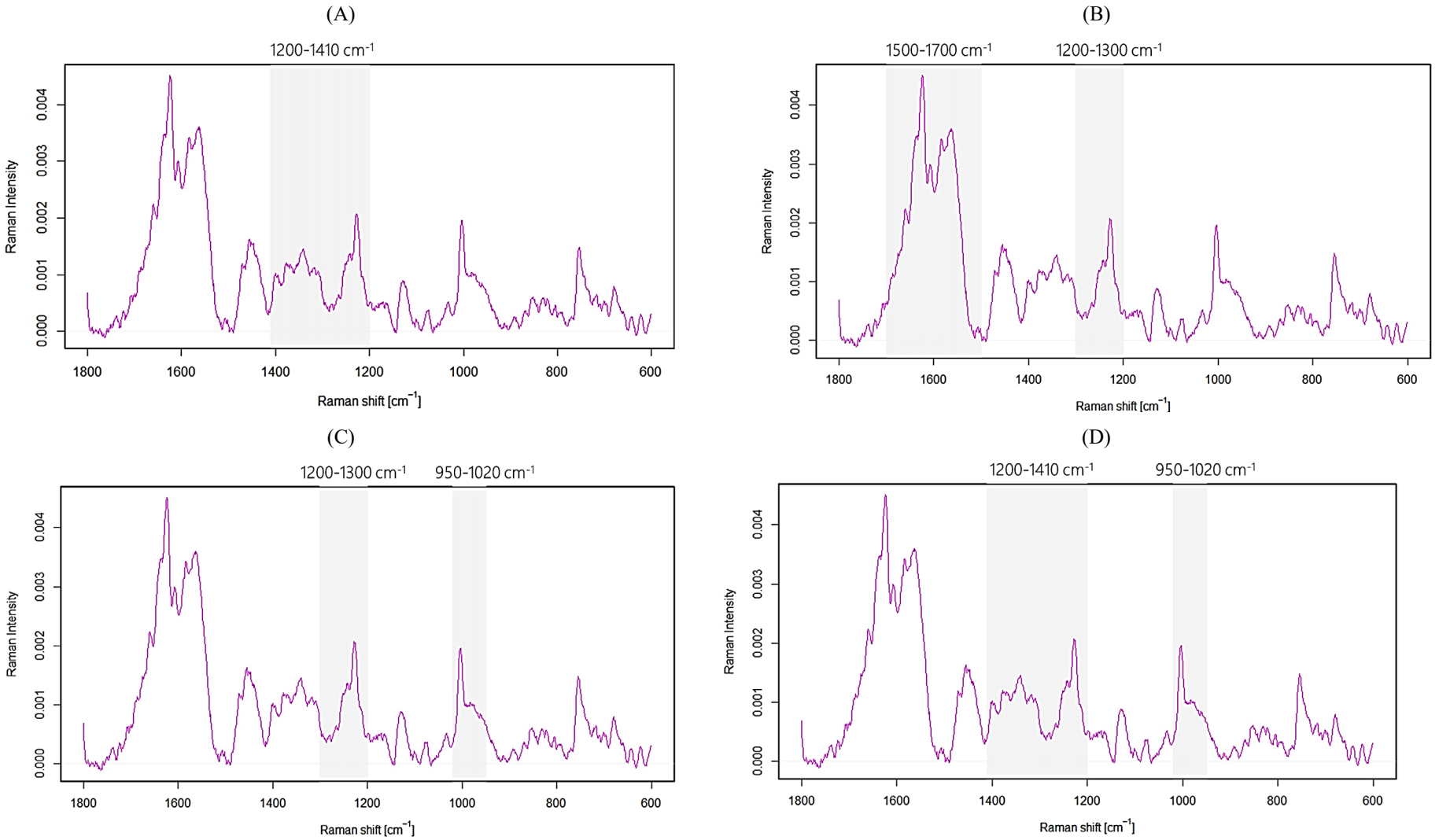

FIGURE 10.3.

Ranges of bloodstains Raman signatures and their combinations (highlighted in greyish) used for developing different LR models. Spectral range A corresponds to 1200–1410 cm^{-1} (A); spectral range B corresponds to 1500–1700 cm^{-1} combined with 1200–1300 cm^{-1} (B); spectral range C corresponds to 1200–1300 cm^{-1} combined with 950–1020 cm^{-1} (C); and spectral range D corresponds to 1200–1410 cm^{-1} combined with 950–1020 cm^{-1} (D).

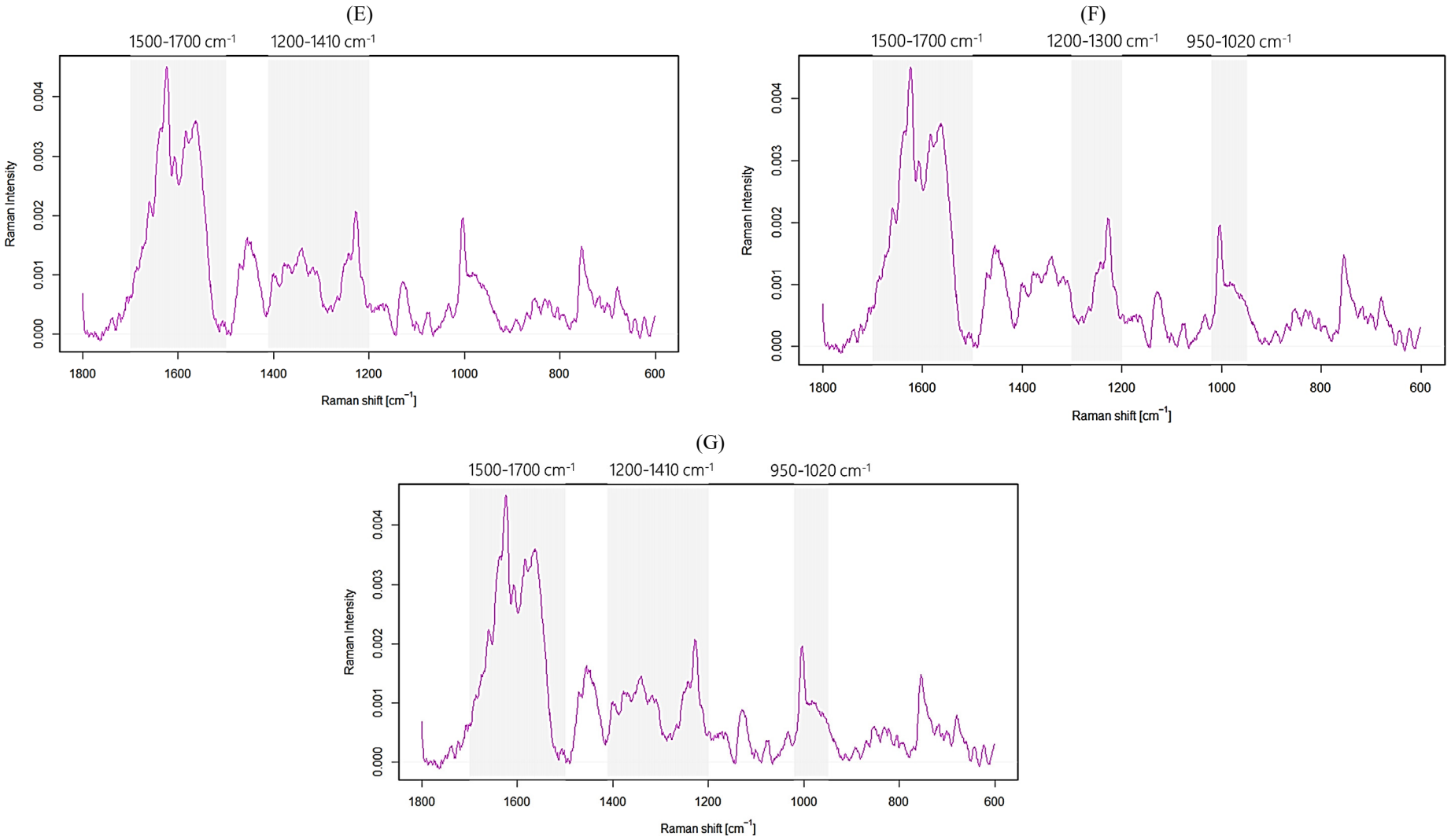

FIGURE 10.3. (CONTINUED)

Ranges of bloodstains Raman signatures and their combinations (highlighted in greyish) used for developing different LR models. Spectral range E corresponds to 1500–1700 cm^{-1} combined with 1200–1410 cm^{-1} (E); spectral range F corresponds to 1500–1700 cm^{-1} combined with 1200–1300 cm^{-1} and 950–1020 cm^{-1} (F); and spectral range G corresponds to 1500–1700 cm^{-1} combined with 1200–1410 cm^{-1} and 950–1020 cm^{-1} (G).

In the beginning, let us focus briefly – as automation and objectivization of pre-processing should limit our concerns regarding its effectiveness – on the issue of preparing spectra for further data analysis. It is generally agreed that mathematical pre-processing, quite often, is the only possible way to generate reproducible qualitative and quantitative data, and the methods used are strictly dependent on investigated signals. In the case of Raman spectroscopy-derived signals, usually, two basic pre-processing steps are vitally crucial for feasible analysis. The first of these are baseline correction methods to remove the baseline effects arising, among others, due to fluorescence and other additive features in the spectra. The second group consists of normalization procedures whose task is to remove multiplicative effects related to, for instance, laser intensity fluctuations or out-of-focus contributions. Thus, normalization usually boils down to multiplying the signal by a scaling value to make the corresponding intensities, which, in theory, should not pose any differences, as much comparable across spectra as possible. Consequently, it is reasonable to expect that the normalization methods will have the most significant influence on minimizing the casual variations within different sources (differently-aged bloodstains), and in the long term, also on the performance of the developed LR models. Hence, when analyzing the effectiveness of pre-processing methods, it seems that special attention should be paid to false negative rates (Figure 10.4, Table 10.4).

While analyzing the pre-processing methods used and the resulting false responses for each of the developed models, it would be a truism to say that the type of approach used has an influential effect on models' performance. It is a well-documented correspondence. Another cliché would be to say that there is no universal combination of pre-processing methods, and their selection is individually determined by the type of distortion present in the recorded signals. Distortions that can also occur to different degrees in different parts of the same signal. This can be seen by taking a quick look at Table 10.3, where, for almost each of the seven spectrum segments considered, GA selected a different combination of pre-processing methods. One can also notice that denoising and baseline correction methods practically do not present any trend indicating that any applied methods are evidently better than the others. And, perhaps, at this point, the discussion should end. After all, the GA-based procedure was designed to select the best method for the analysis objective – herein distinguishing samples of different ages – by maximizing the b^2/w^2 ratio (and thus also by minimizing the within-group variance through appropriately chosen signal normalization methods). However, on a closer inspection of the pre-processing results, it is hard to resist the impression that some tendency is observed among mentioned normalization methods. An analysis of the false negative responses obtained for individual LR models, shown in the boxplots presented in Figure 10.4, reveals that the lowest error rates were characterizing models developed on the following spectral ranges: 1200–1410 cm^{-1} (marked as the black box) and 1200–1300 cm^{-1} combined with 950–1020 cm^{-1} (marked as the green box). This observation is also supported by the empirical cross entropy (ECE) plots presented in Figures 10.5 and 10.6, as LR

models based on these two spectral ranges yield incomparably more satisfying ECE outcomes[‡‡‡‡‡]. In both cases (denoted as *A* and *C* in Table 10.3 and Figures 10.5, 10.6), PQN – and not SNV – was used as the normalization method. And of course, the most logical conclusion would be to say that this difference in models' performance is simply due to the varying spectral ranges used to construct the LR models. In other words, that variants A and C, covering the ranges 1200–1410 cm^1 and 1200–1300 cm^1 combined with 950–1020 cm^{-1}, respectively, are characterized by bands that exhibit the most pronounced time-related variations (high values of b^2/w^2 ratios). This would confirm the results from the first part of the study, shown, for example, in Figure 9.12. However, if that was the only case, similar performance models should be obtained for a similar spectral range D, consisting of 1200–1410 cm^{-1} and 950–1020 cm^{-1} regions, where different pre-processing techniques were applied depending on the selection of training and test datasets. Nevertheless, here once again, more effective models (lower false negative responses and ECE values) are generated when PQN is used as the normalization method. Hence it seems that the outcome depends more on the pre-processing than the chosen spectral range. This becomes evident by comparing the blue boxplots characterizing the false negatives in Figure 10.4 and ECE plots in Figure 10.5D and 10.6D.

Having outlined a pre-processing strategy that remarkably supports discrimination of differently-aged blood traces, another objective (indicated in the third point) pursued in the present dissertation was achieved:

1. Development of a Raman-based analytical method allowing for non-invasive and representative probing of the chemical composition of degrading bloodstains.
2. Collection of the spectral signatures of blood traces over the desired aging period.
3. Setting out a chemometric strategy for the pre-processing of obtained Raman spectra.
4. Designing the LR models for solving the comparison problem between the questioned bloodstain and the reference material(s) created "artificially."
5. Development of the LR models validation protocol.

[‡‡‡‡‡] As a reminder, it should be added that the illustration of the LR model's performance is reflected in the relative position of all three ECE curves. When the experimental curve lies between the neutral and calibrated curves, the reduction of information loss due to the model in regard to neutral curve (LR = 1) is observed. In general, the lower the experimental curve is located, the better the performance of the LR model as it explains more information.

TABLE 10.3. Pre-processing strategies applied to sets °1 and °2 found using a genetic algorithm (GA).

		RECOVERED: SET °1, REFERENCE: SET °2	RECOVERED: SET °2, REFERENCE: SET °1
Spectral range **A** 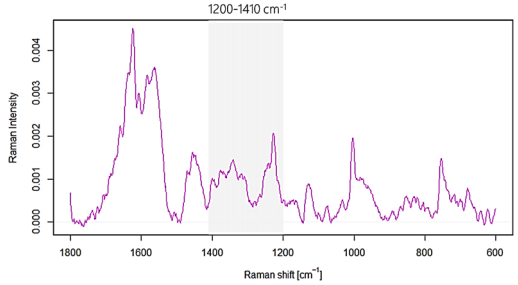	denoising	SG, polynomial degree $p = 3$	DWT, Daubechies Least Asymmetric 4 $d = 10$, t = universal, c = soft, sd = mad
	baseline correction	SNIP, clipping window $w = 26$	RBE, $h = 0.4$, $b = 2$
	normalization	PQN	PQN
Spectral range **B** 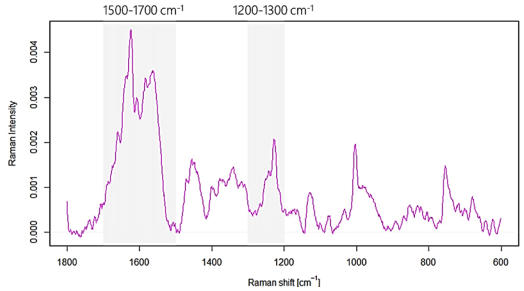	denoising	DWT, Daubechies Least Asymmetric 8 $d = 10$, t = SURE, c = soft, sd = mad	DWT, Coiflets 1 $d = 10$, t = universal, c = soft, sd = mad
	baseline correction	CWTAsWPLS, $m = 2$, $\lambda = 1 \cdot 10^8$	polyQR, polynomial degree $p = 5$, $q = 0.05$
	normalization	SNV	SNV
Spectral range **C** 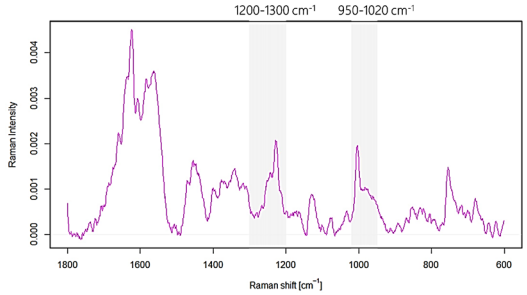	denoising	DWT, Coiflets 5 $d = 10$, t = universal, c = soft, sd = mad	DWT, Daubechies Least Asymmetric 4 $d = 10$, t = SURE, c = soft, sd = mad
	baseline correction	RBE, $h = 0.4$, $b = 2.2$	RBE, $h = 0.3$, $b = 2.5$
	normalization	PQN	PQN

d – decomposition level for denoising, t – threshold estimation, c – thresholding policy, sd – dispersion estimate, m – order of differences, λ – penalty, h – the proportion of signal points for the local regression, b – robustness parameter, q - quantile

TABLE 10.3. (continued)

		RECOVERED: SET °1, REFERENCE: SET °2	RECOVERED: SET °2, REFERENCE: SET °1
Spectral range **D** 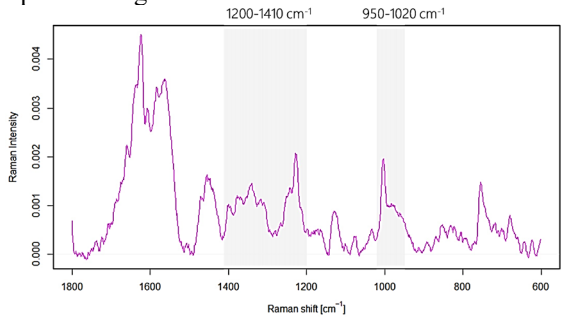	denoising	DWT, Coiflets 5 d = 10, t = universal, c = soft, sd = mad	DWT, Coiflets 1 d = 10, t = SURE, c = soft, sd = mad
	baseline correction	multiWAsPLS, m = 2, $\lambda = 1 \cdot 10^9$	polyQR, polynomial degree p = 5, q = 0.05
	normalization	SNV	PQN
Spectral range **E** 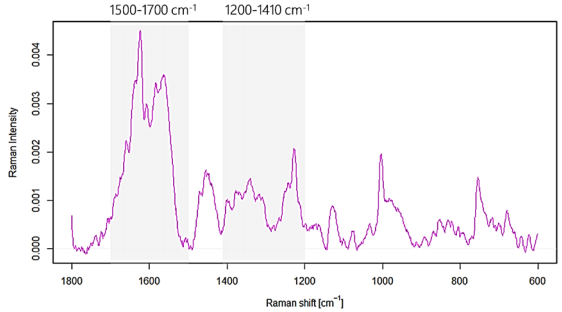	denoising	SG, polynomial degree p = 3	SG, polynomial degree p = 5
	baseline correction	polyQR, polynomial degree p = 6, q = 0.01	pWAsPLS, m = 2, $\lambda = 1 \cdot 10^6$, w = 0.001
	normalization	SNV	SNV
Spectral range **F** 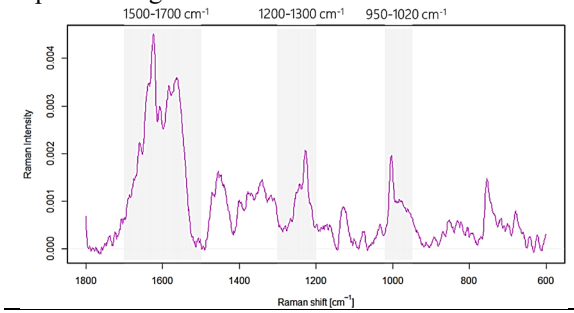	denoising	DWT, Daubechies Least Asymmetric 4 d = 10, t = universal, c = soft, sd = mad	DWT, Daubechies Least Asymmetric 8 d = 10, t = SURE, c = soft, sd = mad
	baseline correction	CWTAsWPLS, m = 2, $\lambda = 2 \cdot 10^8$	SNIP, clipping window w = 30
	normalization	SNV	SNV

d – decomposition level for denoising, t – threshold estimation, c – thresholding policy, sd – dispersion estimate, m – order of differences, λ – penalty, μ – penalty term, q – quantile, w - weights

TABLE 10.3. (continued)

		RECOVERED: SET °1, REFERENCE: SET °2	RECOVERED: SET °2, REFERENCE: SET °1
Spectral range **G** 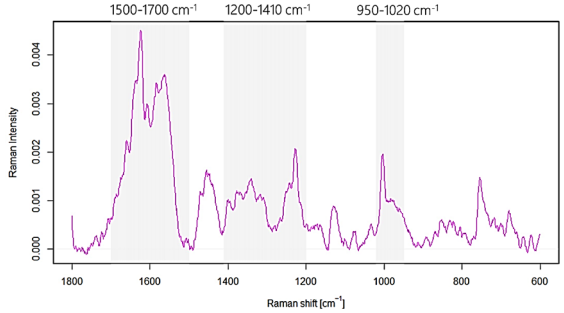	denoising	SG, polynomial degree p = 4	DWT, Coiflets 1 d = 10, t = SURE, c = soft, sd = mad
	baseline correction	SNIP, clipping window w = 26	multiWAsPLS, m = 2, λ = 10, $\mu = 1 \cdot 10^8$
	normalization	SNV	SNV

d – decomposition level for denoising, t – threshold estimation, c – thresholding policy, sd – dispersion estimate, m – order of differences, λ – penalty, μ – penalty term

10.2.1.2 Validation of the likelihood ratio models

Figure 10.4 comprehensively portrays the overall performance of the LR models under investigation, computed using the first database (set °1) for training the model and obtaining the reference bloodstain samples, the second one (set °2) employed as the source of recovered bloodstains (testing the LR models), and vice versa. Each boxplot indicated in a different color corresponds to a different spectral range used for developing the model (from A to G defined in Figure 10.3) and depicts the false positive as well as false negative outcomes yielded from all ten test sets (as the procedure of selecting training and test datasets was repeated ten times).

The general findings (also demonstrated in Table 10.4) expose that false positive (FP) rates obtained for each of the seven model variants are somewhat more comparable to each other than the levels of false negative (FN) answers (note the scale on the *y*-axis). FP oscillated around 20%, and the dispersion of results within each model is not as evident as in the case of FN.

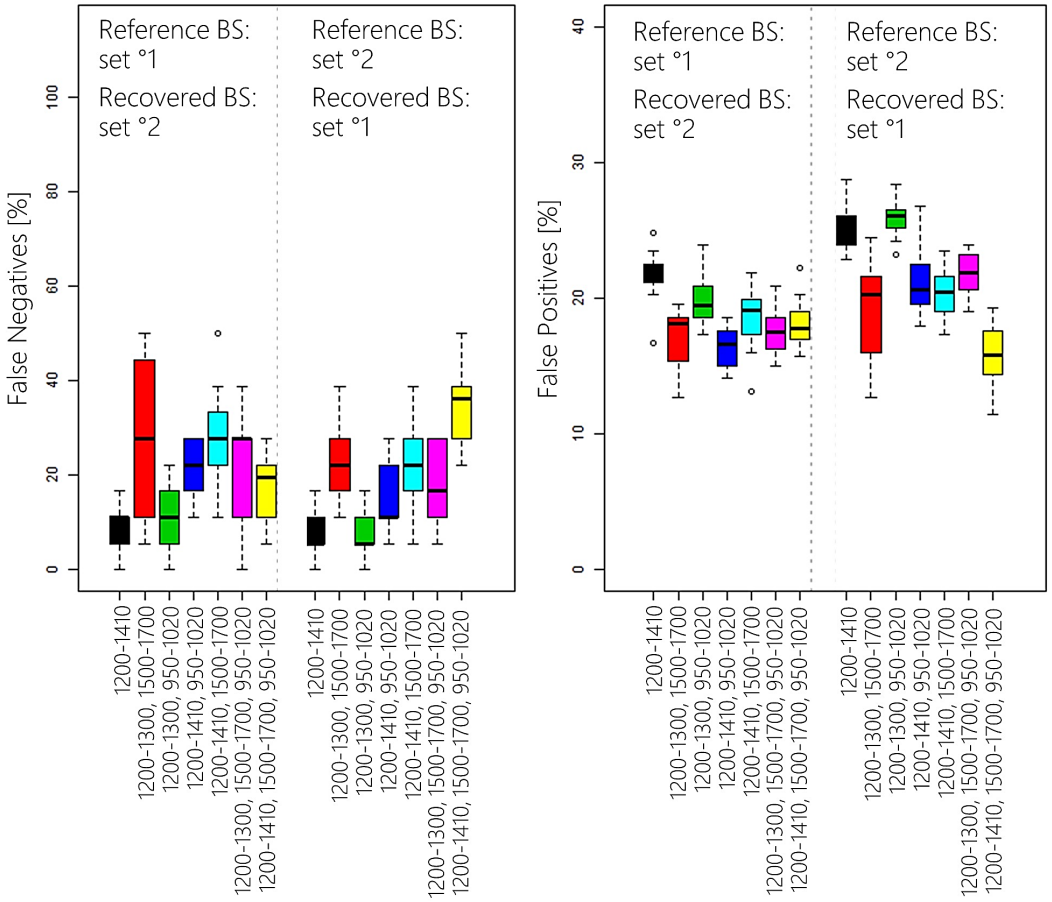

FIGURE 10.4.

The levels of false negative and false positive responses of LR models constructed for Raman spectra of bloodstains prepared using the preprocessing strategies indicated by the genetic algorithm (GA).

TABLE 10.4. Performances of developed LR models based on different spectral ranges (A–G) assessed through the mean values of false positive and false negative rates.

LR models based on the spectral range [cm^{-1}]	RECOVERED: SET °1, REFERENCE: SET °2		RECOVERED: SET °2, REFERENCE: SET °1	
	False negatives [%]	False positives [%]	False negatives [%]	False positives [%]
A: 1200-1410	**9.45***	21.62	**6.67**	25.26
B: 1200-1300; 1500-1700	27.77	17.22	22.22	19.35
C: 1200-1300; 950-1020	**11.12**	20.03	**7.78**	25.94
D: 1200-1410; 950-1020	22.23	16.42	13.88	21.54
E: 1200-1410; 1500-1700	28.33	18.51	22.22	20.36
F: 1200-1300; 1500-1700; 950-1020;	22.23	17.64	16.68	21.75
G: 1200-1410; 1500-1700; 950-1020;	17.22	18.17	35.55	15.94

*Bolded values indicate the lowest false negative rates obtained.

This observation can be easily explained by a high similarity of compared bloodstain samples at a more advanced stage of degradation. Inconsiderable differences between the spectral characteristics of blood traces, a consequence of a slow-down in the aging process, appear to equally affect the LR models' capability to distinguish between differently-aged samples, leading to the increase in the levels of FP answers. The observed misleading support toward the hypothesis about the common source of bloodstains (H_1) obviously cannot be reduced by implementing any other pre-processing techniques or signals manipulation in general. This is because the factor that really determines the FP answers here is the rate of blood degradation itself and the ability to monitor it with a given analytical technique. Moreover, reporting FP responses over the entire analyzed aging period is simply pointless due to its low information content. It should be clear that the longer the degradation time, the higher percentage of incorrect answers will be obtained. Consequently, it is much more reasonable to present the FP rates in relation to time elapsed since bloodstains deposition. An example of such dependency for LR models developed for spectral range A and B is shown in Figures 10.5A and 10.5 B, respectively. The percentage of correctly distinguished differently-aged blood traces plotted against the aging time indicates that both models' usefulness significantly decreases after about 170 hours (approx. seven days) of degradation. As can be seen, even though the overall performance of these models is entirely different (due to FN

rates, 9.45% and 27.77% for models A and B, respectively), their ability to correctly discriminate between differently-aged samples over time is relatively similar.

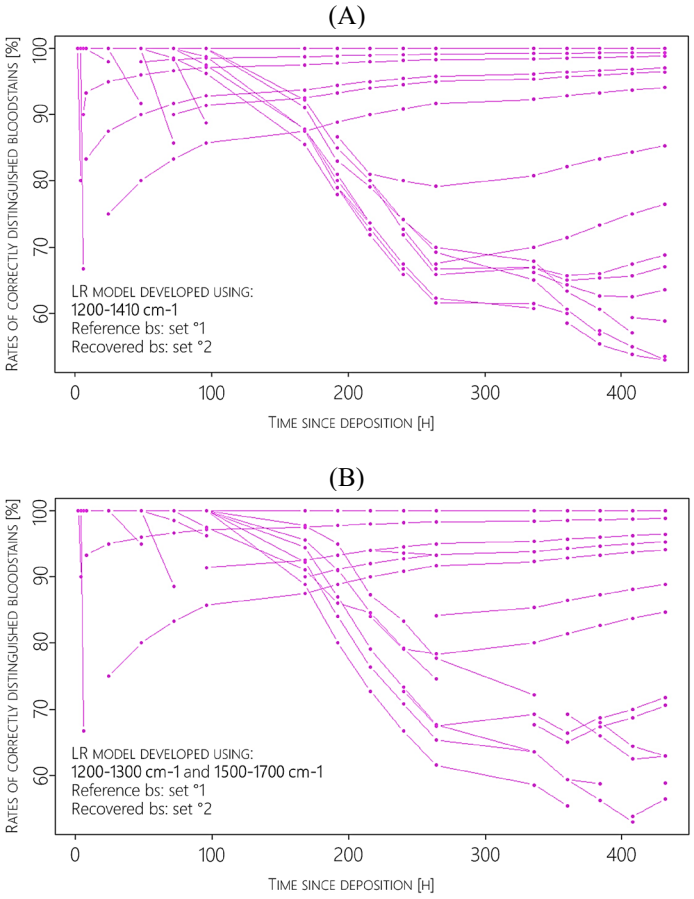

FIGURE 10.5.

The percentage of correctly distinguished differently-aged blood traces in the function of aging time [h] obtained when using LR models developed for spectral range A (A) and B (B).

Consequently, the factor that will actually differentiate the developed LR models concerning their effectiveness in solving the considered comparison problem will be the already mentioned reduction of within-source variations, reflected in the percentage of false negative answers. After inspection of boxplots in Figure 10.4 corresponding to FN responses and Table 10.4, it becomes clear that LR models based on PQN-normalized spectral ranges A (1200–1410 cm^{-1}) and C (1200–1300 cm^{-1} combined with 950–1020 cm^{-1}) outperform the remaining LR models. False negatives rates for these two models' variants (bolded in the above Table 10.4) are less dispersed and oscillate around 10%, while for the remaining spectral ranges, they reach ca. 30%. Thus, once again, it turns out that from the dating perspective, the most informative Raman features are the Hb aggregation markers (e.g., 1255 cm^{-1} or 976 cm^{-1}) and so-called oxidation markers located between 1300–1400 cm^{-1} (see *5.1.3.3 Vibrations associated with prosthetic groups of proteins – iron protoporphyrin IX*). Interestingly, the greater the proportion of the 1500–1700 cm^{-1} range in the model being developed, the worse its performance. An example of this is an LR model developed based on spectral range B, namely 1200–1300 cm^{-1} combined

with 1500–1700 cm^{-1}. This may suggest that bands occurring in this range, which contains the core-size and spin state markers (see *5.1.3.3 Vibrations associated with prosthetic groups of proteins – iron protoporphyrin IX*), are more susceptible to random variation (e.g., resulting from dietary factors) than changes due to bloodstains aging.

Finally, Figures 10.6 and 10.7 present the empirical cross entropy plots in a modified way compared to standard ECE curves introduced in the theoretical part of the thesis. In this case, the experimental and calibrated curves (indicated in red and blue, respectively) are replaced by the sets of boxplots positioned at the considered prior odds. Each boxplot accounts for the ECE values calculated for a given prior odds using the available likelihood ratio values. Figures 10.6 and 10.7 portray LR models' performance for seven different spectral ranges (A–G).

The ECE plots prove that LR models based on spectral ranges A (1200–1410 cm^{-1}) and C (1200–1300 cm^{-1} combined with 950–1020 cm^{-1}) demonstrate the most desirable performances. For these models, the reduction of information loss (or gain of information) reaches even ca. 50% (e.g., Figure 10.7A), which given the small databases, is a relatively acceptable outcome. In other words, it means that after the bloodstain evidence analysis using developed LR models, a relatively large amount of information concerning the uncertainty about the correct hypotheses was explained. The ECE values also evidenced that the models based on 1500–1700 cm^{-1}-containing regions were indisputably the worst solutions. Not only did they deliver the highest rates of false negative answers, but they also yielded incomparably inferior ECE outcomes. Therefore, employing these models for bloodstains' age evaluation may lead to more misleading conclusions than when the samples are not investigated at all, assuming the neutrality of the likelihood ratio values (LR = 1). It should also be noted that in the case of poorly performing models, the ECE plots deviated from the desired bell-shaped curves. The ECE values went beyond the neutral curve, especially for the positive logarithm of the prior odds, i.e., $\log_{10}\text{Odds}(H_1) > 0$. This deterioration may be caused by only a single sample delivering strong misleading support towards the incorrect hypothesis (in this case – H_1). Despite all the aforementioned merits of the ECE, it is quite a common problem. It should be remembered that this methodology somehow lacks robustness, as it is susceptible to even a single LR value that provides strong support for the incorrect scenario. In particular, when small databases are considered, the penalty assigned to a misleading LR value might outweigh the importance given to the LRs supporting the correct hypothesis. Therefore, examiners dealing with scarce databases should be urged to investigate the ECE results with extreme caution. For this reason, it might also be interesting to explore the problem further in the future, trying to verify whether the obtained poor LR model performance, assessed using the ECE approach, may be caused by just a single misleading value.

What is more, some differences between the experimental and calibrated ECE plots, obtained even for well-performing models (e.g., Figures 10.6A or 10.6C), hold promise for improving the models' effectiveness. The simplest way to refine the model may be to expand its databases to capture better all the relevant features characteristic for the whole population of the analyzed bloodstains.

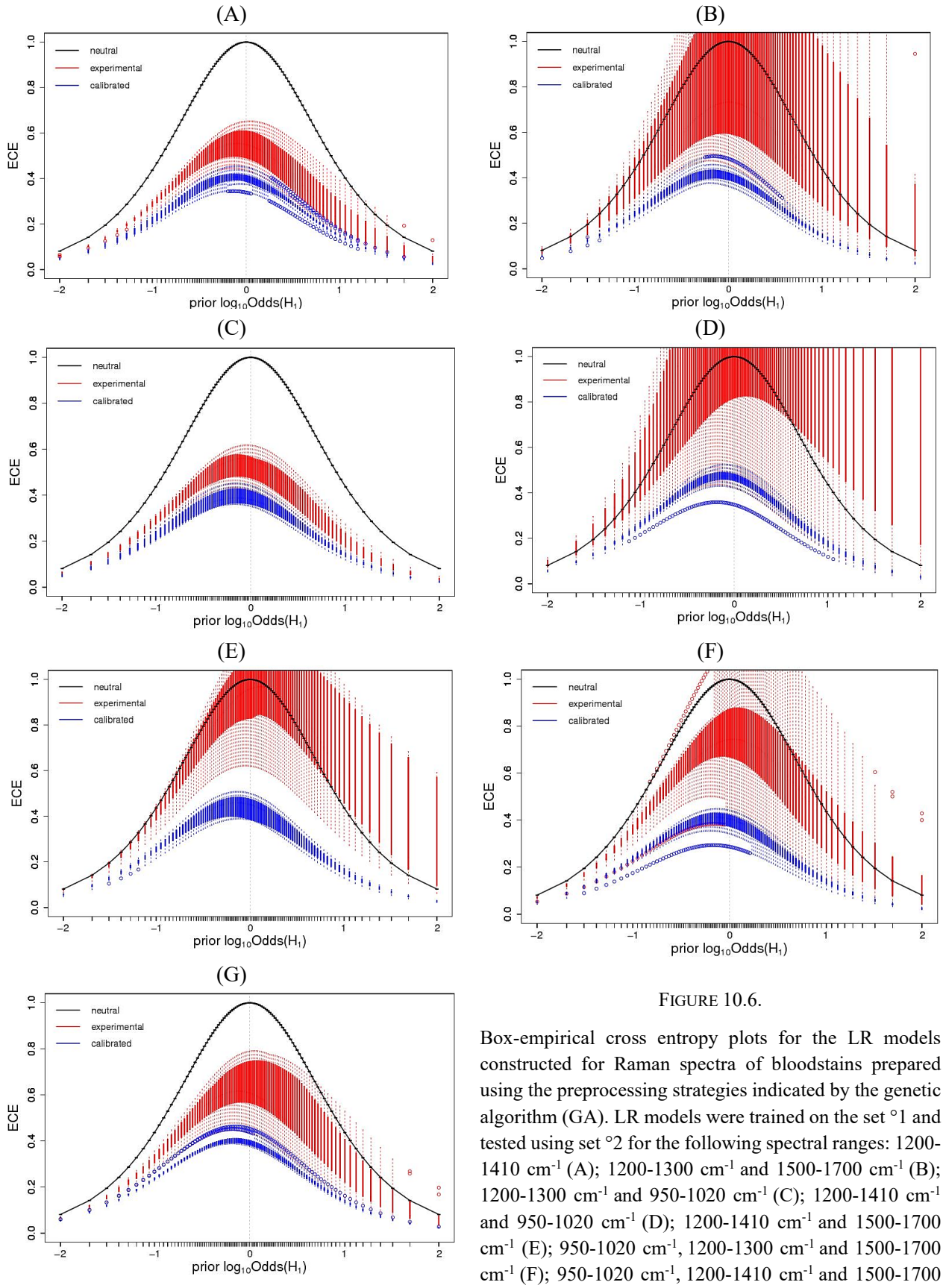

FIGURE 10.6.

Box-empirical cross entropy plots for the LR models constructed for Raman spectra of bloodstains prepared using the preprocessing strategies indicated by the genetic algorithm (GA). LR models were trained on the set °1 and tested using set °2 for the following spectral ranges: 1200-1410 cm^{-1} (A); 1200-1300 cm^{-1} and 1500-1700 cm^{-1} (B); 1200-1300 cm^{-1} and 950-1020 cm^{-1} (C); 1200-1410 cm^{-1} and 950-1020 cm^{-1} (D); 1200-1410 cm^{-1} and 1500-1700 cm^{-1} (E); 950-1020 cm^{-1}, 1200-1300 cm^{-1} and 1500-1700 cm^{-1} (F); 950-1020 cm^{-1}, 1200-1410 cm^{-1} and 1500-1700 cm^{-1} (G).

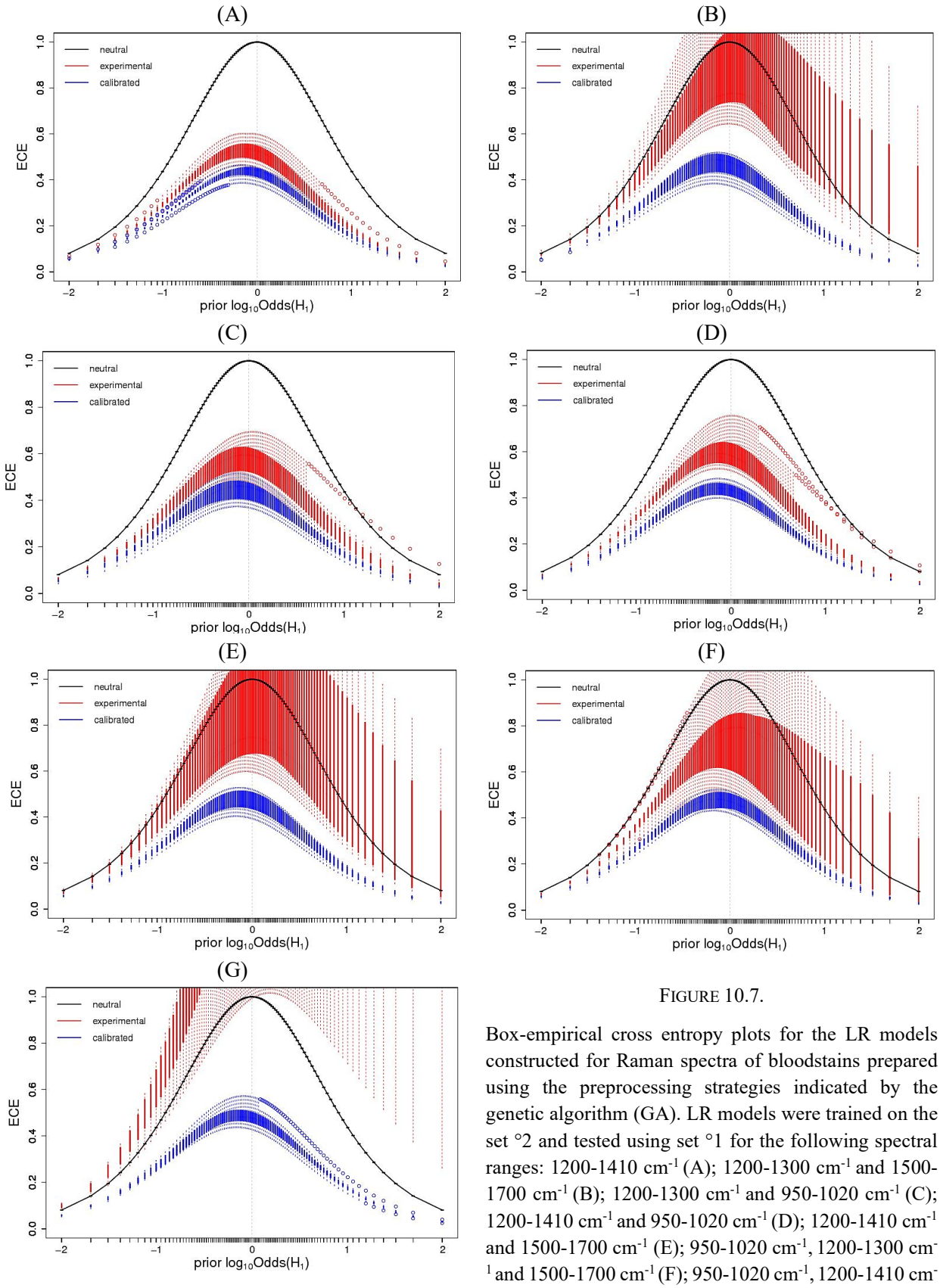

FIGURE 10.7.

Box-empirical cross entropy plots for the LR models constructed for Raman spectra of bloodstains prepared using the preprocessing strategies indicated by the genetic algorithm (GA). LR models were trained on the set °2 and tested using set °1 for the following spectral ranges: 1200-1410 cm^{-1} (A); 1200-1300 cm^{-1} and 1500-1700 cm^{-1} (B); 1200-1300 cm^{-1} and 950-1020 cm^{-1} (C); 1200-1410 cm^{-1} and 950-1020 cm^{-1} (D); 1200-1410 cm^{-1} and 1500-1700 cm^{-1} (E); 950-1020 cm^{-1}, 1200-1300 cm^{-1} and 1500-1700 cm^{-1} (F); 950-1020 cm^{-1}, 1200-1410 cm^{-1} and 1500-1700 cm^{-1} (G).

Nonetheless, even if LR models developed in this thesis were based on scarce datasets, the provided results for best-performing models were deemed satisfactory. It would be naive to expect impeccable results. The obtained values will always be affected by errors. However, it would be way more erroneous to completely ignore database features than to apply the LR approach based on small databases.

10.2.2 Increasing the data variability – implementation of set °3 in LR models development

Likelihood ratio models based on two bloodstains databases (set °1 and set °2), employed in the previous subchapter, can be viewed as preliminary results in support of the feasibility of the novel dating approach. However, as already described in the *Materials and Methods* section, and more precisely in *10.1.1. Samples preparation*, apart from these two sets of bloodstains, which were degrading under comparable storage conditions during the first day of the aging process, a third database (set °3) was also prepared and subjected to supervised degradation. Unlike the previous bloodstains, the samples constituting the third database of blood traces were deposited under relatively higher temperature conditions. It is worth recalling that while in the case of bloodstains' sets °1 and °2, the temperature was 23.5 °C and 22.8°C, respectively, the set °3 was created when the temperature in the laboratory equaled 30.8 °C. Hence, instead of dismissing these results, they were treated as an opportunity to study the impact of such a short-term variation in the aging conditions on the performance of LR models. Of course, this minor deviation from the main analytical route of the thesis cannot be termed as a comprehensive study. On the contrary, there is no doubt that it is rather superficial. Nevertheless, it might provide valuable insight into the robustness of the proposed approach, setting the direction for further research.

Similar to Raman spectra constituting the first two databases, before developing LR models encompassing the third collection of samples, instrumental signals characterizing bloodstains were subjected to pre-processing guided by the genetic algorithm. The selected pre-processing methods are summarized in Tables 10.5 and 10.6, depending on the combination of the training and test sets used. As can be seen from the tables provided, at this stage of the discussion, attention will only be paid to the models that have previously been characterized by the best performance metrics, namely those based on the spectral range A and spectral range C, corresponding to 1200–1410 cm^{-1} and 1200–1300 cm^{-1} combined with 950–1020 cm^{-1}, respectively. The performance characteristics of the remaining LR models (developed for spectral ranges B, D–G), together with the pre-processing strategies used for signal preparation, can be found in *Appendix A*.

TABLE 10.5. Pre-processing strategies applied to sets °1 and °3 found using a genetic algorithm (GA).

		RECOVERED: SET °1, REFERENCE: SET °3	RECOVERED: SET °3, REFERENCE: SET °1
Spectral range A 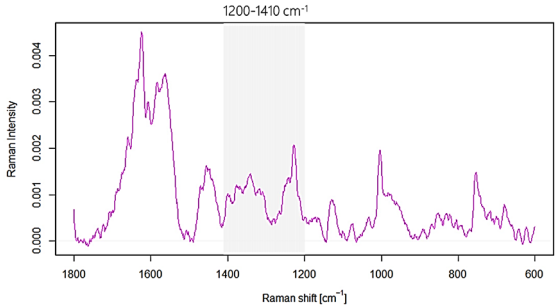	denoising	SG, polynomial degree p = 4	SG, polynomial degree p = 3
	baseline correction	SNIP, clipping window w = 26	SNIP, clipping window w = 26
	normalization	SNV	PQN
Spectral range C 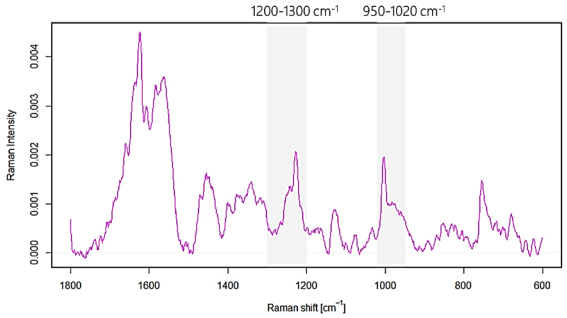	denoising	DWT, Daubechies Least Asymmetric 4 d = 10, t = universal, c = soft, sd = mad	DWT, Coiflets 5 d = 10, t = universal, c = soft, sd = mad
	baseline correction	RBE, h = 0.3, b = 2.5	RBE, h = 0.4, b = 2.2
	normalization	PQN	PQN

d – decomposition level for denoising, t – threshold estimation, c – thresholding policy, sd – dispersion estimate, m – order of differences, λ – penalty, q – quantile, w – weights, p – polynomial degree, h – the proportion of signal points for local regression, b – robustness parameter

TABLE 10.6. Pre-processing strategies applied to sets °2 and °3 found using a genetic algorithm (GA).

		RECOVERED: SET °1, REFERENCE: SET °3	RECOVERED: SET °3, REFERENCE: SET °1
Spectral range A 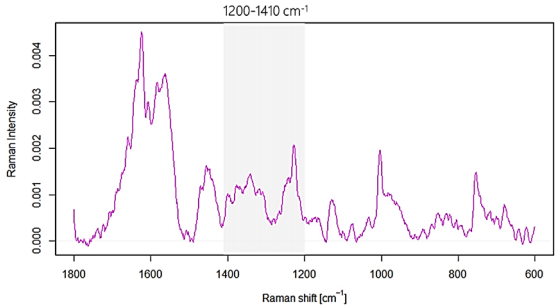	denoising	SG, polynomial degree p = 4	DWT, Daubechies Least Asymmetric 4 d = 10, t = universal, c = soft, sd = mad
	baseline correction	SNIP, clipping window w = 26	RBE, h = 0.4, b = 2
	normalization	SNV	PQN
Spectral range C 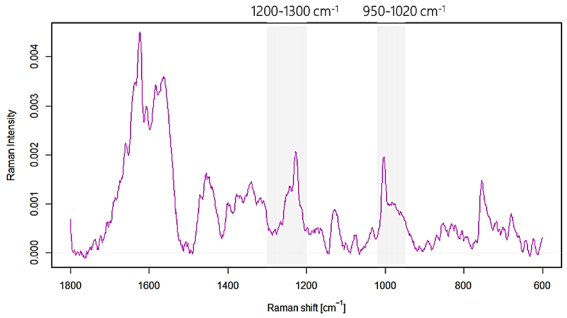	denoising	DWT, Daubechies Least Asymmetric 4 d = 10, t = universal, c = hard, sd = mad	DWT, Daubechies Least Asymmetric 4 d = 10, t = SURE, c = soft, sd = mad
	baseline correction	RBE, h = 0.3, b = 2.5	RBE, h = 0.3, b = 2.5
	normalization	PQN	PQN

d – decomposition level for denoising, t – threshold estimation, c – thresholding policy, sd – dispersion estimate, q – quantile, w – weights, p – polynomial degree, h – the proportion of signal points for local regression, b – robustness parameter

The outcomes of the obtained LR models, once again, are presented in the form of mean values of false positive and false negative rates (Table 10.7).

TABLE 10.7. Performances of developed LR models based on the spectral ranges A and C assessed through the mean values of false positive and false negative rates.

LR models based on the spectral range [cm^{-1}]	**False negatives [%]**		**False positives [%]**	
	Recovered: set °1 Reference: set °3	Recovered: set °3 Reference: set °1	Recovered: set °1 Reference: set °3	Recovered: set °3 Reference: set °1
A: 1200–1410	**23.90***	**17.22**	27.05	25.23
C: 1200–1300; 950–1020	37.78	42.22	24.03	22.03
	Recovered: set °2 Reference: set °3	Recovered: set °3 Reference: set °2	Recovered: set °2 Reference: set °3	Recovered: set °3 Reference: set °2
A: 1200–1410	56.12	54.44	22.31	23.34
C: 1200–1300; 950–1020	76.12	63.89	18.53	22.16

*Bolded values indicate the lowest false negative rates obtained.

The performance of each LR model was also evaluated by applying the ECE approach (Figures 10.8 and 10.9). Unfortunately, even a cursory glance at these results leaves no illusions: LR models developed after implementation of the third set deteriorated considerably. Also, this time, no significant differences between the false positive responses characterizing different LR models were observed. Thus, the factor determining the effectiveness of models in solving the comparison problem, once again, will be the rate of incorrect discrimination of bloodstains characterized by the same age (false negative answers). Should it come as a surprise? Not necessarily. After all, by introducing a set of bloodstains, most likely characterized by different aging kinetics (due to temperature difference), the variability of Raman signatures of blood traces corresponding to the same TSD might have been increased, contributing to elevated false negative rates.

When databases denoted as set °1 and set °3 were used for training and testing the models, the best outcomes were obtained for spectral range A (1200–1410 cm^{-1}), confirming the earlier findings concerning the amount of time-related information encrypted in different parts of Raman signatures (see *10.2.1.2 Validation of the likelihood ratio models*). Nevertheless, false negative answers, oscillating around 20%, were almost twice as high as in the case of models based on set °1 and set °2, developed previously. According to the ECE plots (Figures 10.8A and 10.8C), these LR models managed to reduce the information loss from 100% to approximately 60% at best, which can hardly be considered satisfactory.

Moving on to the following combinations, namely the LR models trained and tested using sets°2 and °3, the situation is only getting worse. Even though the spectral range A still provides the lowest rates of false negatives, using the term “the lowest” in this context is an oxymoron. The rates of incorrect discrimination of the equally-aged bloodstains are skyrocketing as they reach almost 60%. The poor performance of developed models is also readily observable in the ECE plots shown in Figure 10.9. This indicates that neither of the models developed after implementing the set °3 in the calculation run can be regarded as an effective method for estimating the age of bloodstains; hence their application in the practical proceedings would be completely nonsensical.

The deterioration of LR models presented in this subsection, relative to those developed for bloodstains degrading under relatively the same conditions (sets °1 and °2), should not be surprising. What may be puzzling, though, is the significant difference between the models trained and tested using the set °1 together with the set °3, and the set °2 combined with the °3. The observed disproportion between false negatives rates indicates that there must be at least one additional source of variability that interfered with the dynamics of the aging process in addition to the temperature factor. To suggest a potential answer, let us consider again Figure 10.1 depicting the general scheme of the supervised aging process of these three different bloodstains sets. From the figure, it can be presumed that a different initial composition might have characterized blood traces included in these databases, as they were deposited in three consecutive months. Unfortunately, the biochemical composition of deposited blood was in no way controlled during the study, making it difficult to draw any conclusions that are not just informative guesses. There is no doubt, however, that the aspect of blood variability requires further investigation. One cannot simply assume that the process of blood degradation will always follow the same pathways, irrespective of the donor condition. Not to mention the donor-to-donor variations in the case of lack of the suspect. And suppose it turns out that the aging kinetics is strongly influenced by the biochemical composition of blood, which reflects dietary factors, health condition, or even lifestyle. In that case, any attempts to apply the novel dating approach in forensic practice will hardly be possible to achieve.

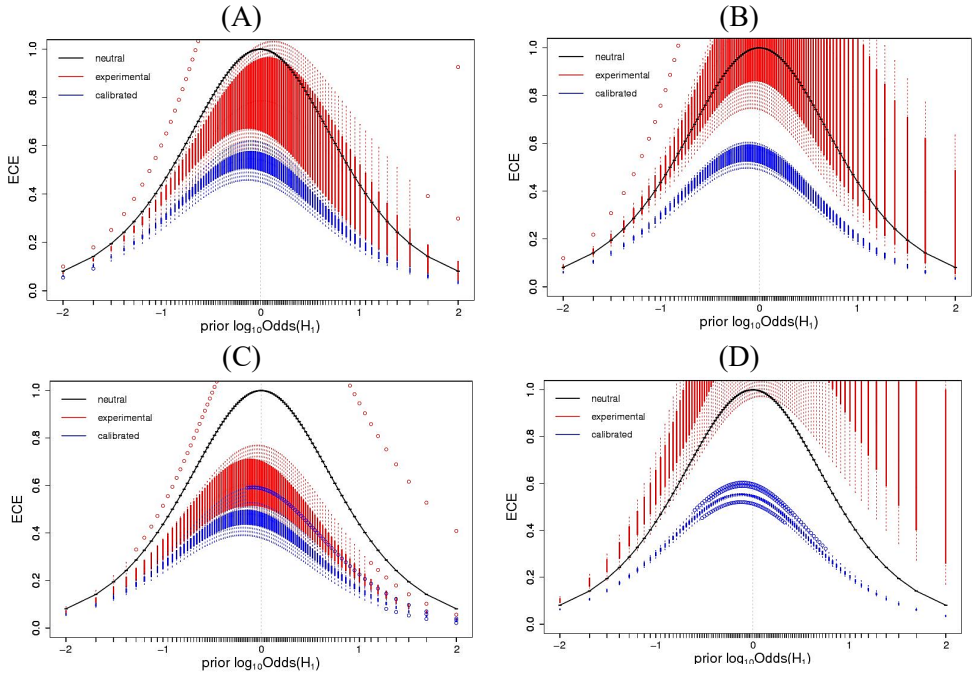

FIGURE 10.8.

Box-empirical cross entropy plots for the LR models constructed for Raman spectra of bloodstains prepared using the preprocessing strategies indicated by the genetic algorithm (GA). The first two LR models were trained on the set °1 and tested using set °3 for the following spectral ranges: 1200-1410 cm^{-1} (A); 1200-1300 cm^{-1} and 950-1020 cm^{-1} (B). For the remaining two, LR models were trained on the set °3 and tested using set °1 for the following spectral ranges: 1200-1410 cm^{-1} (C); 1200-1300 cm^{-1} and 950-1020 cm^{-1} (D).

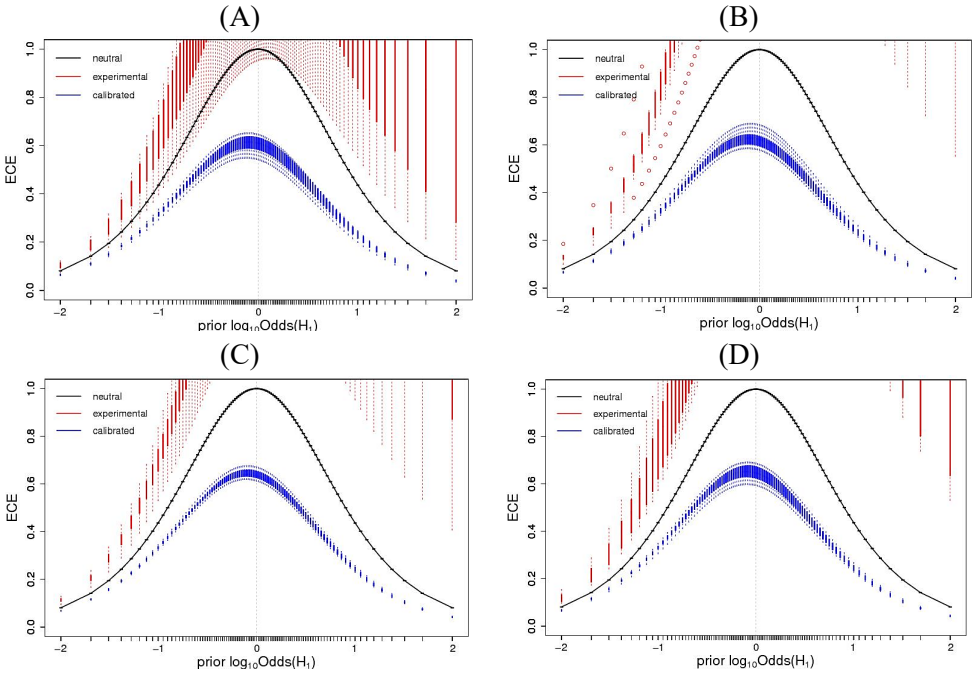

FIGURE 10.9.

Box-empirical cross entropy plots for the LR models constructed for Raman spectra of bloodstains prepared using the preprocessing strategies indicated by the genetic algorithm (GA). The first two LR models were trained on the set °2 and tested using set °3 for the following spectral ranges: 1200-1410 cm^{-1} (A); 1200-1300 cm^{-1} and 950-1020 cm^{-1} (B). For the remaining two, LR models were trained on the set °3 and tested using set °2 for the following spectral ranges: 1200-1410 cm^{-1} (C); 1200-1300 cm^{-1} and 950-1020 cm^{-1} (D).

10.3 Conclusions

The task undertaken in the final experimental chapter of the present thesis was focused on substituting a case-suited comparison problem for the conventional dating approach to address the impediments resulting from the variability of aging kinetics. In order to do so, a strategy named a MODIFIED RELATIVE DATING APPROACH was developed and validated. Its critical aspect was based on estimating the (dis)similarity between the stage of evidence decomposition and sets of reference materials obtained through supervised aging using likelihood ratio models. In other words, *Chapter 10* addressed the two final objectives of the thesis:

All the research stages can be summarized in the following key elements:

1. Development of a Raman-based analytical method allowing for non-invasive and representative probing of the chemical composition of degrading bloodstains.
2. Collection of the spectral signatures of blood traces over the desired aging period.
3. Setting out a chemometric strategy for the pre-processing of obtained Raman spectra.
4. Designing the LR models for solving the comparison problem between the questioned bloodstain and the reference material(s) created "artificially."
5. Development of the LR models validation protocol.

The results presented in this chapter provided preliminary confirmation of the effectiveness of the proposed dating approach. The LR models for solving the comparison problem between the questioned bloodstain and the reference material(s) created "artificially" were deemed satisfactory provided that samples used for training and validating models were characterized by similar aging kinetics. This requirement can be met in practical terms by strictly controlling the degradation conditions (such as temperature, relative humidity, or even light exposure), which should be as close as possible to those during the alleged aging of evidential bloodstains.

Unfortunately, as could have been expected, even minor changes in the supervised aging procedure (such as observed difference in temperature during the first day of degradation) might have contributed to alteration in degradation kinetics of reference materials. In turn, such an increase in data variability led to a significant deterioration of LR models' performance. Obviously, obtained results do not prejudge the future position of the proposed dating approach as they are simply insufficient to draw firm conclusions. However, it is just realistic to presume that providing reference materials as similar as possible to the evidence deposited during the alleged offense[§§§§§] is the key to success with the modified relative dating approach. Thus, future research efforts should identify factors that may affect the

[§§§§§] Both in terms of their initial compositions and aging kinetics.

bloodstains' degradation because precisely these factors should be strictly regulated during supervised aging. And while the influence of environmental factors may be controlled with relatively high precision (e.g., by introducing a climatic chamber to simulate specific storage conditions), regulating other influential factors (primarily the initial composition of blood) may pose a substantial problem. And this slightly pessimistic conclusion leaves a question mark over the validity of the proposed dating approach and its practical potential, especially in a situation of belated identification of the potential bloodstains' "donor."

| *CHAPTER 11*

SUMMARY AND FUTURE PERSPECTIVES

Despite the best efforts, there will always be a gap between what is (what we know) and what should be (what we want to know). In this sense, science is utopian. Just like many assumptions and objectives formulated at the beginning of each new research journey. It does not mean, however, that the time and effort invested in the development of these (at times naïve) concepts turn out to be lost. Properly conducted study always somehow complements our knowledge – if not by providing direct answers, then at least by eliminating certain doubts about our understanding of the issue at hand. How, then, has the research presented in this thesis influenced our perception of what is possible regarding bloodstains dating? Let us take a final look.

Forensic investigation of blood traces enables the acquisition of a whole host of "profiling" information, making it easier to identify the person of interest. Nevertheless, in order to demonstrate any evidential value of such a trace, a link to a crime has to be established. The more incontestable this link is, the better. Therefore, to strengthen the trace-crime connection, information about bloodstain's age, provided by estimating time elapsed since its deposition (TSD), is often a crucial piece of the puzzle. Dozens of researchers, without success so far, attempted to provide reliable dating methods by probing different aspects of the aging process. Due to these failed trials combined with the high forensic value of sought information, the bloodstains age estimation method is still considered a *holy grail* of forensic science, which was also pursued throughout this thesis.

The objective of the presented research was to verify the possibility of estimating the age of blood deposits – characterized by Raman signatures – through their comparison with "artificially" created reference materials. Thus, the conventional quest for the bloodstains dating method, based on regression analysis, was replaced with a discrimination problem, solvable through the likelihood ratio approach. The implementation of the proposed framework obviously requires an alternative hypothesis on the course of events, in addition to the one formulated by the prosecutor. This is because instead of providing a direct answer to the question *When was the bloodstain deposited?,* forensic expert indicates which of the reference materials – the one prepared according to the prosecutor's or the defense's scenario – is more similar[******] to the evidentiary sample. Hence, from an interpretative point of view, the application of the discussed dating framework is rather limited to the evaluative stage of the forensic process, where the analytical findings are used to assess different available hypotheses regarding the same criminal event. Surprisingly, such an endeavor has never been attempted or at least never reported in the literature.

[******] In their degree of degradation.

The problem addressed in the present thesis was twofold. The **FIRST PART** was aimed to **DEVELOP AN ANALYTICAL METHOD SERVING AS A TOOL FOR PROBING THE STATE OF BLOODSTAINS DEGRADATION** (*Chapter 9*). The choice of **RAMAN SPECTROSCOPY**, coherent with the technique's maturation as a potent tool in analyzing biospecimens, **TURNED OUT TO BE THE RIGHT ONE**. The crucial piece of information here was that Raman spectra exhibited clear time-dependency. Changes in spectral characteristics, reflected mainly in such spectral features as hemoglobin aggregation (1255 cm^{-1} and 976 cm^{-1}) and oxidation markers (between 1300–1400 cm^{-1}), are well-recognized effects of the formation of Hb degradation products. Additionally, to circumvent limitations experienced with single-point measurements, namely the risk of laser-induced degradation of hemoglobin and subsampling errors, the rotating mode of spectral acquisition was introduced, which significantly streamlined the measurement process. The combination of these features with the non-destructiveness of the method and the availability of Raman spectrometers in most forensic laboratories makes it ideally suited for casework applications. However, does it mean that Raman spectroscopy can be considered a panacea for tracing blood degradation processes? The answer is: not always. Despite its indisputable merits, Raman spectroscopy is not, and will probably never be, the ideal method for dating blood traces.

Perhaps the most significant disadvantage of Raman spectroscopy is the time scope of its applicability. In this study, the performance of LR models developed on the basis of Raman signatures understood in terms of their ability to discriminate between differently-aged blood traces significantly deteriorated after approximately seven days of degradation. And even if the applicability of the Raman signatures in the dating procedure could be extended through some improvements, e.g., in better selection of time-dependent spectral features, there still will be a problem of increasing baseline. It has been observed that as blood aging progresses, the Raman scattering is being gradually obscured by the background signal, rendering Raman spectra “illegible” after ca. two months of degradation. And, in fact, **PROPOSING AN ANALYTICAL METHOD WITH A SUFFICIENT TIME RESOLUTION TO MAKE AN INFORMATIVE CONTRIBUTION TO THE CASEWORK MIGHT BE THE MOST CHALLENGING ASPECT FOR ANY PROPOSED TECHNIQUE**. It should be realized that the evidence is not always analyzed in the immediate aftermath of a crime. In some rare instances, it may not be investigated in the laboratory for weeks, not to mention that detection of the crime itself also takes time. And while the former issue can be addressed by prioritizing the time-centered examinations in the forensic laboratories, the latter remains entirely independent of forensic experts. Suppose that the competing hypotheses are whether the evidence was the consequence of some unrelated event or the criminal offense, which took place three days earlier. In such a case, the dating approach – depending on occurring delays – might be forced to distinguish between bloodstains of 7 and 10, but also 39 and 42, or even 257 and 260 days of age. If not more. Regardless of the exact numbers, the point is: the older the material, the more difficult it becomes to estimate the age of the questioned trace reliably.

Another obstacle may be the substrate interfering with the measurement. The presented study was restricted to aluminum sample holders, which were not contributing to the spectrometer output

signal. However, as well known, evidential bloodstains may be deposited on different types of materials, so the effect of the substrate on the measurement is to be expected. One of these effects, a relatively common phenomenon in Raman spectroscopy, is fluorescence that overlaps spectrally with the signature, making it very difficult – if not impossible – to interpret. Therefore, a robust dating method should accommodate the largest possible group of potential substrates.

Given the above limitations of Raman spectroscopy, one could ask whether it is possible to propose a single analytical method better suited to characterizing the stage of bloodstains' degradation. The current state of knowledge suggests that not necessarily. Does it mean that any further improvement of the first component of the proposed approach, namely the analytical method serving as a tool for probing the state of bloodstains degradation, is unattainable? Again, the answer is: not necessarily. Indeed, it might be unrealistic to expect a single method to meet analytical requirements posed by any possible evidential bloodstain. Nevertheless, it might be interesting to consider introducing a ”multiplex” approach of complementary analytical techniques focused on monitoring different aspects of the aging process, at best in both short- and long-term time scales. For example, a combination of Raman, UV-Vis, MIR, and NIR spectroscopies, could provide information not only about degradation changes typical of hemoglobin (Raman and UV-Vis spectroscopy) but also other bloodstains' protein components (MIR spectroscopy) and water content (NIR spectroscopy). Such a solution would also provide an in-built cross-checking system and, through that, strengthen the reliability of forensic reporting. And for these reasons, it is also a research direction that the author would like to continue within the following years. Of course, in many situations, due to the characteristics of the evidence (e.g., type of substrate), it would be impossible to apply all methods simultaneously. In such a case, it would be beneficial to develop a forensic dating protocol, a sort of analytical guideline, defining the best dating approach given the contextual information and properties of questioned bloodstain evidence, thereby formalizing the age estimation task.

The **SECOND PART** of the research problem addressed in the presented thesis involved **DEVELOPING LIKELIHOOD RATIO MODELS FOR ASSESSING THE SIMILARITY BETWEEN THE RAMAN SIGNATURES OF EVIDENTIAL AND REFERENCE BLOODSTAINS** (*Chapter 10*). Given the inherent variability of analyzed materials and the multidimensionality of the considered issue, the capability of established models to discriminate between differently-aged samples was surprisingly satisfying, **PROVIDING PRELIMINARY EVIDENCE OF THE EFFECTIVENESS OF THE PROPOSED DATING FRAMEWORK**. The performance of the LR models was assessed by false answer rates and empirical cross-entropy (ECE) plots. The **BEST MODELS**, founded on the 1200–1410 cm^{-1} and 1200–1300 cm^{-1} combined with 950–1020 cm^{-1} ranges, delivered approximately **10% OF FALSE NEGATIVES** and **20% FALSE POSITIVE ANSWERS**, while the **ECE PLOTS** evidenced ca. **50% REDUCTION OF INFORMATION LOSS**. The false negative rates are gratifying, while the decent ECE results, at this point, should not be too much of a concern. As already mentioned, when combined with scarce databases, ECE often leads to misleading conclusions due to its sensitivity to individual LR values in support of the incorrect

hypothesis. Consequently, this aspect of performance estimations might require further analysis to verify whether the obtained ECE values indeed characterize the model that requires improvements or, perhaps, results from a deteriorating impact of a single, strong incorrect LR response. In contrast, the 20% level of false positives may not be entirely satisfactory, especially since these types of incorrect responses can misplace the person of interest at the crime scene during the incident. Unfortunately, the level of false positive answers is not the product of improper pre-processing or data modeling, but rather an effect of significant slow down in bloodstains aging processes that could no longer be effectively monitored by Raman spectroscopy. A solution to this problem may be the already mentioned implementation of other analytical techniques capable of probing the state of bloodstains degradation over more extended periods.

Nevertheless, the most obvious but, at the same time, the most important conclusion of the presented research is that **THE HIGH REPRODUCIBILITY OF THE SUPERVISED AGING PROCEDURE IS THE DETERMINING FACTOR FOR RELIABLE DATING**. As demonstrated within the course of the study, in order to reach valid TSD estimates, bloodstains serving as reference samples for building models must replicate the aging process of the evidence as accurately as possible. Irrespective of the monitoring method applied, the bloodstains' resultant aging profile is dependent on the aging kinetics, which is affected by such influential factors as the substrate, environmental conditions persisting during aging, and the initial composition of the bloodstain. Therefore, the success of the proposed approach will depend on how much the above factors influence degradation and, above all, on how much it is possible to control them during supervised aging.

From the practical perspective, providing a suitable SUBSTRATE constitutes the slightest problem. It usually should be possible to remove a fragment of the material on which the evidence was initially deposited or simply provide a material of the same characteristics for the supervised aging procedure. It is also worth remembering that even though the issue of the substrate itself is often ignored during aging studies, it should not be wholly diminished, primarily when the monitored aging parameter is directly related to water content. It is well established that the substrate influences bloodstains' size, shape, and thickness, which dictates the drying time. And since *ex vivo* transformations of Hb (e.g., the oxidation process) proceed faster in dry rather than liquid blood, the substrate used during the supervised aging process should not be neglected.

The STORAGE CONDITIONS were generally found to be highly influential factors, with the temperature being a particularly important variable, which was also initially proven in the presented thesis. Therefore, providing degradation conditions like those expected at the crime scene is a fundamental step toward replicating the evidence aging kinetics. As it is not difficult to conclude, ensuring appropriate environmental conditions would not be a problem. In order to simulate some specific storage settings, specialized climatic chambers regulating temperature, relative humidity, and light exposure can and should be employed. The problem, however, might be to identify the aging conditions of the evidence in the first place. If no or limited information is available, it may be necessary

to run several parallel aging processes under the most likely conditions to determine the possible error limit. However, given that not only single factors but also their interactions – as yet unexplored – can regulate the degradation, the number of possible combinations, and thus the supervised aging scenarios, increases. Therefore, to finally truly understand the effect of storage conditions on the bloodstains' degradation and, through that, reduce the necessary workload by indicating just those influential factors that require regulation during supervised aging, experimental design methods should be implemented. Only in this way, a complete understanding of the relationship between inputs (environmental factors) and outputs (bloodstains degradation expressed through some aging parameters/markers) can be acquired and subsequently used during the aging reconstruction of the questioned bloodstains.

And while the previous two factors can be controlled during supervised aging, the last one – the initial composition of blood deposit – is not only challenging to regulate but also to determine. The chemical make-up of blood is influenced by a person's diet, lifestyle, medication history, to name just a few. Hence, if only the assumptions about the relationship between bloodstains' initial composition and degradation kinetics are confirmed, an extra layer of complexity would be added to the proposed concept of dating. A layer that cannot be so easily removed. The optimistic scenario, therefore, assumes that preliminary conclusions about blood composition-aging kinetics dependence are wrong. As soon as extensive research is performed, it may turn out that the initial composition of the blood does not regulate the rate of its aging. After all, the high error rates of LR models – observed after introducing the third set of bloodstains – could simply result from the fact that donor-related biochemical changes to the composition of blood were more pronounced in the Raman spectra than subtle time-related alterations. On the other hand, if the correspondence between the initial composition and blood aging kinetics is confirmed, it is expected that the proposed approach still might be applicable, for example, in the case of quick suspect identification. In such a situation, the reference sample will most likely (factors such as alcohol content cannot be excluded) be quite similar in composition to the evidence bloodstain.

The presented thesis demonstrated the possibility of evaluating the age of blood deposits through their comparison with “artificially” created reference materials. However, the proposed approach – on no account – can be readily implemented in practical proceedings. Not surprisingly, though. After all, the estimation of time elapsed since bloodstains deposition presents all the ingredients of an exceptionally complex problem. And, interestingly, the question of time does not confine itself to blood deposits. It is important to mention that the dating problem is similarly faced on numerous occasions when after collecting evidence (such as other types of body fluids, organic gunshot residues, fingerprints, etc.), their relevance to the investigated criminal assault is questioned. Consequently, the case-by-case approach founded on the idea of comparing the evidence with some reference materials should be of a wider forensic application. Thus, even if intra- and inter-donor variability ultimately prevents implementing a modified relative dating procedure in blood-centered investigations, the proposed framework is still expected to enrich the forensic arsenal of analytical tools. In this regard, this novel dating approach is quite universal – it just requires to be complemented with an analytical

technique adequate for characterizing aging profiles of the forensic trace of interest, while the fundamental idea of dating remains the same. And without a doubt, no matter what type of evidence is being analyzed, the road leading to this *holy grail* of forensics is lengthy and tortuous. However, it is an important one to take and, with the proposed approach, it may be finally headed in the right direction. Obviously, there are no illusions that further refinements of the method, aimed at transferring the novel framework for blood evidence evaluation into forensic practice, will be continually handicapped by new questions for which no answers are readily available. But isn't that exactly what science is all about?

LIST OF FIGURES

LIST OF TABLES

REFERENCES

[1] Paul L. Kirk, Crime Investigation: Physical Evidence and the Police Laboratory, Interscience, New York-London, 1953.

[2] Peter R. De Forest, What is trace evidence, in: Brian Caddy (Ed.), Forensic Examination of Glass and Paint: Analysis and Interpretation, Taylor & Francis, 2002, pp.1–24.

[3] C. Roux, J. Robertson, Trace evidence overview, in: J.Siegel, P. J. Saukko, M. Houck (Eds.), Encyclopedia of Forensic Science, Elsevier, 2013, pp. 279–285.

[4] E. Locard, L'enquête criminelle et les méthodes scientifiques, Flammarion, Paris, 1920.

[5] A. Martyna, Differentiation of microtraces based on their features obtained using advanced instrumental analytical techniques, supported by chemometric tools and likelihood ratio approach for forensic purposes (doctoral dissertation). 2016.

[6] J. Zięba-Palus, Forensic examinations of micro-traces, Forensic Sci. Crimino. 2 (2017) 1–3.

[7] T. Trejos, S. Koch, A. Mehltretter, Scientific foundations and current state of trace evidence – a review, Forensic Chem. 18 (2020) 100223.

[8] G. Zadora, A. Martyna, D. Ramos, C. Aitken, Statistical Analysis in Forensic Science: Evidential Value of Multivariate Physicochemical Data, Wiley, Chichester, 2014.

[9] *Trace* (n.d.). In Online Etymology Dictionary. https://www.etymonline.com/word/trace

[10] *Trace* (n.d.). In Cambridge Dictionary. https://dictionary.cambridge.org/pl/dictionary/english/trace

[11] K. Landsteiner, Zur Kenntnis der antifermativen, lytischen und agglutinierenden Wirkungendes Blutserums und der Lymphe, Zentbl. Bakt. Parasitkde 27 (1900) 357–363.

[12] A.J. Jeffreys, V. Wilson, S.L. Thein, Hypervariable 'minisatellite' regions in human DNA, Nature 314 (1985) 67–73.

[13] A.J. Jeffreys, V. Wilson, S.L. Thein, Individual-specific 'fingerprints' of human DNA, Nature 316 (1985) 76–79.

[14] A.J. Jeffreys, J.F. Brookfield, R. Semeonoff, Positive identification of an immigration test-case using human DNA fingerprints, Nature 317 (1985) 818–819.

[15] N. S. Templeton, The polymerase chain reaction: History methods, and applications, Diag. Mol. Pathol. 1 (1992) 58–72.

[16] T. Bevel, R. Gardner, Bloodstain Pattern Analysis, third ed., Taylor & Francis, Boca Raton, 2008.

[17] S. H. James, P. E. Kish, T. P. Sutton, Principles of Bloodstain Pattern Analysis: Theory and Practice (Practical Aspects of Criminal & Forensic Investigations), first ed., Taylor & Francis, Boca Raton, 2005.

[18] G. Zadora, Application of bloodstain pattern analysis in the reconstruction of events, Probl. Forensic Sci. 100 (2014) 295–306.

[19] K. Choromański, Bloodstain Pattern Analysis in Crime Scenarios, first ed., Springer, Singapore, 2020.

[20] ENFSI Guideline for Evaluative Reporting in Forensic Science. Strengthening the Evaluation of Forensic Results across Europe. European Network of Forensic Science Institutes, 2015.

[21] S. Gupta, Criminology: Written in blood, Nature 549 (2017) 24–25.

[22] Examination and interpretation of patterns for reconstruction, in: H. A. Harris, H. C. Lee (Eds.), Introduction to Forensic Science and Criminalistics, Taylor & Francis, Boca Raton, 2002, pp. 81–91.

[23] R.H. Bremmer, K.G. de Bruin, M.J.C. van Gemert, T.G. van Leeuwen, M.C.G. Aalders, Forensic quest for age determination of bloodstains, Forensic Sci. Int. 216 (2012) 1–11.

[24] G. Zadora, A. Menżyk, In the pursuit of the holy grail of forensic science – Spectroscopic studies on the estimation of time since deposition of bloodstains, TrAC 105 (2018) 137–165.

[25] V. Sharma, R. Kumar, Trends of chemometrics in bloodstain investigations, TrAC 107 (2018) 181–195.

[26] M. Aalders, L. Wilk, Investigating the Age of Blood Traces: How Close Are We to Finding the Holy Grail of Forensic Science?, in: S. Francese (Ed.), Emerging Technologies for the Analysis of Forensic Traces, Springer, Cham, 2019, pp. 109–128.

[27] *O.J. Simpson trial* (n.d.), In Britannica. https://www.britannica.com/event/O-J-Simpson-trial

[28] The O.J. Simpson Murder Trial: Excerpts of Opening Statements by Simpson Prosecutors, Los Angeles Times, https://www.latimes.com/archives/la-xpm-1995-01-25-mn-24229-story.html, 1995 (n.d.).

[29] C. Weyermann, O. Ribaux, Situating forensic traces in time, Sci. Justice 52 (2012) 68–75.

[30] L. Tomellini, De l'emplol d'une table chromatiqie pour les taches du sang, Arch. d'Antropologie criminelle de Criminol. 14 (1907) 2.

[31] O. Leers, Die forensische Blutuntersuchung, Springer, Berlin, 1910.

[32] D. Patterson, Use of reflectance measurements in assessing the colour changes of ageing bloodstains, Nature 187 (1960) 688–689.

[33] S.S. Kind, D. Patterson, G.W. Owen, Estimation of the age of dried blood stains by spectrophotometric method, Forensic Sci. 1 (1972) 27–54.

[34] H. Inoue, F. Takabe, M. Iwasa, Y. Maeno, Identification of fetal hemoglobin and simultaneous estimation of bloodstain age by high-performance liquid chromatography, Int. J. Legal Med. 104 (1991) 127–131.

[35] H. Inoue, F. Takabe, M. Iwasa, Y. Maeno, Y. Seko, A new marker for estimation of bloodstain age by high performance liquid chromatography, Forensic Sci. Int. 57 (1992) 17–27.

[36] E. Botonjic-Sehic, C.W. Brown, M. Lamontagne, M. Tsaparikos, Forensic Application of Near-Infrared Spectroscopy: Aging of Bloodstains, Spectroscopy 24 (2009) 1–9.

[37] R.H. Bremmer, A. Nadort, M.J.C. van Gemert, T.G. van Leeuwen, M.C. Aalders, Age estimation of blood stains by hemoglobin derivative determination using reflection spectroscopy, Forensic Sci. Int. 206 (1–3) (2010) 166–171.

[38] K.C. Doty, G. McLaughlin, I.K. Lednev, A Raman "spectroscopic clock" for bloodstain age determination: the first week after deposition, Anal. Bioanal. Chem. 408 (2016) 3993–4001.

[39] H. Lin, Y. Zhang, Q. Wang, B. Li, S. Fan, Z. Wang, Species identification of bloodstains by ATR-FTIR spectroscopy: the effects of bloodstain age and the deposition environment, Int. J. Legal Med. (2017), DOI 10.1007/s00414-017-1634-2.

[40] R. Kumar, K. Sharma, V. Sharma, Bloodstain age estimation through infrared spectroscopy and Chemometric models, Sci. Justice 60 (2020) 538–546.

[41] P. Oliveri, C. Malegori, M. Casale, Chemometrics: multivariate analysis of chemical data, in: Y. Pico (Ed.) Chemical Analysis of Food, second ed., Academic Press, 2020, pp. 33–76.

[42] Y. N. Harari, Sapiens: A Brief History of Humankind, Havrill Secker, London, 2014, p. 104.

[43] A. Comte. Cours de Philosophie Positive, Bachelier, Paris, 1830.

[44] A. L. Pomerantsev, Chemometrics in Excel, first ed., Wiley & Sons, Hoboken, New Jersey, 2014, pp. 3–7.

[45] K. Kjeldahl, R. Bro, Some common misunderstandings in chemometrics, J. Chemom. 24 (2010) 558–564.

[46] O. Ribaux, S. Walsh, P. Margot, The contribution of forensic science to crime analysis and investigation: forensic intelligence, Forensic Science International 156 (2006) 171–181.

[47] O. Ribaux, A. Baylon, C. Roux, O. Delémont, E. Lock, C. Zingg, P. Margot, Intelligence-led crime scene processing. Part I: forensic intelligence, Forensic Science International 195 (2010) 10–16.

[48] Kind, S.S., Crime investigation and the criminal trial: a three chapter paradigm of evidence. J. Forensic Sci. Soc. 34 (1994) 155–164.

[49] D. A. Stoney, Transfer evidence, in: C. G. G. Aitken, D. A. Stoney (Eds), The Use of Statistics in Forensic Science, Prentice Hall, New York, 1991, pp. 107–138.

[50] D. Hazard, The Relevancy in Forensic Science. An epistemological and empirical investigation (Doctoral dissertation). 2014.

[51] D. Hazard, The relevant physical trace in criminal investigation, J. Forensic Sci. Med. 2 (2016) 208–212.

[52] P. Thanakiatkrai, A. Yaodam, T. Kitpipit, Age estimation of bloodstains using smartphones and digital image analysis. Forensic Sci. Int. 233 (2013) 288–297.

[53] J. Shin, S. Choi, J.-S. Yang, J. Song, J.-S. Choi, H.-I. Jung, Smart Forensic Phone: Colorimetric analysis of a bloodstain for age estimation using a smartphone, Sens. Actuators, B 243 (2017) 221–225.

[54] A. Girod, R. Ramotowski, S. Lambrechts, P. Misrielal, M. Aalders, C. Weyermann, Fingermark age determinations: Legal considerations, review of the literature and practical propositions, Forensic Sci. Int. 262 (2016) 212–226.

[55] A. Menżyk, G. Zadora, M. Sajewicz, Physicochemical analysis of ink − dating and establishing the sequence of intersecting lines of ink entries, Probl. Forensic Sci. 104 (2015) 279−302.

[56] M. D. Gallidabino, C. Weyermann, Time since last discharge of firearms and spent ammunition elements: state of the art and perspectives, Forensic Sci. Int. 311 (2020) 110290.

[57] J. Grant, The diaries of Adolf Hitler, Sci. Justice 25 (1985) 189.

[58] J. Grant, The Mussolini Diary, J. Forensic Sci. Soc. 9 (1969) 43−44.

[59] Diary of the Hitler Diary Hoax, The New Yorker, (n.d.), https://www.newyorker.com/books/page-turner/diary-of-the-hitler-diary-hoax

[60] E. Rentschler, The Fascination of a Fake: The Hitler Diaries, New Ger. Crit. 90 (2003) 177−192.

[61] G. D. Smith, J. F. Hamm, D. A. Kushel, C. E. Rogge, What's Wrong with this Picture? The Technical Analysis of a Known Forgery, in: P. L. Lang, R. A. Armitage (Eds), Collaborative Endeavors in the Chemical Analysis of Art and Cultural Heritage Materials, American Chemical Society, Danvers, MA, 2012, pp. 1–21.

[62] R. J. H. Clark, Pigment identification by spectroscopic means: an arts/science interface, C. R. Chimie 5 (2002) 7–20.

[63] L. Burgio, R. J. H. Clark, L. Sheldon, G. D. Smith, Pigment Identification by Spectroscopic Means: Evidence Consistent with the Attribution of the Painting Young Woman Seated at a Virginal to Vermeer, Anal. Chem. 77 (2005) 1261–1267.

[64] C. Weyermann, J. Almog, J. Bügler, A. A. Cantu, Minimum requirements for application of ink dating methods based on solvent analysis in casework, Forensic Sci. Int. 210 (2011) 52–62.

[65] A. A. Cantu, R. S. Prough, On the Relative Aging of Ink – The Solvent Extraction Technique, J. Forensic Sci. 32 (1987) 1151–1174.

[66] R. L. Brunelle, K. R. Crawford, Advances in the forensic analysis and dating of writing ink, Charles C. Thomas, Springfield, Illinois, 2003.

[67] The European Network of Forensic Science Institutes. https://enfsi.eu/ (accessed 13 October 2020).

[68] A. Koenig, C. Weyermann, Ink dating, part I: statistical distribution of selected ageing parameters in a ballpoint inks reference population, Sci. Justice 58 (2018) 17–30.

[69] P.A. Margot, A question of time, Sci. Justice 40 (2000) 64–71.

[70] A. Girod-Frais, Dating of Fingermarks: Fiction or Reality?, SIAK-Journal − Journal for Police Science and Practice, 9 (2019) 21–34.

[71] R.H. Bremmer, A. Nadort, T.G. van Leeuwen, M.J. van Gemert, M.C. Aalders, Age estimation of blood stains by hemoglobin derivative determination using reflectance spectroscopy, Forensic Sci. Int. 206 (2011) 166–171.

[72] E. Austin, P. Hildebrand, The art and science of forensic meteorology, Phys. Today 67 (2014) 32–37.

[73] C. G. G. Aitken, F. Taroni, Statistics and the Evaluation of Evidence for Forensic Scientists, second ed., Chichester, 2004, pp. 1–34.

[74] A. Biedermann, F. Taroni, P. Garbolino, Equal prior probabilities: can one do any better? Forensic Sci. Int. 172 (2007) 85–93.

[75] Law and Disorder, Mistakes Were Made (But Not By Me): Why We Justify Foolish Beliefs, Bad Decisions, and Hurtful Acts, in: C. Tavris, E. Aronson (Editors), Harcourt, Orlando, 2007, pp. 126–157.

[76] I. Dror, J. Melinek, J. L. Arden, J. Kukucka, S. Hawkins, J. Carter, D. S. Atherton, Cognitive bias in forensic pathology decisions, J. Forensic Sci. 66 (2021) 1–7.

[77] H.J. Butler, L. Ashton, B. Bird, G. Cinque, K. Curtis, J. Dorney, K. Esmonde-White, N.J. Fullwood, B. Gardner, P.L. Martin-Hirsch, M.J. Walsh, M.R. McAinsh, N. Stone, F.L. Martin, Using Raman spectroscopy to characterize biological materials, Nat. Protoc. 11 (2016) 664–687.

[78] C.G. Atkins, K. Buckley, M.W. Blades, R.F.B. Turner, Raman spectroscopy of blood and blood components, Appl. Spectrosc. 71 (2017) 767–793.

[79] S.Z. Hu, K.M. Smith, T.G. Spiro, Assignment of protoheme resonance Raman spectrum by heme labeling in myoglobin, J. Am. Chem. Soc. 118 (1996) 12638–12646.

[80] D.L. Rousseau, M.R. Ondrias, Raman scattering, in: D.L. Rousseau (Ed.), Optical Techniques in Biological Research, Academic press, inc., Orlando, 1984, pp. 100–108.

[81] C. G. G. Aitken, F. Taroni, The history of forensic statistics: a thematic perspective, in: D. Banks, K. Kafadar, D. H. Kaye, M. Tackett (Eds), Handbook of Forensic Statistics, Chapman and Hall/CRC, London, 2020, pp. 3–36.

[82] J. F. Dailey, Dailey's Notes on Blood, second ed., Medical Consulting Group, Springfield, 1993.

[83] J. B. Henry, Clinical Diagnosis and Management by Laboratory Methods, 12th ed., W.B. Saunders Company, 2001.

[84] V. Kumar, A. K. Abbas, N. Fausto, Robbins and Cotran Pathological Basis of Disease, 7th ed., Elsevier Saunders, 2004.

[85] M. Ferenc, Anatomical Considerations in Bloodstains Pattern Analysis, in: T. Bevel, R. Gardner (Eds), Bloodstain Pattern Analysis, third ed., Taylor & Francis, Boca Raton, 2008, pp. 136–148.

[86] R. S. Franco, Measurement of Red Cell Lifespan and Aging, Transfus. Med. Hemother. 39 (2012) 302–307.

[87] Hemoglobin, Portrait of a protein in action, in: J.M. Berg, J.L. Tymoczko, L. Stryer (Eds), Biochemistry, W. H. Freeman, New York, 2002, pp. 191–210.

[88] Y. Wu, Y. Hu, J. Cai, S. Ma, X. Wang, Y. Chen, Y. Pan, Time-dependent surface adhesive force and morphology of RBC measured by AFM, Micron 40 (2009) 359–364.

[89] S. Strasser, A. Zink, G. Kada, P. Hinterdorfer, O. Peschel, W.M. Heckl, A.G. Nerlich, S. Thalhammer, Age determination of blood spots in forensic medicine by force spectroscopy, Forensic Sci. Int. 170 (2007) 8–14.

[90] Y. Chen, J. Cai, Membrane deformation of unfixed erythrocytes in air with time lapse investigated by tapping mode atomic force microscopy, Micron 37 (2006) 339–346.

[91] T. Smijs, F. Galli, A. van Asten, Forensic potential of atomic force microscopy, Forensic Chem. 2 (2016) 93–104.

[92] M. F. Perutz, M. G. Rossmann, A. F. Cullis, H. Muirhead, A. C. T. North, Structure of haemoglobin: a three-dimensional Fourier synthesis at 5.5-A. Resolution, obtained by X-ray analysis, Nature 185 (1960) 416–422.

[93] A.J. Marengo-Rowe, Structureefunction relations of human hemoglobins, Proc. Bayl. Univ. Med. Cent. 19 (2006) 239–245.

[94] G. J. Kato, F. B. Piel, C. D. Reid, M. H. Gaston, K. Ohene-Frempong, L. Krishnamurti, W. R. Smith, J. A. Panepinto, D. J. Weatherall, F. F. Costa, E. P. Vichinsky, Sickle cell disease, Nat Rev Dis Primers. 4 (2018).

[95] Bloodstain Pattern Analysis, in: M. Houck, F. Crispino, T. McAdam, The Science of Crime Scenes, second ed., Academic Press, Kidlington, Oxford, 2017, pp. 323–330.

[96] A. Kapralov, I. I. Vlasova, W. Feng, A. Maeda, K. Walson, V. A. Tyurin, Z. Huang, R. K. Aneja, J. Carcillo, H. Bayır, V. E. Kagan, Peroxidase Activity of Hemoglobin·Haptoglobin Complexes: covalent aggregation and oxidative stress in plasma and macrophages, J Biol Chem. 284 (2009) 30395–30407.

[97] P.C. Champe, R. A. Harvey, D. R. Ferrier, Biochemistry Lippincott's Illustrated Reviews Series, Third ed., Lippincott Williams & Wilkins, 2005.

[98] N. V. Bhagavan, Chung-Eun Ha, Essentials of Medical Biochemistry, Second Ed., Academic Press, Kidlington, Oxford, 2015

[99] W. Auwärter, D. Écija, F. Klappenberger, J. V. Barth, Porphyrins at interfaces, Nature Chem. 7 (2015) 105–120.

[100] .P. Collins, J.H. Dawson, Recent History of Heme-Containing Proteins: Advances in Structure, Functions, and Reaction Intermediate Determination, in: J. Reedijk, K. Poeppelmeier (Eds), Comprehensive Inorganic Chemistry II, Second ed, Elsevier, 2013, pp. 65–102.

[101] T.G. Spiro, T.C. Strekas, Resonance Raman spectra of heme proteins. Effects of oxidation and spin state, J. Am. Chem. Soc. 96 (1974) 338–345.

[102] J.M. Rifkind, O. Abugo, A. Levy, J. Heim, Detection, formation, and relevance of hemichromes and hemochromes, Methods Enzymol. 231 (1994) 449–480.

[103] J. Umbreit, Methemoglobindit's not just blue: a concise review, Am. J. Hematol. 82 (2007) 134–144.

[104] T. Kanias, J.P. Acker, Biopreservation of red blood cells – the struggle with hemoglobin oxidation, FEBS Journal 277 (2010) 343–356.

[105] K.E.Barrett, S. M.Barman, S. Boitano, H.Brooks, Ganong's Review of Medical Physiology, 24th ed, The McGraw–Hill Companies, New York, 2012.

[106] B. Faivre, P. Menu, P. Labrude, C. Vigneron, Hemoglobin autooxidation/oxidation mechanisms and methemoglobin prevention or reduction processes in the bloodstream, Art. Cells, Blood Subs. Immob. Biotech. 26 (1998) 17–26.

[107] F. B. Jensen, Acute and chronic influence of temperature on red blood cell anion exchange, J. Exp. Biol. 204 (2001) 39–45.

[108] A. Mansouri, A.A. Lurie, Concise review: methemoglobinemia, Am. J. Hematol. 42 (1993) 7–12.

[109] F. R Smith, C. Nicloux, D. Brutin, A new forensic tool to date human blood pools, Scientific Reports 10 (2020) 1–12.

[110] N. Laan, F. Smith, C. Nicloux, D. Brutin, Morphology of drying blood pools, Forensic Sci. Int. 267 (2016) 104–109.

[111] N. Laan, C. Compain, L. Seyve, B. Polack, C. Nicloux, F. Caton, The influence of coagulation on the drying dynamics of blood pools, Forensic Sci. Int. 305 (2019) 110008.

[112] F. Ramsthaler, P. Schmidt, R. Bux, S. Potente, C. Kaiser, M. Kettner, Drying properties of bloodstains on common indoor surfaces, Int. J. Legal Med. 126 (2012) 739–746.

[113] B. Sobac, D. Brutin, Desiccation of a sessile drop of blood: Cracks, folds formation and delamination, Colloids Surf. A Physicochem. Eng. Asp. 448 (2014) 34–44.

[114] K. Sefiane, On the formation of regular patterns from drying droplets and their potential use for biomedical applications, J. Bionic Eng. 7 (2010) 82–93.

[115] K. Sefiane, Patterns from drying drops, Adv. Colloid Interface Sci. 206 (2014) 372–381.

[116] *State v. Peterson* (n.d.), in Internet Archive Wayback Machine. http://www.aoc.state.nc.us/www/public/sc/opinions/2007/547-06-1.htm

[117] T. L. Laber, Diameter of a bloodstain as a function of origin. Distance fallen and volume of drop, IABPA News 2 (1985) 12–16.

[118] T. L. Laber, B. P. Epstein, Bloodstain pattern analysis, Callen, Minneapolis, 1983.

[119] T. Yamamato, G. Palmer, The valence and spin state of iron in oxyhemoglobin as inferred from resonance Raman spectroscopy, J. Biol. Chem. 248 (1973) 5211–5213.

[120] T. G. Spiro (Ed.,) Resonance Raman Spectra of Heme and Metalloproteins, Biological Applications of Raman Spectroscopy, vol. 3, Wiley, New York, 1987.

[121] S. Nagatomo, M. Nagai, T. Kitagawa, A New Way To Understand Quaternary Structure Changes of Hemoglobin upon Ligand Binding On the Basis of UV-Resonance Raman Evaluation of Intersubunit Interactions, J. Am. Chem. Soc. 133 (2011) 10101–10110.

[122] J. Dissing, A. Søndervang, S. Lund, Exploring the limits for the survival of DNA in bloodstains, J. Forensic Leg. Med. 17 (2010) 392–396.

[123] E.K. Hanson, J. Ballantyne, A blue spectral shift of the hemoglobin Soret band correlates with the age (time since deposition) of dried bloodstains, PLoS One 5 (2010) 12830.

[124] M.F. Colombo, R. Sanches, Hydration-dependent conformational states of hemoglobin equilibrium and kinetic behavior, Biophys. Chem. 36 (1990) 33–39.

[125] A. Riccio, L. Vitagliano, G. di Prisco, A. Zagari, L. Mazzarella, The crystal structure of a tetrameric hemoglobin in a partial hemichrome state, Proc. Natl. Acad. Sci. U. S. A. 99 (2002) 9801–9806.

[126] R. H. Bremmer, D. M. de Bruin, M. de Joode, W. Jan Buma, T. G. van Leeuwen, M. C. G. Aalders, Biphasic oxidation of oxy-hemoglobin in bloodstains, PLoS One 6 (2011) 21845.

[127] G. Edelman, Spectral Analysis of Blood Stains at the Crime Scene (Doctoral dissertation), 2014.

[128] E. A. Rachmilewitz, J. Peisach, W. E. Blumberg, Studies on the stability of oxyhemoglobin A and its constituent chains and their derivatives, J. Biol. Chem. 246 (1971) 3356–3366.

[129] K. Guo, N. Zhegalova, S. Achilefu, M.Y. Berezin, Bloodstain age analysis: to- ward solid state fluorescent lifetime measurements, Proc. SPIE 8572 (2013) 857214.

[130] K. Guo, S. Achilefu, M.Y. Berezin, Dating bloodstains with fluorescence lifetime measurements, Chemistry 18 (2012) 1303–1305.

[131] S. Mc Shine, K. Suhling, A. Beavil, B. Daniel, N. Frascione, The applicability of fluorescence lifetime to determine the time since the deposition of biological stains, Anal. Methods 9 (2017) 2007–2013.

[132] J. Agudelo, C.Huynh, J. Halámek, Forensic determination of blood sample age using a bioaffinity-based assay, Analyst 140 (2015) 1411–1415.

[133] J. Agudelo, L. Halámková, E. Brunelle, R. Rodrigues, C. Huynh, J. Halámek, Ages at a Crime Scene: Simultaneous Estimation of the Time since Deposition and Age of Its Originator, Anal Chem 88 (2016) 6479–6484.

[134] M. Bauer, S. Polzin, D.r Patzelt, Quantification of RNA degradation by semi-quantitative duplex and competitive RT-PCR: a possible indicator of the age of bloodstains?, Forensic Sci. Int. 138 (2003) 94–103.

[135] S. Anderson, B. Howard, G. R. Hobbs, Clifton P. Bishop, A method for determining the age of a bloodstain, Forensic Sci. Int.148 (2005) 37–45.

[136] S. Anderson, G. R. Hobbs, Clifton P. Bishop, Multivariate Analysis for Estimating the Age of a Bloodstain, J Forensic Sci. 56 (2011) 186–193.

[137] B.J.A. Larkin, Bloodstain Pattern Analysis: Scratching the Surface (Doctoral dissertation), 2015.

[138] E. Botonjic-Sehic, C.W. Brown, M. Lamontagne, M. Tsaparikos, Forensic application of near-infrared spectroscopy: aging of bloodstains, Spectroscopy 24 (2009) 1–9.

[139] H. Sun, Y. Dong, P. Zhang, Y. Meng, W. Wen, N. Li, Z. Guo, Accurate age estimation of bloodstains based on visible reflectance spectroscopy and chemometrics methods, IEEE Photon. J. 9 (2017).

[140] G. Edelman, V. Manti, S.M. van Ruth, T. van Leeuwen, M. Aalders, Identification and age estimation of blood stains on colored backgrounds by near infrared spectroscopy, Forensic Sci. Int. 220 (2012) 239–244.

[141] K. C. Doty, C. K. Muro, I. K. Lednev, Predicting the time of the crime: bloodstain aging estimation for up to two years, Forensic Chem. 5 (2017) 1–7.

[142] M. Lekka, P. Laidler, D. Gil, J. Lekki, Z. Stachura, A.Z. Hrynkiewicz, Elasticity of normal and cancerous human bladder cells studied by scanning force microscopy, Eur. Biophys. J. Biophys. Lett. 28 (1999) 312–316.

[143] M. Bryszewska, C. Watala, W. Torzecka, Changes in fluidity and composition of erythrocyte-membranes and in composition of plasma-lipids in type-I diabetes, Brit. J. Haematol. 62 (1986) 111–116.

[144] O.K. Baskurt, Mechanisms of blood rheology alterations, in: O.K. Baskurt, M.R. Hardeman, M.W. Rampling, H.J. Meiselman (Eds), Handbook of Hemorheology and Hemodynamics, IOS Press, Amsterdam, 2007, pp. 170–190.

[145] J.W. Buenger, V.F. Mauro, Organic nitrate-induced methemoglobinemia, Ann. Pharmacother. 23 (1989) 283–288.

[146] T.L. Laber, R.P. Epstein, Substrate effects on the clotting time of human blood, Can. Soc. Forensic Sci. J. 34 (2001) 209–214.

[147] G. J. Edelman, M. C. G. Aalders, Blood degradation and bloodstain age estimation, in: E.M.J. Schotsmans, N. Marquez-Grant, S.L. Forbes (Eds), Taphonomy of Human Remains, Wiley, Chichester, 2017, pp. 53–64.

[148] D.A. Sears, M.M. Udden, J. Thomas, Carboxyhemoglobin levels in patients with sickle-cell anemia: relationship to hemolytic and vasoocclusive severity, Am. J. Med. Sci. 322 (2001) 345–348.

[149] N .J. Wald, M. Idle, J. Boreham, A. Bailey, Carbon monoxide in breath in relation to smoking and carboxyhaemoglobin levels, Thorax 36 (1981) 366–369.

[150] N.R. Woebkenberg, R.A. Mostardi, D.L. Ely, D. Worstell, Carboxyhemoglobin and methemoglobin levels in residents living in industrial and non-industrial communities, Environ. Res. 26 (2011) 347–352.

[151] G. J. Edelman, T. G. van Leeuwen, M. C. G. Aalders, Hyperspectral imaging for the age estimation of blood stains at the crime scene, Forensic Sci. Int. 223 (2012) 72–77.

[152] H. Shuval, N. Gruener, Epidemiological and toxicological aspects of nitrates and nitrites in the environment, Am. J. Public Health 62 (1972) 1045–1052.

[153] K. M. Marzec, A. Rygula, B. R. Wood, S. Chlopicki, M. Baranska, High-resolution Raman imaging reveals spatial location of heme oxidation sites in single red blood cells of dried smears, J. Raman Spectrosc. 46 (2014) 76–83.

[154] K. Canene-Adams, J.W. Erdman Jr., Absorption, transport, distribution in tissues and bioavailability, in: G. Britton, S. Liaaen-Jensen, H. Pfander (Eds), Carotenoids, Nutrition and Health, vol. 5, Birkh€auser Verlag, Basel, 2009, pp. 115–144.

[155] A. Vaya, M.Simo, M. Santaolaria, J. Todolí, J. Aznar, Red blood cell deformability in iron deficiency anaemia, Clin. Hemorheol. Microcirc. 33 (2005) 75–80.

[156] R. T. Card, L. R. Weintraub, Metabolic abnormalities of erythrocytes in severe iron deficiency, Blood 37 (1971) 725–732.

[157] E. Nagababu, S. Gulyani, C. J. Earley, R. G. Cutler, M. P. Mattson, J. M. Rifkind, Iron-deficiency anemia enhances red blood cell oxidative stress, Free Radic. Res. 42 (2008) 824–829.

[158] L. Fewtrell, Drinking-water nitrate, methemoglobinemia, and global burden of disease: a discussion, Environ. Health Perspect. 112 (2004) 1371–1374.

[159] J. W. Buenger, V. F. Mauro, Organic nitrate-induced methemoglobinemia, Ann. Pharmacother. 23 (1989) 283–288.

[160] P. Fraser, C. Chilvers, Health aspects of nitrate in drinking water, Sci. Total Environ. 18 (1981) 103–116.

[161] E. Hanson, A. Albornoz, J. Ballantyne, Validation of the hemoglobin (Hb) hypsochromic shift assay for determination of the time since deposition (TSD) of dried bloodstains, Forensic Sci. Int. Genet. Suppl. Ser. 3 (2011) e307–e308.

[162] B. Li, P. Beveridge, W.T. O'Hare, M. Islam, The age estimation of blood stains up to 30 days old using visible wavelength hyperspectral image analysis and linear discriminant analysis, Sci. Justice 53 (2013) 270–277.

[163] T. Miki, A. Kai, M. Ikeya, Electron spin resonance of bloodstains and its application to the estimation of time after bleeding, Forensic Sci. Int. 35 (1987) 149–158.

[164] T. Matsuoka, T. Taguchi, J. Okuda, Estimation of bloodstain age by rapid determinations of oxyhemoglobin by use of oxygen electrode and total hemoglobin, Biol. Pharm. Bull. 18 (1995) 1031–1035.

[165] Y. Fujita, K. Tsuchiya, S. Abe, Y. Takiguchi, S. Kubo, H. Sakurai, Estimation of the age of human bloodstains by electron paramagnetic resonance spectroscopy: long-term controlled experiment on the effects of environmental factors, Forensic Sci. Int. 152 (2005) 39–43.

[166] R. Leardi, Experimental Design in Chemistry: A Tutorial, Anal. Chim. Acta 652 (2009) 161–172.

[167] M. Tsuruga, A. Matsuoka, A. Hachimori, Y. Sugawara, K. Shikama, The molecular mechanism of autoxidation for human oxyhemoglobin, J. Biol. Chem. 273 (1998) 8607–8615.

[168] F. Zapata, M. Fernández de la Ossa, C. García-Ruiz, Emerging spectrometric techniques for the forensic analysis of body fluid, TrAC 64 (2015) 53–63.

[169] M. Meinke, G. Müller, J. Helfmann, M. Friebel, Optical properties of platelets and blood plasma and their influence on the optical behavior of whole blood in the visible to near infrared wavelength range, J. Biomed. Opt. 12 (2007).

[170] N. Bosschaart, G.J. Edelman, M.C.G. Aalders, T.G. van Leeuwen, D.J. Faber, A literature review and novel theoretical approach on the optical properties of whole blood, Lasers Med. Sci. 29 (2014) 453–479.

[171] J. T. Kuenstner, K. H. Norris, Spectrophotometry of human hemoglobin in the near infrared region from 1000 to 2500 nm, J. Near Infrared Spectrosc. 2 (1994) 59–65.

[172] J. Flammer, M. Mozaffarieh, H. Bebie, The interaction between light and matter, in: J. Flammer, M. Mozaffarieh, H. Bebie (Editors), Basic Sciences in Ophthalmology, Springer-Verlag, Berlin Heidelberg, 2013, pp. 21–39.

[173] H. Barańska, Laser Raman spectrometry: Analytical applications, Distributors, Halsted Press, 1987.

[174] B. Li, P. Beveridge, W.T. O'Hare, M. Islam, The estimation of the age of a blood stain using reflectance spectroscopy with a microspectrophotometer, spectral pre-processing and linear discriminant analysis, Forensic Sci. Int. 212 (2011) 198–204.

[175] H. Lin, Y. Zhang, Q. Wang, B. Li, P. Huang, Z. Wang, Estimation of the age of human bloodstains under the simulated indoor and outdoor crime scene conditions by ATR-FTIR spectroscopy, Sci Rep. 7 (2017) 13254.

[176] R. Kumar, K. Sharma, V. Sharma, Bloodstain age estimation through infrared spectroscopy and Chemometric models, Sci. Justice 60 (2020) 538–546.

[177] P. Lemler, W.R. Premasiri, A. DelMonaco, L.D. Ziegler, NIR, Raman spectra of whole human blood: effects of laser-induced and in vitro hemoglobin denaturation, Anal. Bioanal. Chem. 406 (2014) 193–200.

[178] T.C. Strekas, T.G. Spiro, Hemoglobin: resonance Raman spectra, Biochim. Biophys. Acta Protein Struct. 263 (1972) 830–833.

[179] H. Brunner, H. Sussner, A. Mayer, Resonance Raman scattering on the haem group of oxy- and deoxyhaemoglobin, J. Mol. Biol. 70 (1972) 153–156.

[180] H. Brunner, H. Sussner, Resonance Raman scattering on haemoglobin, Biochim. Biophys. Acta 310 (1973) 20–31.

[181] T. Yamamoto, G. Palmer, D. Gill, I.T. Salmeen, L. Rimai, The valence and spin state of iron in oxyhemoglobin as inferred from resonance Raman spectroscopy, J. Biol. Chem. 248 (1973) 5211–5213.

[182] K. Nagai, T. Kitagawa, H. Morimoto, Quaternary structures and low frequency molecular vibrations of haems of deoxy and oxyhaemoglobin studied by resonance Raman scattering, J. Mol. Biol. 36 (1980) 271–289.

[183] B. R. Wood, B. Tait, D. McNaughton, Micro-Raman characterisation of the R to T state transition of haemoglobin within a single living erythrocyte, Biochim. Biophys. Acta e Mol. Cell Res. 1539 (2001) 58–70.

[184] B. R. Wood, L. Hammer, D. McNaughton, Resonance Raman spectroscopy provides evidence of heme ordering within the functional erythrocyte, Vib. Spectrosc. 38 (2005) 71–78.

[185] B. R. Wood, L. Hammer, L. Davis, D. McNaughton, Raman microspectroscopy and imaging provides insights into heme aggregation and denaturation within human erythrocytes, J. Biomed. Opt. 10 (2005) 14005–14013.

[186] B. R. Wood, A. Hermelink, P. Lasch, K. R. Bambery, G. T. Webster, M. A. Khiavi, B. M. Cooke, S. Deed, D. Naumann, D. McNaughton, Resonance Raman microscopy in combination with partial dark-field microscopy lights up a new path in malaria diagnostics, Analyst 134 (2009) 1119–1125.

[187] K. C. Doty, C. K. Muro, J. Bueno, L. Halamkova, I. K. Lednev, What can Raman spectroscopy do for criminalistics? J. Raman Spectrosc. 47 (2016) 39–50.

[188] K. C. Doty, I.K. Lednev, Raman spectroscopy for forensic purposes: recent applications for serology and gunshot residue analysis, TrAC 103 (2018) 215–222.

[189] A. Smekal, Zur Quantentheorie der Dispersion, Die Naturwissenschaften 11 (1923) 873–875.

[190] C. V. Raman, K. Krishnan, A New Type of Secondary Radiation. Nature 121 (1928) 501–502.

[191] E. Smith, G. Dent, Introduction, basic theory and principles, in: E. Smith, G. Dent (Eds), Modern Raman Spectroscopy – a Practical Approach, John Wiley & Sons, Ltd, Chichester, 2005, pp. 1–21.

[191] K. Małek (Ed), Vibrational spectroscopy from theory to practice, First ed., Wydawnictwo Naukowe PWN, Warszawa, 2016.

[192] J. R. Ferraro, K. Nakamoto, C. W. Brown, Introductory Raman spectroscopy, Second Ed., Academic Press, 2003.

[193] I. K. Lednev, V. Sikirzhytski, Raman Spectroscopy and Advanced Statistics for Biochemical Research and Analytical Purposes, Am. Pharmac. Review (2012) 44–48.

[194] More Advanced Raman Scattering Techniques, in: E. Smith, G. Dent (Eds), Modern Raman Spectroscopy – a Practical Approach, John Wiley & Sons, Ltd, Chichester, 2005, pp. 223–227.

[195] L. Cui, J. H. Butler, P. L. Martin-Hirsch, F. L. Martin, Aluminium foil as a potential substrate for ATR- FTIR, transflection FTIR or Raman spectrochemical analysis of biological specimens, Anal. Methods 8 (2016) 481–487.

[196] F. Bonnier, A. Mehmood, P. Knief, A. D. Meade, W. Hornebeck, H. Lambkin, K. Flynn, V. McDonagh, C. Healy, T. C. Lee, F. M. Lyng, H. J. Byrne, In vitro analysis of immersed human tissues by Raman microspectroscopy, J. Raman Spectrosc. 42 (2011) 888–896.

[197] A. Rygula, K. Majzner, K.M. Marzec, A. Kaczor, M. Pilarczyk, M. Baranska, Raman spectroscopy of proteins: a review, J. Raman Spectrosc. 44 (2013) 1061–1076.

[198] S E. M. Colaianni, J. Aubard, S. H. Hansen, O. F. Nielsen, Raman spectroscopic studies of some biochemically relevant molecules, Vib. Spectrosc. 9 (1995) 1113–1120.

[199] S. A. Overman, G. J. Thomas Jr., Raman spectroscopy of the filamentous virus Ff (fd, fl, M13): structural interpretation for coat protein aromatics. Biochemistry 34 (1995) 5440–5451.

[200] S. A. Overman, G. J. Thomas Jr., Raman markers of nonaromatic side chains in an alpha-helix assembly: Ala, Asp, Glu, Gly, Ile, Leu, Lys, Ser, and Val residues of phage fd subunits, Biochemistry 38 (1999) 4018–4027.

[201] T. Kitagawa, S. Hirota, Raman Spectroscopy of proteins, John Wiley & Sons Ltd., 2002.

[202] H. Sato, H. Chiba, H. Tashiro, Y. Ozaki, Excitation wavelength-dependent changes in Raman spectra of whole blood and hemoglobin: comparison of the spectra with 514.5-, 720-, and 1064-nm excitation, J. Biomed. Opt. 6 (2001) 366–370.

[203] Proteins, in: J. Twardowski, P. Anzenbacher, Raman and IR Spectroscopy in Biology and Biochemistry, First ed., Polish Scientific Publishers, Warsaw, 1994, pp. 107–202.

[204] R. C. Lord, N. T. Yu, Laser-excited Raman spectroscopy of biomolecules. Native lysozyme and its constituent amino acids, J. Mol. Biol. 50 (1970) 509–24.

[205] M. N. Siamwiza, R. C. Lord, M. C. Chen, T. Takamatsu, I. Harada, H. Matsuura, T. Shimanouchi, Interpretation of the doublet at 850 and 830 cm-1 in the Raman spectra of tyrosyl residues in proteins and certain model compounds, Biochemistry 14 (1975) 4870–4876.

[206] I. Harada, H. Takeuchi, Raman and ultraviolet resonance Raman spectra of proteins and related compounds, in: R. J. H. Clark and R. E. Hester (Eds.), Advances in Spectroscopy, Wiley, New York, 1986, pp. 113–175.

[207] T. Miura, H. Takeuchi, I. Harada, Tryptophan Raman bands sensitive to hydrogen bonding and side-chain conformation, J. Raman Spectrosc. 20 (1989) 667–671.

[208] T. Miura, H. Takeuchi, I. Harada, Raman spectroscopic characterization of tryptophan side chains in lysozyme bound to inhibitors: Role of the hydrophobic box in the enzymatic function, Biochemistry 30 (1991) 6074–6080.

[209] B. Hernández, F. Pflüger, S. G. Kruglik, M. Ghomi, Characteristic Raman lines of phenylalanine analyzed by a multiconformational approach, J. Raman Spectrosc. 44 (2013) 827–833.

[210] M. Tasumi, I. Harada, T. Takamatsu, S. Takahashi, Raman studies of L-histidine and related compounds in aqueous solutions, J. Raman Spectrosc. 12 (1982) 149–151.

[211] H. Takeuchi, Y. Kimura, I. Koitabashi, I. Harada, Raman bands of N-deuterated histidinium as markers of conformation and hydrogen bonding, J. Raman Spectrosc. 22 (1991) 233–236.

[212] H. Li, G. J. Thomas Jr., Studies of virus structure by Raman spectroscopy. Cysteine conformation and sulfhydryl interactions in proteins and viruses. 1. Correlation of the Raman sulfur-hydrogen band with hydrogen bonding and intramolecular geometry in model compounds, J. Am. Chem. Soc. 113 (1991) 456–462.

[213] S. W. Raso, P. L. Clark, C. Haase-Pettingell, J. King, G. J. Thomas Jr., Distinct cysteine sulfhydryl environments detected by analysis of Raman S-hh markers of Cys->Ser mutant proteins, J. Mol. Biol. 307 (2001) 899–911.

[214] B. R. Wood, D. McNaughton, Raman excitation wavelength investigation of single red blood cells in vivo, J. Raman Spectrosc. 33 (2002) 517–523.

[215] B .R. Wood, D. McNaughton, Resonant Raman scattering of heme molecules in cells and in the solid state, in: P. Lasch, J. Kneipp (Editors), Biomedical Vibrational Spectroscopy, Wiley, Chichester, 2008, pp. 181–203.

[216] T. L. Poulos, The Janus nature of heme, Nat. Prod. Rep. 24 (2007) 504–510.

[217] M. Abe, T. Kitagawa, Y. Kyogoku, Resonance Raman spectra of octaethylporphyrinatonickel(II) and meso-deuterated and nitrogen-15 substituted derivatives. II. A normal coordinate analysis, J. Chem. Phys. 69 (1978) 4526–4534.

[218] K. Ramser, E. J. Bjerneld, C. Fant, M. Kall, Importance of substrate and photoinduced effects in Raman spectroscopy of single functional erythrocytes, J. Biomed. Opt. 8 (2003) 173–178.

[219] S. Z. Hu, K. M. Smith, T. G. Spiro, Assignment of protoheme resonance Raman spectrum by heme labeling in myoglobin, J. Am. Chem. Soc. 118 (1996) 12638–12646.

[220] P. T. Filho, J. Terner, R. N. Pittman, E. Proffitt, K. R. Ward, Measurement of hemoglobin oxygen saturation using Raman microspectroscopy and 532-nm excitation, J. Appl. Physiol. 104 (2008) 1809–1817.

[221] S. Asher, Resonance Raman spectroscopy of hemoglobin, Meth. Enzymol. 79 (1981) 371–413.

[222] J. Terner, D. S. Voss, C. Paddock, R. B. Miles, T. G. Spiro, Picosecond Resonance Raman-Spectrum Of The Oxyhemoglobin Photoproduct - Evidence For An Electronically Excited-State, J. Phys. Chem. 86 (1982) 859–861.

[223] B. R. Wood, P. Caspers, G. J. Puppels, S. Pandiancherri, D. McNaughton, Resonance Raman spectroscopy of red blood cells using near-infrared laser excitation, Anal. Bioanal. Chem. 387 (2007) 1691–1703.

[224] S. Boyd, M.F. Bertino, S.J. Seashols, Raman spectroscopy of blood samples for forensic applications, Forensic Sci. Int. 208 (2011) 124–128.

[225] M. Casella, A. Lucotti, M. Tommasini, M. Bedoni, E. Forvi, F. Gramatica, G. Zerbi, Raman and SERS recognition of b-carotene and haemoglobin fingerprints in human whole blood, Spectrochim. Acta, A. Mol. Biomol. Spectrosc. 79 (2011) 915–919.

[226] K. Virkler, I.K. Lednev, Raman spectroscopic signature of blood and its potential application to forensic body fluid identification, Anal. Bioanal. Chem. 396 (2010) 525–534.

[227] V. Sikirzhytski, K. Virkler, I.K. Lednev, Discriminant analysis of Raman spectra for body fluid identification for forensic purposes, Sensors 10 (2010) 2869–2884.

[228] A. J. Berger, T.-W. Koo, I. Itzkan, G. Horowitz, M. S. Feld, Multicomponent blood analysis by near-infrared Raman spectroscopy, Appl. Opt. 38 (1999) 2916–2926.

[229] A.M.K. Enejder, T.-W. Koo, J. Oh, M. Hunter, S. Sasic, M.S. Feld, Blood analysis by Raman spectroscopy, Opt. Lett. 27 (2002) 2004–2006.

[230] Lednev Research Laboratory, University at Albany. https://sites.google.com/site/lednevlab/ (accessed 15.01.21).

[231] M. Asghari-Khiavi, A. Mechler, K.R. Bambery, D. McNaughton, B.R. Wood, A resonance Raman spectroscopic investigation into the effects of fixation and dehydration on heme environment of hemoglobin, J. Raman Spectrosc. 40 (2009) 1668–1674.

[232] W. R. Premasiri, J. C. Lee, L. D. Ziegler, Surface-enhanced Raman scattering of whole human blood, blood plasma, and red blood cells: cellular processes and bioanalytical sensing, J. Phys. Chem. B 116 (2012) 9376–9386.

[233] J.L. Lippert, D. Tyminski, P.J. Desmeules, Determination of the secondary structure of proteins by laser Raman spectroscopy, J. Am. Chem. Soc. 98 (1976) 7075–7080.

[234] H. Ishizaki, P. Balaram, R. Nagaraj, Y.V. Venkatachalapathi, A.T. Tu, Determination of beta-turn conformation by laser Raman spectroscopy, Biophys. J. 36 (1981) 509–517.

[235] R. Dasgupta, S. Ahlawat, R.S. Verma, A. Uppal, P.K. Gupta, Hemoglobin degradation in human erythrocytes with long-duration near-infrared laser exposure in Raman optical tweezers, J. Biomed. Opt. 15 (2010) 055009.

[236] S. Ahlawat, N. Kumar, A. Uppal, P.K. Gupta, Visible Raman excitation laser-induced power and exposure dependent effects in red blood cells, J. Biophotonics 8 (2016) 1–8.

[237] W. H. Woodruff, T. G. Spiro, A circulating sample cell for temperature control in resonance Raman spectroscopy, Appl. Spectrosc. 28 (1974) 74–75.

[238] D. Lucy, Introduction to Statistics for Forensic Scientists, John Wiley & Sons, Ltd, Chichester, 2005.

[239] B. Robertson, G. A. Vignaux, Interpreting Evidence: Evaluating Forensic Science in the Courtroom, John Wiley & Sons, Ltd, Chichester, 1995.

[240] E. Lauterpacht, C. J. Greenwood, A. G. Oppenheimer, Karen Lee (Eds), International Law Reports 160 (1972).

[241] M. J. Saks, J. J. Koehler, The coming paradigm shift in forensic identification science, Science 309(2005) 892–895.

[242] C. Champod, I. W. Evett, A probabilistic approach to fingerprint evidence, J. Forensic Ident. 51 (2001) 101–122.

[243] I. W. Evett, Towards a uniform framework for reporting opinions in forensic science casework, Sci. Justice 38 (1998) 198–202.

[244] J. Gonzalez-Rodriguez, P. Rose, D. Ramos, D. T. Toledano, J. Ortega-Garcia, Emulating DNA: Rigorous quantification of evidential weight in transparent and testable forensic speaker recognition, IEEE/ACM Trans. Audio, Speech, Language Process. 15 (2007) 2104–2115.

[245] D. H. Kaye, J. Koehler, Can Jurors Understand Probabilistic Evidence?, J. R. Sta.t Soc. Ser. A Stat. Soc., 154 (1991) 75–81.

[246] R. Cook, I. W. Evett, G. Jackson, P. J. Jones, J. A. Lambert, A model for case assessment and interpretation. Sci. Justice 38 (1998) 151–156.

[247] W. C. Thompson, in: C. T. Robertson, A. S. Kesselheim (Eds), Blinding as a Solution to Bias, Elsevier Inc., London, 2016, pp. 133–150.

[248] J. Franco-Pedroso, D. Ramos and J. Gonzalez-Rodriguez, Gaussian Mixture Models of Between-Source Variation for Likelihood Ratio Computation from Multivariate Data, PLoS One 11 (2016) e0149958.

[249] C. Champod, F. Taroni, P. Margot, The Dreyfus case – an early debate on conclusions, Int. J. Forensic Doc. Exam. 5 (1999) 446–459.

[250] D. Ramos, Forensic evaluation of the evidence using automatic speaker recognition systems, (Doctoral dissertation), 2007.

[251] J. M. Butler, Forensic DNA Typing: Biology, Technology, and Genetics of STR Markers, Second Ed., Elsevier Academic Press, 2005.

[252] D. J Balding, C. D. Steele, Weight-Of-Evidence for Forensic DNA Profiles, John Wiley & Sons, Ltd, Chichester, 2015.

[253] N. M. Egli, C. Champod, P. Margot, Evidence evaluation in fingerprint comparison and automated fingerprint identification systems-modelling within finger variability, Forensic Sci. Int. 167 (2007) 189–95.

[254] C. Neumann, C. Champod, M. Yoo, T. Genessay, G. Langenburg, Quantifying the weight of fingerprint evidence through the spatial relationship, directions and types of minutiae observed on fingermarks, Forensic Sci Int. 248 (2015) 154–71.

[256] C.G.G. Aitken, G. Zadora, D. Lucy, A two-level model for evidence evaluation. J. Forensic Sci., 52 (2007) 412–419.

[257] G. Zadora, Evaluation of the evidential value of physicochemical data by a Bayesian network approach. J. Chemo., 24 (2010) 346–366.

[258] G. Zadora, D. Ramos, Evaluation of glass samples for forensic purposes – an application of likelihood ratios and an information-theoretical approach. Chemo. Intel. Lab. Sys. 102 (2010) 63–83.

[259] G. Zadora, T. Neocleous, Evidential value of physicochemical data-comparison of methods of database creation. J. Chemo. 24 (2010) 367–378.

[260] G. Zadora, T. Neocleous, Likelihood ratio model for classification of forensic evidence. Anal. Chim. Acta 642 (2009) 266–278.

[261] D. Lucy, G. Zadora, Mixed effects modelling for glass category estimation from glass refractive indices, Forensic Sci. Int. 212 (2011) 189–197.

[262] A. Martyna, K.-E. Sjastad, G. Zadora, D. Ramos, Analysis of lead isotopic ratios of glass objects with the aim of comparing them for forensic purposes, Talanta 105 (2013) 158–166.

[263] A. Martyna, A. Michalska, G. Zadora, Interpretation of FTIR spectra of polymers and Raman spectra of car paints by means of likelihood ratio approach supported by wavelet transform for reducing data dimensionality, Anal. Bioanal. Chem. 407n(2015) 3357–3376.

[264] A. Martyna, G. Zadora, T. Neocleous, A. Michalska, N. Dean, Hybrid approach combining chemometrics and likelihood ratio framework for reporting the evidential value of spectra. Anal.Chim. Acta 931 (2016) 34–46.

[265] A. Michalska, A. Martyna, J. Zieba-Palus, G. Zadora, Application of a likelihood ratio approach in solving a comparison problem of Raman spectra recorded for blue automotive paints. J. Raman Spectrosc. 46 (2015) 772–783.

[266] K. Hoffmann, Statistical Evaluation of the Evidential Value of Human Hairs Possibly Coming from Multiple Sources, J. Forensic Sci. 36 (1991).

[267] I. C. Champod, I. W. Evett, B. Kuchler, Earmarks as evidence: a critical review, J. Forensic Sci. 46 (2001) 1275–1284.

[268] G. Zadora, R. Borusiewicz, J. Zieba-Palus, Differentiation between weathered kerosene and diesel fuel using automatic thermal desorption-GC-MS analysis and the likelihood ratio approach, J. Sep. Sci. 28 (2005) 1467–1475.

[269] G. Pierrini, S. Doyle, C. Champod, T. Taroni, C. Wakelin, D. Lock, Evaluation of preliminary isotopic analysis (13C and 15N) of explosives. A likelihood ratio approach to assess the links between Semtex samples, Forensic Sci. Int. 167 (2007) 43–48.

[270] C. Champod, D. Baldwin, F.Taroni, J. S. Buckleton, Firearm and tool marks identification: the Bayesian approach, AFTE Journal 35 (2003) 307–316.

[271] A. Martyna, D. Lucy, G. Zadora, B.M. Trzcinska, D. Ramos, A. Parczewski, The evidential value of microspectrophotometry measurements made for pen inks, Anal. Meth. 5 (2013) 6788–6795.

[272] A. Bolck, I. Alberink, Variation in likelihood ratios for forensic evidence evaluation of XTC tablets comparison, J. Chemo. 25 (2010) 41–49.

[273] A. Bolck, H. Ni, M. Lopatka, Evaluating score-and feature-based likelihood ratio models for multivariate continuous data: Applied to forensic MDMA comparison, Law, Prob. Risk, 14 (2015) 243–266.

[274] C. Champod, D. Meuwly, The inference of identity in forensic speaker recognition, Speech Com. 31 (2000) 193–203.

[275] T. Ali, L. Spreeuwers, R. Veldhuis, D. Meuwly, Effect of calibration data on forensic likelihood ratio from a face recognition system, IEEE 6th International Conference on Biometrics: Theory, Applications and Systems, BTAS 6712709, 2013.

[276] B.W. Silverman. Density Estimation for Statistics and Data Analysis. Chapman and Hall, London, UK, 1986.

[278] K. M. Pyrek, Forensic Science Under Siege, Elsevier Press, Amsterdam, 2007.

[279] J. Fraser, R. Williams, The contemporary landscape of forensic science, in: J. Fraser, R. Williams (Eds), Handbook of Forensic Science, Willan Publishing, Portland, Oregon, 2009, pp. 1–20.

[280] D. Ramos, J. Gonzalez-Rodriguez, G. Zadora, C. Aitken, Information-Theoretical Assessment of the Performance of Likelihood Ratio Computation Methods, J. Forensic Sci. 58 (2013) 1503–1518.

[281] R. Haraksim, D. Ramos, D. Meuwly and C. E. H. Berger, Measuring coherence of computer-assisted likelihood ratio methods, Forensic Sci. Int. 249 (2015) 123–132.

[282] T. Gneiting, A. Raftery, Strictly proper scoring rules, prediction and estimation, J. Am. Stat. Assoc. 102 (2007) 359–378.

[283] M. Ayer, H.D. Brunk, G. M. Ewing, W. T. Reid, E. Silverman, An empirical distribution function for sampling with incomplete information, Ann. Math. Stat. 26 (1955) 641–647.

[284] D. Ramos, G. Zadora, Information-theoretical feature selection using data obtained by Scanning Electron Microscopy coupled with and Energy Dispersive X-ray spectrometer for the classification of glass traces Anal. Chim. Acta 705 (2011) 207−217.

[285] A. Martyna, G. Zadora, D. Ramos, Forensic comparison of pyrograms using score-based likelihood ratios, J. Anal. Appl. Pyr. 133 (2018) 198–215.

[286] J.M. Roger, et al., Pre-processing Methods, in: S. D. Brown, R. Tauler, B. Walczak (Eds), Comprehensive chemometrics. Chemical and biochemical data analysis, second ed., Elsevier, Oxford, 2020, pp. 1–75.

[287] P. Oliveri, C. Malegori, R. Simonetti, M. Casale, The impact of signal pre-processing on the final interpretation of analytical outcomes - A tutorial, Anal. Chim. Acta. 1058 (2019) 9–17.

[288] P. Lasch, Spectral pre-processing for biomedical vibrational spectroscopy and microspectroscopic imaging, Chemometr. Intell. Lab. Syst. 117 (2012) 100–114.

[289] J. Engel, J. Gerretzen, E. Szymańska, J. J. Jansen, G. Downey, L. Blanchet, L. M. C. Buydens, Breaking with trends in pre-processing?, TrAC 50 (2013) 96–106.

[290] P. Mishra, A. Biancolillo, J. M. Roger, F. Marini, D. N. Rutledge, New data preprocessing trends based on ensemble of multiplepreprocessing techniques, TrAC 132 (2020) 116045.

[291] A. Martyna, A. Menżyk, A. Damin, A. Michalska, G. Martra, E. Alladio, G. Zadora, Improving discrimination of Raman spectra by optimising preprocessing strategies on the basis of the ability to refine the relationship between variance components, Chemom. Intell. Lab. Syst. 202 (2020) 104029.

[292] A. Savitzky, M. Golay, Smoothing and differentiation of data by simplified least squares procedures, Anal. Chem. 36 (1964) 1627–1639.

[293] I. Daubechies, Ten Lectures on Wavelets, CBMS-NSF Regional Conference Series in Applied Mathematics, Philadelphia, USA, 1992.

[294] S. Mallat, A theory for multiresolution signal decomposition: the wavelet representation, IEEE Trans. Pattern Anal. Mach. Intell. 7 (1989) 674–693.

[295] B. Walczak, D. Massart, Wavelets-something for analytical chemistry? TrAC 16 (1997) 451–463.

[296] V. Barclay, R. Bonner, Application of wavelet transforms to experimental spectra: smoothing, denoising, and data set compression, Anal. Chem. 69 (1997) 78–90.

[297] B. Walczak (Ed.), Wavelets in Chemistry, Elsevier: Amsterdam, 2000.

[298] J.-M. Roger, J.-C. Boulet, M. Zeaiter, D.N. Rutledge, Pre-processing Methods, in: S. D. Brown, R. Tauler, B.Walczak (Eds), Comprehensive Chemometrics, Elsevier, Amsterdam, 2020.

[299] K. H. Liland, T. Almøy, B. H. Mevik, Optimal Choice of Baseline Correction for Multivariate Calibration of Spectra, Appl. Spectrosc. 64 (2010) 1007–1016.

[300] D. Wei, S. Chen, Q. Liu, Review of fluorescence suppression techniques in Raman spectroscopy, Appl. Spectrosc. Rev. 20 (2015) 387–406.

[301] C. Lieber, A. Mahadevan-Jansen, Automated method for subtraction of fluorescence from biological Raman spectra, Appl. Spectrosc. 57 (2003) 1363–1367.

[302] J. Zhao, H. Lui, D. McLean, H. Zeng, Automated autofluorescence background subtraction algorithm for biomedical Raman spectroscopy, Appl. Spectrosc. 61 (2007) 1225–1232.

[303] J. Zhao, H. Lui, D. McLean, H. Zeng, Automated autofluorescence background subtraction algorithm for biomedical Raman spectroscopy, Appl. Spectrosc. 61 (2007) 1225–1232.

[304] P. Eilers, A perfect smoother, Anal. Chem. 75 (2003) 3631–3636.

[305] Z. Zhang, S. Chen, Y. Liang, Baseline correction using adaptive iteratively reweighted penalised least squares, Analyst 135 (2010) 1138–1146.

[306] Z. Zhang, S. Chen, Y. Liang, Z.-X. Liu, Q.-M. Zhang, L.-X. Ding, F. Ye, H. Zhou, An intelligent background-correction algorithm for highly fluorescent samples in Raman spectroscopy, J. Raman Spectrosc. 41 (2010) 659–669.

[307] P. Cadusch, M. Hlaing, S. Wade, S. McArthur, P. Stoddart, Improved methods for fluorescence background subtraction from Raman spectra, J. Raman Spectrosc. 44 (2013) 1587–1595.

[308] J. Peng, S. Peng, A. Jiang, J. Wei, C. Li, J. Tan, Asymmetric least squares for multiple spectra baseline correction, Anal. Chim. Acta 683 (2010) 63–68.

[309] C. Ryan, E. Clayton, W. Griffin, S. Sie, D. Cousens, SNIP, a statistic-sensitive background treatment for the quantitative analysis of PIXE spectra in geoscience applications, Nucl. Instrum. Methods Phys. Res. B34 (1988) 396–402.

[310] L. Komsta, Comparison of several methods of chromatographic baseline removal with a new approach based on quantile regression, Anal. Bioanal. Chem. 406 (2014) 1985–1998.

[311] A. Ruckstuhl, M. Jacobson, R. Field, J. Dodd, Baseline subtraction using robust local regression estimation, J. Quant. Spectrosc. Radiat. Transf. 68 (2001) 179–193.

[312] R. J. Barnes, M. S. Dhanoa, S. J. Lister, Standard Normal Variate Transformation and De-Trending of Near-Infrared Diffuse Reflectance Spectra. Appl. Spectrosc. 43 (1989) 772–777.

[313] T. Fearn, The Effect of Spectral Pre-Treatments on Interpretation, NIR news 20 (2009) 15–16.

[314] F. Dieterle, A. Ross, G. Schlotterbeck, H. Senn, Probabilistic quotient normalization as robust method to account for dilution of complex biological mixtures. Application in 1H NMR metabonomics, Anal. Chem. 78 (2006) 4281–4290.

[315] S.M. Kohl, M.S. Klein, J. Hochrein, P.J. Oefner, R. Spang, W. Gronwald, State-of- the art data normalization methods improve NMR-based metabolomic analysis, Metabolomics 8 (2012) 146–160.

[316] J. H. Holland, Adaptation in Natural and Artificial Systems, University of Michigan Press, Ann Arbor, 1975.

[317] S. Forrest, Genetic algorithms: principles of natural selection applied to computation, Science 261 (1993) 872–878.

[318] C. B. Lucasius, G. Kateman, Understanding and using genetic algorithms. Part 1. Concepts, properties and context, Chemometrics Intell. Lab. Syst. 19 (1993) 1–33.

[319] C. B. Lucasius, G. Kateman, Understanding and using genetic algorithms. Part 2. Representation, configuration and hybridization. Chemometrics Intell. Lab. Syst. 25 (1994) 99–145.

[320] C. B. Lucasius, G. Kateman, Gates towards evolutionary large-scale optimization: a software-oriented approach to genetic algorithms—I. General perspective. Comput. Chem. 18 (1994) 127–136.

[321] C. B. Lucasius, G. Kateman, Gates towards evolutionary large-scale optimization: a software-oriented approach to genetic algorithms—II. Toolbox description. Comput. Chem. 18 (1994) 137–156.

[322] D. B. Hibbert, Genetic algorithms in chemistry. Chemometrics Intell. Lab. Syst. 19 (1993) 277–293.

[323] C. B. Lucasius, G. Kateman, Genetic algorithms for large-scale optimization in chemometrics. An application, TrAC 10 (1991) 254–261.

[324] R. Leardi, Genetic algorithms in chemistry, J. Chromatogr. A 1158 (2007) 226–233.

[325] R. M. Jarvis, R. Goodacre, Genetic algorithm optimization for pre-processing and variable selection of spectroscopic data, Bioinformatics 21 (2005) 860–868.

[326] J. Engel, L. Blanchet, B. Bloemen, L. Heuvel, U. Engelke, R. Wevers, L. Buydens, Regularized MANOVA (rMANOVA) in untargeted metabolomics, Anal. Chim. Acta 89 (2015) 1–12.

[327] F. Marini, D. de Beer, N. A. Walters, A. de Villiers, E. Joubert, B. Walczak, Multivariate analysis of variance of designed chromatographic data. A case study involving fermentation of rooibos tea, J Chromatogr A. 1489 (2017) 115–125.

[328] M. Signorile, F. Bonino, A. Damin, S. Bordiga, A novel Raman setup based on magnetic-driven rotation of sample, Top. Catal. 61 (2018) 1491–1498.

[329] A. Damin, et al., European patent No. WO2017077513 (A1), (2017).

[330] P. Beato, E. Schachtl, K. Barbera, Operando Raman spectroscopy applying novel fluidized bed micro-reactor technology. Catal Today 205 (2013) 128–133.

[331] Y. Chua, P. C. Stair, A novel fluidized bed technique for measuring UV Raman spectra of catalysts and adsorbates, J Catal 196 (2000) 66–72.

[332] C. P. Cheng, J. D. Ludowise, G. L. Schrader, Controlled-atmosphere rotating cell for in situ studies of catalysts using laser Raman spectroscopy, Appl Spectrosc 34 (1980) 146–150.

[333] W. Kiefer, H. J. Bernstein, Rotating Raman sample technique for colored crystal powders; resonance Raman effect in solid KMnO4, Appl Spectrosc 25 (1971) 609–613.

[334] D. Rojo-Gama, M. Signorile, F. Bonino, S. Bordiga, Structure– deactivation relationships in zeolites during the methanol-to hydrocarbons reaction: complementary assessments of the coke content, J Catal 351 (2017) 33–48.

[335] M. Signorile, F. Bonino, A. Damin, S. Bordiga, UV-Raman Fingerprint of brønsted sites in MFI zeolites: a useful marker in dealumination detection, J Phys Chem C 120 (2016) 18088–18092.

[336] M. Signorile, F. Bonino, A. Damin, S. Bordiga, In situ resonant UV-Raman spectroscopy of polycyclic aromatic hydrocarbons, J Phys Chem C 119 (2015) 11694–11698.

[337] M. Hazewinkel and Y.N. Subbotin (Eds.), Encyclopedia of Mathematics, Springer, 2001.

[338] R Core Team, R: A Language and Environment for Statistical Computing, R Foundation for Statistical Computing, Vienna, Austria, 2018. URL, https://www.R-project.org/.

[339] J. Kehlet Barton, D.P. Popok, J.F. Black, Thermal analysis of blood undergoing laser photocoagulation, IEEE J. Sel. Top. Quant. 7 (2001) 936–943.

[340] J. F. Black, J. Kehlet Barton, Chemical and structural changes in blood undergoing laser photocoagulation, Photochem. Photobiol. 80 (2004) 89–97.

[341] Y. Ozaki, A. Mizuno, H. Sato, K. Kawauchi, S. Muraishi, Biomedical application of near-infrared Fourier transform Raman spectroscopy. Part I: the 1064-nm excited Raman spectra of blood and methemoglobin, Appl. Spectrosc. 46 (1992) 533–536.

[342] Intrinsic protein fluorescence, in: D.M. Jameson (Ed.), Introduction to Fluorescence, CRC Press, Boca Raton, 2014, pp. 251–276.

[343] N. M. Htun, Y. C. Chen, B. Lim, T. Schiller, G. J. Maghzal, A. L. Huang, K. D. Elgass, J. Rivera, H. G. Schneider, B. R. Wood, R. Stocker, K. Peter, Near-infrared auto- fluorescence induced by intraplaque hemorrhage and heme degradation as marker for high-risk atherosclerotic plaques, Nat. Commun. 8 (2017) 1–16.

[344] U. Neugebauer, A. März, T. Henkel, M. Schmitt, J. Popp, Spectroscopic detection and quantification of heme and heme degradation products, Anal. Bioanal. Chem. 404 (2012) 2819–2829.

[345] E. Nagababu, J. M. Rifkind, Heme degradation during autoxidation of oxyhemoglobin, Biochem. Biophys. Res. Commun. 273 (2000) 839–845.

[346] W. H. Schaefer, T. M. Harris, F. P. Guengerich, Characterization of the enzymatic and nonenzymatic peroxidative degradation of iron porphyrins and cytochrome P-450 heme, Biochem. 24 (1985) 3254–3263.

[347] K. M. Marzec, K. Kochan, A. Fedorowicz, A. Jasztal, K. Chruszcz-Lipska, J. Cz. Dobrowolski, S. Chlopicki, M. Baranska, Raman microimaging of murine lungs: insight into the vitamin A content, Analyst 140 (2015) 2172–2177.

[348] D. Zhang, M. N. Slipchenko, D. E. Leaird, A. M. Weiner, J.-X. Cheng, Spectrally modulated stimulated Raman scattering imaging with an angle-to-wavelength pulse shaper, Opt. Express 21 (2013) 13864–13874.

[349] A. Takamura, D. Watanabe, R. Shimada, T. Ozawa, Comprehensive modeling of bloodstain aging by multivariate Raman spectral resolution with kinetics, Comms. Chem. 2 (2019) 115.

[350] O. Kvalheim, F. Brakstad, Y.-Z. Liang, Preprocessing of analytical profiles in the presence of homoscedastic or heteroscedastic noise, Anal. Chem. 66 (1994) 43–51.

APPENDIX A

TABLE A.1. Pre-processing strategies found using a genetic algorithm (GA).

		RECOVERED: SET °1, REFERENCE: SET °3	RECOVERED: SET °3, REFERENCE: SET °1
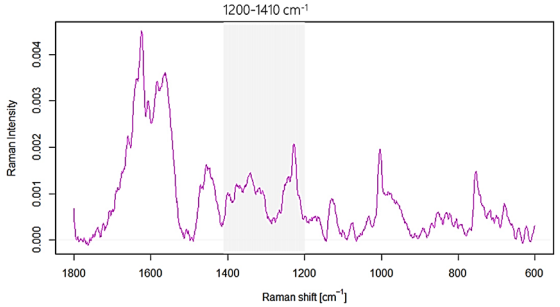	denoising	SG, polynomial degree $p = 4$	SG, polynomial degree $p = 3$
	baseline correction	SNIP, clipping window $w = 26$	SNIP, clipping window $w = 26$
	normalization	SNV	PQN
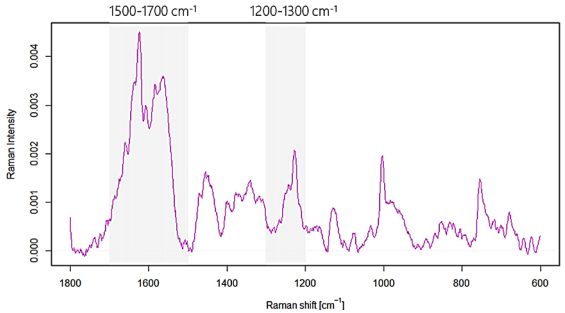	denoising	SG, polynomial degree $p = 4$	DWT, Daubechies Least Asymmetric 8 $d = 10$, t = SURE, c = soft, sd = mad
	baseline correction	reweightedQR, $p = 6$, $q = 0.01$	CWTAsWPLS, $m = 2$, $\lambda = 1 \cdot 10^8$
	normalization	SNV	SNV
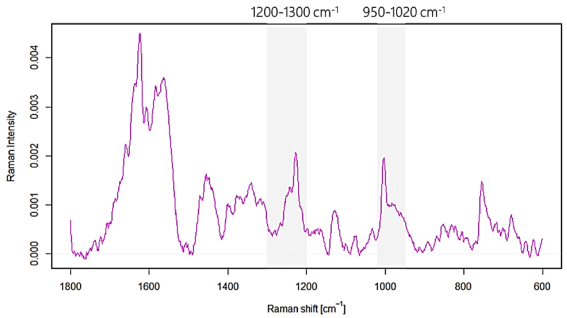	denoising	DWT, Daubechies Least Asymmetric 4 $d = 10$, t = universal, c = soft, sd = mad	DWT, Coiflets 5 $d = 10$, t = universal, c = soft, sd = mad
	baseline correction	RBE, $h = 0.3$, $b = 2.5$	RBE, $h = 0.4$, $b = 2.2$
	normalization	PQN	PQN

d – decomposition level for denoising, t – threshold estimation, c – thresholding policy, sd – dispersion estimate, m – order of differences, λ – penalty, q – quantile, w – weights, p – polynomial degree, h – the proportion of signal points for local regression, b – robustness parameter

TABLE A.1. (continued)

		RECOVERED: SET °1, REFERENCE: SET °3	RECOVERED: SET °3, REFERENCE: SET °1
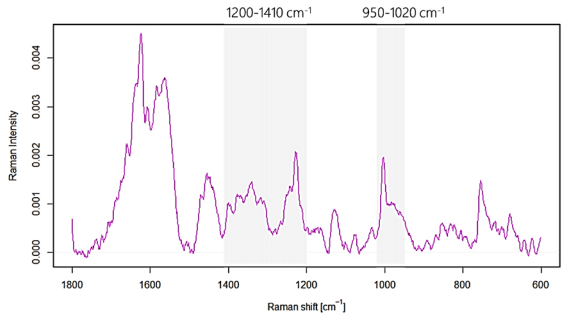	denoising	DWT, Daubechies Least Asymmetric 8 d = 10, t = universal, c = soft, sd = mad	DWT, Coiflets 5 d = 10, t = SURE, c = soft, sd = mad
	baseline correction	pWAsPLS, m = 2, $\lambda = 6 \cdot 10^5$, w = 0.001	multiWAsPLS, m = 2, λ = 10, $\mu = 1 \cdot 10^9$
	normalization	SNV	SNV
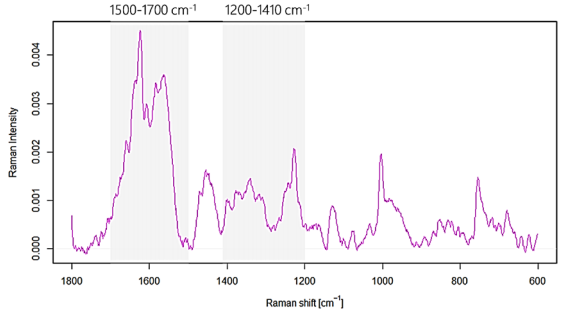	denoising	SG, polynomial degree p = 6	SG, polynomial degree p = 3
	baseline correction	reweightedQR, p = 6, q = 0.01	polyQR, polynomial degree p = 6, q = 0.01
	normalization	SNV	SNV
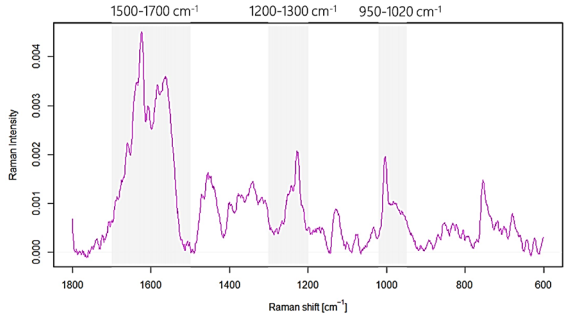	denoising	DWT, Coiflets 1 d = 10, t = universal, c = hard, sd = mad	DWT, Daubechies Least Asymmetric 4 d = 10, t = universal, c = soft, sd = mad
	baseline correction	RBE, h = 0.4, b = 2	CWTAsWPLS, m = 2, $\lambda = 2 \cdot 10^8$
	normalization	PQN	SNV

d – decomposition level for denoising, t – threshold estimation, c – thresholding policy, sd – dispersion estimate, m – order of differences, λ – penalty, q – quantile, w – weights, p – polynomial degree, h – the proportion of signal points for local regression, b – robustness parameter, μ – penalty term

TABLE A.1. (continued)

		RECOVERED: SET °1, REFERENCE: SET °3	RECOVERED: SET °3, REFERENCE: SET °1
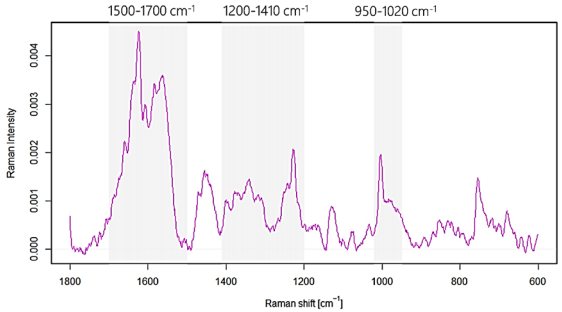	denoising	DWT, Daubechies Least Asymmetric 4 d = 10, t = SURE, c = soft, sd = mad	SG, polynomial degree p = 4
	baseline correction	RBE, h = 0.3, b = 2.5	SNIP, clipping window w = 26
	normalization	PQN	SNV

d – decomposition level for denoising, t – threshold estimation, c – thresholding policy, sd – dispersion estimate, w – weights, h – the proportion of signal points for local regression, b – robustness parameter

TABLE A.2. Pre-processing strategies found using a genetic algorithm (GA).

		RECOVERED: SET °2, REFERENCE: SET °3	RECOVERED: SET °3, REFERENCE: SET °2
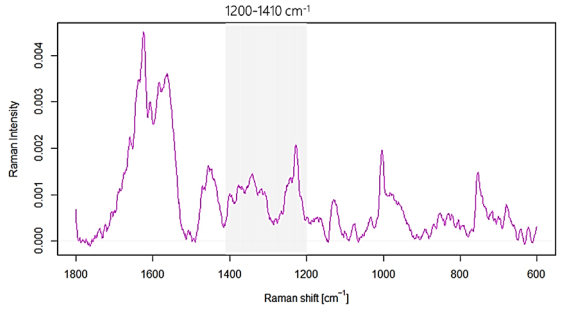	denoising	SG, polynomial degree p = 4	DWT, Daubechies Least Asymmetric 4 d = 10, t = universal, c = soft, sd = mad
	baseline correction	SNIP, clipping window w = 26	RBE, h = 0.4, b = 2
	normalization	SNV	PQN
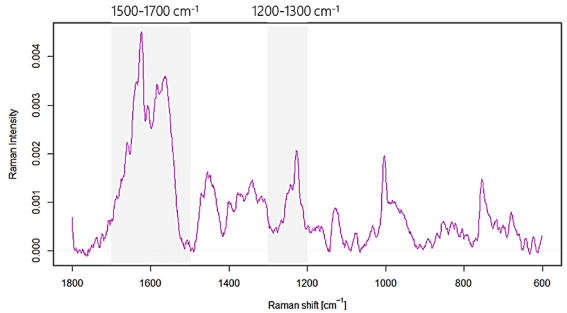	denoising	SG, polynomial degree p = 4	DWT, Coiflets 1 d = 10, t = universal, c = soft, sd = mad
	baseline correction	reweightedQR, p = 6, q = 0.01	polyQR, polynomial degree p = 5, q = 0.05
	normalization	SNV	SNV
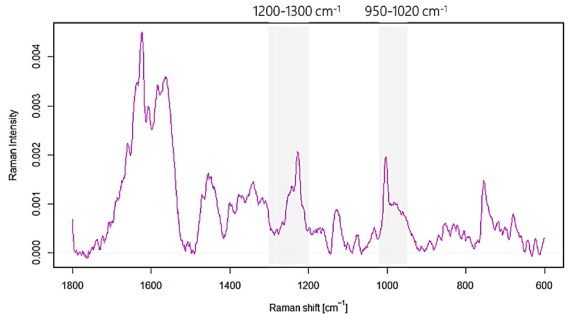	denoising	DWT, Daubechies Least Asymmetric 4 d = 10, t = universal, c = hard, sd = mad	DWT, Daubechies Least Asymmetric 4 d = 10, t = SURE, c = soft, sd = mad
	baseline correction	RBE, h = 0.3, b = 2.5	RBE, h = 0.3, b = 2.5
	normalization	PQN	PQN

d – decomposition level for denoising, t – threshold estimation, c – thresholding policy, sd – dispersion estimate, q – quantile, w – weights, p – polynomial degree, h – the proportion of signal points for local regression, b – robustness parameter

TABLE A.2. (continued)

		RECOVERED: SET °2, REFERENCE: SET °3	RECOVERED: SET °3, REFERENCE: SET °2
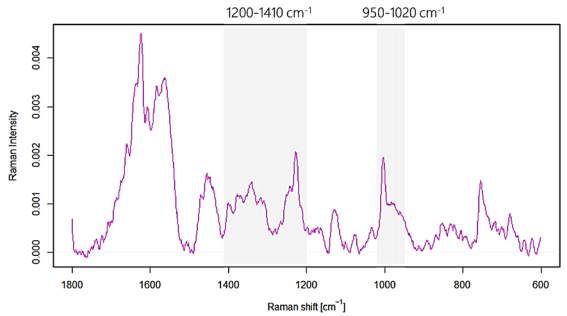	denoising	DWT, Daubechies Least Asymmetric 8 d = 10, t = universal, c = soft, sd = mad	DWT, Coiflets 1 d = 10, t = SURE, c = soft, sd = mad
	baseline correction	pWAsPLS, m = 2, $\lambda = 6 \cdot 10^5$, w = 0.001	polyQR, polynomial degree p = 5, q = 0.05
	normalization	SNV	PQN
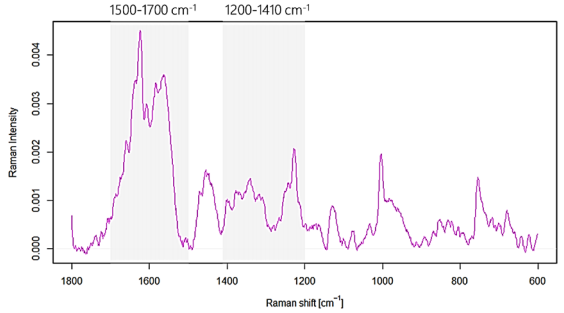	denoising	SG, polynomial degree p = 6	SG, polynomial degree p = 5
	baseline correction	reweightedQR, p = 6, q = 0.01	pWAsPLS, m = 2, $\lambda = 1 \cdot 10^6$, w = 0.001
	normalization	SNV	SNV
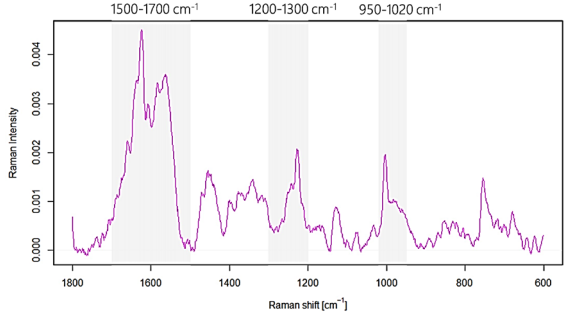	denoising	DWT, Coiflets 1 d = 10, t = universal, c = hard, sd = mad	DWT, Daubechies Least Asymmetric 8 d = 10, t = SURE, c = soft, sd = mad
	baseline correction	RBE, h = 0.4, b = 2	SNIP, clipping window w = 30
	normalization	PQN	SNV

d – decomposition level for denoising, t – threshold estimation, c – thresholding policy, sd – dispersion estimate, m – order of differences, λ – penalty, q – quantile, w – weights, p – polynomial degree, h – the proportion of signal points for local regression, b – robustness parameter

TABLE A.2. (continued)

		RECOVERED: SET °2, REFERENCE: SET °3	RECOVERED: SET °3, REFERENCE: SET °2
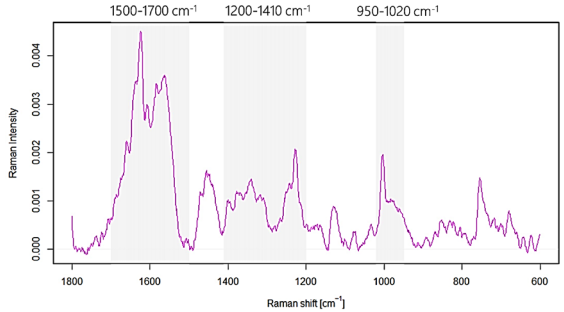	denoising	DWT, Daubechies Least Asymmetric 4 d = 10, t = SURE, c = soft, sd = mad	DWT, Coiflets 1 d = 10, t = SURE, c = soft, sd = mad
	baseline correction	RBE, h = 0.3, b = 2.5	multiWAsPLS, m = 2, λ = 10, $\mu = 1 \cdot 10^8$
	normalization	PQN	SNV

d – decomposition level for denoising, t – threshold estimation, c – thresholding policy, sd – dispersion estimate, m – order of differences, λ – penalty, h – the proportion of signal points for local regression, b – robustness parameter, μ – penalty term

(A)

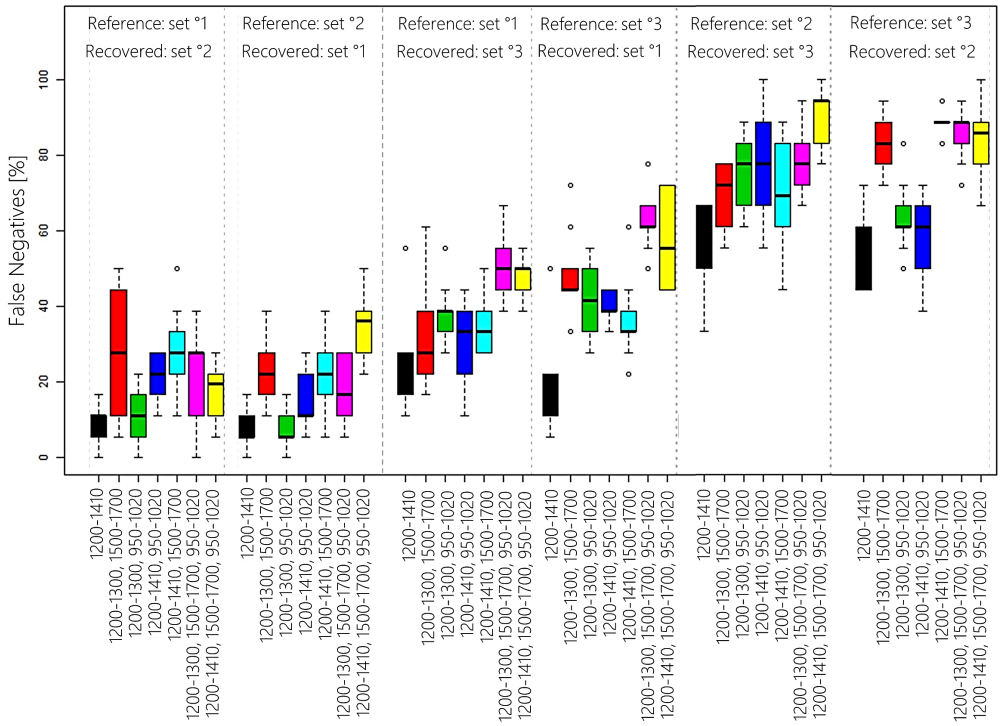

(B)

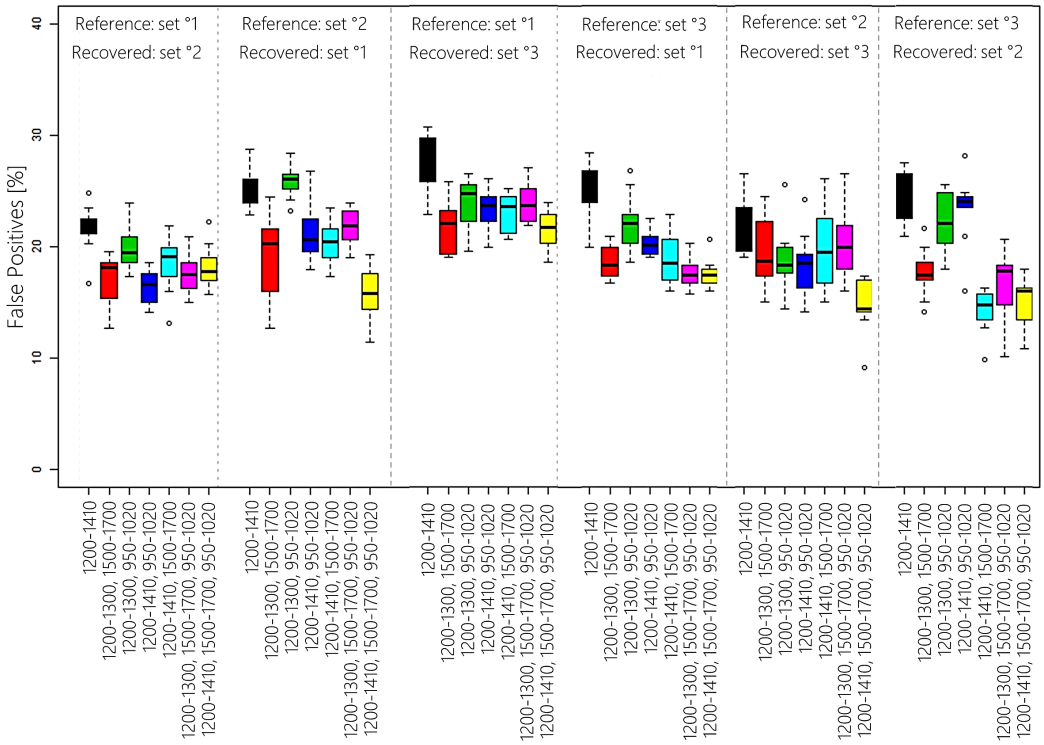

FIGURE A.1.

The levels of false negative (A) and false positive (B) responses of LR models constructed for Raman spectra of bloodstains (developed with all available datasets) prepared using the preprocessing strategies indicated by the genetic algorithm (GA).

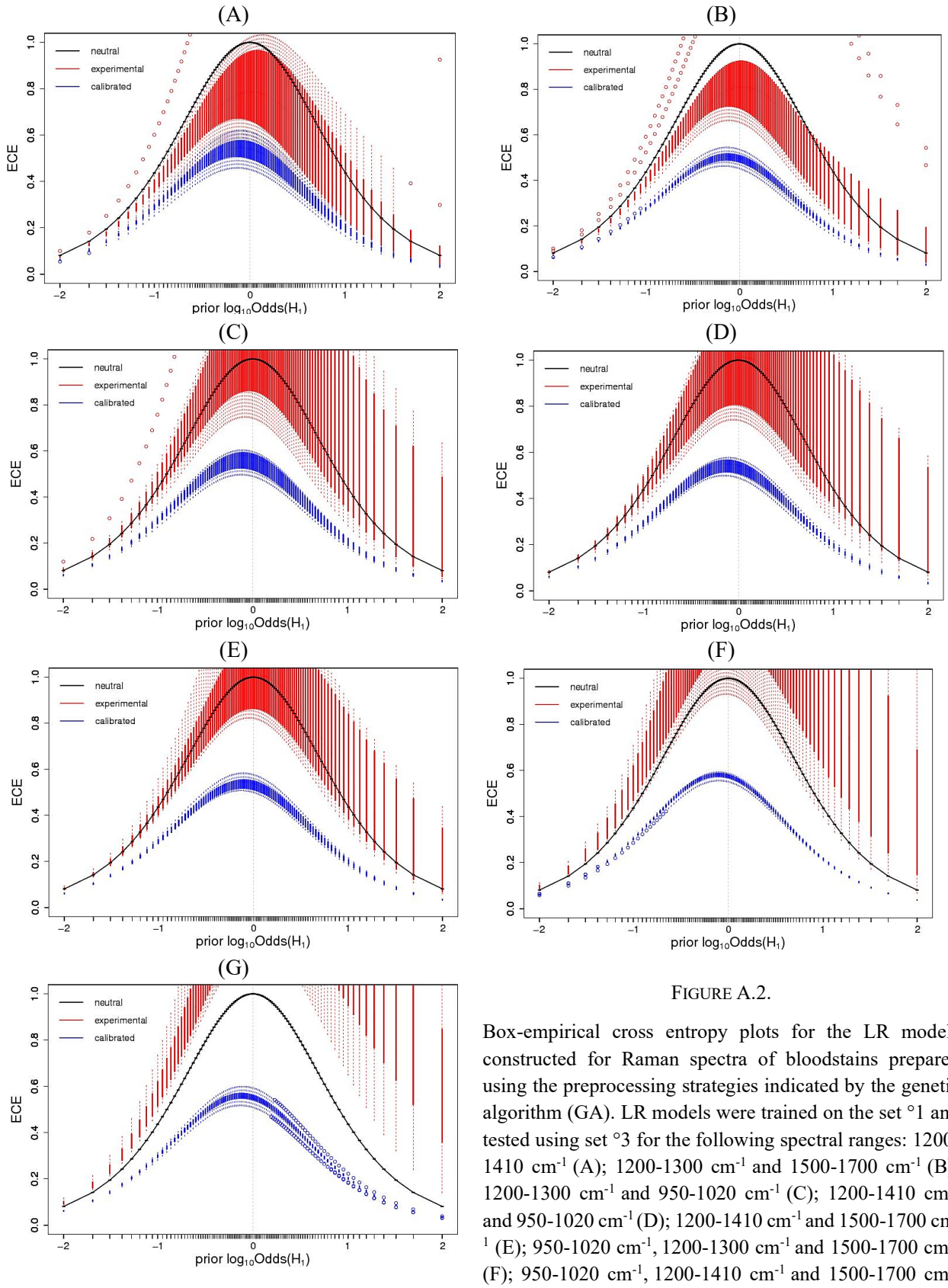

FIGURE A.2.

Box-empirical cross entropy plots for the LR models constructed for Raman spectra of bloodstains prepared using the preprocessing strategies indicated by the genetic algorithm (GA). LR models were trained on the set °1 and tested using set °3 for the following spectral ranges: 1200-1410 cm^{-1} (A); 1200-1300 cm^{-1} and 1500-1700 cm^{-1} (B); 1200-1300 cm^{-1} and 950-1020 cm^{-1} (C); 1200-1410 cm^{-1} and 950-1020 cm^{-1} (D); 1200-1410 cm^{-1} and 1500-1700 cm^{-1} (E); 950-1020 cm^{-1}, 1200-1300 cm^{-1} and 1500-1700 cm^{-1} (F); 950-1020 cm^{-1}, 1200-1410 cm^{-1} and 1500-1700 cm^{-1} (G).

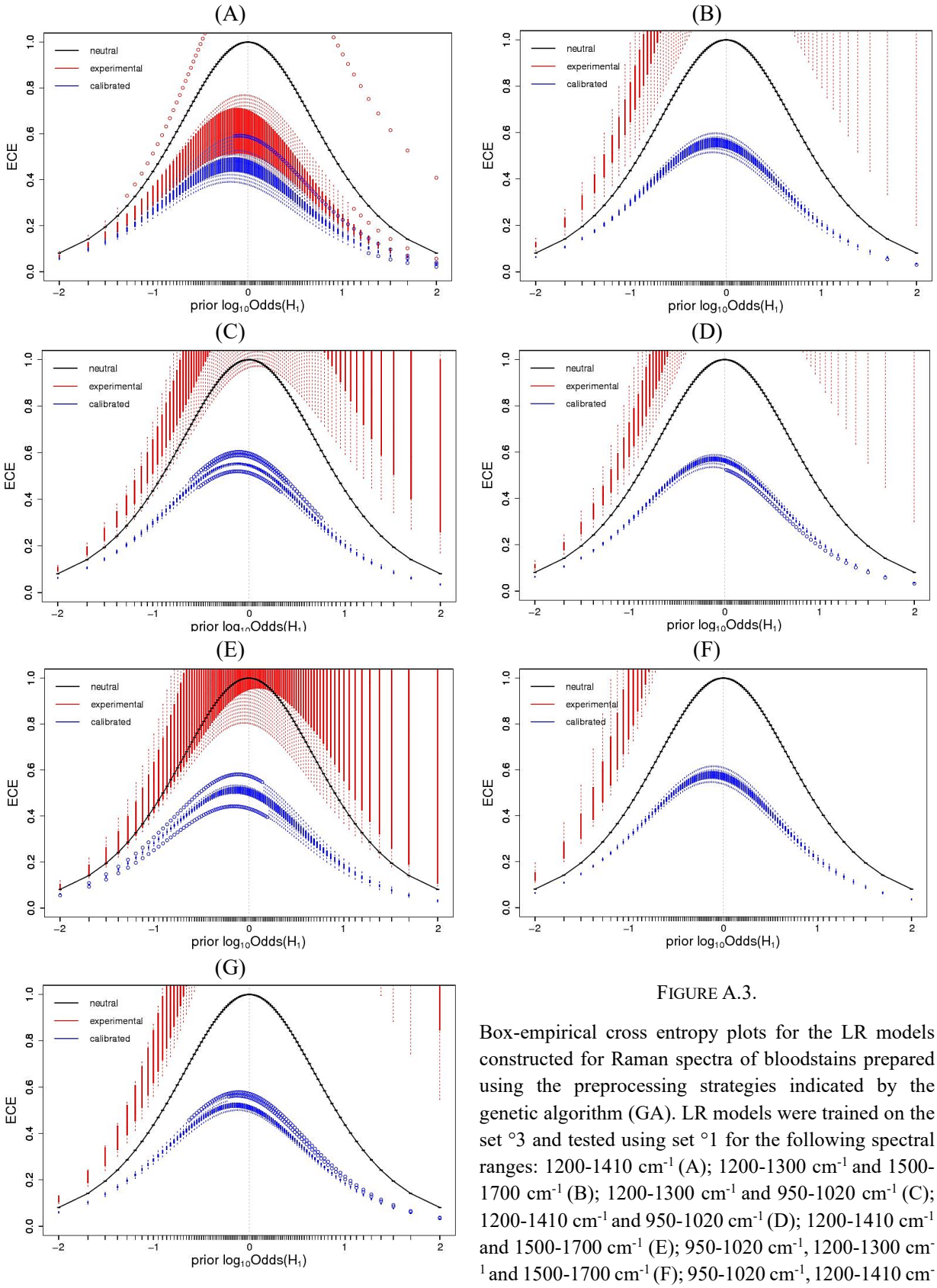

FIGURE A.3.

Box-empirical cross entropy plots for the LR models constructed for Raman spectra of bloodstains prepared using the preprocessing strategies indicated by the genetic algorithm (GA). LR models were trained on the set °3 and tested using set °1 for the following spectral ranges: 1200-1410 cm^{-1} (A); 1200-1300 cm^{-1} and 1500-1700 cm^{-1} (B); 1200-1300 cm^{-1} and 950-1020 cm^{-1} (C); 1200-1410 cm^{-1} and 950-1020 cm^{-1} (D); 1200-1410 cm^{-1} and 1500-1700 cm^{-1} (E); 950-1020 cm^{-1}, 1200-1300 cm^{-1} and 1500-1700 cm^{-1} (F); 950-1020 cm^{-1}, 1200-1410 cm^{-1} and 1500-1700 cm^{-1} (G).

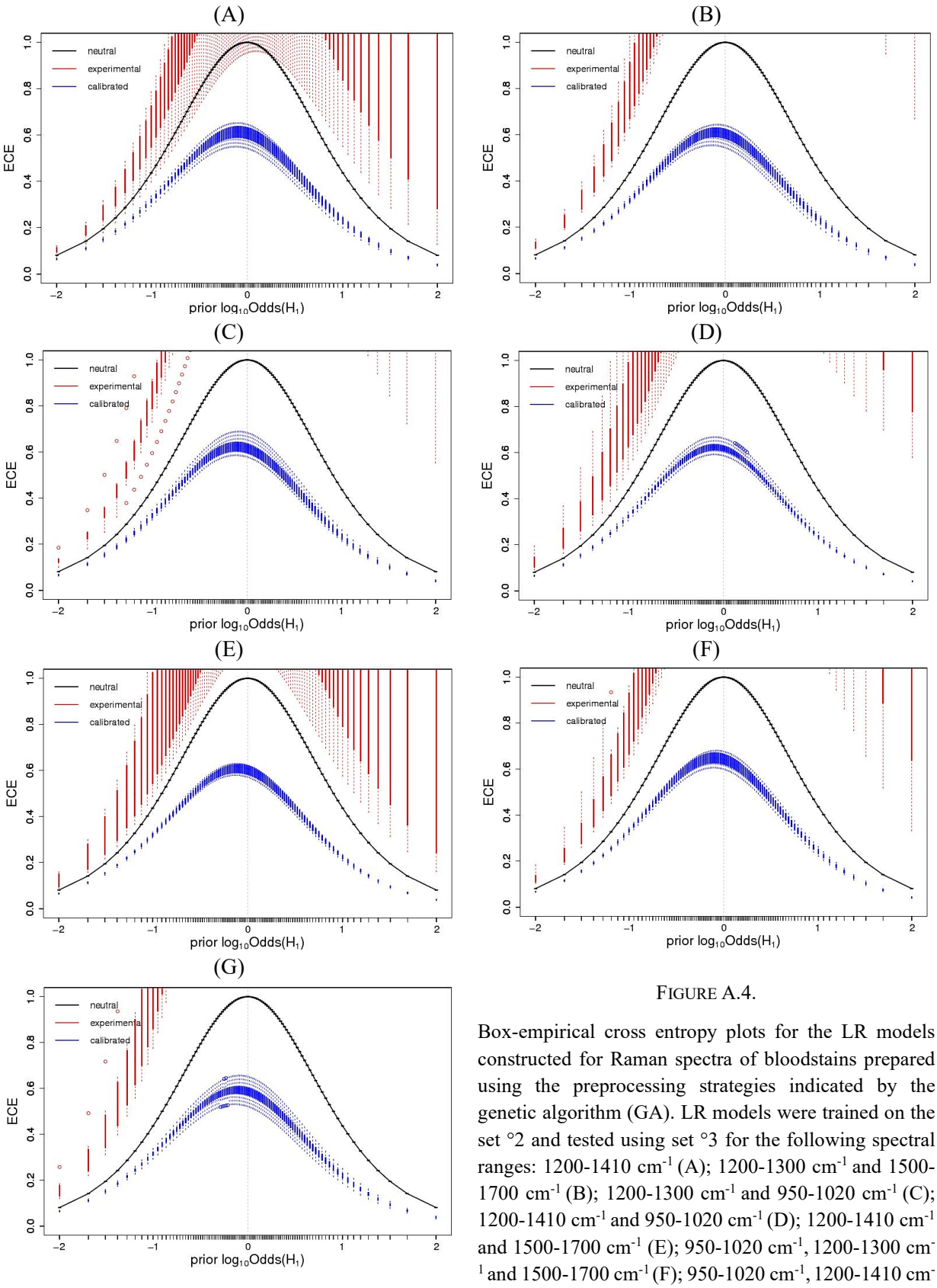

FIGURE A.4.

Box-empirical cross entropy plots for the LR models constructed for Raman spectra of bloodstains prepared using the preprocessing strategies indicated by the genetic algorithm (GA). LR models were trained on the set °2 and tested using set °3 for the following spectral ranges: 1200-1410 cm^{-1} (A); 1200-1300 cm^{-1} and 1500-1700 cm^{-1} (B); 1200-1300 cm^{-1} and 950-1020 cm^{-1} (C); 1200-1410 cm^{-1} and 950-1020 cm^{-1} (D); 1200-1410 cm^{-1} and 1500-1700 cm^{-1} (E); 950-1020 cm^{-1}, 1200-1300 cm^{-1} and 1500-1700 cm^{-1} (F); 950-1020 cm^{-1}, 1200-1410 cm^{-1} and 1500-1700 cm^{-1} (G).

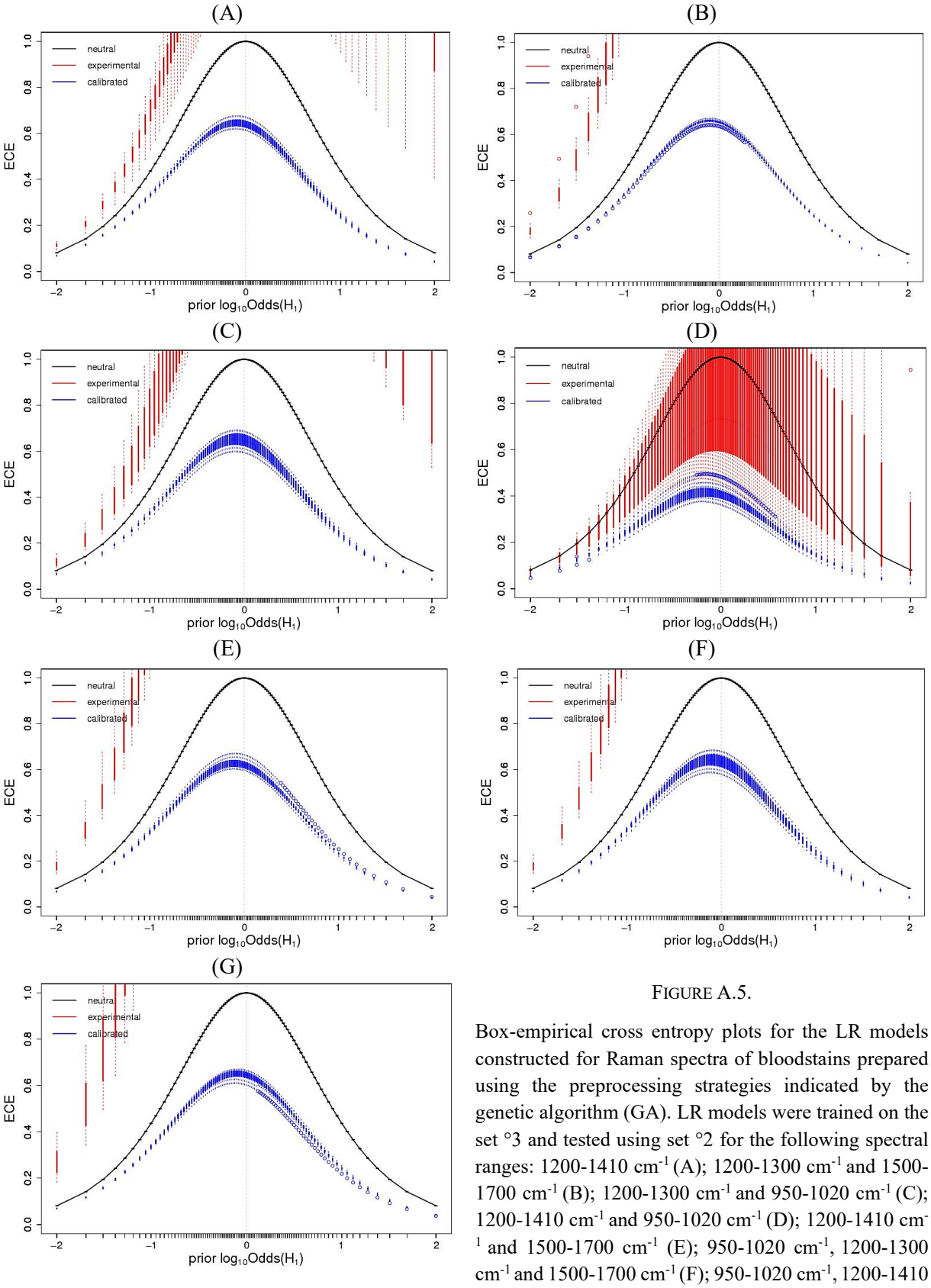

FIGURE A.5.

Box-empirical cross entropy plots for the LR models constructed for Raman spectra of bloodstains prepared using the preprocessing strategies indicated by the genetic algorithm (GA). LR models were trained on the set °3 and tested using set °2 for the following spectral ranges: 1200-1410 cm^{-1} (A); 1200-1300 cm^{-1} and 1500-1700 cm^{-1} (B); 1200-1300 cm^{-1} and 950-1020 cm^{-1} (C); 1200-1410 cm^{-1} and 950-1020 cm^{-1} (D); 1200-1410 cm^{-1} and 1500-1700 cm^{-1} (E); 950-1020 cm^{-1}, 1200-1300 cm^{-1} and 1500-1700 cm^{-1} (F); 950-1020 cm^{-1}, 1200-1410 cm^{-1} and 1500-1700 cm^{-1} (G).

APPENDIX B

ALICJA MENŻYK

Address of residence: Aleksandra Fredry 34, 41–400 Myslowice, Poland
Phone number: +48 660 285 608
E-mail: alicja.menzyk@us.edu.pl

EMPLOYMENT HISTORY

26.04.2021–	**Research and Teaching Assistant** Institute of Chemistry, Faculty of Science and Technology, University of Silesia in Katowice
04.01.2021–	**Forensic Science Technician** Microtraces Analysis Section, Institute of Forensic Research, Krakow, Poland (part-time employment)
07.10.2019– –19.02.2021	**Research and Teaching Assistant** Institute of Chemistry, Faculty of Science and Technology, University of Silesia in Katowice (part-time employment)

EDUCATION

2015–	**Doctoral Programme in Chemical Sciences**, Institute of Chemistry, Faculty of Science and Technology, University of Silesia in Katowice, Poland **Title of the Thesis**: Toward a Raman-based approach for estimating the time elapsed since bloodstains deposition – Development of a novel framework for blood evidence evaluation
2013–2015	**Master's degree** in Chemistry (specialization: medicinal chemistry), Institute of Chemistry, University of Silesia in Katowice, Poland **Title of the Thesis**: Zastosowanie chromatografii cienkowarstwowej w badaniach tuszy pieczątkowych dla potrzeb wymiaru sprawiedliwości
2010–2013	**Bachelor's degree** in (specialization: medicinal chemistry), Institute of Chemistry, University of Silesia in Katowice, Poland **Title of the Thesis**: Zastosowanie techniki GC/MS do wykrywania morfiny i jej metabolitów w moczu

RESEARCH EXPERIENCE

10.2019–02.2020	Erasmus+ traineeship at the Università degli Studi di Genova (Italy); Spectroscopic studies (FT-NIR, FTIR, and UV-VIS) on bloodstains' degradation processes
10.2018–03.2019	Erasmus+ traineeship at the Università degli Studi di Torino (Italy); Research aimed at establishing a bloodstains' supervised aging procedure
10.2017–01.2018	Erasmus+ traineeship at the Università degli Studi di Torino (Italy); Raman studies on bloodstains' degradation processes
17.06–08.07.2017	Research stay at the Università degli Studi di Torino (Italy); Preliminary research on the feasibility of bloodstains dating using Raman spectroscopy
08–10.2015	Erasmus+ traineeship in the CINQUIFOR research group at the La Universidad de Alcalá (Spain); Forensic applications of vibrational spectroscopy
09–10.2014	Traineeship at the Sapienza Università di Roma (Dipartimento di Chimica e Tecnologie del Farmaco); Separation of racemic mixtures of amino acid derivatives using UFLC-DAD
03–26.02.2014	Traineeship at the KU Leuven (Faculty of Engineering Technology), Gent (Belgium); Ultra- and nanofiltration of protein hydrolysates and their analysis by AAS, HPLC-SE, IC (Ion Chromatography), TOC (Total Organic Carbon)

COURSES ATTENDED

13.10.2020	Scientific Foundations for Bloodstain Pattern Analysis, International Association of Bloodstain Pattern Analysts (online webinar)
13–17.01.2020	School of Multivariate Analysis, Department of Pharmacy, University of Genoa, Genova, Italy
11–15.11.2019	School of Experimental Design, Department of Pharmacy, University of Genoa, Genova, Italy
09–13.09.2019	Basic Bloodstain Pattern Analysis Course, Loci Forensics B.V., Nieuw-Vennep, Netherlands
13–15.09.2016	FORSTAT workshop – Forensic Evidence Evaluation Problems and Applications, Krakow, Poland
28–30.06.2016	SEDY (Security dyes) workshop, National Forensic Laboratory, Ljubljana, Slovenia

RESEARCH ACHIEVEMENTS

a) publications (the total impact factor: 19.114, *h*-index: 4)

1. A. Martyna, **A. Menżyk**, A. Damin, A. Michalska, G. Martra, E. Alladio, G. Zadora, Improving discrimination of Raman spectra by optimising preprocessing strategies on the basis of the ability to

refine the relationship between variance components, *Chemometrics and Intelligent Laboratory Systems* 2020 (202) 104029, **IF=2.786**.

2. **A. Menżyk**, A. Damin, A. Martyna, E. Alladio, M. Vincenti, G. Martra, G. Zadora, Toward a novel framework for bloodstains dating by Raman spectroscopy: how to avoid sample photodamage and subsampling errors, *Talanta* 2020 (209) 120565, **IF=4.916**.

3. G. Zadora, **A. Menżyk**, In the pursuit of the holy grail of forensic science – Spectroscopic studies on the estimation of time since deposition of bloodstains, *Trends in Analytical Chemistry* 2018 (105) 137–165, **IF= 7.621**.

4. **A. Menżyk**, A. Martyna, G. Zadora, Evidential value of polymeric materials - chemometric tactics for spectral data compression combined with likelihood ratio approach, *Analyst* 2017 (142) 3867–3888, **IF= 3.791**.

5. **A. Menżyk**, G. Zadora, M. Sajewicz, Physicochemical analysis of inks and methods of evidence evaluation - a review, *Problems of Forensic Sciences* 2015 (104) 245–278.

6. **A. Menżyk**, G. Zadora, M. Sajewicz, Physicochemical analysis of ink - dating and establishing the sequence of intersecting lines of ink entries, *Problems of Forensic Sciences* 2015 (104) 279–302.

b) popular science publications

1. Menżyk A., Ślady mówią, *Gazeta Uniwersytecka UŚ* 2020 (208) 24–26.

2. Menżyk A., Letting the traces speak, *No Limits* 2020 (2) 30–31.

c) book chapters

1. Menżyk A., Zadora G., Wybrane metody instrumentalne w datowaniu plam krwawych dla celów sądowych, [w:] Bioanalityka, [Ed.:] Staneczko-Baranowska I., Buszewski B., Wydawnictwo Naukowe PWN SA.

2. Menżyk A., Zadora G., Recent advances in the forensic dating of blood traces: A minireview, [in:] Handbook of Bioanalytics, [Ed.:] Staneczko-Baranowska I., Buszewski B., Springer (**accepted**).

d) conference talks (presented in person)

1. **A. Menżyk**, G. Zadora, Pogoń za (nie)możliwym, czyli kilka refleksji nad datowaniem plam krwawych, IV Konferencja Młodych Chemików Sądowych, 31/05–1/06.2019, Bialystok, Poland (**best young speaker award**).

2. **A. Menżyk**, A. Martyna, G. Zadora, A. Damin, G. Martra, M. Vincenti, Problem datowania plam krwawych dla potrzeb wymiaru sprawiedliwości. W poszukiwaniu panaceum, Seminarium naukowe Instytutu Ekspertyz Sądowym im. Prof. dra Jana Sehna, 02/04/2019, Krakow, Poland.

3. **A. Menżyk**, A. Martyna, A. Damin, G. Zadora, G. Martra, M. Vincenti, E. Alladio, Beyond a reasonable doubt – Combining analytical methods with likelihood ratio approach for situating blood traces in time, Workshop „The use of multivariate statistics in clinical and forensic applications," 10/01/2019, Turin, Italy (**invited lecture**).

4. **A. Menżyk,** G. Zadora, Czy to tylko kwestia czasu? - Problem datowania dla potrzeb wymiaru sprawiedliwości, „Pomiędzy Naukami" Zjazd Fizyków i Chemików – VII Ogólnopolska Konferencja dla Studentów i Doktorantów, 14/09/2018, Chorzow, Poland.

5. **A. Menżyk,** A. Damin, A. Martyna, G. Zadora, G. Martra, M. Vincenti, E. Alladio, The quest for the 'Holy Grail' of forensic science – dating blood traces with a chemometric-enhanced Raman spectroscopy, 8th European Academy of Forensic Science Conference, 29–31/08/2018, Lyon, France.

6. **A. Menżyk,** A. Martyna, A. Damin, G. Zadora, G. Martra, M. Vincenti, E. Alladio, Ramanowskie datowanie plam krwawych – osiągalny cel czy utopijna wizja?, X Polska Konferencja Chemii Analitycznej, 1–5/07/2018, Lublin, Poland.

7. **A. Menżyk,** A. Damin, A. Martyna, G. Zadora, G. Martra, M. Vincenti, E. Alladio, A question of time - Estimating the age of bloodstains with Raman spectroscopy, Advanced Techniques of Vibrational Spectroscopy, 21–22/06/2018, Krakow, Poland.

8. **A. Menżyk,** G. Zadora, Datowanie plam krwawych – pięta achillesowa współczesnych nauk sądowych, „Pomiędzy Naukami" Zjazd Fizyków i Chemików – VI Ogólnopolska Konferencja dla Studentów i Doktorantów, 15/09/2017, Chorzow, Poland.

9. **A. Menżyk,** A. Martyna, G. Zadora, Czy próbka porównawcza i dowodowa stanowiły niegdyś całość? – wykorzystanie hybrydowych modeli ilorazu wiarygodności w ocenie wartości dowodowej widm NIR oraz FTIR materiałów polimerowych, Sympozjum Młodych Naukowców Wydziału Fizyki, 9–10/06/2017, Warszawa, Poland.

10. **A. Menżyk,** A. Martyna, G. Zadora, FT-IR versus NIR - porównanie efektywności hybrydowych modeli ilorazu wiarygodności w ocenie wartości dowodowej widm materiałów polimerowych, VI Konferencja Chemometria i Metrologia w Analityce, 1–3/03/2017, Poznan, Poland.

11. **A. Menżyk,** A. Martyna, G. Zadora, Materiały polimerowe jako niemy świadek – ocena danych spektroskopowych z wykorzystaniem modeli ilorazu wiarygodności, II Ogólnopolska Konferencja Naukowa Krimed „Metody badawcze w kryminalistyce i medycynie sądowej", 18/11/2016, Lublin, Poland.

12. **A. Menżyk,** A. Martyna, G. Zadora, Szacowanie wartości dowodowej materiałów polimerowych – chemometryczna strategia kompresji danych wielowymiarowych w celu konstrukcji modeli ilorazu wiarygodności, „Pomiędzy Naukami" Zjazd Fizyków i Chemików – V Ogólnopolska Konferencja dla Studentów i Doktorantów, 16/09/2016, Chorzow, Poland.

e) co-authored conference talks (the name of the presenting author is underlined)

1. G. Zadora, A. Martyna, **A. Menżyk**, A. Michalska, Metody obliczeniowe w chemii sądowej, Seminarium naukowe Jagiellońskiego Centrum Rozwoju Leków (JCET), 08/11/2019, Krakow, Poland.

2. G. Zadora, A. Martyna, A. Michalska, **A. Menżyk**, Hybrid likelihood ratio models – recent developments, X Colloquium Chemiometricum Mediterraneum, 12–14/06/2019, Menorca, Spain.

3. A. Martyna, **A. Menżyk**, G. Zadora, A. Damin, G. Martra, M. Vincenti, E. Alladio, Optimizing the pre-processing strategy of Raman spectra through genetic algorithms – a step toward reliable dating of blood traces, X Colloquium Chemiometricum Mediterraneum, 12–14/06/2019, Menorca, Spain.

4. G. Zadora, A. Martyna, A. Michalska, **A. Menżyk**, Chemik analityk jako biegły sądowy, IV Konferencja Młodych Chemików Sądowych, 31/05–1/06.2019, Bialystok, Poland.

5. G. Zadora, A. Martyna, A. Michalska, **A. Menżyk**, Współczesne podejście do oceny wiarygodności wersji zdarzenia, Seminarium Naukowe Polskiego Towarzystwa Kryminalistycznego, 26/04/2019, Warszawa, Poland.

6. A. Martyna, **A. Menżyk**, A. Damin, G. Zadora, G. Martra, M. Vincenti, E. Alladio, Optymalizacja procedury przygotowania widm Ramana do modeli ilorazu wiarygodności w ocenie wieku plam krwawych, VII Konferencja „Chemometria i Metrologia w Analityce", 6–8/03/2019, Poznan, Poland.

7. G. Zadora, A. Martyna, A. Michalska, **A. Menżyk**, Walidacja hybrydowych modeli ilorazu wiarygodności, VII Konferencja „Chemometria i Metrologia w Analityce", 6–8/03/2019, Poznan, Poland.

8. **A. Menżyk**, G. Zadora, A. Damin, A. Martyna, G. Martra, M. Vincenti, E. Alladio, To tylko kwestia czasu? – W poszukiwaniu nowej metodyki datowania plam krwawych, XXIII Konferencja „Nowoczesne metody instrumentalne w analizie śladowej", 10–11/12/2018, Krakow, Poland.

9. G. Zadora, A. Martyna, A. Michalska, **A. Menżyk**, Hybrydowe modele ilorazu wiarygodności, IV Ogólnopolska Konferencja „Fizykochemiczne badania śladów kryminalistycznych", 20–23/11/2018, Bronislawow, Poland.

10. A. Martyna, G. Zadora, A. Michalska, **A. Menżyk**, Likelihood ratio models for physicochemical data – creation and applications, FORSTAT Workshop, 18–20/09/2018, Linköping, Sweden.

11. A. Martyna, G. Zadora, A. Michalska, **A. Menżyk**, Likelihood ratio models for physicochemical data – creation and applications, European Union Agency For Law Enforcement Training (CEPOL), 10–13/09/2018, Budapest, Hungary.

12. G. Zadora, A. Martyna, **A. Menżyk**, A. Michalska, H.-E. Gäbler, A. Bahr, Hybrid likelihood ratio models, 8th European Academy of Forensic Science Conference, 29–31/08/2018, Lyon, France.

13. G. Zadora, A. Martyna, **A. Menżyk**, A. Michalska, H.-E. Gäbler, A. Bahr, Hybrydowe modele ilorazu wiarygodności, X Polska Konferencja Chemii Analitycznej, 1–5/07/2018, Lublin, Poland.

14. A. Martyna, G. Zadora, A. Michalska, P. Własiuk, **A. Menżyk**, Interpreting highly multivariate data for forensic purposes within the likelihood ratio framework, MULTI-modal Imaging of FOREnsic SciEnce Evidence tools for Forensic Science, Action CA16101 Conference, Uncovering Forensic Imaging Capabilities, 6–9/11/2017, Krakow, Poland.

15. G. Zadora, A. Martyna, A. Michalska, P. Własiuk, **A. Menżyk**, Interpretacja danych fizykochemicznych z wykorzystaniem testu ilorazu wiarygodności i metod chemometrycznych, VI Konferencja Chemometria i Metrologia w Analityce, 1–3/03/2017, Poznan, Poland.

16. G. Zadora, A. Martyna, A. Michalska, P. Własiuk, **A. Menżyk**, Likelihood ratio models supported by chemometric tools – overview of recent models, Symposium on Chemometrics in Forensic Sciences, 26/01/2017, Turin, Italy.

f) conference posters

1. **A. Menżyk**, A. Martyna, G. Zadora, A. Damin, G. Martra, M. Vincenti, Toward a novel framework for bloodstains dating - Development of an improved Raman-based procedure using sample rotation, Seminarium "Nano and Fast Vibrational Spectroscopy", 17–18/06/2019, Krakow, Poland.

2. **A. Menżyk**, A. Martyna, G. Zadora, A. Damin, G. Martra, M. Vincenti, E. Alladio, pierwszy krok ku nowej metodyce datowania plam krwawych – Charakterystyka procesów degradacyjnych

z wykorzystaniem spektroskopii Ramana, IV Konferencja Młodych Chemików Sądowych, 31/05–1/06.2019, Bialystok, Poland.

3. **A. Menżyk**, A. Martyna, G. Zadora, A. Damin, G. Martra, M. Vincenti, Krytycznym okiem o ramanowskim datowaniu plam krwawych, XIII Seminarium Naukowe „Aktualne Problemy Chemii Analitycznej", 17/05/2019, Katowice, Poland (**best poster award**).

4. **A. Menżyk,** A. Martyna, G. Zadora, A. Damin, G. Martra, M. Vincenti, E. Alladio, The many facets of pre-processing in Raman spectroscopy of biological samples – a step toward reliable dating of blood traces, 8th European Academy of Forensic Science Conference, 29–31/08/2018, Lyon, France.

5. **A. Menżyk,** G. Zadora, A. Damin, A. Martyna, G. Martra, M. Vincenti, E. Alladio, Ramanowska charakterystyka zmian starzeniowych plam krwawych - Rotacja próbki jako antidotum na problem niejednorodności próbki, X Polska Konferencja Chemii Analitycznej, 1–5/07/2018, Lublin, Poland.

6. **A. Menżyk,** A. Martyna, A. Damin, G. Zadora, G. Martra, M. Vincenti, E. Alladio, Rola algorytmów genetycznych w optymalizacji procedury wstępnego przygotowania widm ramanowskich, X Polska Konferencja Chemii Analitycznej, 1–5/07/2018, Lublin, Poland.

7. **A. Menżyk**, A. Damin, A. Martyna, G. Zadora, G. Martra, M. Vincenti, E. Alladio, Datowanie plam krwawych z wykorzystaniem spektroskopii Ramana, XII Seminarium Naukowe „Aktualne Problemy Chemii Analitycznej", 11/05/2018, Katowice, Poland.

8. **Menżyk A**., A. Martyna, G. Zadora, FTIR versus NIR - chemometric solution to the problem of spectral data evaluation with likelihood ratio (LR) approach, 10th International Conference on Forensic Inferences and Statistics, 5–8/09/2017, Minneapolis, USA.

9. **A. Menżyk**, G. Zadora, Rezonansowa spektroskopia Ramana jako potencjalne narzędzie datowania plam krwawych, Sympozjum Młodych Naukowców Wydziału Fizyki, 9–10/06/2017, Warszawa, Poland.

10. **A. Menżyk**, G. Zadora, W poszukiwaniu świętego Graala współczesnej kryminalistyki - produkty degradacji hemoglobiny jako potencjalne źródło informacji o czasie powstania plam krwawych, XI Seminarium Naukowe „Aktualne Problemy Chemii Analitycznej", 12/05/2017, Katowice, Poland (**best poster award**).

11. **A. Menżyk**, A. Martyna, G. Zadora, Optymalizacja modeli ilorazu wiarygodności poprzez wybór odpowiedniej metody wstępnego przygotowania danych, VI Konferencja Chemometria i Metrologia w Analityce, 1–3/03/2017, Poznan, Poland.

12. **A. Menżyk**, A. Martyna, G. Zadora, Materiały polimerowe w rękach biegłego sądowego - ocena wartości dowodowej widm spektroskopowych z wykorzystaniem ilorazu wiarygodności, XXI Konferencja „Nowoczesne metody instrumentalne w analizie śladowej", 8–9/12/2016, Warszawa, Poland (**best poster award**).

13. **A. Menżyk**, G. Zadora, A. Martyna, Analiza porównawcza polimerowych części samochodowych i przedmiotów codziennego użytku z wykorzystaniem spektroskopii w bliskiej podczerwieni, X Seminarium Naukowe „Aktualne Problemy Chemii Analitycznej", 13/05/2016, Katowice, Poland.

g) co-authored conference posters (the name of the presenter is underlined)

1. A. Martyna, **A. Menżyk**, G. Zadora, A. Damin, G. Martra, M. Vincenti, E. Alladio, Statyczna czy rotacyjna? – Porównanie ramanowskich procedur pomiarowych służących datowaniu plam krwawych,

XXIII Konferencja „Nowoczesne metody instrumentalne w analizie śladowej”, 10–11/12/2018, Krakow, Poland.

2. A. Martyna, G. Zadora, **A. Menżyk**, A. Michalska, Rozwój modeli ilorazu wiarygodności w interpretacji danych dla potrzeb wymiaru sprawiedliwości, 61 Zjazd Naukowy Polskiego Towarzystwa Chemicznego, 17–21/09/2018, Krakow, Poland.

CONFERENCE ORGANIZING ACTIVITIES

Od 2019	The organizer of the conference for young scientists SCIENCE BEYOND DISCIPLINES, organized by the Graduate Student Government of the Faculty of Science and Technology at the University of Silesia in Katowice, Poland